Thick binder free electrodes for Li-ion battery using Spark Plasma Sintering and templating approach

Rakesh Elango

Thèse de Doctorat

Mention : Chimie
Spécialité : Chimie et Electrochimie des Solides

présentée à ***l'Ecole Doctorale en Sciences Technologie et Santé (ED 585)***

de l'Université de Picardie Jules Verne

par

Rakesh Elango

pour obtenir le grade de Docteur de l'Université de Picardie Jules Verne

Thick binder free electrodes for Li-ion battery using Spark Plasma Sintering and templating approach

Soutenue le 13 septembre 2018, après avis des rapporteurs, devant le jury d'examen :

M. J.-P. PEREIRA-RAMOS, Directeur de Recherche, CNRS	**Rapporteur**
M. P. ROZIER, Maître de Conférences -HDR	**Rapporteur**
M^{me} C. LABERTY, Professeur	**Examinateur**
M^{me} C. GUERY, Professeur	**Examinateur**
M. C. DELACOURT, Chargé de recherche, CNRS-HDR	**Directeur de thèse**
M. V. SEZNEC, Maître de Conférences	**Co-encadrant**
M. M. MORCRETTE, Ingénieur de Recherche CNRS	**Invité**

Acknowledgments

This Ph.D thesis would not have been possible without the support of the several people who helped me during these three years.

First, I want to thank the members of the jury of my PhD defense, the professors Jean Pierera Ramos (GESMAT, Thiais), Patrick Rozier (CIRIMAT, Toulouse), Christel Laberty (UPMC, Paris) and Claude Guery (LRCS, Amiens) for having found the time to read my thesis and for their precious insights on this work.

Charles Delacourt, thank you for your precious advises and for having dealt with my stubbornness and anxiety for the past three years.

Vincent, you have been much more than a PhD supervisor, you have been a role model: in every difficult moment of my PhD, a ten minutes conversation with you was sufficient to re-find my enthusiasm and my will to get back to work. Thank you for all the suggestions and the corrections that made me grown up during these three years.

I want to thank the two important people: Mathieu Morcerette and Arnaud Demortiere, without with this work would never have been possible: Mathieu, you have been so helpful in scientific discussions, analyzing the results and many returns during the manuscript corrections and defense presentation which greatly improved my scientific level.

Arnaud, I sincerely thank you for your extreme care towards me both personally and professionally. I greatly enjoy the time spending in the tomography analysis, manuscript corrections and scientific discussions.

Also, I want to thank all the people of the LRCS lab, Amiens for their constant support. Thank you Christian, Dominique, Alejandro, Virginie, Carine, Christophe (IEMN), Renald, Gregory, Matthieu, Arash, Aman, Alexis, Vicky, Mariem, Yin, Garima, Alae, Tatiana, Zeliang, Tuan Tu, Xavier, Simon, Amina, Yue for being always ready to help in the laboratory and for being always interested and supportive to my work. An important part of this study has been realized at the Argonne Photon Source, ANL and I am very grateful to Vincent de Andrade for the tomography measurements.

Finally, I want to thank all my family members especially Rajeshwari (Wife), Riyanshika (Daughter), Elango and Bharathy Meenal (Parents), Prabhu (Brother), Dhivya, Prabhav, Pranav, Muthayammal, Parameshwari, Venkatesh whose support was very strong during these three years.

Hoping that I have not forgotten anyone, thank you again to each of you.

SUMMARY

Chapter 1: Introduction and bibliography 9

Chapter 1

Introduction and Bibliography

1.1 The need for energy storage

Over the past century, many scientific inventions and technological innovations are seen in various fields like information technology, automobile industries and so on. These improvements make our life easier but at the same time, currently there are two main problems which are threatening our life in this modern world. The first is the energy demand which is continuously increasing day by day as a consequence of fast growing population and improved economic development [1]. According to the International Energy Agency (IEA) statistics, for the past four decades from 1973-2014, the global electricity generation has increased from 6,131 to 23,816 TWh which is almost four times higher in magnitude. This total electricity generation is done with the help of various renewable and non-renewable energy sources present all over the world. Out of which, the major contribution of energy supply (around 80%) is from burning of fossil fuels such as coal, oil and natural gas and the remaining is being allocated to biomass, nuclear, hydropower and renewable energies (Figure 1.1) [2]. The two major drawbacks associated with these non-renewable sources are that they are limited in supply and not eco-friendly in nature. Non-renewable coal and oil resources are depleting continuously and according to Greenpeace and EREC's Energy (R)evolution scenario, it is estimated that around 2090, there will be no more coal and oil available on Earth [3].

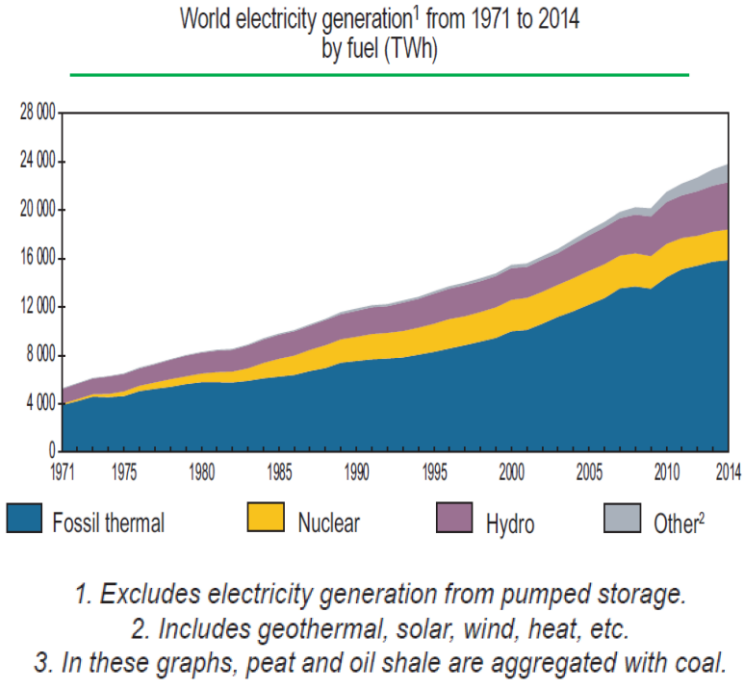

Figure 1.1 *Various types of energy sources contributed for world electricity generation from 1971 to 2014 [2]. Continuous increase in energy demand is supplied by different energy sources due to increased population and fast economic development.*

Another environmental problem which we are facing now is the release of hazardous greenhouse gases such as CO_2 that causes global warming as a consequence of burning of fossil fuels and it is estimated that the Earth's surface temperature will increase from 2 to 6 °C at the end of 21st century, as shown in Figure 1.2 [4]. This urgent problem instigates researchers and environmentalists to search for alternative renewable energy sources such as solar, geo thermal and bio-mass leading to the mitigation of poisonous CO_2 emissions and the decrease of greenhouse gas emission. However, the common unavoidable issue in these renewable systems is their intermittent supply. Nuclear energy is another alternative source to produce a large amount of energy but the safety concerns are taken into account to limit the usage of nuclear sources. In order to overcome the disadvantages of these energy sources, the energy storage and conversion technologies come in board to store the electrical energy and can be delivered whenever there is a need for energy [5].

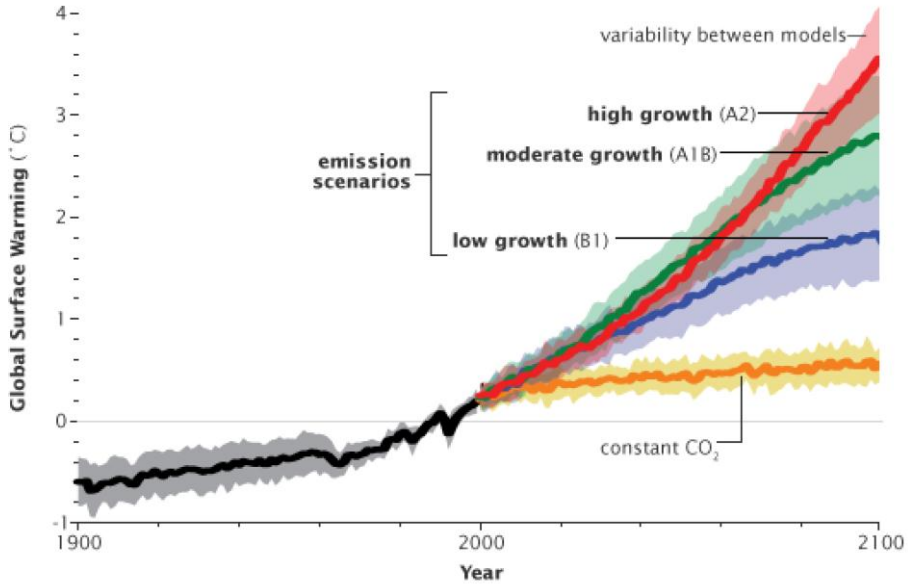

Figure 1.2 *Earth's surface temperature vs CO_2 emissions rate [4] Fast growth rate of CO2 is modeled as a result of emission of greenhouse gases due to the burning of fossil fuels. This result estimates the earth's surface temperature will be increased from 2-6 °C in the year 2100.*

In our modern society, the energy consumed is mainly in the form of electric power. Typically, it is produced in power stations and distributed to the end users through a network of suppliers. The objective of suppliers is to move towards smart grids capable of integrating and managing all types of energy production either continuous or intermittent [6]. Then, the energy will be supplied efficiently to all types of facilities such as factories, offices, cities, dwellings irrespective of time or seasons with a

lower cost. In this type of organization, two categories of energy storage are available, either stationary or embedded. For wind and photovoltaic devices, energy generation is not constant as shown in Figure 1.3 and depending on the season or time of the day respectively. Others such as nuclear energy can operate continuously but cannot be started or stopped according to the request. In order to compensate all these variations in production and consumption, it is essential to store the produced energy in surplus amount and used it later when it is necessary. In this case, the stationary energy storage facilities are used in order to guarantee the stability of the network. The embedded energy storage facilities are used as portable devices in many applications such as transport, multimedia, household appliances and tools. So, finally one can come into a conclusion that the energy has to be stored in either small or large scale and energy storage technologies are essential for day to day activities.

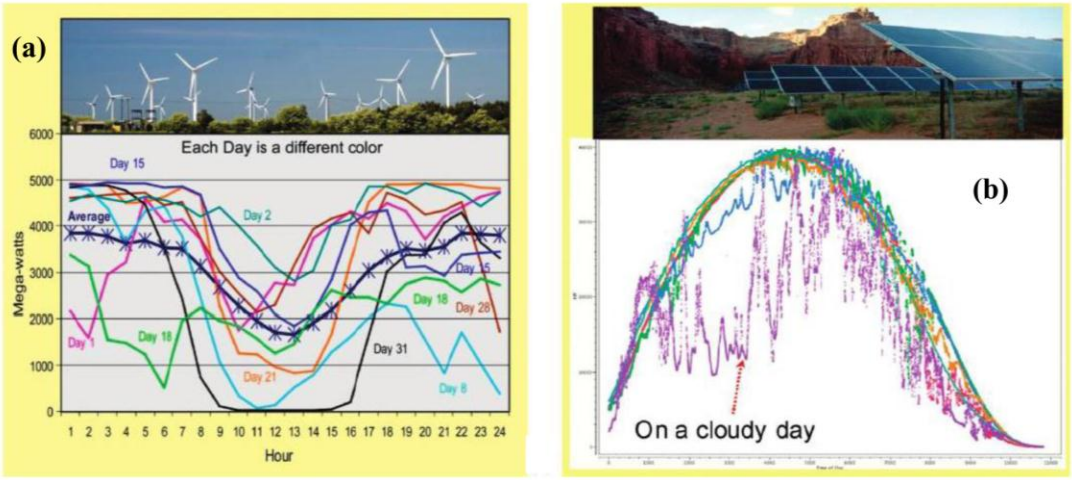

Figure 1.3 *(a) Amount of electricity generated by a) Wind and b) solar power sources. Drastic fluctuations in the supply of energy are observed in both wind and solar power making it less efficient for electrical energy generation facilities.*

1.2 Battery

A battery is an electrochemical storage device. It converts chemical energy into electrical energy and *vice versa*. By design, a battery is a stack of many electrochemical cells connected in series or parallel depending upon the applications required. A single cell consists of a positive electrode (cathode), electrolyte and negative electrode (anode) as seen in Figure 1.4. The separator is a porous membrane filled with electrolyte placed between the electrodes that permits ionic conduction (Ex: Li^+ ions in the case of Li-ion batteries) between them and avoids the electrical connection leading to short circuit of the cell. During discharge, the positive ions migrate from the anode to the cathode and move in the

opposite direction when the battery is charging. Simultaneously, electrons are moving in the external circuit, which generates electricity. The energy difference of the electrochemical potential of anode and cathode is the overall cell potential, also known as open circuit potential. Batteries also have the advantage of storing and restoring energy directly with a remarkable efficiency of between 75 and 95%. They can be flexibly manufactured by changing the following parameters:

- Size and design (from a few micrometers to storage benches)
- Specific power / specific energy ratio
- Short or long term usage
- Stationary or embedded usage.

Batteries are mainly classified into two types: primary and secondary batteries. Primary batteries are the one time dischargeable batteries whose lifetime and cycling capacity is very limited. The secondary batteries are the rechargeable batteries because the redox reactions, oxidation and reduction, are taking place reversibly during charge and discharge. This chapter is mainly about the state of the art of the rechargeable Li-ion batteries, their components and the main properties, leaving out the other battery types which are out of the scope of my thesis.

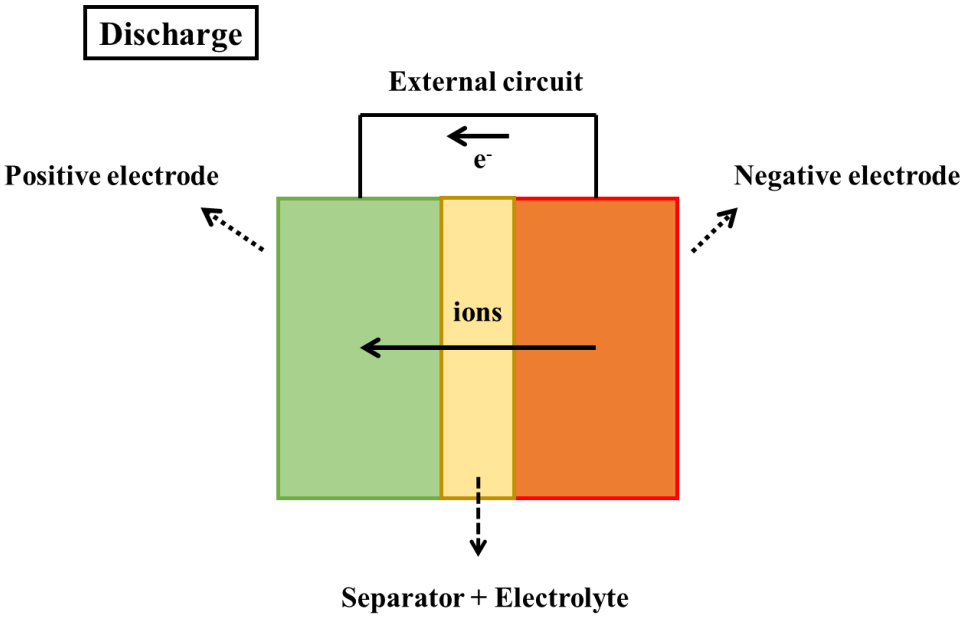

Figure 1.4 *Schematic of a generic electrochemical cell. Electron exchange is occurring at a given potential in each electrode, normally paired with an ion exchange through the electrolyte filled separator.*

The first primary battery was developed by Alessandro Volta in the early 19th century and was based on copper and zinc electrodes with a separator made of cloth absorbed by the electrolyte. He piled a large number of cells, which made the Volta's pile very famous. This created a strong basement for the invention of other electrochemical processes such as water electrolysis. However, the major setback for this Volta's pile is that it cannot be recharged. However, this work motivated other researchers to develop the secondary batteries which can be recharged and usable for multiple times. After a few years, French physicist Gaston Plante developed the lead acid battery which was the first rechargeable battery ever developed in history. It involves an electrochemical reaction between the lead anode, the lead oxide cathode and the sulphuric acid electrolyte which becomes reversible by passing a reverse current through the battery, thus recharging it. This was considered as a low cost rechargeable battery for almost 150 years and is still one of the ongoing commercialized batteries used for automobile and standby applications. However, Lead is a heavy metal and toxic in nature. This reduces the energy density of lead acid batteries to a minimum extent and not suitable for portable or less weight applications. Later, researchers developed nickel cadmium and nickel metal hydride batteries with higher energy density. However, the aqueous electrolyte used in these systems limits its cell potential, thereby lowering the energy density. The continuous quest of researchers enabled to develop the high energy density lithium based batteries.

Lithium is the most reducing element of the periodic classification (-3.04 V vs. SHE) and also one of the lightest metal (M = 6.94 g / mol) making it an ideal anode material and allowing to design batteries with very high energy density [7]. Before entering the history of the Li-ion battery, the first lithium metal battery was introduced by S. Whittingham in 1973. It involves the rechargeable battery design with TiS_2 as positive electrode and metallic lithium as negative electrode [7]. The word "intercalation" was first termed in his work and is now vastly used in almost all the literature related to Li-ion batteries. It means that the metal ion (Li^+) is inserted into a host matrix without affecting the structural integrity of the electrode material. Dr.Whittingham's work was later commercialized by Exxon. Later, TiS_2 was replaced by MoS_2 leading to the commercialization of first Li-based battery by Moli Energy® popularly called the Moli Cell. However, within a short period of its introduction, the cells experienced safety issues such as explosion after a few cycles, due to the high reactivity of metallic lithium. Then, it was realized that the dendrite formation on the surface of lithium penetrating through the separator caused short circuit and led to a hazardous activity. Later, a patent was published by Mizushuma et al. replacing the lithium metal with graphite and LCO as cathode leading to the introduction of the Li-ion

battery [8]. This work was first commercialized by SONY in 1991. Since its beginning, the energy density has been greatly improved from 100 to 240 Wh/kg and is believed to reach the energy density of 330 Wh/kg in the forthcoming years as shown in figure 1.5. A brief overview of Li ion battery technologies will be discussed in the next section.

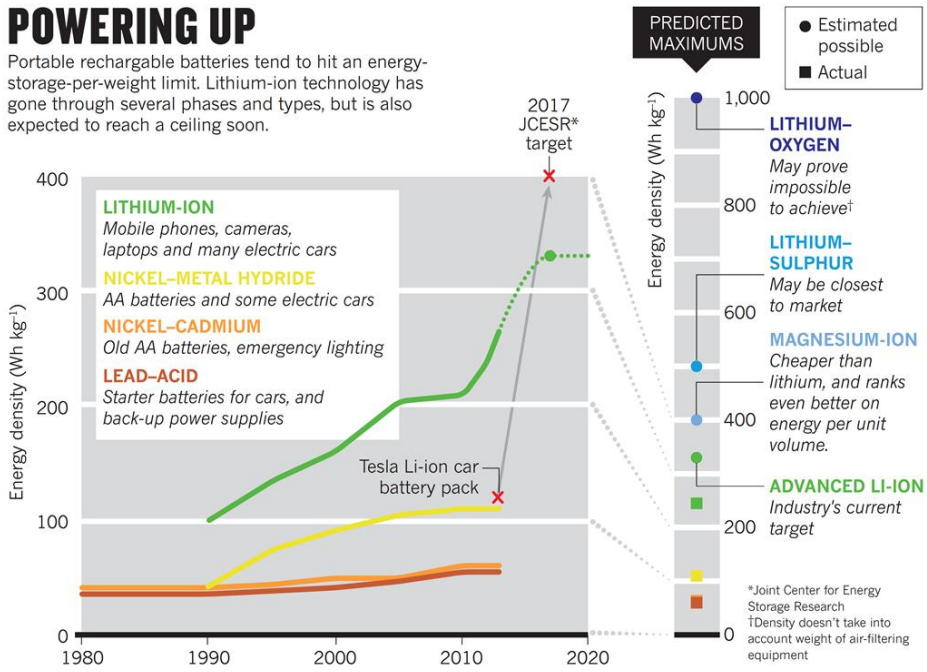

Figure 1.5 *Fast improvement in the energy density by Li-ion battery as seen over the years compared to other battery technologies and approaching towards 320 Wh/kg in near future [9].*

1.3 Li-ion batteries and their components

Li-ion batteries have attracted enormous attention from the industry to the scientific community, due to their reliability, longer shelf life, good cyclability and high coulombic efficiency, especially the excellent gravimetric and volumetric storage energy density. Today, they are widely used as power source for portable electronic devices and electric vehicles [10], [11]. The mechanism of a Li-ion battery is shown in Figure 1.6: it involves the shuttling process of lithium ions back and forth taking place between the positive and negative electrodes during cell charging and discharging. In this example, the system uses graphite as the anode and layered Li-intercalated compound (Ex: $LiCoO_2$) as the cathode.

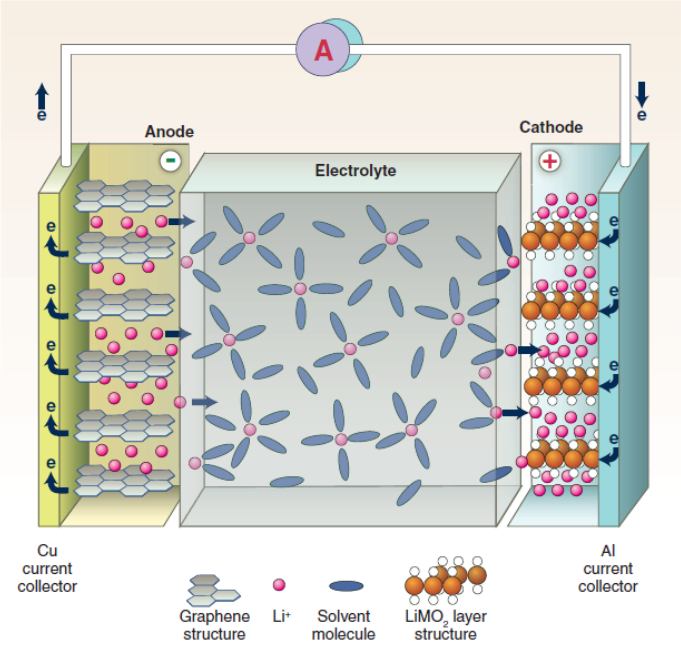

Figure 1.6 Schematic of mechanism of Li-ion battery. The negative electrode (anode) is a graphitic carbon and positive electrode (cathode) is a Li-intercalation compound – usually an oxide because of its higher potential. Both electrodes are able to reversibly insert and remove Li ions from their respective structures. The electrodes are separated by a non-aqueous electrolyte that transports Li ions between the electrodes. Reprinted from [6].

During the process of charge, lithium is extracted from the cathode, inducing the oxidation of transition metal Co^{3+} which releases electrons to the external circuit through the current collector. The lithium will then migrate to the negative electrode where it is reduced to its metallic state. Upon discharge, opposite processes take place, consequently leading to the lithium back to the cathode, giving rise to the rechargeability of LIBs. The reactions involved during the discharge process can be written as the following equations and all three reactions will be reversed during the charge.

During Discharge:

Positive electrode: $$Li_{0.5}CoO_2 + 0.5Li^+ + e^- \rightarrow LiCoO_2 \quad (1.1)$$

Negative electrode: $$LiC_6 \rightarrow C_6 + Li^+ + e^- \quad (1.2)$$

Overall cell reaction: $$LiC_6 + CoO_2 \rightarrow C_6 + LiCoO_2 \quad (1.3)$$

1.3.1 Positive electrodes

Since the introduction of the Li-ion battery technology, the researchers focused to identify many innovative cathode materials which have high theoretical capacity and voltage. The other criteria for a good cathode material are good electronic conductivity as well as chemical and structural stability during intercalation/de-intercalation. From the last decades, the major group of cathode materials are layered oxides (ex: $LiCoO_2$), spinel type phases (ex: $LiMn_2O_4$) and polyanionic materials such as $LiFePO_4$. In the case of $LiCoO_2$, very high operating voltage between 3.5 and 4.2 vs lithium and low polarization led to the commercialization of Li-ion battery by SONY in 1991. However, high material cost and structural distortion at $Li_{0.5}CoO_2$ limit its usage and reversible capacity to one half of its theoretical capacity (275 mAh/g).

In parallel, relatively cheaper spinel compounds like $LiMn_2O_4$ were developed. $LiMn_2O_4$ shows 3 plateaus in total: in reduction at 3V and oxidation at 3.9 V and 4.1 V vs Li. However, its commercialization was heavily stopped due to the rapid capacity fading. This was improved by doping of metal atoms such as Al and F ($LiMn_{2-x}Al_xO_4F_y$) and Ni by forming $LiNi_{0.5}Mn_{1.5}O_4$ and replacing alternative electrolyte salts such as LiBOB instead of $LiPF_6$ salt. $Li(Ni_{1/3}Co_{1/3}Mn_{1/3})O_2$ is an alternative cathode material that offer longer calendar life for HEV application [12], [13].

Though layered oxides or spinels experienced a commercial success, some of the difficulties such as capacity fading, toxicity, sustainability and safety urged scientists to search for another class of cathode materials such as polyanion based materials ($LiMXO_4$). A well-known example of this class is Phospho-olivine $LiFePO_4$ material ($AMPO_4$) which was first discovered by Padhi *et al*. [14]. Even though the theoretical capacity is lower than that of layered compounds due to the addition of many polyanionic groups (XO_4), they are more thermally and structurally stable, cost effective, safe and also chemically stable to the electrolytes. Nowadays, LFP is one of the competitive candidates for the electric vehicles due to its high rate capability and increased safety.

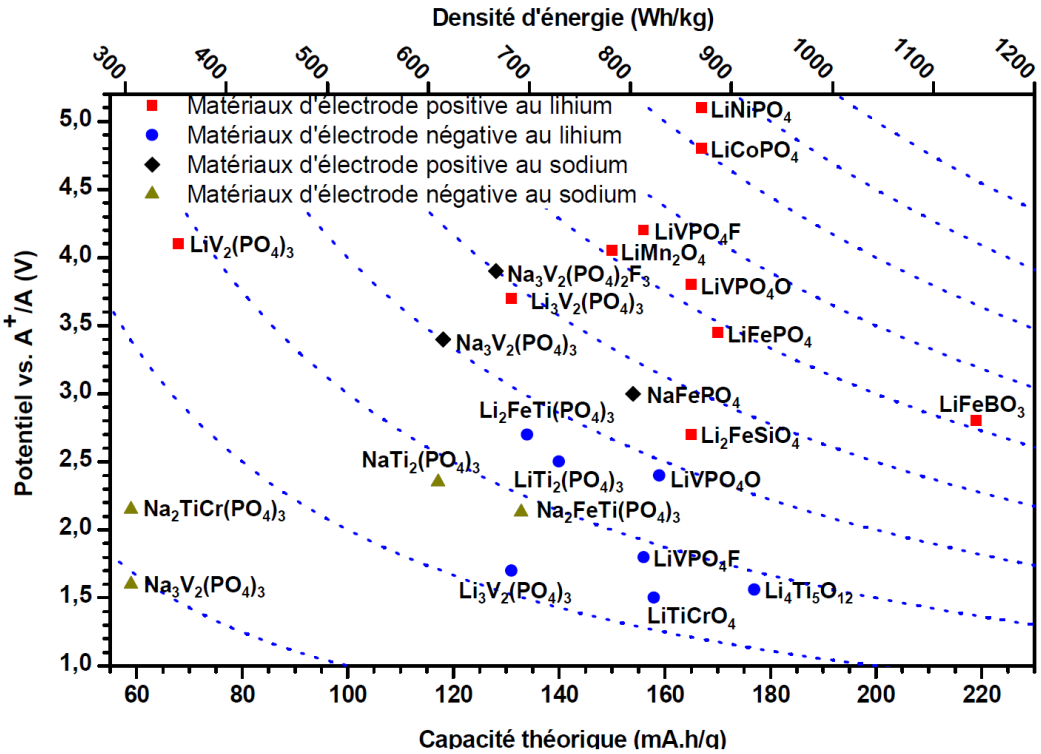

Figure 1.7 Potential vs theoretical capacity and energy density of various electrode materials of lithium and sodium ion batteries[15].

Some of the other polyanionic compounds such as pyrophosphates $Li_2MP_2O_7$ [16], silicates Li_2MSiO_4, borates $LiMBO_3$ [17], hydroxyl and fluorophosphates ($LiFePO_4OH$) and sulfates ($LiFeSO_4OH$) are available in the state of the art [18]. A comprehensive plot (Figure 1.7) was reprinted from the PhD thesis of Fabien Lalère, former PhD student of LRCS, Amiens [15] explaining the thermodynamical potential and theoretical gravimetric capacity of the different positive and negative electrodes of the Li-ion battery.

1.3.3 Negative Electrodes

Since its introduction in 1991 to till date, graphite is serving as a strong candidate for the negative electrode due to its high theoretical capacity of 372 mAh/g, its cheap cost, its high abundance and its possibility to achieve higher reversible capacity (450 mAh/g) than theoretical capacity because of its chemical processing methods and mechanical milling modifications. However, it also faces some of the safety issues by undergoing thermal runaways due to lithium plating at fast charge rate. To overcome these problems, carbon alternative materials such as lithium transition metal nitrides ($Li_{3-x}Co_xN$), silicon [19] and Tin-antimony alloys [20] are developed, which show higher reversible capacity. But, large volume expansion of the active material occurs during charge/discharge, leading to poor cyclability and less Coulombic efficiency. This hinders to make it as commercial anode material.

Another class of anode material is spinel $Li_4Ti_5O_{12}$ which is used in stationary power supplies due to its high theoretical capacity (175 mAh/g). It involves almost zero volume expansion during charge/ discharge and high lifetime but relatively higher voltage (1.5 V) compared to other anode materials such as graphite, which leads to diminishing the overall cell potential and thereby to low energy density. Nevertheless, it is considered as an important material because of its better cycling performance such as high power rechargeability with ensured safety, easy fabrication and low cost precursors. For example, a safer Li-ion battery using LFP and LTO electrodes with conventional liquid electrolyte was demonstrated using a prototype for electric vehicle showing the charge-discharge curve obtained at C/24 rate (Fig 1.8). This can be charged/discharged within few minutes, passes the safety tests, and has a very long shelf life. It retains full capacity even after 20,000 cycles performed at high charge rate of 10C (6 min) and discharge rate of 5C (12 min) [21].

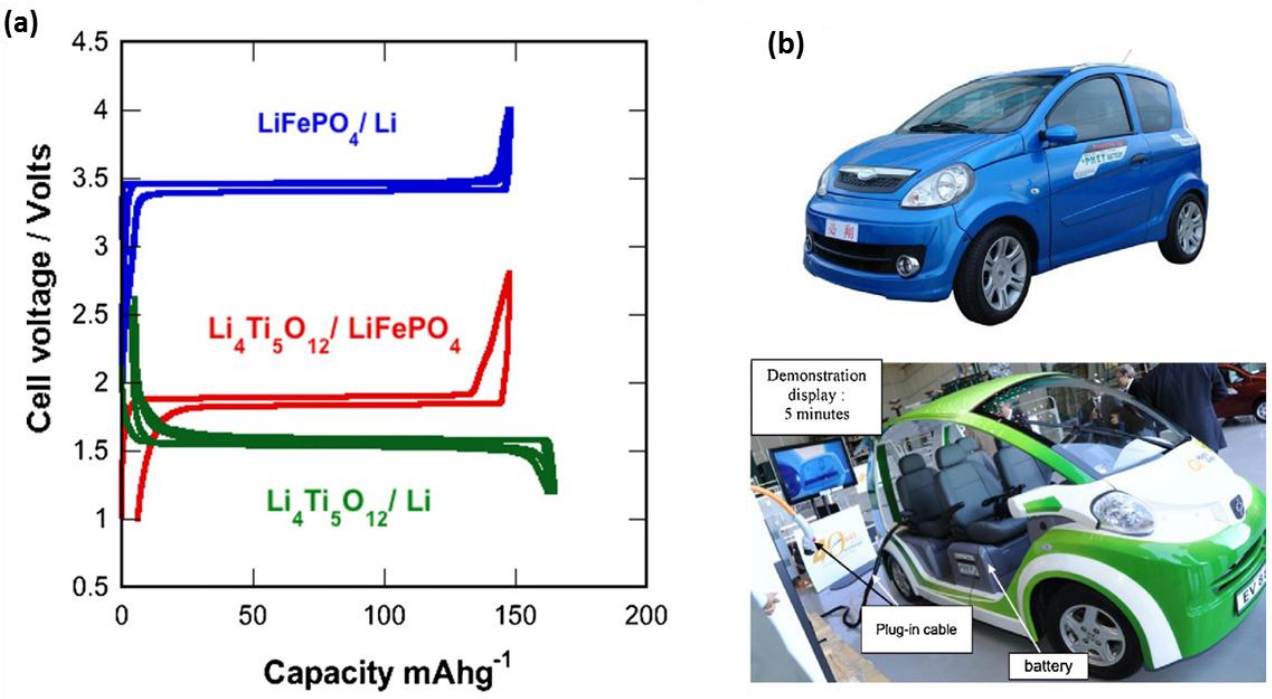

Figure 1.8 *a) Voltage–capacity cycle showing the charge-discharge plateau with much less polarization for LFP/Li, LTO/Li and LFP/LTO equipped with liquid electrolyte (1M LiPF6- EC-DEC). b) Electric cars equipped with C-LFP/LTO battery demonstrated the 5 minutes charging time with 500 V, 125 A charging station.*

1.3.4 Electrolytes

Electrolytes are the ionic conducting medium between the composite electrodes responsible for their rate capability and energy efficiency. The main criteria for the electrolyte are large stability window at high potential, good ionic conductivity, low melting and high boiling point and low vapour pressures. Most of the liquid based electrolytes are the dissolution of lithium based salt such as $LiPF_6$, $LiClO_4$, LiBOB in non-aqueous organic solvents such as ethylene carbonate, dimethyl carbonate, ethylene carbonate, ethyl methyl carbonate whose molecular structures are shown in figure 1.9. This is because water based electrolytes limit their usage at high potential and because of the high reactivity of lithium on water. The most common electrolyte mixture is composed of a lithium salt of 1M $LiPF_6$ dissolved in 1:1 wt % of EC: DMC solvent. Ethylene carbonate has a high dielectric constant but high viscosity values due to the interaction between molecules which hinders the mass transport of solutes. For that reason, a mixture of organic solvents such as diethylene carbonate, propylene carbonate and ethyl methyl carbonate was added in a specific ratio [22], [23].

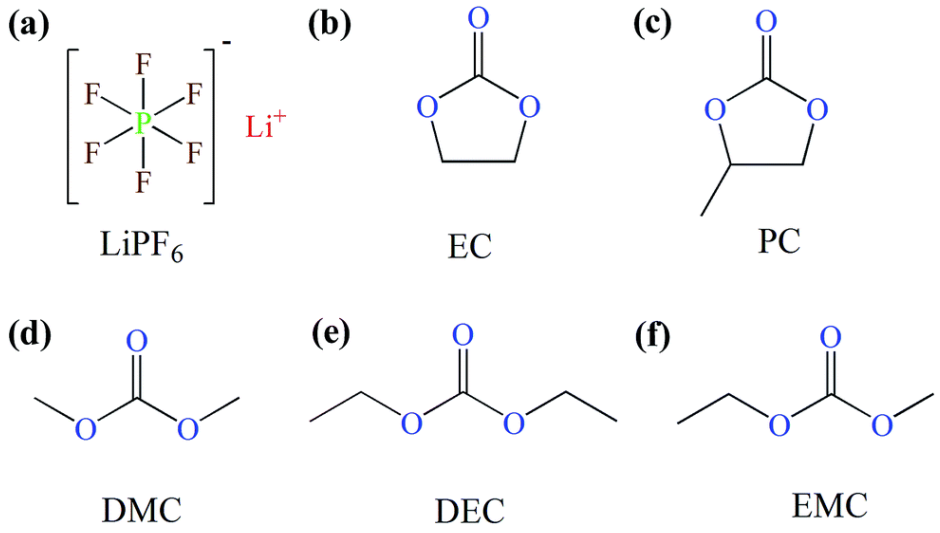

Figure 1.9 *Molecular structures of commonly used electrolyte salt and organic solvents in LIBs. (a) $LiPF_6$ salt, (b) Ethylene Carbonate, (c) Propylene Carbonate, (d) Di Methyl Carbonate, (e) Di Ethylene Carbonate, (f) Ethyl Methyl Carbonate [24].*

Polymer gels are another class of electrolytes containing alkali metal salts dissolved within the polymer host such as polyethylene oxide (PEO), polyvinylindene fluoride (PVDF), polyacrylonitrile (PAN), polymethyl metha acrylate (PMMA). Though polymer electrolytes are considered as low ionic conductivity electrolytes, some of the polyacrylonitrile based polymer electrolytes use ternary solvents (EC-PC-BC-3-methyl-2-oxazolidione) to improve the ionic conductivity (2.98 $*10^{-3}$ S/cm @ 25 °C) close to liquid electrolytes (10^{-3} to 10^{-2} S/cm @RT) [26],[27]. The electrochemical performance of graphite/ LCO cells are assembled with another class of new ionic liquids as electrolyte made of such as N-methoxymethyl-N,N-dimethylethyl-ammonium bis(trifluoromethane-sulfonyl)imide (MMDMEA-TFSI)-containing electrolyte solutions with and without fluoroethylene carbonate (FEC) [27].

Nowadays, solid electrolytes are getting more attention because of their excellent safety characteristics and because they possess almost equal or even more ionic conductivity than liquid electrolytes [28]–[30]. The main important properties of any electrolyte are ionic conductivity, lithium ion diffusion coefficient, cation transference number and an additional parameter called thermodynamic coefficient which is a measure of how the thermodynamic driving force relates to concentration gradients of the electrolyte and the activity coefficient. So, the accurate determination of above mentioned transport properties are needed and various experimental and modeling studies are done to determine the properties and also to understand the influence of salt composition, type of solvents and electrolyte, temperature in the electrochemical performance [26]–[31].

1.3.5 Inactive components

Apart from the active materials which play a role in the intercalation/de-intercalation reaction, conductive carbon (e.g. carbon black, graphite) is added to improve the electrical conductivity of the composite electrodes. In general, some of the active materials possess low electrical conductivity such as LFP ($<10^{-9}$ S cm^{-1}) [37], LTO ($<10^{-13}$ S cm^{-1})[38], etc. and thus carbon additives are coated on the surface of the particles or synthesized in nanosize particles to enhance the electrical conductivity of the system. Allotropes of carbon such as single walled and multiwalled carbon nanotubes [39], graphene sheets [40] and carbon free conducting agents such as RuO_2 [41], conducting polymers [42] are coated to enhance the electronic conductivity of the active material. Moreover, insulating materials such as alumina (Al_2O_3) and Li_3PO_4 are coated on the surface of the composite electrode materials using Atomic Layer Deposition (ALD) to minimize the electronic contact resistance and improve the surface stability of the coated materials. It is proven that these oxide coatings done on the conventional positive electrodes like $LiCoO_2$ lower the acidity of the non-aqueous electrolytes by scavenging water and hydrogen fluoride (HF) leading to a stable capacity retention [43].

Binders are another class of additives added to enhance the mechanical integrity of the composite electrode. They enable the interconnected network not to have any discontinuities by holding all the materials together as well as coating on the current collector. Generally, low cost polymers (e.g. polyvinylidene fluoride-PVDF) or water soluble binders (Carboxy methyl cellulose) are used. Sometimes, conducting polymers are used so that they maintain the electronic conductivity and mechanical stability of the percolating network [40]–[44] . Though these additives are not contributing to the capacity, they are occupying from 5 to 25 wt % of the total weight of the electrode depending on the applications and electrolytes used as shown in table 1.1.

Table 1.1 *Formulation of positive electrodes fabricated for Li ion batteries [49]. Inactive mass contributed by binder and carbon black ranges from 5-30 wt% in the electrode level enabling the decrease in energy density of LIB.*

Active material	AM (wt. %)	Binder (wt. %)	Carbon black (wt. %)	References
$LiMn_2O_4$	85	5	10	[50]
NMC	88	6	6	[51]
$Li_{1.04}Mn_{1.96}O_4$	75	5	20	[52]
NMC	86	7	7	[53]
$LiCoO_2$	92	4	4	[54]
$LiMn_2O_4$	92	6	2	[55]
$LiCoO_2$	90	5	5	[56]
NMC	84	8	8	[57]
LCO	75	5	20	[58]
$LiMn_2O_4$	70	5	25	[59]

Separators are the electrically insulating material for providing pathway for ionic conduction between the electrodes. Also, they prevent short circuiting between the two composite electrodes. Glass fiber and polymer such as polyethylene, polypropylene are the common separator materials used while assembling LIB. Current collectors are the electrically conducting material on top of which the electrode slurry is coated, which is used for the charge collection and to pass it to the external load. However, it does not contribute to the electrochemical reaction but it should be electrochemially inert at the corresponding working voltages. Copper and aluminum foils are the common materials used for anode and cathode respectively. The composite (slurry) thicknesses can range from 75 to 200 μm on top of thin (12–20 μm) metal foil current collectors for typical commercial Li-ion batteries. After slurry coating on the curent collector, it is subjected to calendering (apply pressure by passing through big calender rolls) to maintain the uniform thickness and adjust the optimised porosity based on the active material type, composition and usage. From the battery level, separator, curent collector, tabs, welding connections, pouches and packaging container are the supplementary materials occupying around 50 wt% and more than 2/3rd of total battery volume.

1.4 Important Properties and Parameters of Li ion batteries

1.4.1 Energy Density

Energy density is an important property that can be explained by how much energy one can store in the battery in a given weight or volume. From a thermodynamical perspective, theoretical energy density of any electrochemical system that can be obtained from Gibb's free energy ($\Delta_r G°$) for any electrochemical reaction at standard conditions is given in equation 4. In this equation (4), n refers to the number of the charge transferred during the electrochemical reaction per mole reactant, E is the thermodynamic equilibrium voltage and F is the Faraday constant. Energy density can always be measured in terms of mass or volume of the total battery system and from equations (4-6), theoretical energy density can be expressed as a product of capacity and voltage or the integration of the thermodynamic voltage-capacity curve for capacity-balanced electrodes divided by the maximum weight or volume of the system reaches during cycling.

$$\Delta_r G° = -nF \times E \tag{1.4}$$

$$\varepsilon_M = \frac{-\Delta_r G°}{\boldsymbol{\Sigma M}} \quad \text{(or)} \quad \varepsilon_V = \frac{-\Delta_r G°}{\boldsymbol{\Sigma V}} \tag{1.5}$$

$$= \frac{nF}{\boldsymbol{\Sigma M}} \times E \quad \text{(or)} \quad \frac{nF}{\boldsymbol{\Sigma V}} \times E$$

$$Capacity = \frac{nF}{3.6M}\,(\mathrm{mAh/g})$$

$$Energy\ density\ (\varepsilon_M\ or\ \varepsilon_V) = Capacity\ X\ Voltage \tag{1.6}$$

$$\left(\frac{Wh}{L} or \frac{Wh}{kg}\right) = \left(\frac{Ah}{L} or\ \frac{Ah}{kg}\right) \times V$$

As clearly seen from equation 1.6, two simple ways to increase the energy density of the electrochemical system is to discover new high potential (polyanionic materials) or high theoretical capacity materials (lithium rich layered compounds) and illustrated in figure 1.10a. Till now since its commercialization, the energy density of LIB has been increasing consistently from 240 to 700 Wh/L by employing cell engineering as shown in figure 1.10b [60]. The theoretical energy density of 1172 different electrochemical systems including Li, Na, Mg, Al, Zn based batteries was calculated based on the Gibb's free energy of the electrochemical reactions [61].

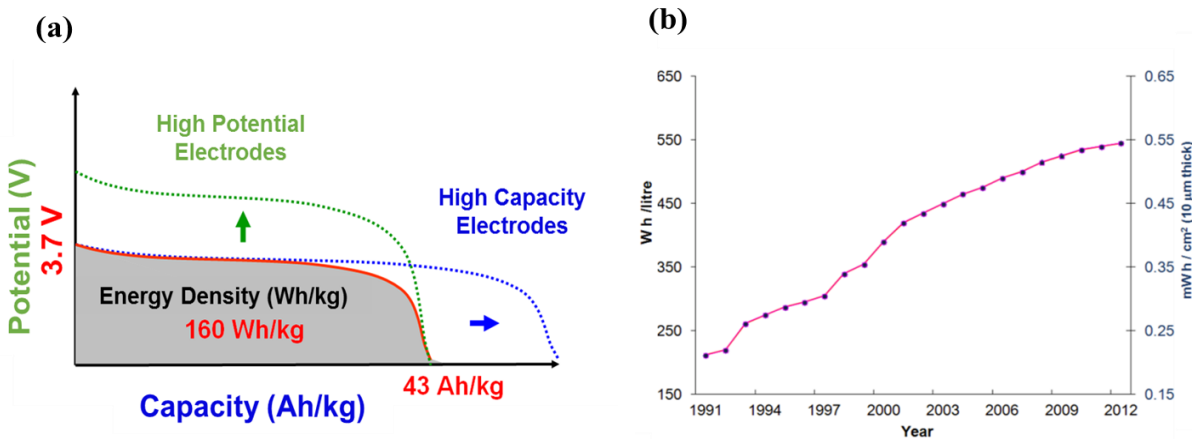

Figure 1.10 *a) Ways to improve energy density (b) Progress in volumetric energy density of LIB since its commercialization [60].*

Though high potential or capacity materials are discovered, the maximum energy density of the full battery cannot be achieved to its fullest. One main reason is that more than half of the battery weight and 2/3rd of the battery volume is occupied by the electrochemically inactive materials and the different cell designs of Li-ion batteries are illustrated in figure 1.11. The electrochemically inactive materials such as current collectors are used to transport the electrical charges externally, the binder helps to ensure the adhesion of slurry to the current collector and conductive carbon is used to increase the electronic conductivity of the material. At the same time, some of the disadvantages, such as usage of liquid electrolyte based Li-ion battery limits the working of high potential materials due to the electrolyte decomposition, need to be addressed.

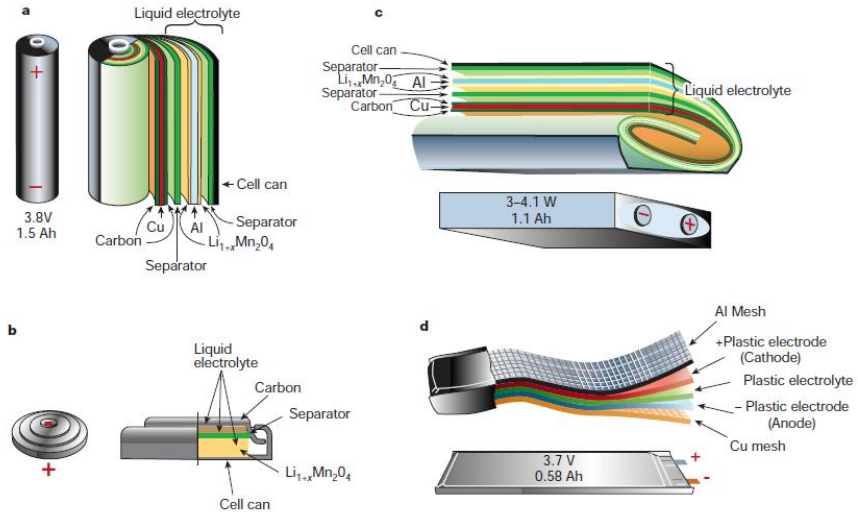

Figure 1.11 *Various Li-ion battery configurations available in the market. a) Cylindrical b) coin c) prismatic and d) thin and flat. About 50% in battery mass and more than 2/3rd of battery volume is occupied by inactive materials irrespective of different configurations. Reprinted from [62].*

For anyone chosen material, the energy density of the Li-ion battery can be improved by the following strategies:

- Increasing the thickness of the composite electrodes leads to an increase in active material (AM) loading (i.e. amount of active material packed per unit area in mg/cm^2) [58]–[60].
- Decreasing/avoiding the electrochemically inactive materials like binder, conductive carbon and current collector.

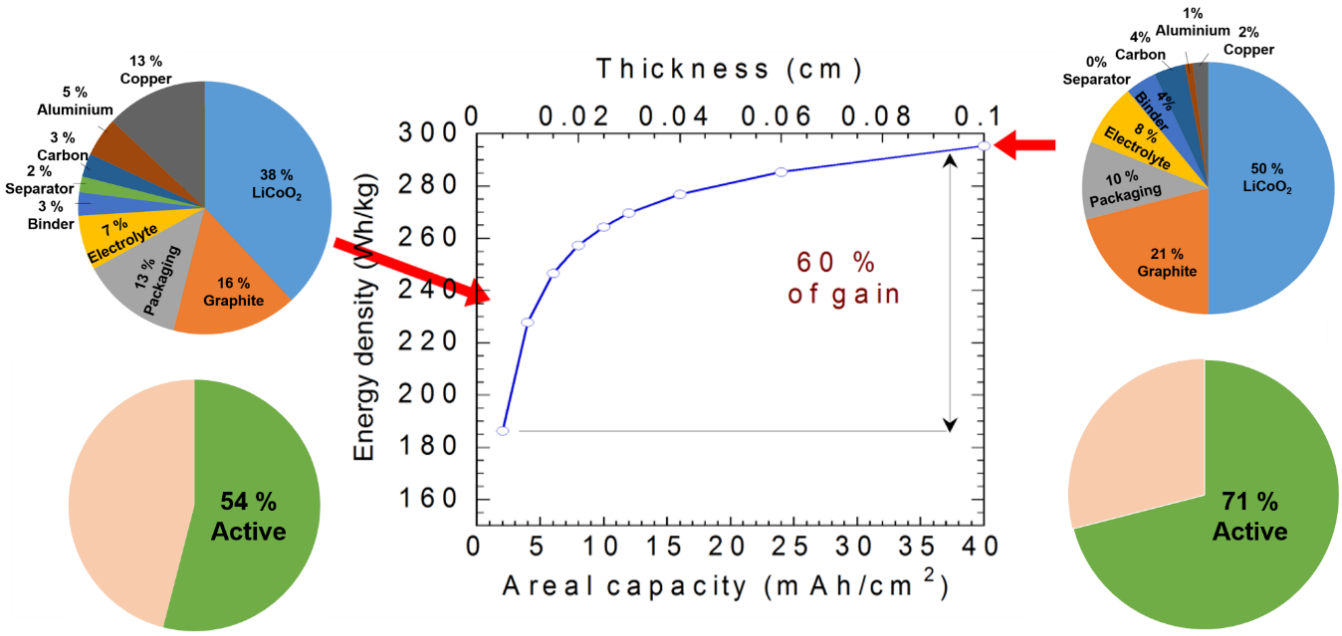

Figure 1.12 *Comparison of energy density values obtained as a function of electrode thickness.*

Figure 1.12 shows the energy density of Li-ion batteries having an electrode of 100 micron thickness are yielding energy density of 230 Wh/kg. However, the increase of electrode thickness from 100 to 1000 µm results in 60% of gravimetric energy density gain, up to 295 Wh/kg. These calculations were done in our laboratory and clearly show the increase in energy density can be obtained by rising the electrode thickness and simultaneous decreasing inactive materials. This strategy was also evidently supported by various modeling studies stating that increasing the thickness of electrodes leads to a relatively high energy density along with the reduction of cost [66], [67]. Cell engineering is a concept adopting the changes in electrode formulation and architectural design leading to the improvement of gravimetric and volumetric energy density. Still, there is a big room for improvement to increase the practical energy density of Li-ion battery.

The binder is an additive added to increase the mechanical strength and binding nature of the active material along with the conductive agents in the slurry. However, the presence of binders in the electrodes decreases the accessible specific area of the active materials and/or increases the electrode tortuosity, and increases the electrochemical polarization of the electrodes. Higher weight % of binder also decreases the gravimetric energy density due to inactive mass increase of the battery. This motivated the researchers to develop binder free electrodes for many electrochemical devices such as Li-ion batteries[68]–[73] and super capacitors [74]–[77]. In general, the binder free electrodes are prepared for flexible, light weight applications because high thickness electrode without binder will get easily cracked or peeled off when metal current collectors are bent. To avoid these problems, carbon based materials such as graphene thin films, carbon nanotubes electrodes are prepared to avoid binder/current collector, to target high power rate applications with the compromise of a low energy density. Strategies like foreign metal ion doping, reducing active material particle size and alternative processing such as electro deposition techniques were done to develop binder free electrodes for high power super capacitors [74]–[79]. For example, thin layers of nano silicon anodes with uniform particle size distribution were prepared using electrophoretic deposition method by applying current for short span of time (5-60 s) and experimental setup is shown in figure 1.13. In this work, surface modified nano Si and Acetylene Black particles are bonded tightly together forming a 3D porous structured thin film electrode on copper substrate without the need of binder. Improved electrochemical performance such as rate capability is seen in figure 1.13c and explained due to the 3D porous structure of the electrode that alleviates volume expansion of silicon during the charge and discharge processes and facilitates faster transport kinetics of lithium ions [80].

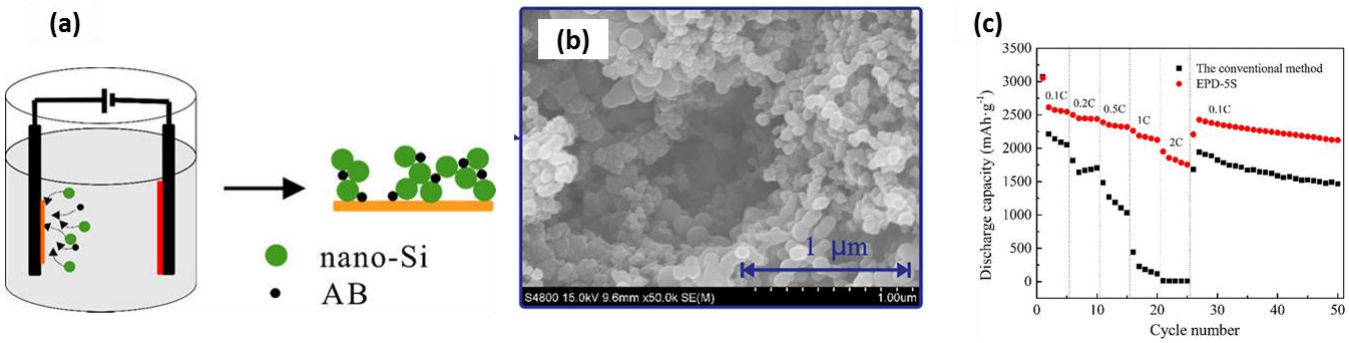

Figure 1.13 *Electrodeposition of nano silicon and its electrochemical performance. a) Application of short current pulse accelerates the uniform coating of nano silicon present in the electrochemical bath. b) SEM image clearly shows the nano size of silicon coated with acetylene black. c) Superior performance of ED silica is observed from the rate capability tests compared to the conventional method. Reprinted from [80].*

1.4.2 Power density

High charge and discharge rate is highly possible in Li-ion battery which makes it more useful for hybrid and plugin electric vehicles applications. Power density can be measured by applying short current pulse in a very short time, typically 10-20 seconds. Generally, the capacitors and electrochemical capacitors display more power than batteries because they undergo surface adsorption reactions of charged species of electrode material but achieve relatively very low energy density. However, for the Li-ion battery one can obtain both high energy and power densities by storing charges in the bulk of the material and achieving ultra-high discharge rates. For example, in 2009, Ceder *et al*. developed a conventional battery $LiFePO_4$ material prepared by creating an ion conducting surface phase through controlled stoichiometry during synthesis, which obtains high capacity at ultra-high charge and discharge rates [81].

1.4.3 Porosity and pore size

The electrode porosity can be defined as the ratio of the pore volume to the entire electrode volume. The porosity factor (Є) of the commercial electrode containing active material, conductive carbon and binder can be measured according to the equation 1.7, where V is volume, M is mass, P is mass fraction and ρ is density of the materials.

$$\epsilon = \frac{V_{electrode} - \sum V_{component}}{V_{electrode}} = \frac{V_{electrode} - M_{electrode}\left(\frac{P_{\mathrm{AM}}}{\rho_{\mathrm{AM}}} + \frac{P_{\mathrm{CB}}}{\rho_{\mathrm{CB}}} + \frac{P_{\mathrm{binder}}}{\rho_{\mathrm{binder}}}\right)}{V_{electrode}} \qquad (1.7)$$

Experimentally, the electrode porosity can be measured by gas adsorption methods such as Helium gas Pycnometer, Accelerated surface area Porosimetry (ASAP), Mercury porosimetry. Image analysis techniques including X-Ray Computed Tomography (XRCT) and Focused Beam coupled with Scanning Electron Microscopy (FIB-SEM) are used to quantify the electrode microstructural properties such as pore volume fraction, specific surface area, particle or pore size distribution and tortuosity [82], [83]. The relationship between the electrode architecture and its electrochemical performance was studied using 3D imaging techniques [84]. In particular, XRCT is a non-destructive technique that allows probing the entire thickness of the electrodes and enables to measure the above mentioned geometric parameters. One disadvantage of this imaging technique is the difficulty of distinguishing the

carbon and binder mixture from the porous volume due to their low X-ray attenuation difference. So, this technique is very well suited for the analysis of binder free electrodes. For example, X-ray computed tomography was done for LFP/C electrode and after the reconstruction of images; pore network can be clearly seen with the minimal amount of isolated pores compared to the large amount of connected pores shown in fig 1.14c.

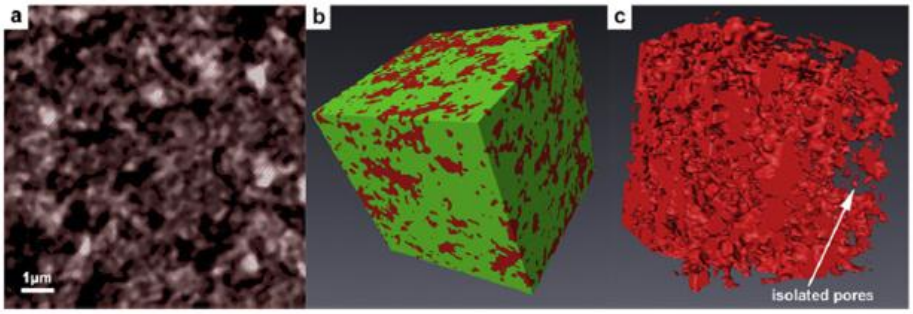

Figure 1.14 *X-ray computed tomography (XCT) 3D image reconstruction of cropped cube of LFP/C electrode (15 µm×15 µm×15 µm) after the segmentation (a) in a single slice, (b) LFP/C cube (green-LFP/C and red-pores) with 28.68% porosity and (c) Interconnected pore network with few closed pores are observed. Image reconstruction was done by Avizo and ImageJ software [82].*

1.4.4 Tortuosity

The influence of the porous microstructure on the macroscopic behavior is well explained by the property of network termed as tortuosity (τ). Tortuosity can be measured based on different ways. First, tortuosity can be explained as a measure of the elongation of the transport path due to the porous architecture due to porous separators or electrodes (L_{eff}) with respect to the straight distance *(L)* as seen in equation 1.8 and the relation between the bulk and effective conductivity is shown in equation 1.9.

$$\tau = \frac{L_{eff}}{L} \tag{1.8}$$

$$\sigma_{eff} = \sigma \frac{\epsilon}{\tau^2} \tag{1.9}$$

The accuracy of physical models is related to the transport throughout the continuous solid and liquid phase and also greatly dependent of critical parameters such as electrode tortuosity. Tortuosity of the porous media such as battery electrodes, separators and support membranes for fuel cells can be determined in several ways such as experimental methods like electrical impedance spectroscopy and

geometric, diffusion methods [69]–[73]. Recently, Gasteiger *et al.* [90] measured the tortuosity of commercially battery separators and electrodes such as graphite and $LiFePO_4$ electrodes using electrical impedance technique. In this interesting work, they used a symmetric cell setup by following the blocking electrode configuration to eliminate the charge transfer reaction. They carried out EIS experiments by using non-intercalating electrolyte in order to avoid the lithium intercalation reaction between the electrodes. Using transmission line model, effective ionic resistivity of the electrode is well fitted with the impedance measurements and found the average tortuosity values are 4.3 ± 0.6 for graphite electrodes having 43% porosity, which is three times higher than the value of $\tau = 1.5$ which would be predicted by the Bruggeman equation for spherical particles with $\alpha = 0.5$. In effective pore models, mostly Bruggeman relation was used as a baseline to relate the pore volume and tortuosity for spherical shaped particles as shown in equation 1.10 [84], [91].

$$\tau = \epsilon^{-0.5} \tag{1.10}$$

Geometrically, tortuosity is defined as the ratio of the average shortest path length through the porous microstructure divided by the electrode thickness '*D*' as shown in equation 1.11. However, geometrical tortuosity values are overestimated because these are highly dependent on the sampling volume size, voxel neighboring definition and distance propagation direction. To avoid the single mean tortuosity value along each axis, tortuosity spatial distribution maps and histogram are studied for each orthogonal direction of $LiCoO_2$ electrode [92], [93] (Figure 1.15).

$$\tau = \frac{min < L >}{D} \tag{1.11}$$

$$(\sigma_{bulk}.\nabla\emptyset) = 0 \tag{1.12}$$

Electrode tortuosity can be determined from solving the diffusion equation written in equation 1.12. The solution of this diffusion equation gives the potential distribution within the microstructure and leads to the determination of current density [94]. Several imaging techniques such as FIB/SEM, X-ray nano computed tomography and their 3D reconstruction of the electrode images were done to deduce the corresponding microstructural parameters such as volume fractions, volume-specific surface areas.

Also, tortuosity of the three individual electrode phases such as active material, pore and carbon black tortuosity can be obtained [84], [92], [93].

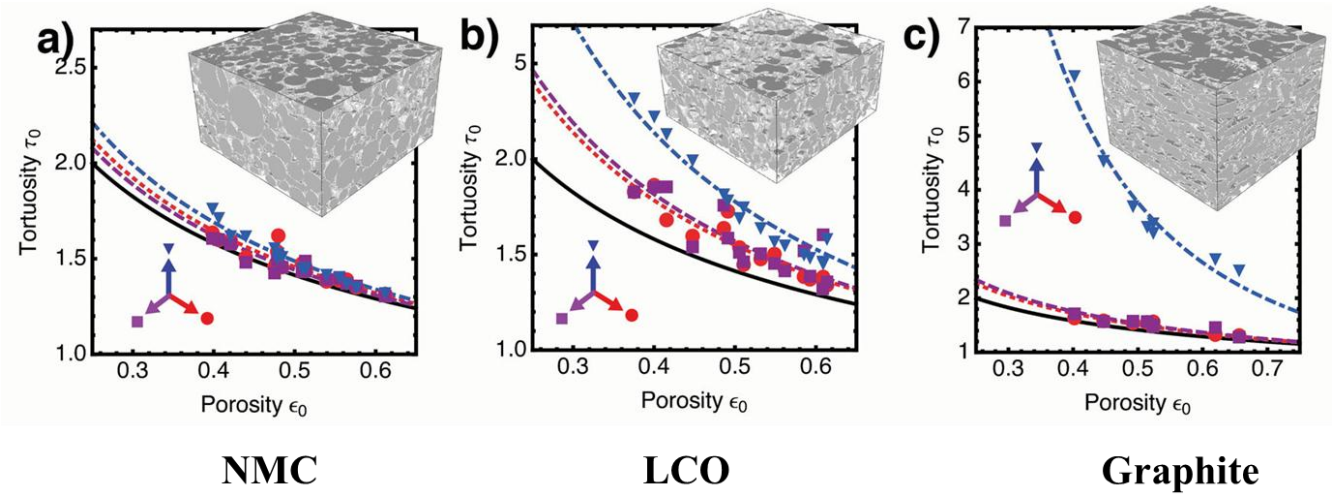

Figure 1.15 *Tortuosity measured for 3 electrodes a) NMC, b) LCO and c) Graphite using numerical differential effective medium (DEM) approximation method. Large degree of anisotropy was observed for graphite compared to other two electrodes that can be explained by high tortuosity values and big deviation from the classical Bruggeman relation.*

Several softwares such as Matlab, ScanIP and ParCell3D are available to deduce the tortuosity values from the 2D image stacks obtained using numerical diffusion simulations. Recently, Tjaden *et al* [95] have done the systematic approach of calculating tortuosity of the porous medium for electrochemical devices leading to the contradictory results between different methods such as geometric (Pore centroid and fast marching method), flux based imaging and diffusion cell experiments as shown in figure 1.16. Lower values for geometry methods and higher values for diffusion cell experiments are observed. Flux based simulations (Tau factor and Heat flux) values are the most reliable methods in which the tortuosity values are sensitive with porosity values.

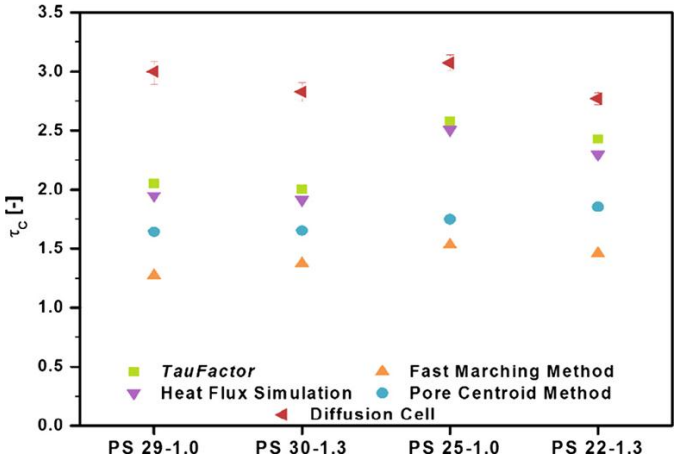

Figure 1.16 *Variation of tortuosity values of four porous support samples of partially-stabilized zirconia samples calculated by geometric, simulation and diffusion cell-based tortuosity values.*

1.5 Possibilities to increase high energy density of LIB

1.5.1 Thick Electrodes

In general, thick electrodes are fabricated with sufficient pore volume present in the electrodes to reduce the mass transfer limitations. For example, in battery chemistries such as Ni-Cd and Ni-MH batteries, the electrodes are possessing 80%-85% porosity and aqueous electrolytes are used because of higher ionic conductivity. However, larger porosity or using more amount of electrolyte is leading to the reduction of active material content of less than 50% by volume and resulting in low overall volumetric energy density. First, increasing the electrode thickness or active material loading per unit surface area of electrodes (in mg/cm^2) can improve the energy density because of increased volume ratio of the active materials as shown in figure 1.17a. Secondly, thick electrodes can minimize the inactive material content such as current collector, separator, and binder thereby reducing material cost [96]. This was proven by various cost modeling studies such as Batpac model and other studies [66], [67] with the assumption of increasing the electrode thickness and also changing the electrode processing methods like aqueous processing instead of using hazardous solvents like N-Méthyl-2-pyrrolidone (NMP), reduction of the anode electrolyte wetting and SEI-layer formation time will also lead to overall battery cost reduction [67].

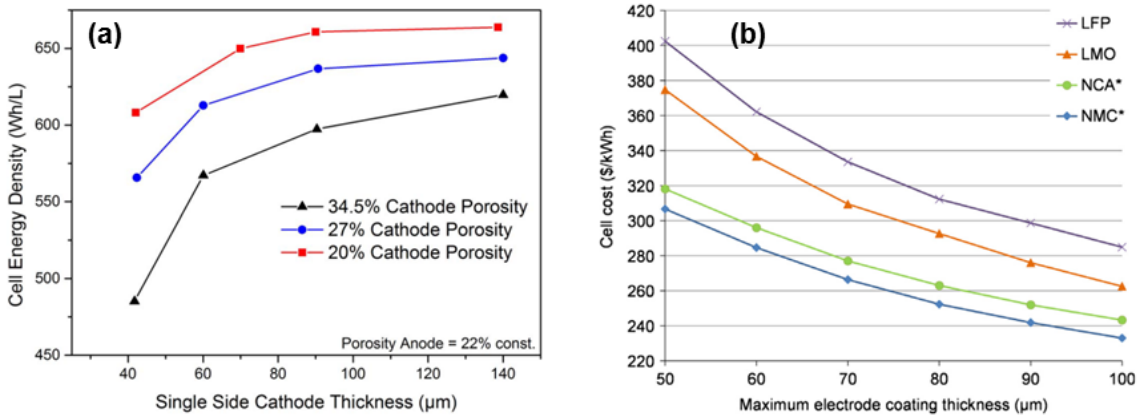

Figure 1.17 *Effect of cathode thickness in the LIB energy density: a) Increase in cathode thickness/ active material loading leads to increase in volumetric energy density. b) Similar trend is observed for four different cathodes showing reduction in cell cost and increase in areal capacity. Reprinted from [66], [96].*

In general, thick electrodes are designed for high energy density and thin electrodes for high power density applications. This is due to the fact that thicker electrodes undergo high cell polarization and lithium-ion transport limitations across the bulk electrode at high C-rates. This phenomena was proved by Zheng *et al.* by reporting the electrochemical performance of different NMC and LFP commercial electrodes versus graphite with different thicknesses [97]. As clearly shown in figure 1.18, the increase in cathode thickness from 25 to 108 µm increases the specific energy from 550 to 700 Wh/L for LFP/G cells and a similar increasing trend is reported for NMC electrodes in the same work.

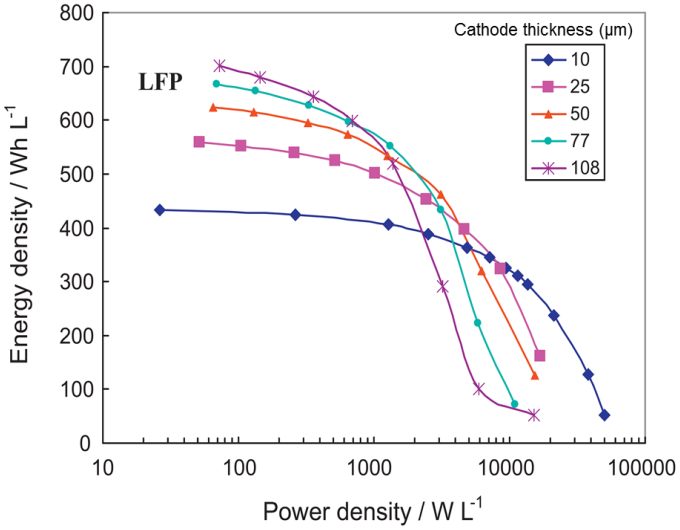

Figure 1.18 *Ragone plot of LFP/G cell with different cathode thicknesses [97]. Linear increase energy density as thickness and decrease in power density which is due to increase in Ohmic drop and diffusion limitations for the thicker electrodes.*

A similar work done by Yu *et al*. reported the discharge capacity for conventional $LiFePO_4$/ Graphite electrodes with varied range of cathode thickness (15–120 μm) [98] and reported the increase in cell polarization and the lithium ion diffusion limitations in the liquid phase as the two crucial problems need to be addressed for the thick electrodes. Overall, it is very evident that fabricating thick electrodes can hugely increase the energy density and thus we aim at fabricating thick electrodes to increase the energy density. The available fabrication methods for thick electrodes in the state of art are discussed in the next section.

1.5.2 Methods to prepare thick electrodes

In Li-ion batteries, several groups have attempted to make textile electrodes[99], sinter the active material without current collector and 3D metal current collectors as supports to increase the active material loading for lithium storage alloys [100], [101]. These strategies can help to improve the electrical performances only to a certain extent but will not improve the active materials utilization completely. Another important aspect for the thick electrodes is the large degree of inhomogeneities of phase separation, state of charge, ion transport and concentration gradient of electrolytes at high discharge rates and crystallinity breakdown during cell operation are seen. In order to visualize and map these non-homogeneous behaviors, several in-situ and operando techniques are available such as synchrotron X-ray micro diffraction [102], X-ray absorption spectroscopy (XAFS) [103], X-ray diffraction with reflection geometry [104], X-ray absorption spectroscopy (XAS) [105] and neutron in-depth profiling [106]. At the same time, higher active material loading of electrodes will suffer from manufacturing limitations such as electrode delamination, flaking and cracking of electrodes. These problems can be overcome by using variety of cell architectures such as embroidered metal foams as current collectors [107], [108] and sintered electrodes [109], [110] as shown in table 1.2.

Table 1.2 *Thick electrodes available in literature with different cell designs.*

Material	Method	Cathode thickness (μm)	Authors	References
$LiCoO_2$	Sintering/Co-extrusion	220	Bae *et al.*	[111]
$LiCoO_2$	Sintering/ Magnetic templating	310	Sander *et al.*	[112]
$LiFePO_4$	Sintering	1000	Qin *et al.*	[109]
$Li(Ni_{0.33}Mn_{0.33}Co_{0.33})O_2$, $LiFePO_4$	Tape casting	24-104	Zheng *et al.*	[113]
$Li(Ni_{0.33}Mn_{0.33}Co_{0.33})O_2$, Graphite	Tape casting	50-250	Singh *et al.*	[63]
$Li(Ni_{0.33}Mn_{0.33}Co_{0.33})O_2$, Graphite	Metal foam	600-1200	Wang *et al.*	[114]
$Li(Ni_{0.33}Mn_{0.33}Co_{0.33})O_2$, Graphite	Tape casting	70-320	Singh *et al.*	[115]
NiCrAl alloy	Metal foam	300-600	Yang *et al.*	[116]

Out of these methods, sintering is one of the promising techniques used to fabricate thicker electrodes. For example, Qin *et al.*[109] prepared 1 mm thick sintered LFP electrodes using citric acid as a pore forming agent resulting in a pore size equivalent to the particle size of the citric acid as shown in the figure 1.19. The volumetric energy density was calculated showing 500 Wh/L with respect to the volume of a single electrode. But the value is still lower than the commercially available Li ion batteries (700 Wh/L). So, a better technology is needed to improve the sintering capability of the battery materials and make the system more efficient and faster.

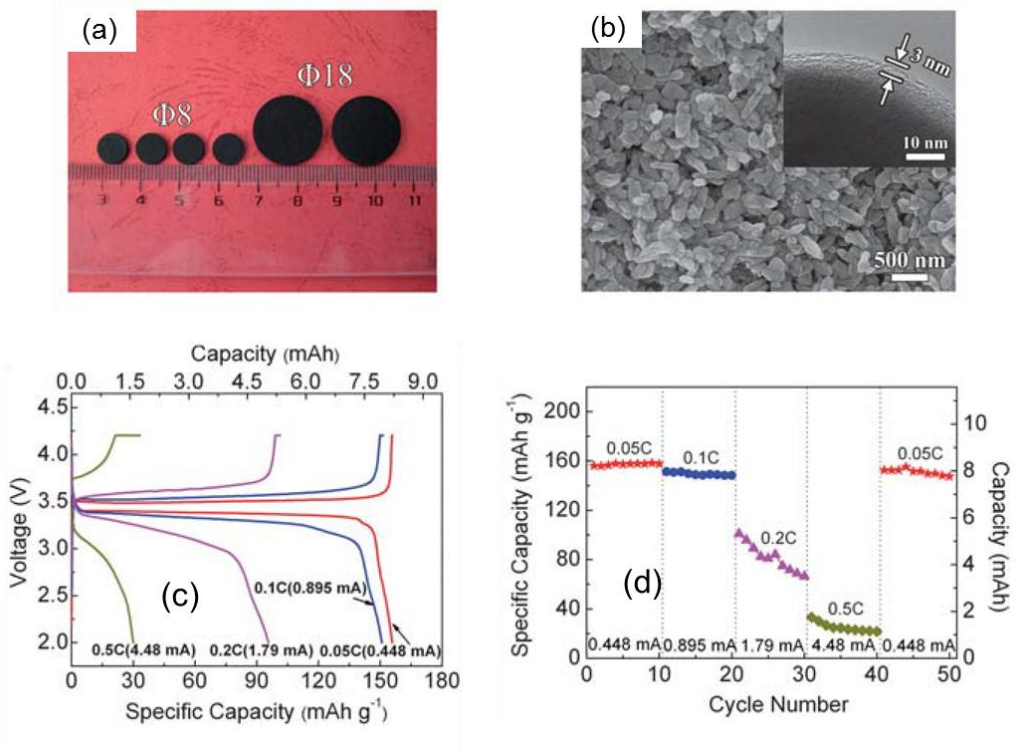

Figure 1.19: *Fabrication of thick carbon coated LFP electrode using conventional sintering [109]. a) Digital photograph of different sizes of sintered electrode prepared at 700 °C for 7 hours b) Carbon coated LFP electrode with 90 nm-3 µm pore size equivalent to the size of citric acid as porogen. c) Charge-discharge curve at different C-rates. d) Poor performance at 0.2 C and 0.5 C rates are co-related to the smaller pore size due to poor Li diffusion.*

Spark Plasma Sintering (SPS) is a recent technique used to fabricate thick electrodes and solid electrolytes for lithium and sodium ion batteries. The principle, operation and motivation of SPS will be discussed in detail in the next chapter. Two years before, a comprehensive literature review was published by Kali *et al.* about the state of art of lithium based electrodes and electrolytes done by SPS [117]. It is explained that the number of papers about the electrodes and electrolytes using SPS are rapidly increasing and thus the significance of this new technique is clearly explained. Some of the recent works done for the commercial electrode materials are discussed. For example, Takeuchi *et al.* fabricated the $LiFePO_4$ [118], [119], $LiNi_{0.8}Co_{0.15}Al_{0.05}O_2$ [120] and Li_2S/C [121], [122] electrodes using SPS, which shows their widespread use for different systems and highlighted the very good electrical contact between the particles. This leads to the reduction of interfacial resistance and better electrochemical performance of pellets was acheived than the conventionally blended powders. Arachi *et al.*[123] reported the dense and phase pure $Li_{2-x}FeSi_{1-x}P_xO_4$ based electrodes, with minimum carbon content (<3 wt. %), possessing improved ionic and electronic conductivities. Apart from Li-ion battery, activated carbon-PVDF composite electrodes are also prepared for super-capacitor applications using SPS, showing higher capacitance values and very high power density [124], [125].

Table 1.3 *Electrode fabrication using Spark Plasma sintering.*

Electrodes	Temperature (K)	Pressure (mpa)	Time (min)	References
$LiFePO_4$	873	-	-	[119]
Li_2CoPO_4F	773-973	25	4	[126]
$Li_{2-x}FeSi_{1-x}P_xO_4$	873-1073	-	5-30	[123]
$LiNi_{0.8}Co_{0.15}Al_{0.05}O_2$	523	500	1	[127]
$Li_{1.05}Mn_{1.95}O_4$	573	30	60	[128]
Li_2S	673-1273	20	-	[122]
Sn-Sb alloys	673	7	5	[129]
Activated carbon	1273	25	1	[124]
ZrO_2	1573	30	2	[130]

Nano particle synthesis of cathode material was done using SPS technique. For example, the fluorophosphate material Li_2CoPO_4F was prepared during SPS by Botto *et al*. [126]. As shown in figure 1.20, SEM images of LCPF are displaying its nano-size and the electrochemical performance is better than the conventional tape casted electrodes as shown in figure 1.20.

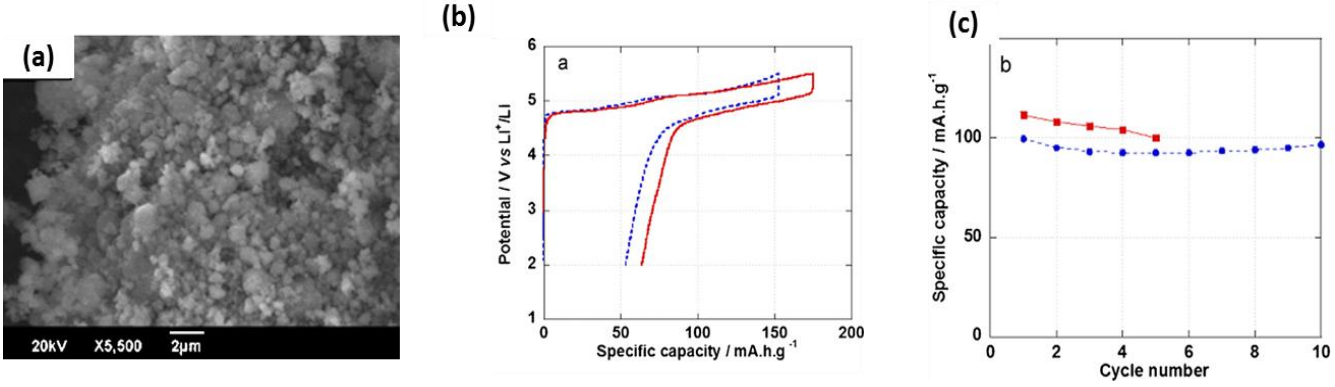

Figure 1.20 *$LiCoPO_4$ electrode fabricated using SPS [126].*

On the other hand, SPS technique was adopted for the preparation of solid electrolytes, mainly ceramic materials having very high ionic conductivity. Solid electrolytes are seeking a greater attention nowadays due to their safety characteristics and their ionic conductivity comparable to that of liquid

electrolytes [131]–[136]. In general, there are two classes of solid electrolytes for lithium-ion batteries: Organic polymers and inorganic ceramics. The main difference between these two is their mechanical properties. Polymers are mostly used for flexible devices due to their low elastic moduli and limited by high temperature processing because of the low thermal stabilty. However, ceramic electrolytes are possessing high elastic moduli suitable for high temperature processing methods such as SPS and rigid battery designs are possible in thin film devices [165]–[170]. Solid electrolytes such as LIthium Super-Ionic CONductor (LISICON) and NAtrium Super-Ionic CONductor (NASICON) materials are having less interfacial resistances to improve the ionic conductivity [123]. Ceramic electrolytes are composed of sulfides, oxides or phosphates [28], [143]. SPS involves the preparation of ceramic electrolytes preferentially rather than polymer electrolytes by showing good adhesion, avoiding segregation of secondary phases with reduced crystallite size, high grain-grain boundary and comparable ionic conductivity to liquid electrolytes [25], [139], [144], [145].

Table 1.4 *Comparison of SPS and conventional sintering (CS) for solid state electrolytes [146]. Higher density and ionic conductivity was observed using SPS compared to Conventional sintering (CS).*

Sample	**Temp. (°C)**	**Pressure (Mpa)**	**Density**		**Ionic conductivity @ RT (S/cm)**	
			(SPS)	**(CS)**	**(SPS)**	**(CS)**
$LiTi_2(PO_4)_3$	950	75	90 %	60 %	$8.6 * 10^{-5}$	$6.0 * 10^{-5}$
$Li_{1.3}Al_{0.3}Ti_{1.7}(PO_4)_3$	950	75	98 %	71 %	$1.1 * 10^{-2}$	$6.2 * 10^{-3}$
$Li_{1.3}Cr_{0.3}Ti_{1.7}(PO_4)_3$	850	75	86 %	51 %	$3.6 * 10^{-3}$	$2.9 * 10^{-4}$
$Li_{1.3}Fe_{0.3}Ti_{1.7}(PO_4)_3$	700	75	95 %	65 %	$1.0 * 10^{-3}$	$2.3 * 10^{-5}$

Cold pressing is a mechanical pressing method without applying temperature which is employed to prepare the all solid state battery (ASSB) but the applied pressure influences the compactness and ionic conductivity of the solid electrolyte layer. The comparison of conventional and spark plasma sintering density values for the NASICON type solid electrolytes was shown in table 1.4 explaining very high compactness up to 90-98% was reached thereby high ionic conductivity [173]–[177]. One step SPS treatment of anode-solid electrolyte-cathode layers were fabricated by Lalère *et al.* leading to all solid state sodium ion battery (ASSB) which is a safer, alternative solution to conventional liquid electrolyte batteries [151], [152]. As seen in figure 1.21, a digital photo of the full battery shows a clear multi layered pellet with defined thickness of 0.56 mm and diameter of 10.2 mm as shown in figure 1.21b.

The corresponding SEM images (figure 1.21c) of the three layered battery show good interfaces with high grain-grain bonding and defined thickness. The charge-discharge curve (figure 1.21d) shows that there is a less polarization and almost 90% of theoretical capacity is achieved at low C-rate.

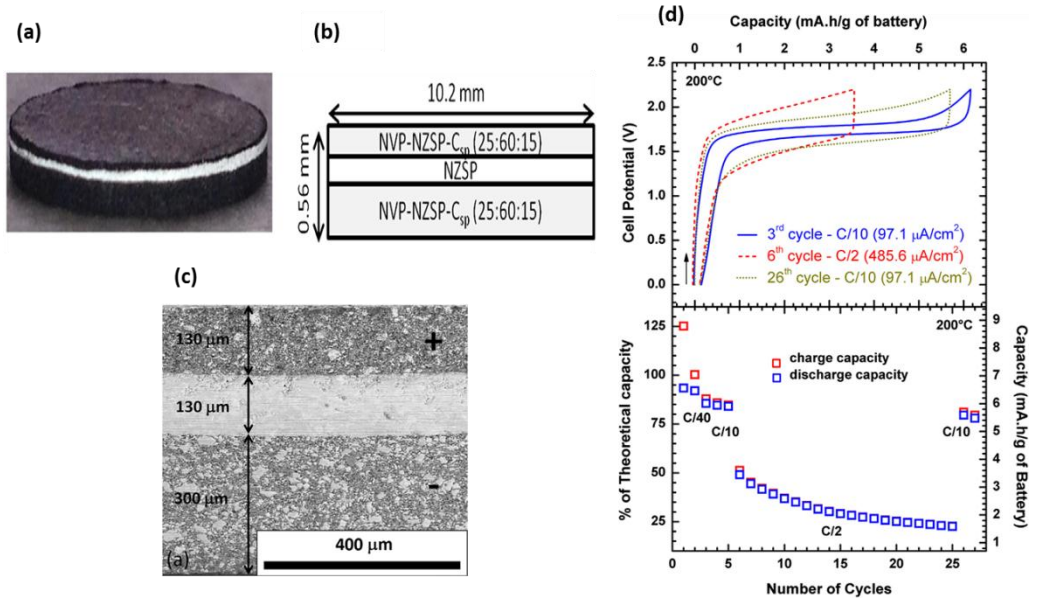

Figure 1.21 *All solid state sodium ion battery fabricated using SPS technique. a) and b) Digital photograph and corresponding schematic of the three layered $Na_3V_2(PO_4)_3$ - $Na_3Zr_2Si_2PO_{12}$ - $Na_3V_2(PO_4)_3$ battery, c) SEM image of NVP-NZSP-NVP battery clearly shows the well-defined interface between the layers obtained in a single step SPS technique. d) Good electrochemical performance of NVP-NZSP-NVP all solid state sodium ion battery was achieved at very high temperature of 200 °C.*

1.5.4 Porous electrodes of Li ion batteries and preparation methods

Electrodes of Li-ion batteries are generally porous in nature. These pores are intentionally created in the electrodes to improve their electrochemical performance. Some of the benefits of porous electrode are listed below.

- Pores will enable the liquid electrolyte to pass through the electrode surface especially for the thick and dense electrodes.
- Charge transfer in electrode/electrolyte interface is greatly improved because of the large surface area created by the pores.
- The pores are surrounded by their walls and this reduces the path length for diffusion based on different pore sizes and complete utilization of active material will be achieved thereby increasing the specific capacity at high C-rates.
- Though the large porosity decreases the volumetric capacity, optimum value is needed and performance of porous electrodes is always higher when compared to non-porous electrodes.
- Porous electrodes can also stabilize or reduce the volume expansion during intercalation/deintercalation of the composite electrodes.

Different methods such as electrospinning [153], aerogel techniques [154], chemical vapour deposition [155], gas purging, templating, and non templating methods are adopted to create porous architectures for active materials or current collectors. Surfactant agents are added with the precursors of the active material to increase the surface area by the pore formation inside the active material surface. For example, thermally degradable surfactants such as poly (ethylene-co-butylene)-block poly (ethylene oxide) diblock copolymer are added with active material precursors to fabricate hierarchically ordered pores in the active material (Ex: $Li_4Ti_5O_{12}$) anode electrodes for Li-ion batteries [156], [157]. Out of different methods, the templating method is chosen due to its simplicity and the description and motivation of templating method in our thesis will be discussed in detail below.

Templating is the powerful cost efficient method adopted to fabricate porous electrodes for many electrochemical systems such as batteries, fuel cells and super capacitors. Templates are the sacrificial agents added along with the active material and later they are either dissolved or carbonized after the heat treatment forming a well interconnected pore network with uniform pore size distribution. The selection of the templating agents is very important and for example, the final pore size of the

electrodes are mainly dependent on many microstructural properties such as particles size, shape and type of templating agents. According to the electrode pore size, they are classified as micropores (less than 2 μm), mesoporous (2-50 μm) and macropores (above 50 μm). The effects of pore size were also studied in other energy storage devices like supercapacitors and fuel cells [158]–[161]. Also, it can be related to the texture of the electrode but also on the residual pores present on the active material, ordered or disordered based on their arrangement. Anisotropic materials with varied shapes and sizes [162] are synthesized and used as a pore forming/ structure directing agent to create regular porous structures. Though different methods are available in the literature, salt templating is a simplified, cost efficient method to achieve controllable porosity and pore size in the electrodes, which will be discussed in the next section.

Based on the thermal stability, pore creating templates are divided into two categories: soft and hard templates. Soft templates are mostly thermally decomposable polymers at lower temperature, including polyurethane (PU), polystyrene (PS), polymethyl methacrylate (PMMA) and amphiphilic block polymers. Polymers offer the advantage of avoiding the extra etching step but at the same time, larger shrinkage is observed that leads to 20-40% smaller final pores spacing than the repeat distance between the templating spheres. Hard templates are thermally stable inorganic solids such as sodium chloride [163], silica gel [164], silica nanoparticles [165], Na_2CO_3 and $Ni(OH)_2$ in which templates were removed by hazardous chemical etching or dissolving with solvents. The methods such as colloidal crystal templating [166] and nano casting [167] are available in literature to create hierarchically porous structures for Li-ion batteries. The schematic shown in fig 1.22 illustrates the different architectures of silica electrodes such as tubular, spherical pores obtained according to the initial shape of the templates.

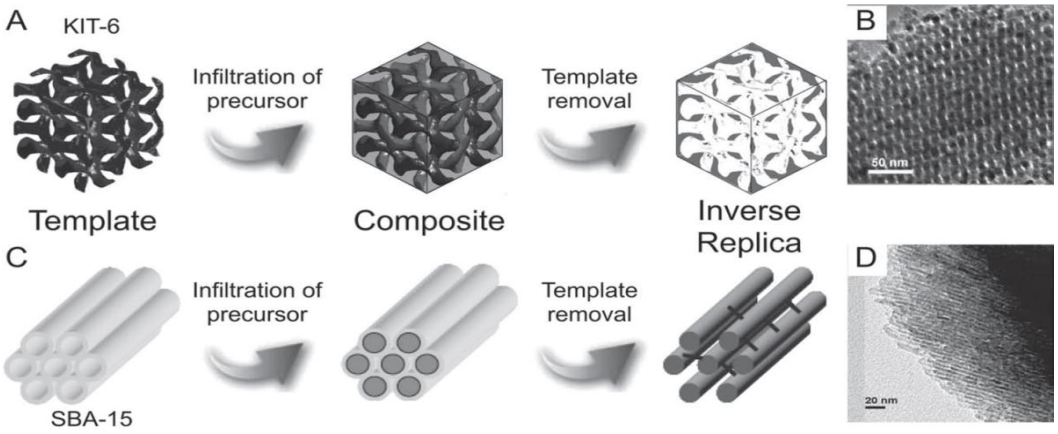

Figure 1.22 *Schematic of templating methods to create porous electrodes[168]. KIT-6 and SBA-15 are the silica material used as hard templates creating micro/meso pores in the electrode material obtained by chemical etching.*

Though the templating method can be done by different strategies such as chemical, magnetic and electrochemical methods, a relatively simple method is missing. For example, Endres *et al.* [169] reported the template assisted electrochemical method for preparing macroporous Al films by electrodepositing chloraluminate ionic liquid within a polystyrene template on a copper support. In this method, the metal particle grows on top of the substrate with the effective filling of pores by the metallic product. However, the complex synthesis makes it impractical for conventional electrode fabrication. Another interesting work by Y.M.Chang *et al.* reported the fabrication of 220 μm thick templated LCO porous electrodes by co-extrusion of carbon black-binder mixture as a feed rod and/or template and sintered along with the active material. As shown in figure 1.23a, repeated extrusion up to 3 times and sintering was done by creating vertically aligned cylindrical pores with less pore spacing for lithium ion diffusion during the cell operation [111]. Also, the same group reported a similar strategy of using magnetic templates by means of colloidal suspensions mixed with LCO particles. An external magnetic field is applied to align the magnetic particles and later removed to create aligned vertical channels inside the LCO electrodes which are designed to show better electrochemical properties than homogenous distribution of pores. Though this method is considered strenuous, they reported very high areal capacity value of around 7 mAh/cm^2 vs lithium at 2C rate, higher than conventional battery electrodes [112].

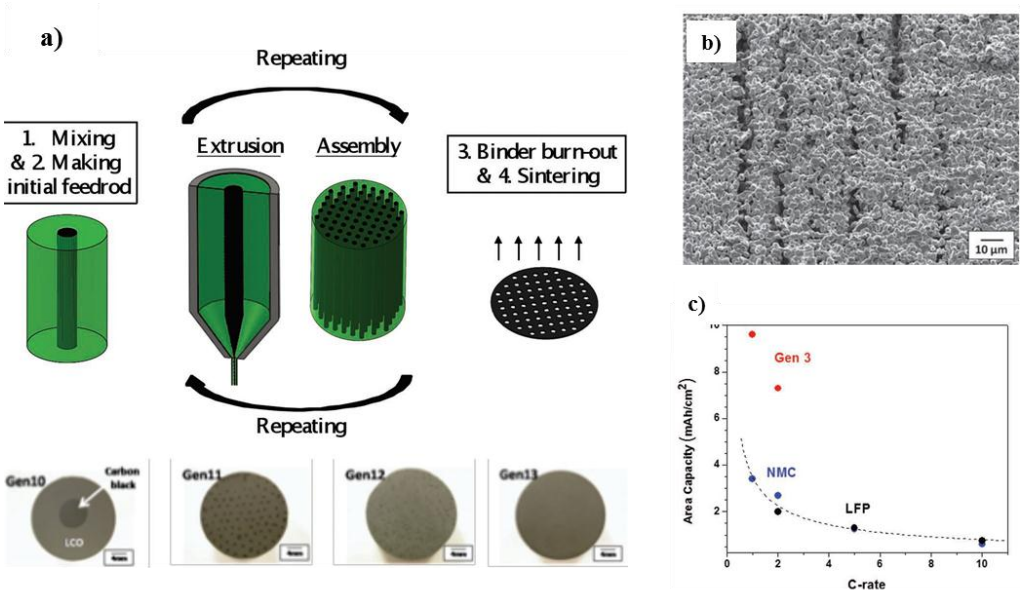

Figure 1.23 *Co-extrusion/sintering of LCO electrodes and its electrochemistry[110]. a) Initial feed rod of carbon/binder mixture surrounded by LCO active material was extruded multiple times to obtain periodic array and then sintered feed rod turns to porous channels. b) SEM images show the macro-pore channels where controlled channel spacings are observed. c) Higher areal capacity at 1C and 2C rate is compared to conventional electrodes.*

Recently, templating materials are fabricated with varied pore size ranging from nano- to micrometer and increased performance is obtained due to their high mechanical and thermal stabilities. The main criteria for the pore forming agents should be 1) Chemically inert to the host material, 2) Stable at high temperature during heat treatment and 3) Cost effective and environmentally friendly. In most cases, silica is used as template because of meeting all the above mentioned criteria. High temperature resistant silica (SBA-15 and KIT-6) [170] or the periodic mesoporous carbon materials (CMK-3 and CMK-8) [171] were used as the pore forming agent in the literature. For example, porous LFP nanowires are prepared using silica template (SBA-15) with a thickness of 7 nm and specific surface area of 105 m^2/g (BET) and pores of 5.9 nm (BJH analysis of nitrogen sorption at 77 K) with high gravimetric capacity of 137 mAh/g at 15 C [172]. However, recycling of silica uses the HF or NaOH etching which is not good for the environment and carbon templates require elevated temperature for the thermal decomposition [173]. This incomplete removal of silica particles will have a direct influence on the electrochemical behavior. So, the usage of environmentally benign and thermally stable template was needed and it should be easily adopted for large scale fabrication.

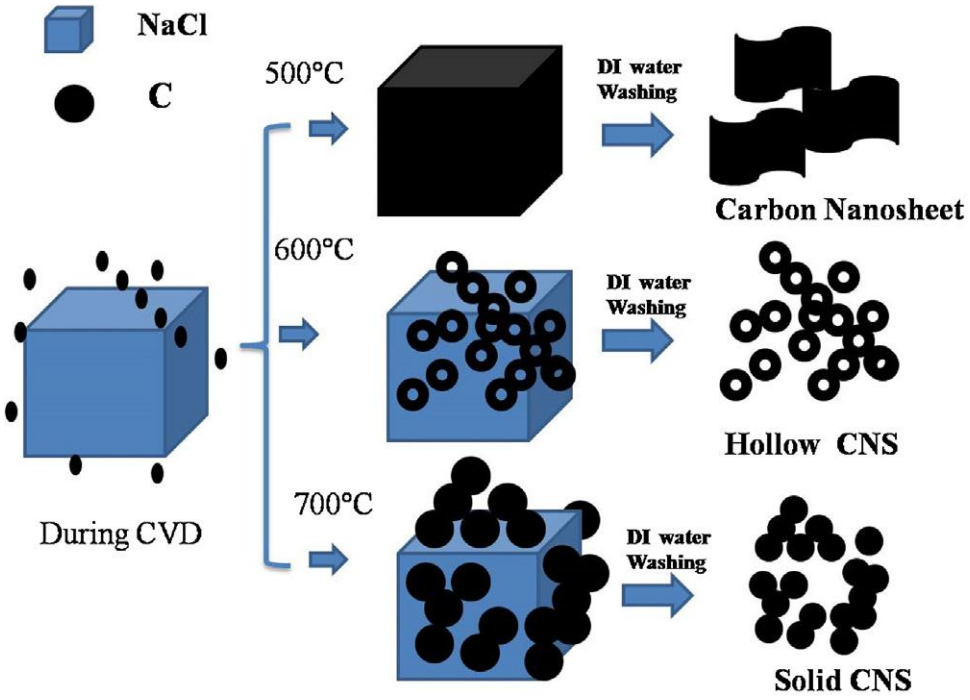

Figure 1.24 *Schematic of carbon nanosphere obtained using salt templating [155].*

These requirements are fulfilled by simply prepared and easily washable salts like NaCl due to its high solubility in water (as high as 26.5 g in 100 g of water at 20°C) and thermal stability [174]. Also, NaCl remains as an environmental friendly and cost effective template to fabricate porous electrodes for lithium batteries [175]. NaCl is rich in abundance, cubic in particle shape, environmentally benign, cheap and also used in our day to day life applications such as cooking, medical and pharmaceutical industries. Gao Li *et al* fabricated porous Si-based anode material using NaCl and they claim that the electrochemical performance is highly improved due to the pores created by the salt that enable the material to reduce the volume expansion occurred during the operation [176]–[179]. The macroporous networks created by the salt particles promote the diffusion of electrolyte into the inner area of the electrodes and thus the rapid lithium transport can be achieved with the short lithium diffusion distance. Li *et al.* has reported the growth of graphene paper using NaCl as a sacrificial template using microwave plasma–enhanced chemical vapor deposition method [180]. Zhao *et al*. has prepared hierarchical porous carbon monoliths using Iron catalyst with coated NaCl template by CVD as shown in figure 1.24 [72]. It is worth to mention that the NaCl was used extensively as a template for the growth of 1D and 2D carbon nanostructures such as Carbon nanotubes (CNTs), spongy CNT paper, and carbon nano fiber (CNF) with different catalyst nanoparticles [163], [181], [182].

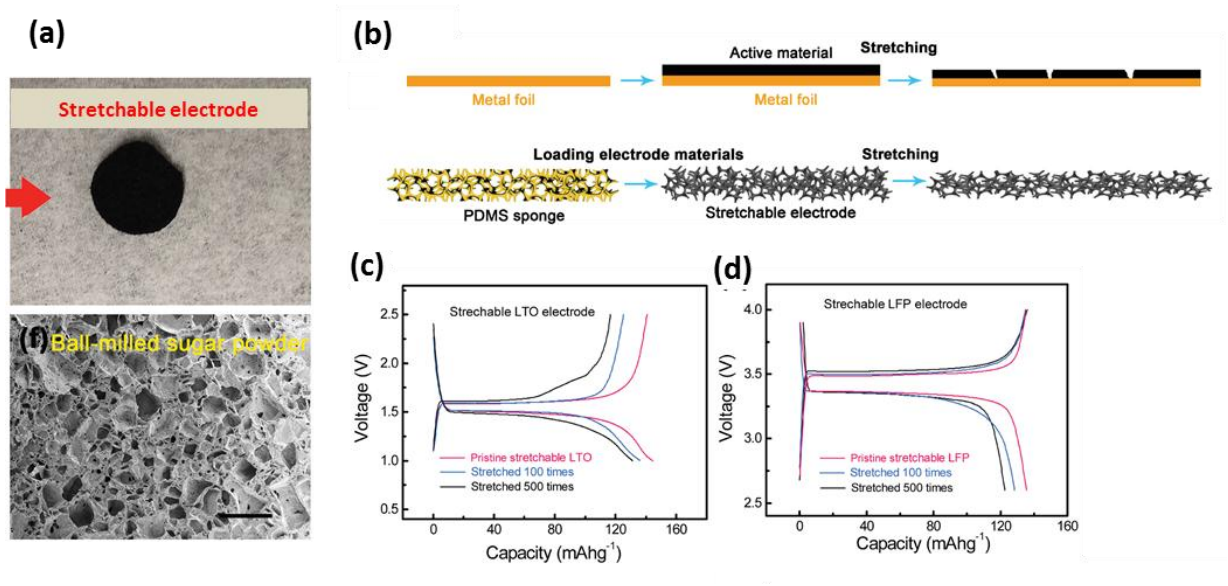

Figure 1.25 *3D porous sponge inspired LFP and LTO electrodes by sugar templating. a) Stretchable LFP/LTO electrode and corresponding SEM images of the porous LFP or LTO electrode with pore size equivalent to the initial sugar particles size. Scale bar: 500 µm. b) Schematic of conventional and stretching electrode fabrication method. c) and d) Charge-discharge profiles showing enhanced performance of stretchable electrodes vs lithium. Reprinted from [183].*

Other than NaCl, other salts such as potassium chloride and zinc chloride or their mixture can be used as a pore creating agent and help to rise the operating temperature to 1000 °C to create vertically aligned carbon nanosheets [184]. Various polymers such as polyvinyl chloride (PVC), poly methyl methacrylate (PMMA) and polyethylene oxide (PEO) are also used as pore forming agents to create hierarchically porous piezo ceramic materials by sintering at very high temperature (1200 °C) [185]. Recently, sugar was used as a pore forming agent to create 3D porous sponge-inspired electrode for stretchable lithium-ion batteries as shown in figure 1.25 [183]. In summary, out of varied methods available in literature, templating methods are very efficient scalable methods applicable for preparing porous electrodes with well controlled and interconnected microstructures useful for several battery systems.

1.7 Aim of the Thesis

The main goal of the thesis was to fabricate thick binder free electrodes for Li-ion batteries using Spark Plasma Sintering (SPS) and templating approach and to obtain high areal capacity for Li-ion batteries to improve energy density. In my thesis, thick electrodes are fabricated using SPS installed in Laboratoire de Réactivité et Chimie des Solides (LRCS, Amiens, France). The PhD thesis is composed of four working chapters. The first chapter is about a broad overview of batteries and a bibliographic review of strategies of achieving high energy density for Li-ion batteries and methods to fabricate thick electrodes. It is very clear that since its commercialization, the energy density of Li-ion batteries was constantly improving with the help of a varied range of advanced techniques and strategies to prepare the active material in first place up to the final battery production. So, in our thesis by combining the SPS technique and templating approach, thick and binder free electrodes are fabricated to achieve the high energy density of Li-ion batteries and the overall schematic is shown in figure 1.26.

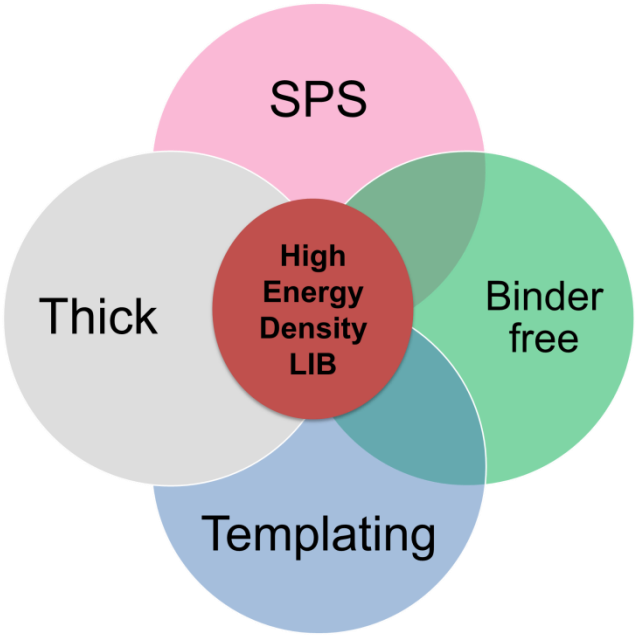

Figure 1.26 *Combined approach of fabricating thick binder free templated electrodes using SPS.*

The second chapter focuses on principle, motivation of combining SPS and templating approach supported by the experimental results of prominent battery materials such as $LiFePO_4$ (LFP) and $Li_4Ti_5O_{12}$ (LTO). This ensures the possibility of making thick electrodes and investigating their electrochemical properties such as areal capacity, which is an essential parameter to increase energy

density. Several characterization techniques such as XRD, SEM-EDX, ASAP porosimetry have been used to study the morphological and microstructural characteristics of the LFP and LTO thick electrodes fabricated by the SPS/ templating approach. The influence of additional carbon used in the LFP electrode composition was compared with the bare LFP electrode. The effect of pore inhomogeneity of LFP thick electrode on edges and center of the electrode was studied by their respective cross section SEM images and the influence in rate capability was reported. The capacity retention and rate capability tests of LFP and LTO half cells were carried out. Also, a full battery was assembled using the 1 mm thick LFP and LTO sintered electrodes at C/20 rate and the capacity retention performance are discussed. Finally, the areal capacity of the thick binder free sintered electrodes is compared with the literature works to assess the electrochemical properties.

The optimization of critical parameters such as porosity, pore size and thickness of LFP electrodes fabricated by SPS/templating approach is investigated in chapter 3. The electrochemical performance of Li-ion batteries is largely dependent on the electrode parameters. First, the effect of pores size in the 1 mm thick LFP electrode was done and involves the synthesis of templating agents with different particles size distribution. The 3D view of thick LFP electrodes are analyzed by the micro computed tomography and key parameters such as tortuosity, porosity, pore size distribution and specific surface area are determined for the thick electrodes. Synchrotron X-ray Transmission microscopy was done in collaboration with Argonne National laboratory for the analysis of 3D LFP and LTO electrodes with different pore sizes. Detailed imaging analysis using Tau factor software was done for the thick electrodes to determine useful parameters such as porosity, pore size distribution, electrode tortuosity in 3 directions, anisotropy factor and specific surface area of thick electrodes and is discussed in Chapter 3. A comparative study of the tortuosity determination of thick electrodes using different methods like Electrical impedance spectroscopy, transmission line model (in collaboration with Dr. Charles Delacourt in LRCS) and tomography techniques of LFP electrodes was done. This helps to identify the reliable method of measuring electrode tortuosity and understand its influence on the electrochemical behavior. The electrochemical characterization such as galvanostatic cycling and electrical impedance spectroscopy of thick LFP electrodes is correlated with the tomography data analysis. A systematic study by fabricating LFP electrodes with various thicknesses from 0.5 mm to 3 mm was done using the SPS/templating approach. The electrochemical performances are reported in chapter 3 to assess the mass transport limitations of the thick LFP electrodes.

Chapter 4 deals with the improvement towards the surface mechanism of thick LFP electrodes by alumina coating using Atomic Layer Deposition (ALD) and its influence in the electrochemical properties are compared. This chapter also reports the preparation and fabrication of thick electrodes using other active materials such as $Na_3V_2(PO_4)_3F$ and Sn-Sb alloy electrodes are done using SPS and salt templating strategy. The structural and morphological properties such as porosity, pore size distribution are characterized using XRD, SEM and EDX for the thick electrodes. The synthesis procedure of pure SnSb material and thick electrode fabrication is reported. Structural and electrochemical characterization was discussed. The different configurations of LFP electrodes such as single step multilayered full battery composed of LFP-LCZP-LTO and multilayer of pores are reported with their first electrochemical results.

1.8 References

[1] D. Larcher and J.-M. Tarascon, "Towards greener and more sustainable batteries for electrical energy storage," *Nat. Chem.*, vol. 7, no. 1, pp. 19–29, Nov. 2014.

[2] "International Energy Agency." [Online]. Available: https://www.iea.org/. [Accessed: 11-Jul-2017].

[3] "Why we must quit coal | Greenpeace International." [Online]. Available: http://www.greenpeace.org/international/en/campaigns/climate-change/coal/. [Accessed: 06-Nov-2017].

[4] H. Riebeek, "Global Warming : Feature Articles," 03-Jun-2010. [Online]. Available: https://earthobservatory.nasa.gov/Features/GlobalWarming/page5.php. [Accessed: 07-Aug-2017].

[5] P. Poizot and F. Dolhem, "Clean energy new deal for a sustainable world: from non-CO2 generating energy sources to greener electrochemical storage devices," *Energy Environ. Sci.*, vol. 4, no. 6, p. 2003, 2011.

[6] B. Dunn, H. Kamath, and J.-M. Tarascon, "Electrical Energy Storage for the Grid: A Battery of Choices," *Science*, vol. 334, no. 6058, pp. 928–935, Nov. 2011.

[7] M. S. Whittingham, "Electrical Energy Storage and Intercalation Chemistry," *Science*, vol. 192, no. 4244, pp. 1126–1127, Jun. 1976.

[8] K. Mizushima, P. C. Jones, P. J. Wiseman, and J. B. Goodenough, "LixCoO2 (0< x<-1): A new cathode material for batteries of high energy density," *Mater. Res. Bull.*, vol. 15, no. 6, pp. 783–789, 1980.

[9] R. Van Noorden, "A better battery," *Nature*, vol. 507, no. 7490, p. 26, 2014.

[10] J. Liu *et al.*, "Materials Science and Materials Chemistry for Large Scale Electrochemical Energy Storage: From Transportation to Electrical Grid," *Adv. Funct. Mater.*, vol. 23, no. 8, pp. 929–946, Feb. 2013.

[11] M. R. Palacín, "Recent advances in rechargeable battery materials: a chemist's perspective," *Chem. Soc. Rev.*, vol. 38, no. 9, p. 2565, 2009.

[12] I. Belharouak, Y.-K. Sun, J. Liu, and K. Amine, "Li(Ni1/3Co1/3Mn1/3)O2 as a suitable cathode for high power applications," *J. Power Sources*, vol. 123, no. 2, pp. 247–252, Sep. 2003.

[13] S.-L. Wu *et al.*, "High rate capability of Li (Ni1/3Mn1/3Co1/3) O2 electrode for Li-ion batteries," *J. Electrochem. Soc.*, vol. 159, no. 4, pp. A438–A444, 2012.

[14] A. K. Padhi, K. S. Nanjundaswamy, and J. B. Goodenough, "Phospho-olivines as positive-electrode materials for rechargeable lithium batteries," *J. Electrochem. Soc.*, vol. 144, no. 4, pp. 1188–1194, 1997.

[15] "Thèse Lalère Fabien LRCS.pdf." .

[16] S. Nishimura, M. Nakamura, R. Natsui, and A. Yamada, "New Lithium Iron Pyrophosphate as 3.5 V Class Cathode Material for Lithium Ion Battery," *J. Am. Chem. Soc.*, vol. 132, no. 39, pp. 13596–13597, Oct. 2010.

[17] V. Legagneur *et al.*, "LiMBO3 (M=Mn, Fe, Co):," *Solid State Ion.*, vol. 139, no. 1, pp. 37–46, Jan. 2001.

[18] C. Masquelier and L. Croguennec, "Polyanionic (Phosphates, Silicates, Sulfates) Frameworks as Electrode Materials for Rechargeable Li (or Na) Batteries," *Chem. Rev.*, vol. 113, no. 8, pp. 6552–6591, Aug. 2013.

[19] J. Yin, M. Wada, K. Yamamoto, Y. Kitano, S. Tanase, and T. Sakai, "Micrometer-Scale Amorphous Si Thin-Film Electrodes Fabricated by Electron-Beam Deposition for Li-Ion Batteries," *J. Electrochem. Soc.*, vol. 153, no. 3, p. A472, 2006.

[20] J. Hassoun, G. Derrien, S. Panero, and B. Scrosati, "A SnSb–C nanocomposite as high performance electrode for lithium ion batteries," *Electrochimica Acta*, vol. 54, no. 19, pp. 4441–4444, Jul. 2009.

[21] K. Zaghib *et al.*, "Safe and fast-charging Li-ion battery with long shelf life for power applications," *J. Power Sources*, vol. 196, no. 8, pp. 3949–3954, Apr. 2011.

[22] V. Etacheri *et al.*, "Effect of Fluoroethylene Carbonate (FEC) on the Performance and Surface Chemistry of Si-Nanowire Li-Ion Battery Anodes," *Langmuir*, vol. 28, no. 1, pp. 965–976, Jan. 2012.

[23] H. Zhao *et al.*, "Propylene carbonate (PC)-based electrolytes with high coulombic efficiency for lithium-ion batteries," *J. Electrochem. Soc.*, vol. 161, no. 1, pp. A194–A200, 2014.

[24] C. Han *et al.*, "A review of gassing behavior in $Li_4Ti_5O_{12}$-based lithium ion batteries," *J Mater Chem A*, vol. 5, no. 14, pp. 6368–6381, 2017.

[25] J. Y. Song, Y. Y. Wang, and C. C. Wan, "Review of gel-type polymer electrolytes for lithium-ion batteries," *J. Power Sources*, vol. 77, no. 2, pp. 183–197, 1999.

[26] D. Peramunage, D. M. Pasquariello, and K. M. Abraham, "Polyacrylonitrile-Based Electrolytes with Ternary Solvent Mixtures as Plasticizers," *J. Electrochem. Soc.*, vol. 142, no. 6, pp. 1789–1798, Jan. 1995.

[27] N.-S. Choi, Y. Lee, S.-S. Kim, S.-C. Shin, and Y.-M. Kang, "Improving the electrochemical properties of graphite/LiCoO2 cells in ionic liquid-containing electrolytes," *J. Power Sources*, vol. 195, no. 8, pp. 2368–2371, Apr. 2010.

[28] K. Takada, "Progress and prospective of solid-state lithium batteries," *Acta Mater.*, vol. 61, no. 3, pp. 759–770, Feb. 2013.

[29] J. G. Kim *et al.*, "A review of lithium and non-lithium based solid state batteries," *J. Power Sources*, vol. 282, pp. 299–322, May 2015.

[30] Y. Kato *et al.*, "High-power all-solid-state batteries using sulfide superionic conductors," *Nat. Energy*, vol. 1, no. 4, p. 16030, Mar. 2016.

[31] A. Nyman, T. G. Zavalis, R. Elger, M. Behm, and G. Lindbergh, "Analysis of the Polarization in a Li-Ion Battery Cell by Numerical Simulations," *J. Electrochem. Soc.*, vol. 157, no. 11, p. A1236, 2010.

[32] A. Nyman, M. arten Behm, and G. Lindbergh, "A Theoretical and Experimental Study of the Mass Transport in Gel Electrolytes II. Experimental Characterization of LiPF6-EC-PC-P (VdF-HFP)," *J. Electrochem. Soc.*, vol. 158, no. 6, pp. A636–A643, 2011.

[33] A. Nyman, M. Behm, and G. Lindbergh, "Electrochemical characterisation and modelling of the mass transport phenomena in LiPF6–EC–EMC electrolyte," *Electrochimica Acta*, vol. 53, no. 22, pp. 6356–6365, Sep. 2008.

[34] H. Lundgren, M. arten Behm, and G. Lindbergh, "Electrochemical characterization and temperature dependency of mass-transport properties of LiPF6 in EC: DEC," *J. Electrochem. Soc.*, vol. 162, no. 3, pp. A413–A420, 2015.

[35] Y. Ma, M. Doyle, T. F. Fuller, M. M. Doeff, L. C. De Jonghe, and J. Newman, "The measurement of a complete set of transport properties for a concentrated solid polymer electrolyte solution," *J. Electrochem. Soc.*, vol. 142, no. 6, pp. 1859–1868, 1995.

[36] S. G. Stewart and J. Newman, "The Use of UV/vis Absorption to Measure Diffusion Coefficients in LiPF[sub 6] Electrolytic Solutions," *J. Electrochem. Soc.*, vol. 155, no. 1, p. F13, 2008.

[37] Y.-S. Hu, Y.-G. Guo, R. Dominko, M. Gaberscek, J. Jamnik, and J. Maier, "Improved Electrode Performance of Porous LiFePO4 Using RuO2 as an Oxidic Nanoscale Interconnect," *Adv. Mater.*, vol. 19, no. 15, pp. 1963–1966, Aug. 2007.

[38] C. H. Chen *et al.*, "Studies of Mg-Substituted Li4−xMg x Ti5O12 Spinel Electrodes (0≤x≤1) for Lithium Batteries," *J. Electrochem. Soc.*, vol. 148, no. 1, pp. A102–A104, Jan. 2001.

[39] L.-F. Cui, L. Hu, J. W. Choi, and Y. Cui, "Light-Weight Free-Standing Carbon Nanotube-Silicon Films for Anodes of Lithium Ion Batteries," *ACS Nano*, vol. 4, no. 7, pp. 3671–3678, Jul. 2010.

[40] G. Zhou *et al.*, "Graphene-Wrapped Fe3O4 Anode Material with Improved Reversible Capacity and Cyclic Stability for Lithium Ion Batteries," *Chem. Mater.*, vol. 22, no. 18, pp. 5306–5313, Sep. 2010.

[41] Y.-M. Chiang, N. Meethong, and Y.-H. Kao, "Reply to Comment on 'Aliovalent Substitutions in Olivine Lithium Iron Phosphate and Impact on Structure and Properties,'" *Adv. Funct. Mater.*, vol. 20, no. 2, pp. 189–191, Jan. 2010.

[42] K.-S. Park, S. B. Schougaard, and J. B. Goodenough, "Conducting-Polymer/Iron-Redox- Couple Composite Cathodes for Lithium Secondary Batteries," *Adv. Mater.*, vol. 19, no. 6, pp. 848–851, Mar. 2007.

[43] Y. Oh, D. Ahn, S. Nam, and B. Park, "The effect of Al2O3-coating coverage on the electrochemical properties in LiCoO2 thin films," *J. Solid State Electrochem.*, vol. 14, no. 7, pp. 1235–1240, Jul. 2010.

[44] H. Zhao *et al.*, "Conductive Polymer Binder for High-Tap-Density Nanosilicon Material for Lithium-Ion Battery Negative Electrode Application," *Nano Lett.*, vol. 15, no. 12, pp. 7927–7932, Dec. 2015.

[45] H. Zhao *et al.*, "High Capacity and High Density Functional Conductive Polymer and SiO Anode for High-Energy Lithium-Ion Batteries," *ACS Appl. Mater. Interfaces*, vol. 7, no. 1, pp. 862–866, Jan. 2015.

[46] M. Wu *et al.*, "Toward an Ideal Polymer Binder Design for High-Capacity Battery Anodes," *J. Am. Chem. Soc.*, vol. 135, no. 32, pp. 12048–12056, Aug. 2013.

[47] S.-J. Park *et al.*, "Side-Chain Conducting and Phase-Separated Polymeric Binders for High-Performance Silicon Anodes in Lithium-Ion Batteries," *J. Am. Chem. Soc.*, vol. 137, no. 7, pp. 2565–2571, Feb. 2015.

[48] J. Xu, S.-L. Chou, Q. Gu, H.-K. Liu, and S.-X. Dou, "The effect of different binders on electrochemical properties of LiNi1/3Mn1/3Co1/3O2 cathode material in lithium ion batteries," *J. Power Sources*, vol. 225, pp. 172–178, Mar. 2013.

[49] T. Marks, S. Trussler, A. J. Smith, D. Xiong, and J. R. Dahn, "A Guide to Li-Ion Coin-Cell Electrode Making for Academic Researchers," *J. Electrochem. Soc.*, vol. 158, no. 1, p. A51, 2011.

[50] D. Aurbach, K. Gamolsky, B. Markovsky, Y. Gofer, M. Schmidt, and U. Heider, "On the use of vinylene carbonate (VC) as an additive to electrolyte solutions for Li-ion batteries," *Electrochimica Acta*, vol. 47, no. 9, pp. 1423–1439, 2002.

[51] N. Yabuuchi and T. Ohzuku, "Electrochemical behaviors of LiCo1/3Ni1/3Mn1/3O2 in lithium batteries at elevated temperatures," *J. Power Sources*, vol. 146, no. 1–2, pp. 636–639, Aug. 2005.

[52] T. Aoshima, K. Okahara, C. Kiyohara, and K. Shizuka, "Mechanisms of manganese spinels dissolution and capacity fade at high temperature," *J. Power Sources*, vol. 97, pp. 377–380, 2001.

[53] S. Jouanneau, D. D. MacNeil, Z. Lu, S. D. Beattie, G. Murphy, and J. R. Dahn, "Morphology and Safety of Li[Ni[sub x]Co[sub 1−2x]Mn[sub x]]O[sub 2] (0≤x≤1/2)," *J. Electrochem. Soc.*, vol. 150, no. 10, p. A1299, 2003.

[54] N.-S. Choi, Y. Lee, S.-S. Kim, S.-C. Shin, and Y.-M. Kang, "Improving the electrochemical properties of graphite/LiCoO2 cells in ionic liquid-containing electrolytes," *J. Power Sources*, vol. 195, no. 8, pp. 2368–2371, Apr. 2010.

[55] M.-H. Ryou *et al.*, "Effect of fluoroethylene carbonate on high temperature capacity retention of LiMn2O4/graphite Li-ion cells," *Electrochimica Acta*, vol. 55, no. 6, pp. 2073–2077, Feb. 2010.

[56] K. Abe, H. Yoshitake, T. Kitakura, T. Hattori, H. Wang, and M. Yoshio, "Additives-containing functional electrolytes for suppressing electrolyte decomposition in lithium-ion batteries," *Electrochimica Acta*, vol. 49, no. 26, pp. 4613–4622, Oct. 2004.

[57] C. S. Johnson, N. Li, C. Lefief, and M. M. Thackeray, "Anomalous capacity and cycling stability of xLi2MnO3·(1−x)LiMO2 electrodes (M=Mn, Ni, Co) in lithium batteries at 50°C," *Electrochem. Commun.*, vol. 9, no. 4, pp. 787–795, Apr. 2007.

[58] A. M. Kannan, L. Rabenberg, and A. Manthiram, "High Capacity Surface-Modified LiCoO[sub 2] Cathodes for Lithium-Ion Batteries," *Electrochem. Solid-State Lett.*, vol. 6, no. 1, p. A16, 2003.

[59] T. Tsuji, Y. Tatsuyama, M. Tsuji, K. Ishida, S. Okada, and J. Yamaki, "Preparation of LiMn2O4 nanoparticles for Li ion secondary batteries by laser ablation in water," *Mater. Lett.*, vol. 61, no. 10, pp. 2062–2065, Apr. 2007.

[60] J. F., M. Hasan, S. Patil, D. P., and T. Clancy, "Energy Storage: Battery Materials and Architectures at the Nanoscale," in *ICT - Energy - Concepts Towards Zero - Power Information and Communication Technology*, G. Fagas, Ed. InTech, 2014.

[61] C.-X. Zu and H. Li, "Thermodynamic analysis on energy densities of batteries," *Energy Environ. Sci.*, vol. 4, no. 8, p. 2614, 2011.

[62] J.-M. Tarascon and M. Armand, "Issues and challenges facing rechargeable lithium batteries," *Nature*, vol. 414, no. 6861, pp. 359–367, 2001.

[63] M. Singh, J. Kaiser, and H. Hahn, "A systematic study of thick electrodes for high energy lithium ion batteries," *J. Electroanal. Chem.*, vol. 782, pp. 245–249, Dec. 2016.

[64] Z. Du *et al.*, "Enabling aqueous processing for crack-free thick electrodes," *J. Power Sources*, vol. 354, pp. 200–206, Jun. 2017.

[65] N. Aguiló-Aguayo, P. P. Espiñeira, A. P. Manian, and T. Bechtold, "Three-dimensional embroidered current collectors for ultra-thick electrodes in batteries," *RSC Adv*, vol. 6, no. 74, pp. 69685–69690, 2016.

[66] G. Patry, A. Romagny, S. Martinet, and D. Froelich, "Cost modeling of lithium-ion battery cells for automotive applications," *Energy Sci. Eng.*, vol. 3, no. 1, pp. 71–82, Jan. 2015.

[67] "BatPaC - Battery Performance and Cost model - Home," 17-Jul-2017. [Online]. Available: http://www.cse.anl.gov/BatPac/. [Accessed: 17-Jul-2017].

[68] L. Shen, Q. Che, H. Li, and X. Zhang, "Mesoporous NiCo2O4 Nanowire Arrays Grown on Carbon Textiles as Binder-Free Flexible Electrodes for Energy Storage," *Adv. Funct. Mater.*, vol. 24, no. 18, pp. 2630–2637, May 2014.

[69] J. Qin, Q. Zhang, Z. Cao, X. Li, C. Hu, and B. Wei, "MnOx/SWCNT macro-films as flexible binder-free anodes for high-performance Li-ion batteries," *Nano Energy*, vol. 2, no. 5, pp. 733–741, Sep. 2013.

[70] X. Huang *et al.*, "Homogeneous CoO on Graphene for Binder-Free and Ultralong-Life Lithium Ion Batteries," *Adv. Funct. Mater.*, vol. 23, no. 35, pp. 4345–4353, Sep. 2013.

[71] D.-H. Ha, M. A. Islam, and R. D. Robinson, "Binder-Free and Carbon-Free Nanoparticle Batteries: A Method for Nanoparticle Electrodes without Polymeric Binders or Carbon Black," *Nano Lett.*, vol. 12, no. 10, pp. 5122–5130, Oct. 2012.

[72] N. Zhao *et al.*, "Hierarchical porous carbon with graphitic structure synthesized by a water soluble template method," *Mater. Lett.*, vol. 87, pp. 77–79, Nov. 2012.

[73] C. Ban *et al.*, "Nanostructured Fe3O4/SWNT Electrode: Binder-Free and High-Rate Li-Ion Anode," *Adv. Mater.*, vol. 22, no. 20, pp. E145–E149, May 2010.

[74] Z. Zuo, T. Y. Kim, I. Kholmanov, H. Li, H. Chou, and Y. Li, "Ultra-light Hierarchical Graphene Electrode for Binder-Free Supercapacitors and Lithium-Ion Battery Anodes," *Small*, vol. 11, no. 37, pp. 4922–4930, Oct. 2015.

[75] X. Huang, B. Sun, S. Chen, and G. Wang, "Self-Assembling Synthesis of Free-standing Nanoporous Graphene–Transition-Metal Oxide Flexible Electrodes for High-Performance Lithium-Ion Batteries and Supercapacitors," *Chem. – Asian J.*, vol. 9, no. 1, pp. 206–211, Jan. 2014.

[76] G. Zhang, W. Li, K. Xie, F. Yu, and H. Huang, "A One-Step and Binder-Free Method to Fabricate Hierarchical Nickel-Based Supercapacitor Electrodes with Excellent Performance," *Adv. Funct. Mater.*, vol. 23, no. 29, pp. 3675–3681, Aug. 2013.

[77] S. D. Perera *et al.*, "Vanadium Oxide Nanowire–Carbon Nanotube Binder-Free Flexible Electrodes for Supercapacitors," *Adv. Energy Mater.*, vol. 1, no. 5, pp. 936–945, Oct. 2011.

[78] Y. Hu, X. Li, J. Wang, R. Li, and X. Sun, "Free-standing graphene–carbon nanotube hybrid papers used as current collector and binder free anodes for lithium ion batteries," *J. Power Sources*, vol. 237, pp. 41–46, Sep. 2013.

[79] X. Wang *et al.*, "N-Doped Graphene-SnO2 Sandwich Paper for High-Performance Lithium-Ion Batteries," *Adv. Funct. Mater.*, vol. 22, no. 13, pp. 2682–2690, Jul. 2012.

[80] Y. Yang, D. Chen, B. Liu, and J. Zhao, "Binder-Free Si Nanoparticle Electrode with 3D Porous Structure Prepared by Electrophoretic Deposition for Lithium-Ion Batteries," *ACS Appl. Mater. Interfaces*, vol. 7, no. 14, pp. 7497–7504, Apr. 2015.

[81] B. Kang and G. Ceder, "Battery materials for ultrafast charging and discharging," *Nature*, vol. 458, no. 7235, pp. 190–193, Mar. 2009.

[82] L. A. Jiao *et al.*, "3D structural properties study on compact LiFePO4s based on X-ray computed tomography technique," *Powder Technol.*, vol. 281, pp. 1–6, Sep. 2015.

[83] T. Hutzenlaub, A. Asthana, J. Becker, D. R. Wheeler, R. Zengerle, and S. Thiele, "FIB/SEM-based calculation of tortuosity in a porous LiCoO2 cathode for a Li-ion battery," *Electrochem. Commun.*, vol. 27, pp. 77–80, Feb. 2013.

[84] M. Ender, J. Joos, T. Carraro, and E. Ivers-Tiffée, "Three-dimensional reconstruction of a composite cathode for lithium-ion cells," *Electrochem. Commun.*, vol. 13, no. 2, pp. 166–168, Feb. 2011.

[85] B. Tjaden, J. Lane, P. J. Withers, R. S. Bradley, D. J. L. Brett, and P. R. Shearing, "The application of 3D imaging techniques, simulation and diffusion experiments to explore transport properties in porous oxygen transport membrane support materials," *Solid State Ion.*, vol. 288, pp. 315–321, May 2016.

[86] Y. S. Wu, L. J. van Vliet, H. W. Frijlink, and K. van der Voort Maarschalk, "The determination of relative path length as a measure for tortuosity in compacts using image analysis," *Eur. J. Pharm. Sci.*, vol. 28, no. 5, pp. 433–440, Aug. 2006.

[87] M. Ebner, D.-W. Chung, R. E. García, and V. Wood, "Tortuosity Anisotropy in Lithium-Ion Battery Electrodes," *Adv. Energy Mater.*, vol. 4, no. 5, p. 1301278, Apr. 2014.

[88] M. Letellier, V. Fierro, A. Pizzi, and A. Celzard, "Tortuosity studies of cellular vitreous carbon foams," *Carbon*, vol. 80, pp. 193–202, Dec. 2014.

[89] J. Landesfeind, J. Hattendorff, A. Ehrl, W. A. Wall, and H. A. Gasteiger, "Tortuosity determination of battery electrodes and separators by impedance spectroscopy," *J. Electrochem. Soc.*, vol. 163, no. 7, pp. A1373–A1387, 2016.

[90] J. Landesfeind, J. Hattendorff, A. Ehrl, W. A. Wall, and H. A. Gasteiger, "Tortuosity Determination of Battery Electrodes and Separators by Impedance Spectroscopy," *J. Electrochem. Soc.*, vol. 163, no. 7, pp. A1373–A1387, Jan. 2016.
[91] J. Newman, "Optimization of porosity and thickness of a battery electrode by means of a reaction-zone model," *J. Electrochem. Soc.*, vol. 142, no. 1, pp. 97–101, 1995.
[92] Y. K. Chen-Wiegart, R. DeMike, C. Erdonmez, K. Thornton, S. A. Barnett, and J. Wang, "Tortuosity characterization of 3D microstructure at nano-scale for energy storage and conversion materials," *J. Power Sources*, vol. 249, pp. 349–356, Mar. 2014.
[93] S. J. Cooper *et al.*, "Image based modelling of microstructural heterogeneity in LiFePO 4 electrodes for Li-ion batteries," *J. Power Sources*, vol. 247, pp. 1033–1039, Feb. 2014.
[94] N. Epstein, "On tortuosity and the tortuosity factor in flow and diffusion through porous media," *Chem. Eng. Sci.*, vol. 44, no. 3, pp. 777–779, 1989.
[95] B. Tjaden, D. P. Finegan, J. Lane, D. J. L. Brett, and P. R. Shearing, "Contradictory concepts in tortuosity determination in porous media in electrochemical devices," *Chem. Eng. Sci.*, vol. 166, pp. 235–245, Jul. 2017.
[96] K. G. Gallagher *et al.*, "Optimizing areal capacities through understanding the limitations of lithium-ion electrodes," *J. Electrochem. Soc.*, vol. 163, no. 2, pp. A138–A149, 2016.
[97] H. Zheng, J. Li, X. Song, G. Liu, and V. S. Battaglia, "A comprehensive understanding of electrode thickness effects on the electrochemical performances of Li-ion battery cathodes," *Electrochimica Acta*, vol. 71, pp. 258–265, Jun. 2012.
[98] S. Yu, Y. Chung, M. S. Song, J. H. Nam, and W. I. Cho, "Investigation of design parameter effects on high current performance of lithium-ion cells with LiFePO4/graphite electrodes," *J. Appl. Electrochem.*, vol. 42, no. 6, pp. 443–453, Jun. 2012.
[99] L. Hu *et al.*, "Lithium-Ion Textile Batteries with Large Areal Mass Loading," *Adv. Energy Mater.*, vol. 1, no. 6, pp. 1012–1017, Nov. 2011.
[100] D. Song, Y. Wang, Y. Wang, L. Jiao, and H. Yuan, "Electrochemical hydrogen storage performance of AB5-CoB composites synthesized by a simple mixing method," *Rare Met.*, vol. 28, no. 6, p. 629, Dec. 2009.
[101] L. Trahey, J. T. Vaughey, H. H. Kung, and M. M. Thackeray, "High-Capacity, Microporous Cu6Sn5 – Sn Anodes for Li-Ion Batteries," *J. Electrochem. Soc.*, vol. 156, no. 5, pp. A385–A389, Jan. 2009.
[102] J. Liu, M. Kunz, K. Chen, N. Tamura, and T. J. Richardson, "Visualization of Charge Distribution in a Lithium Battery Electrode," *J. Phys. Chem. Lett.*, vol. 1, no. 14, pp. 2120–2123, Jul. 2010.
[103] M. Katayama *et al.*, "X-ray absorption fine structure imaging of inhomogeneous electrode reaction in LiFePO4 lithium-ion battery cathode," *J. Power Sources*, vol. 269, pp. 994–999, Dec. 2014.
[104] M. R. Roberts *et al.*, "Direct Observation of Active Material Concentration Gradients and Crystallinity Breakdown in LiFePO $_4$ Electrodes During Charge/Discharge Cycling of Lithium Batteries," *J. Phys. Chem. C*, vol. 118, no. 13, pp. 6548–6557, Apr. 2014.
[105] G. Ouvrard *et al.*, "Heterogeneous behaviour of the lithium battery composite electrode LiFePO4," *J. Power Sources*, vol. 229, pp. 16–21, May 2013.
[106] M. Bianchini *et al.*, "A new null matrix electrochemical cell for Rietveld refinements of in-situ or operando neutron powder diffraction data," *J. Electrochem. Soc.*, vol. 160, no. 11, pp. A2176–A2183, 2013.
[107] H. Li *et al.*, "Ultra-thick graphene bulk supercapacitor electrodes for compact energy storage," *Energy Env. Sci*, vol. 9, no. 10, pp. 3135–3142, 2016.

[108] W. Zhang *et al.*, "Binder-free graphene foams for O2 electrodes of Li–O2 batteries," *Nanoscale*, vol. 5, no. 20, pp. 9651–9658, Sep. 2013.
[109] X. Qin, X. Wang, J. Xie, and L. Wen, "Hierarchically porous and conductive LiFePO4 bulk electrode: binder-free and ultrahigh volumetric capacity Li-ion cathode," *J. Mater. Chem.*, vol. 21, no. 33, p. 12444, 2011.
[110] W. Lai *et al.*, "Ultrahigh-Energy-Density Microbatteries Enabled by New Electrode Architecture and Micropackaging Design," *Adv. Mater.*, vol. 22, no. 20, pp. E139–E144, May 2010.
[111] C.-J. Bae, C. K. Erdonmez, J. W. Halloran, and Y.-M. Chiang, "Design of Battery Electrodes with Dual-Scale Porosity to Minimize Tortuosity and Maximize Performance," *Adv. Mater.*, vol. 25, no. 9, pp. 1254–1258, Mar. 2013.
[112] J. S. Sander, R. M. Erb, L. Li, A. Gurijala, and Y.-M. Chiang, "High-performance battery electrodes via magnetic templating," *Nat. Energy*, vol. 1, no. 8, p. 16099, Jul. 2016.
[113] H. Zheng, J. Li, X. Song, G. Liu, and V. S. Battaglia, "A comprehensive understanding of electrode thickness effects on the electrochemical performances of Li-ion battery cathodes," *Electrochimica Acta*, vol. 71, pp. 258–265, Jun. 2012.
[114] J. S. Wang, P. Liu, E. Sherman, M. Verbrugge, and H. Tataria, "Formulation and characterization of ultra-thick electrodes for high energy lithium-ion batteries employing tailored metal foams," *J. Power Sources*, vol. 196, no. 20, pp. 8714–8718, Oct. 2011.
[115] M. Singh, J. Kaiser, and H. Hahn, "Effect of Porosity on the Thick Electrodes for High Energy Density Lithium Ion Batteries for Stationary Applications," *Batteries*, vol. 2, no. 4, p. 35, Nov. 2016.
[116] G.-F. Yang, K.-Y. Song, and S.-K. Joo, "Ultra-thick Li-ion battery electrodes using different cell size of metal foam current collectors," *RSC Adv.*, vol. 5, no. 22, pp. 16702–16706, Feb. 2015.
[117] R. Kali and A. Mukhopadhyay, "Spark plasma sintered/synthesized dense and nanostructured materials for solid-state Li-ion batteries: Overview and perspective," *J. Power Sources*, vol. 247, pp. 920–931, Feb. 2014.
[118] P. P. Prosini, M. Carewska, S. Scaccia, P. Wisniewski, S. Passerini, and M. Pasquali, "A New Synthetic Route for Preparing LiFePO[sub 4] with Enhanced Electrochemical Performance," *J. Electrochem. Soc.*, vol. 149, no. 7, p. A886, 2002.
[119] T. Takeuchi *et al.*, "Preparation of dense LiFePO4/C composite positive electrodes using spark-plasma-sintering process," *J. Power Sources*, vol. 146, no. 1–2, pp. 575–579, Aug. 2005.
[120] T. Takeuchi, M. Tabuchi, K. Ado, and K. Tatsumi, "Improvement of rate capability in rechargeable lithium-ion batteries using oxide-based active materials–carbon composite cathodes," *J. Power Sources*, vol. 174, no. 2, pp. 1063–1068, Dec. 2007.
[121] T. Takeuchi *et al.*, "Preparation of Li 2 S–FePS 3 composite positive electrode materials and their electrochemical properties," *Solid State Ion.*, vol. 288, pp. 199–203, May 2016.
[122] T. Takeuchi *et al.*, "All-Solid-State Lithium Secondary Battery with Li[sub 2]S–C Composite Positive Electrode Prepared by Spark-Plasma-Sintering Process," *J. Electrochem. Soc.*, vol. 157, no. 11, p. A1196, 2010.
[123] Y. Arachi, Y. Higuchi, R. Nakamura, Y. Takagi, and M. Tabuchi, "Synthesis and electrical property of Li2−xFeSi1−xPxO4 as positive electrodes by spark-plasma-sintering process," *J. Power Sources*, vol. 244, pp. 631–635, Dec. 2013.
[124] B. Daffos, G. Chevallier, C. Estournès, and P. Simon, "Spark plasma sintered carbon electrodes for electrical double layer capacitor applications," *J. Power Sources*, vol. 196, no. 3, pp. 1620–1625, Feb. 2011.
[125] J. Li, L. Wang, T. He, and W. Jiang, "Transport properties of hot-pressed bulk carbon nanotubes compacted by spark plasma sintering," *Carbon*, vol. 47, no. 4, pp. 1135–1140, Apr. 2009.

[126] E. Dumont-Botto, C. Bourbon, S. Patoux, P. Rozier, and M. Dolle, "Synthesis by Spark Plasma Sintering: A new way to obtain electrode materials for lithium ion batteries," *J. Power Sources*, vol. 196, no. 4, pp. 2274–2278, Feb. 2011.
[127] T. Takeuchi, M. Tabuchi, K. Ado, and K. Tatsumi, "Improvement of rate capability in rechargeable lithium-ion batteries using oxide-based active materials–carbon composite cathodes," *J. Power Sources*, vol. 174, no. 2, pp. 1063–1068, Dec. 2007.
[128] T. Takeuchi, M. Tabuchi, A. Nakashima, H. Kageyama, and K. Tatsumi, "Preparation of Dense Li[sub 1.05]Mn[sub 1.95]O[sub 4]/C Composite Positive Electrodes Using Spark-Plasma-Sintering-Process," *Electrochem. Solid-State Lett.*, vol. 8, no. 4, p. A195, 2005.
[129] P. Nithyadharseni *et al.*, "Spark plasma-sintered Sn-based intermetallic alloys and their Li-storage studies," *J. Solid State Electrochem.*, vol. 20, no. 6, pp. 1743–1751, Jun. 2016.
[130] K. Biswas, A. Mukhopadhyay, B. Basu, and K. Chattopadhyay, "Densification and microstructure development in spark plasma sintered WC–6 wt% ZrO2 nanocomposites," *J. Mater. Res.*, vol. 22, no. 06, pp. 1491–1501, Jun. 2007.
[131] H. Takahara *et al.*, "All-Solid-State Lithium Secondary Battery Using Oxysulfide Glass," *J. Electrochem. Soc.*, vol. 151, no. 10, p. A1539, 2004.
[132] J. W. Fergus, "Ceramic and polymeric solid electrolytes for lithium-ion batteries," *J. Power Sources*, vol. 195, no. 15, pp. 4554–4569, Aug. 2010.
[133] X. Xu, Z. Wen, X. Yang, and L. Chen, "Dense nanostructured solid electrolyte with high Li-ion conductivity by spark plasma sintering technique," *Mater. Res. Bull.*, vol. 43, no. 8–9, pp. 2334–2341, Aug. 2008.
[134] P. Knauth, "Inorganic solid Li ion conductors: An overview," *Solid State Ion.*, vol. 180, no. 14–16, pp. 911–916, Jun. 2009.
[135] H. Aono, E. Sugimoto, Y. Sadaoka, N. Imanaka, and G. Adachi, "Ionic conductivity of solid electrolytes based on lithium titanium phosphate," *J. Electrochem. Soc.*, vol. 137, no. 4, pp. 1023–1027, 1990.
[136] S. Ahmad, "RETRACTED ARTICLE: Polymer electrolytes: characteristics and peculiarities," *Ionics*, vol. 15, no. 3, pp. 309–321, Jun. 2009.
[137] S. Teng, J. Tan, and A. Tiwari, "Recent developments in garnet based solid state electrolytes for thin film batteries," *Curr. Opin. Solid State Mater. Sci.*, vol. 18, no. 1, pp. 29–38, Feb. 2014.
[138] S. Ramakumar, C. Deviannapoorani, L. Dhivya, L. S. Shankar, and R. Murugan, "Lithium garnets: Synthesis, structure, Li + conductivity, Li + dynamics and applications," *Prog. Mater. Sci.*, vol. 88, pp. 325–411, Jul. 2017.
[139] M. Kotobuki, S. Song, R. Takahashi, S. Yanagiya, and L. Lu, "Improvement of Li ion conductivity of Li 5 La 3 Ta 2 O 12 solid electrolyte by substitution of Ge for Ta," *J. Power Sources*, vol. 349, pp. 105–110, May 2017.
[140] S.-W. Baek, J.-M. Lee, T. Y. Kim, M.-S. Song, and Y. Park, "Garnet related lithium ion conductor processed by spark plasma sintering for all solid state batteries," *J. Power Sources*, vol. 249, pp. 197–206, Mar. 2014.
[141] Y. Wang, P. Yan, J. Xiao, X. Lu, J.-G. Zhang, and V. L. Sprenkle, "Effect of Al 2 O 3 on the sintering of garnet-type Li 6.5 La 3 Zr 1.5 Ta 0.5 O 12," *Solid State Ion.*, vol. 294, pp. 108–115, Oct. 2016.
[142] R. Orrù, R. Licheri, A. M. Locci, A. Cincotti, and G. Cao, "Consolidation/synthesis of materials by electric current activated/assisted sintering," *Mater. Sci. Eng. R Rep.*, vol. 63, no. 4–6, pp. 127–287, Feb. 2009.
[143] S. Duluard *et al.*, "Lithium conducting solid electrolyte Li1.3Al0.3Ti1.7(PO4)3 obtained via solution chemistry," *J. Eur. Ceram. Soc.*, vol. 33, no. 6, pp. 1145–1153, Jun. 2013.

[144] M. Perez-Estébanez, M. Peiteado, A. C. Caballero, F. J. Palomares, M. Nygren, and J. Isasi-Marín, "SPS driven lithium differential diffusion in NASICON-like structures," *Bol. Soc. Esp. Cerámica Vidr.*, vol. 55, no. 1, pp. 38–44, Jan. 2016.
[145] H. Yamada, T. Ito, and R. Hongahally Basappa, "Sintering Mechanisms of High-Performance Garnet-type Solid Electrolyte Densified by Spark Plasma Sintering," *Electrochimica Acta*, vol. 222, pp. 648–656, Dec. 2016.
[146] M. Pérez-Estébanez, J. Isasi-Marín, A. Rivera-Calzada, C. León, and M. Nygren, "Spark plasma versus conventional sintering in the electrical properties of Nasicon-type materials," *J. Alloys Compd.*, vol. 651, pp. 636–642, Dec. 2015.
[147] G. Delaizir *et al.*, "The Stone Age Revisited: Building a Monolithic Inorganic Lithium-Ion Battery," *Adv. Funct. Mater.*, vol. 22, no. 10, pp. 2140–2147, May 2012.
[148] H. Aono, E. Sugimoto, Y. Sadaoka, N. Imanaka, and G. Adachi, "Ionic conductivity of solid electrolytes based on lithium titanium phosphate," *J. Electrochem. Soc.*, vol. 137, no. 4, pp. 1023–1027, 1990.
[149] A. Aboulaich *et al.*, "A New Approach to Develop Safe All-Inorganic Monolithic Li-Ion Batteries," *Adv. Energy Mater.*, vol. 1, no. 2, pp. 179–183, Mar. 2011.
[150] M. Agostini, Y. Aihara, T. Yamada, B. Scrosati, and J. Hassoun, "A lithium–sulfur battery using a solid, glass-type P2S5–Li2S electrolyte," *Solid State Ion.*, vol. 244, pp. 48–51, Aug. 2013.
[151] Y. Nishio, H. Kitaura, A. Hayashi, and M. Tatsumisago, "All-solid-state lithium secondary batteries using nanocomposites of NiS electrode/Li2S–P2S5 electrolyte prepared via mechanochemical reaction," *J. Power Sources*, vol. 189, no. 1, pp. 629–632, Apr. 2009.
[152] F. Lalère *et al.*, "An all-solid state NASICON sodium battery operating at 200 °C," *J. Power Sources*, vol. 247, pp. 975–980, Feb. 2014.
[153] S. Lee, J. Ha, J. Choi, T. Song, J. W. Lee, and U. Paik, "3D Cross-Linked Nanoweb Architecture of Binder-Free TiO2 Electrodes for Lithium Ion Batteries," *ACS Appl. Mater. Interfaces*, vol. 5, no. 22, pp. 11525–11529, Nov. 2013.
[154] M. Antonietti, N. Fechler, and T.-P. Fellinger, "Carbon Aerogels and Monoliths: Control of Porosity and Nanoarchitecture via Sol–Gel routes," *Chem. Mater.*, vol. 26, no. 1, pp. 196–210, Jan. 2014.
[155] S. Chandra Kishore, S. Anandhakumar, and M. Sasidharan, "Direct synthesis of solid and hollow carbon nanospheres over NaCl crystals using acetylene by chemical vapour deposition," *Appl. Surf. Sci.*, vol. 400, pp. 90–96, Apr. 2017.
[156] D. Wang *et al.*, "Synthesis and Li-Ion Insertion Properties of Highly Crystalline Mesoporous Rutile TiO_2," *Chem. Mater.*, vol. 20, no. 10, pp. 3435–3442, May 2008.
[157] J. Haetge, P. Hartmann, K. Brezesinski, J. Janek, and T. Brezesinski, "Ordered Large-Pore Mesoporous $Li_4Ti_5O_{12}$ Spinel Thin Film Electrodes with Nanocrystalline Framework for High Rate Rechargeable Lithium Batteries: Relationships among Charge Storage, Electrical Conductivity, and Nanoscale Structure," *Chem. Mater.*, vol. 23, no. 19, pp. 4384–4393, Oct. 2011.
[158] S. Kondrat, C. R. Pérez, V. Presser, Y. Gogotsi, and A. A. Kornyshev, "Effect of pore size and its dispersity on the energy storage in nanoporous supercapacitors," *Energy Environ. Sci.*, vol. 5, no. 4, p. 6474, 2012.
[159] J. Chmiola, G. Yushin, R. Dash, and Y. Gogotsi, "Effect of pore size and surface area of carbide derived carbons on specific capacitance," *J. Power Sources*, vol. 158, no. 1, pp. 765–772, Jul. 2006.
[160] E. Raymundo-Piñero, K. Kierzek, J. Machnikowski, and F. Béguin, "Relationship between the nanoporous texture of activated carbons and their capacitance properties in different electrolytes," *Carbon*, vol. 44, no. 12, pp. 2498–2507, Oct. 2006.

[161] B. Britton and S. Holdcroft, "The Control and Effect of Pore Size Distribution in AEMFC Catalyst Layers," *J. Electrochem. Soc.*, vol. 163, no. 5, pp. F353–F358, 2016.
[162] P. R. Sajanlal, T. S. Sreeprasad, A. K. Samal, and T. Pradeep, "Anisotropic nanomaterials: structure, growth, assembly, and functions," *Nano Rev.*, vol. 2, no. 1, p. 5883, Jan. 2011.
[163] A. Szabó, D. Méhn, Z. Kónya, A. Fonseca, and J. B. Nagy, "'Wash and go': sodium chloride as an easily removable catalyst support for the synthesis of carbon nanotubes," *PhysChemComm*, vol. 6, no. 10, pp. 40–41, 2003.
[164] H. Kim, B. Han, J. Choo, and J. Cho, "Three-Dimensional Porous Silicon Particles for Use in High-Performance Lithium Secondary Batteries," *Angew. Chem.*, vol. 120, no. 52, pp. 10305–10308, Dec. 2008.
[165] Y.-S. Hu, P. Adelhelm, B. M. Smarsly, S. Hore, M. Antonietti, and J. Maier, "Synthesis of Hierarchically Porous Carbon Monoliths with Highly Ordered Microstructure and Their Application in Rechargeable Lithium Batteries with High-Rate Capability," *Adv. Funct. Mater.*, vol. 17, no. 12, pp. 1873–1878, Aug. 2007.
[166] C. M. Doherty, R. A. Caruso, B. M. Smarsly, and C. J. Drummond, "Colloidal Crystal Templating to Produce Hierarchically Porous LiFePO $_4$ Electrode Materials for High Power Lithium Ion Batteries," *Chem. Mater.*, vol. 21, no. 13, pp. 2895–2903, Jul. 2009.
[167] S. Lim, C. S. Yoon, and J. Cho, "Synthesis of Nanowire and Hollow LiFePO $_4$ Cathodes for High-Performance Lithium Batteries," *Chem. Mater.*, vol. 20, no. 14, pp. 4560–4564, Jul. 2008.
[168] A. Vu, Y. Qian, and A. Stein, "Porous Electrode Materials for Lithium-Ion Batteries - How to Prepare Them and What Makes Them Special," *Adv. Energy Mater.*, vol. 2, no. 9, pp. 1056–1085, Sep. 2012.
[169] L. H. S. Gasparotto, A. Prowald, N. Borisenko, S. Z. El Abedin, A. Garsuch, and F. Endres, "Electrochemical synthesis of macroporous aluminium films and their behavior towards lithium deposition/stripping," *J. Power Sources*, vol. 196, no. 5, pp. 2879–2883, Mar. 2011.
[170] Y. Ren *et al.*, "A solid with a hierarchical tetramodal micro-meso-macro pore size distribution," *Nat. Commun.*, vol. 4, Jun. 2013.
[171] F. Kleitz, S. H. Choi, and R. Ryoo, "Cubic Ia3d large mesoporous silica: synthesis and replication to platinum nanowires, carbon nanorods and carbon nanotubes," *Chem. Commun.*, vol. 0, no. 17, pp. 2136–2137, Aug. 2003.
[172] S. Lim, C. S. Yoon, and J. Cho, "Synthesis of Nanowire and Hollow LiFePO4 Cathodes for High-Performance Lithium Batteries," *Chem. Mater.*, vol. 20, no. 14, pp. 4560–4564, Jul. 2008.
[173] X. Zuo *et al.*, "Self-Templating Construction of 3D Hierarchical Macro-/Mesoporous Silicon from 0D Silica Nanoparticles," *ACS Nano*, vol. 11, no. 1, pp. 889–899, Jan. 2017.
[174] S. P. Pinho and E. A. Macedo, "Solubility of NaCl, NaBr, and KCl in Water, Methanol, Ethanol, and Their Mixed Solvents," *J. Chem. Eng. Data*, vol. 50, no. 1, pp. 29–32, Jan. 2005.
[175] X. Fan, X. Jiang, W. Wang, and Z. Liu, "Green synthesis of nanoporous Si/C anode using NaCl template with improved cycle life," *Mater. Lett.*, vol. 180, pp. 109–113, Oct. 2016.
[176] H. Zhao *et al.*, "A Convenient and Versatile Method To Control the Electrode Microstructure toward High-Energy Lithium-Ion Batteries," *Nano Lett.*, vol. 16, no. 7, pp. 4686–4690, Jul. 2016.
[177] X. Fan, X. Jiang, W. Wang, and Z. Liu, "Green synthesis of nanoporous Si/C anode using NaCl template with improved cycle life," *Mater. Lett.*, vol. 180, pp. 109–113, Oct. 2016.
[178] Q. He, C. Xu, J. Luo, W. Wu, and J. Shi, "A novel mesoporous carbon@silicon–silica nanostructure for high-performance Li-ion battery anodes," *Chem. Commun.*, vol. 50, no. 90, pp. 13944–13947, 2014.
[179] X. Zuo *et al.*, "Self-Templating Construction of 3D Hierarchical Macro-/Mesoporous Silicon from 0D Silica Nanoparticles," *ACS Nano*, vol. 11, no. 1, pp. 889–899, Jan. 2017.

[180] N. Li *et al.*, "Free-Standing and Transparent Graphene Membrane of Polyhedron Box-Shaped Basic Building Units Directly Grown Using a NaCl Template for Flexible Transparent and Stretchable Solid-State Supercapacitors," *Nano Lett.*, vol. 15, no. 5, pp. 3195–3203, May 2015.
[181] M. A. Davoodi, J. Towfighi, and A. Rashidi, "Facile synthesis of carbon nanotube/nanofiber paper on a water-soluble support in one-step by chemical vapor deposition," *Chem. Eng. J.*, vol. 221, pp. 159–165, Apr. 2013.
[182] J. Geng *et al.*, "Production of Carbon Nanofibers in High Yields Using a Sodium Chloride Support," *J. Phys. Chem. B*, vol. 109, no. 35, pp. 16665–16670, Sep. 2005.
[183] W. Liu *et al.*, "3D Porous Sponge-Inspired Electrode for Stretchable Lithium-Ion Batteries," *Adv. Mater.*, vol. 28, no. 18, pp. 3578–3583, May 2016.
[184] J. Zhu, K. Sakaushi, G. Clavel, M. Shalom, M. Antonietti, and T.-P. Fellinger, "A General Salt-Templating Method To Fabricate Vertically Aligned Graphitic Carbon Nanosheets and Their Metal Carbide Hybrids for Superior Lithium Ion Batteries and Water Splitting," *J. Am. Chem. Soc.*, vol. 137, no. 16, pp. 5480–5485, Apr. 2015.
[185] B. P. Kumar, H. H. Kumar, and D. K. Kharat, "Study on pore-forming agents in processing of porous piezoceramics," *J. Mater. Sci. Mater. Electron.*, vol. 16, no. 10, pp. 681–686, 2005.

Chapter 2

Fabrication of 1-mm thick $LiFePO_4$ and $Li_4Ti_5O_{12}$ electrodes using Spark Plasma Sintering and templating approach

The second chapter describes first the basic principles and concepts of Spark Plasma Sintering (SPS) technique. Then, the motivation of using SPS to fabricate thick electrodes for lithium ion battery and to couple with templating approach is discussed.

The sodium chloride crystals are used as templating agents added along with the active materials and after SPS densification, the salt particles in the thick pellet are dissolved to create pores inside the thick electrodes for lithium ion diffusion during cell operation. The fabrication procedure and characterization of 1-mm thick $LiFePO_4$ and $Li_4Ti_5O_{12}$ electrodes with 44 % porosity were reported. Thanks to SPS, it was possible to achieve higher active material loading per unit surface area without any mechanical failure such as cracking or particle flaking. X-ray Diffraction (XRD) studies are used to confirm the chemical inactivity of the templating agent with the active material after the sintering process of LFP/LTO-NaCl-C pellets. Then, the morphology of the individual components as well as the sintered electrodes was characterized by Scanning Electron Microscopy (SEM) and Energy X-ray Diffraction (EDX) analysis. The total electrode porosity of the 1-mm thick LFP is measured by three techniques such as Pycnometer, weight loss method based on NaCl dissolution and tomography analysis. The BET surface area measurement of the LFP-C electrode was done by ASAP porosimetry measurements for the 1-mm thick porous electrode. The electrochemical performance of the 1-mm thick binder free LFP and LTO electrodes is reported. For the first time, the areal capacity of LFP and LTO electrodes at slow C-rates are delivering four times higher than the conventionally prepared electrodes of lithium ion batteries.

2.1 Principle and motivation of Spark Plasma Sintering

2.1.1 Principle of SPS

Spark Plasma Sintering (SPS), also called Pulsed Electric Current Sintering (PECS) or Field Assisted Sintering Technique (FAST), is an advanced sintering technique to form high dense and compact materials from powder materials [1]–[3]. Materials such as ceramics, composites, metals, alloys can be prepared using SPS technique [4]. Contrary to the conventional sintering technique, in which an external heating source is used, in the SPS technique the heating rate is obtained by the DC current that provides higher uniform heating leading to a more efficient sintering. Indeed, SPS works on the principle of applying pulsed direct current that provides high heating rates (upto 600 °C/min) by Joule's heating effect.

The SPS unit consists of an uniaxial pressure device (with water cooled), evacuated reaction chamber, pulsed DC current generator and regulating systems for pressure, temperature and position as shown in figure 2.1a. The use of high pulse power source leads to the generation of high current (5000 A) and high heating rates. Temperature measurement controls are done using either pyrometers or thermocouples. Thermocouples are inserted on the die hole (1–2 mm) on the exterior of the die.

The weighed amount of powder was placed in the die made of electrically conducting materials such as graphite, WC (tungsten/carbon) or other refractory alloys. The graphite dies are fragile after a certain value of pressure around 100 Mpa due to their low mechanical properties at lower temperature. Thus, stronger WC dies are used to withstand higher pressure up to 1000 MPa. The rapid sintering of the electrode material was done inside the vacuum chamber in the glove box and the graphite die will be hosting the powder attached with the pistons closed on either side as shown in figure 2.1a. Graphite papers are also used to prevent direct contact between graphite die parts and to easily remove obtained pellets, as well as maintain electric contacts between the pistons and powder materials.

The densification process is carried out by the simultaneous application of high temperature and high pressure to the powder materials in a very short reaction time of few minutes [1], [3], [5], [6]. In the case of conductive powders, DC current (from 0.1 to 1.0 kA) is applied directly on the surface to induce the

sintering as shown in figure 2.1b. In the case of insulating powders, the efficient heat transfer occurs through the Joule heated dies and plungers, thereby efficient sintering takes place.

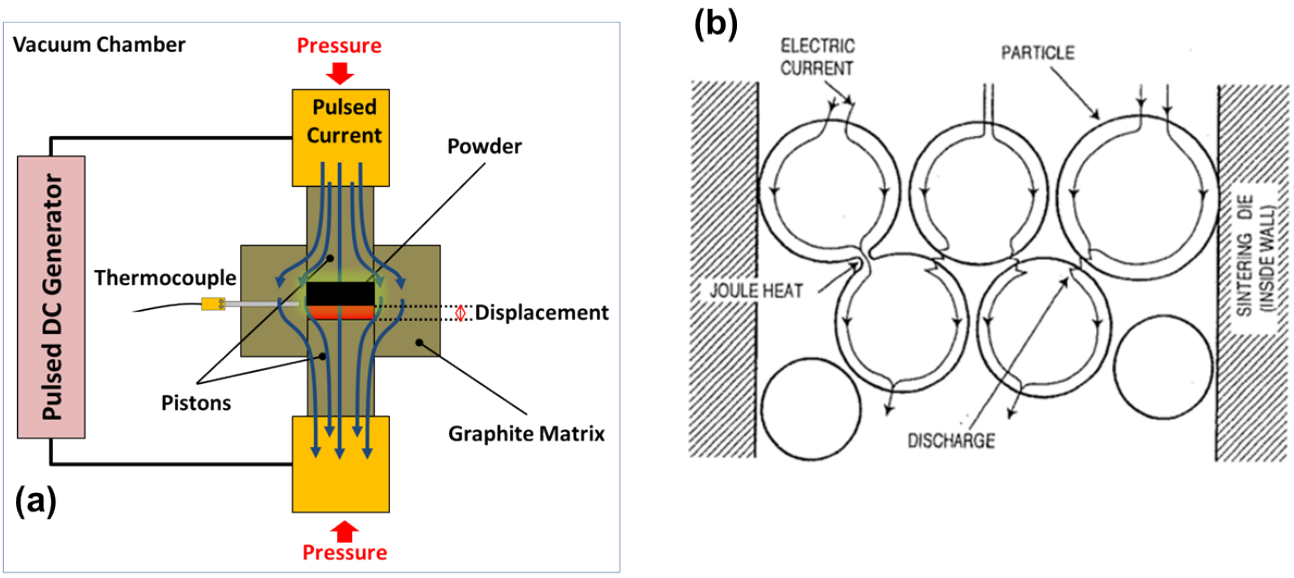

Figure 2.1 *a) Schematic of SPS process showing application of temperature and pressure simultaneously to the graphite die holding the powder in order to prepare thick pellet [7], b) Pathway of direct current passing to the powders forming sinter necks with strong grain-grain bonding and well-connected atomic interfaces [3].*

The consolidation of powders using SPS undergoes mainly three sequences:

(1) The first step of the sintering process by SPS undergoes formation of grain connection called the bridge or neck of matter. This is done by applying a pulsed DC current (from 0.6 to 1 kA) in a short duration between 1 and 300 ms leading to the initial activation of powders as shown in figure 2.1b [3].

(2) The subsequent heating and the densification of the powder eliminate the residual cavities or pores leading to a high compactness of 90-95%. The application of mechanical pressure enhances the diffusion kinetics removing the residual pores and enhances densification by plastic yielding or diffusion creep [8].

(3) Third sequence leads to the nearly complete elimination of pores by forming a fully dense material with suppressed grain growth. The total duration of the SPS sintering densification process is accomplished in less than 20 minutes.

2.1.2 Why use the SPS technique to make thick electrodes?

In the fabrication of conventional electrodes, non-active electrochemical materials such as carbon and binders are blended along with the insulating active materials and hazardous solvents to disperse the composite material homogeneously. The obtained viscous slurry is casted on the current collector and then the slurry coated electrode is dried by passing into a temperature-controlled oven. Calendaring is the next step after the electrode casting and drying steps. Indeed, calendaring is a physical method of pressing the slurry coated electrode under big rolls with varying gaps to achieve the desired thickness. This also helps to improve the particle to particle contact within the electrode and enhances the adhesion between the electrode and current collector.

As already seen in chapter 1, for high energy density Li-ion batteries, the well-controlled fabrication of thick electrodes is crucial [9]. Conventional sintering can be used so as to fabricate thick electrodes but the active materials are sintered with a slow kinetics of heating at a rate of 5 °C/min. As shown in figure 2.2c, SPS densification process undergoes rapid sintering with much reduced time and at lower temperature compared to the conventional sintering method.

The SPS technique is a real solution to overcome particle coarsening issue because the active materials are sintered with the carbon additives at faster reaction kinetics (100 °C/min). The interfacial resistance between different materials is greatly reduced when sintered using SPS treatment than conventionally blended powders [10]. Another main advantage is the minimization of the side reactions such as oxidation of carbon based materials because the SPS unit is installed in Argon filled glove box as shown in figure 2.2a,b. In the conventional method of Li-ion battery production, the inactive mass such as current collector, separator, binder and conductive carbon occupy more than 50% of total weight, which is at the origin of the reduction of Li-ion battery energy density. In our approach, the fabrication of thick electrodes can ultimately reduce the amount of inactive materials especially current collector, separator so that the final gravimetric energy density can be improved.

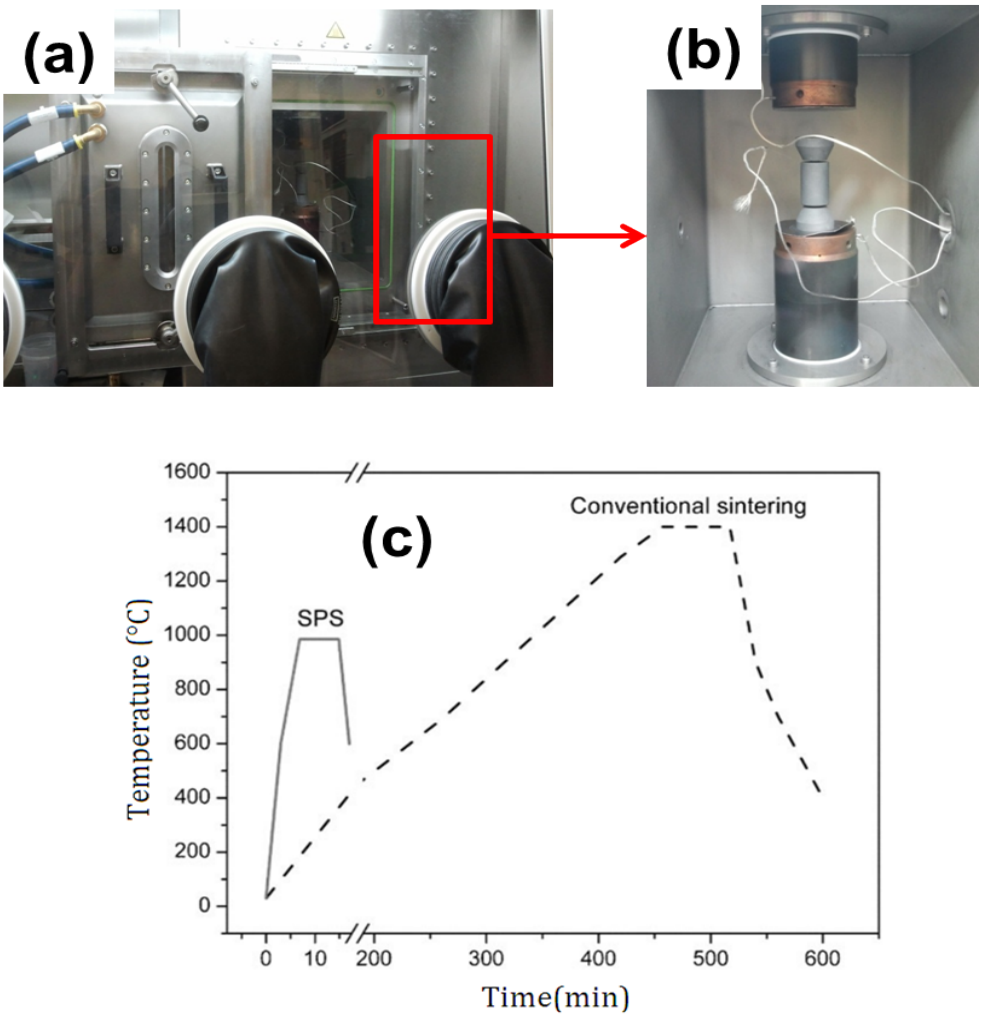

Figure 2.2 *Advantages of SPS technique: a) Digital photograph of SPS technique attached to the glove box installed in LRCS, Amiens, b) Graphite die packed with electrode powder placed in the SPS chamber, c) Comparison of SPS and conventional sintering parameters.*

From the state of art, SPS technique was already proposed to achieve high electrode compactness [6], [11], all solid state battery [12] [13], multilayered materials such as anode/solid electrolyte/cathode with well-defined interfaces [14]. Indeed, thanks to the lower sintering temperature and shorter sintering time compared to conventional sintering as shown in figure 2.2c, it is possible to achieve good grain-grain attachment and reduced side reactions such as decomposition of initial materials or reactivity between different components. SPS being a relatively new technology, only very few Li-ion battery electrodes have been fabricated so far using SPS and many commonly used electrode materials are need to be explored with the optimization of sintering and electrode parameters [19]–[23].

2.1.3 Why combine SPS technique and templating approach?

The compacity of the electrode prepared by SPS is usually from 90 to 99%, which is due to the strong grain-grain bonding. This property can raise the electronic conductivity but the ionic conductivity becomes limited due to the porosity reduction. Therefore, in order to increase the ionic conductivity of thick electrodes, pores are required so that the liquid electrolyte can flow inside the sintered electrodes.

Templating approach is a well-known method to prepare porous electrodes for Li-ion batteries as discussed in the first chapter. However, in the literature, some problems are faced by research groups in removing the silica templates leading to the side reaction with the active materials and liquid electrolyte. This can be clearly observed by the loss of the initial shape of the template agent after its removal [24]. Recently, Y.M. Chang *et al.* [25] reported the LCO sintered electrodes with 70-87 % relative densities done by conventional sintering. Nylon-binder rods are used as templating agents to create vertically aligned porous structures, which is helpful to achieve higher areal capacity.

In our study, a similar approach has been used instead of a conventional sintering; we used powerful SPS technique to make thick porous electrodes. First, a $LiFePO_4$ pellet was prepared without any templating agent. 450 mg of the commercial carbon coated LFP powder was taken in graphite die and the SPS reaction was carried out by simultaneously heating at 650 °C and pressing at 10 kN with a dwelling time of 5 min. The 1-mm thick LFP pellet was prepared after the SPS densification process. The relative density of LFP pellet obtained is 99%.

The electrochemical properties of 1mm thick LFP pellet and carbon coated LFP powder are compared by cycling against metallic lithium individually and LP30 (1M $LiPF_6$ in ethylene carbonate and dimethyl carbonate in 1:1 weight %) was used as a liquid electrolyte. As shown in the figure 2.3, relatively higher capacities were observed for the LFP powder compared to the LFP pellet. The main reason was the better wettability achieved for the LFP powder promoting the better lithium ion diffusion during cycling than 1mm thick LFP pellet as shown in figure 2.3b.

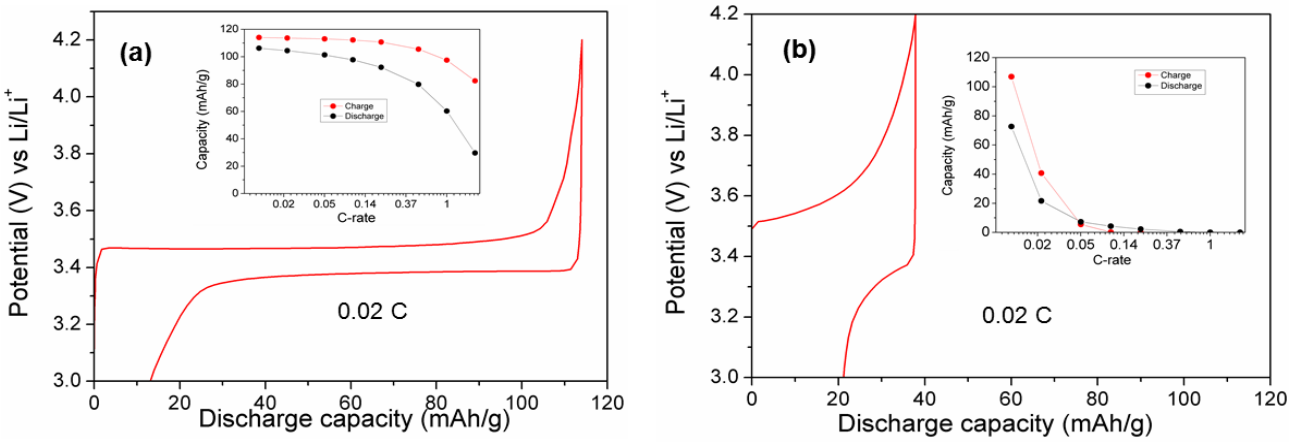

Figure 2.3 *Comparison of charge-discharge performance of a) LFP-C powder/ Li, b) LFP-C pellet/ Li. Ragone plot was given in inset.*

From these first electrochemical results, it clearly turns out that pores are needed for the thick electrode so that lithium ions can diffuse easily into the inner volume to achieve full battery utilization.

The electrochemical performances of the porous electrode are controlled by two main parameters: porosity and tortuosity. High electrode porosity reduces the amount of active material in the composite electrode, thereby lowering the volumetric and gravimetric energy density. High electrode tortuosity is a sign of disorder of the particle arrangement which is dependent on the particle morphology and the tortuosity value is expected to increase during the calendaring step (i.e.) uniaxial pressing of electrodes.

For any porous electrode, the lithium ion diffusion in the liquid phase is rate limiting and this can be characterized by the characteristic time (Eqn. 2.1) of the lithium ion diffusion inside the pores of the electrode which is an extended form of Fick's law of diffusion. The characteristic time is dependent on the electrode thickness and diffusion coefficient of lithium in the liquid phase according to the relation (Eqn. 2.1),

$$T_c \sim \frac{L^2}{D_L} \tag{2.1}$$

where L is the electrode thickness and D_L is the diffusion coefficient of lithium ion in the liquid phase. The characteristic time for lithium ion diffusion in the liquid phase will be increased when there is an increase of electrode thickness effectively due to the squared term in the relation. Thus, the salt templating method was adopted by using sodium chloride crystals as pore forming agents. NaCl crystals are chosen due to their high temperature stability (800 °C) and chemical inertness with the active

material. Hence, the pore forming agents are mixed and sintered along with the active materials and conductive carbon and later pore forming agents are dissolved after the densification process using SPS.

2.1.4 Preparation of sodium chloride crystals

In the state of art, several methods include spray drying, aerosol synthesis, chemical methods [18]–[21], ultra-sonication, precipitation and anti-solvent crystallization method are available to prepare the NaCl crystals in varied ranges of particle sizes. Aerosol techniques are used to nucleate the NaCl crystals with a low diameter capillary tube at high pressure and using citric acid as a precipitating agent [30]. Chemical synthesis of using sodium acetate and benzoyl or phenacyl chloride in an appropriate composition are mixed well to form NaCl particles [27]–[29]. In the literature, chemical agents such as L-Leucine are added along with a precursor during preparation so that these nano-sized agents will act as a coating agent to minimize the agglomeration of nano-sized NaCl particles due to the Ostwald ripening that increases the size of the crystals [34].

In my thesis, NaCl crystals are prepared by chemical (evaporative crystallization and solution method) and physical methods (crushing of NaCl crystals for 20 minutes). In this chapter, we discuss about the salt prepared by the evaporative crystallization only. In this method, the final particle size of NaCl crystals are greatly dependent on the synthesis reaction conditions such as temperature, stirring time, concentration of initial solution and solvent used. In our case, tetraethylene glycol was used as a structure inhibiting agent to control the size/growth of crystals. The lesser molecular weight based solvents such as ethylene glycol results in larger particle size of around 50 μm (not reported here).

A small amount (4 g) of sodium chloride crystals obtained from Sigma Aldrich was dissolved in 10 ml of water and then 40 ml of Tetra ethylene glycol was added to the salt solution. The mixture is well stirred and heated at 80° C and after 3 hours, the crystals with cubic shape are formed as shown in figure 2.4b. Finally, the solution is centrifuged with ethanol and dried at 120 °C in oven to avoid any moisture.

X-ray diffraction (XRD) analysis of as prepared and commercial NaCl crystals was performed using a laboratory D8 Advance Bruker diffractometer (Cu K_α radiation, λ= 1.5418 A°) and the 2θ values are recorded from 20-70°. XRD profiles of as prepared sodium chloride crystals show the narrow crystalline

peaks similar to the commercial salt shown for comparison (Figure 2.4a). The high crystallinity of NaCl (JCPDS no.88-2300) is confirmed and the same lattice constant (a= 5.6413Å) was found as reported in the literature [35]. A slight displacement in diffraction peaks of the as prepared NaCl occurs due to the mis-alignment of salt particles (*i.e.* not flat) in the sample holder.

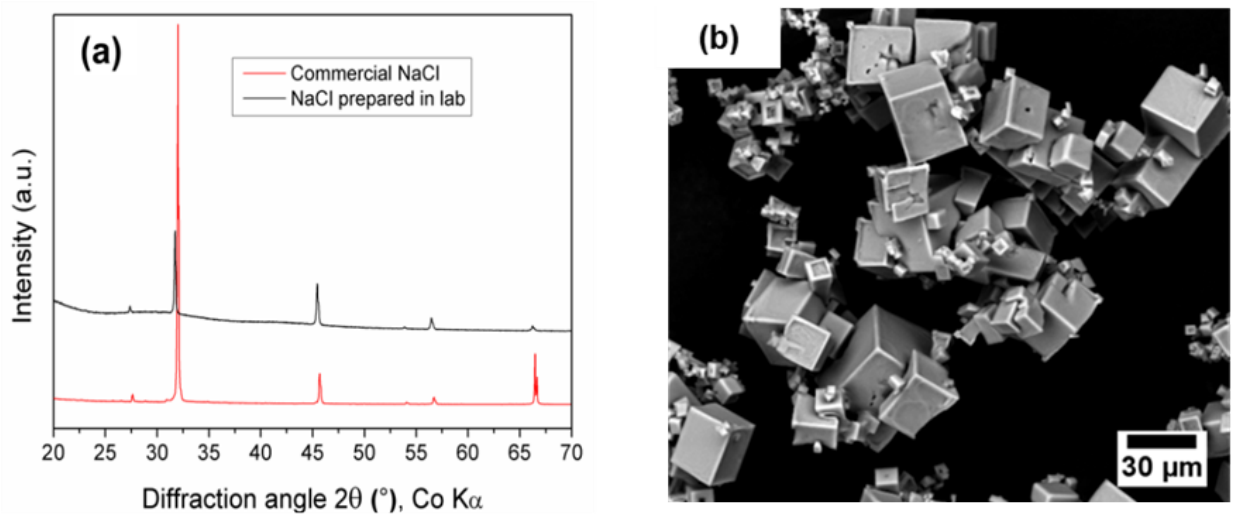

Figure 2.4 *XRD pattern of NaCl template prepared by evaporative crystallization, b) SEM image of cubic shaped salt showing the average particle size is 10 µm.*

High resolution Scanning Electron Microscopy (SEM) analysis of the as-prepared salt particles was performed on a FEI Quanta 200F field emission scanning electron microscope equipped with an energy-dispersive X-ray (EDX) spectrometer and operated at 20 kV under high vacuum. SEM is an essential technique to study the surface morphology of NaCl crystal and porous electrodes. From figure 2.4b, the as prepared salt particles are observed with cubic shape and average particle size of 13.7 ± 6.8 µm determined using FIJI software. The particle size distribution of the as prepared salt particles is reported in chapter 3.

Thermo Gravimetric Analysis (TGA) and Differential Scanning Calorimetry (DSC) analysis of sodium chloride crystals were done before SPS reaction in order to determine the thermal stability of the salt particles present in the LFP-NaCl-C composite. The DSC profile shows an exothermic peak at 800°C corresponding to the melting point of NaCl as shown in figure 2.5. The sudden weight loss (6.89 %) after 850°C can be ascribed to the decomposition of the NaCl crystal after reaching its melting point.

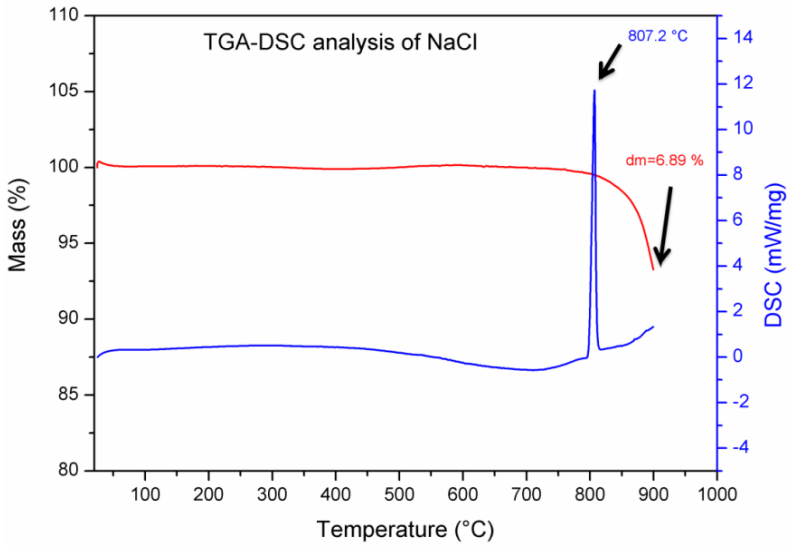

Figure 2.5 *TGA-DSC curve of NaCl showing the melting point of NaCl at 800 °C and decrease in mass after the melting point of crystal.*

Thus, a limiting temperature of 650°C was taken into account for optimizing the SPS program for our experiments to prevent the melting of salt particles in the LFP-NaCl-C composite. After the chemical characterization of individual components such as LFP, LTO and NaCl particles, the LFP-NaCl-C composite are prepared to make thick dense electrodes for lithium ion batteries using SPS and discussed in the next section.

2.2 Fabrication of 1-mm thick $LiFePO_4$ electrodes using SPS technique and templating approach

2.2.1 Preparation of $LiFePO_4$ -NaCl-C composite

The chemical composition in the electrode formulation is one of the main parameters to optimize the best electrochemical performance and plenty of works about the role of carbon additives and binder are reported in the literature. As the intrinsic electronic conductivity of LFP is very low ($\sigma = 10^{-11}$ S/m) at room temperature, various strategies are proposed to improve the electrochemical performance. One strategy consists in coating conducting materials on the surface of the active materials such as graphene sheets [36], [37], conducting polymer [38] and other carbon based additives [39]. Another strategy is to minimize the particle size of the micro-sized active material to the nano-sized structures such as nanoplatelets [40], nanosheets [41] to decrease the lithium diffusion distance thereby increasing the rate

performance of the lithium ion battery. Instead of crushing the large micro-sized active material to nanoparticles, alternative strategies are available such as foreign atoms doping [42] and by making the surface of the active materials porous so that active surface area of the particles is maximized. Sol-gel method was also used to coat the carbon material over the wall of the pores of LFP leading to the percolated nano architecture [43]. For instance, the citric acid is mixed with LFP particles and then during the heat treatment, the evolution of gases from the mixture creates a pore network and at the same time, the solid particles are coated with the carbon particles [44], [45].

The active material for the present study is the carbon coated $LiFePO_4$ obtained commercially from Alyees. The average particle size of the LFP is 200 nm and the particle shape of the LFP powder is spherical, as determined from the SEM image shown in figure 2.6a. Sodium chloride crystal with average particle size of 13.7 ± 6.8 micron was used as a pore forming agent and super P carbon is used as the conducting agent to increase the electrical conductivity of the electrode. The active material (AM), as prepared NaCl and conductive carbon are taken in a volume ratio of 50:40:10 vol.% which corresponds to 62.4-30.8-5.9 weight % (calculated based on their density and volume fraction percentage) and grounded using mortar for 20 minutes to obtain a homogeneous mixture of LFP-NaCl-C composite (Figure 2.6b). This mechanical grinding helps to achieve good contact between the carbon and active materials. As shown in figure 2.6b, the backscattered SEM image of the LFP-NaCl-C composite shows the clear difference between the spherical shaped LFP and cubic shaped NaCl particles.

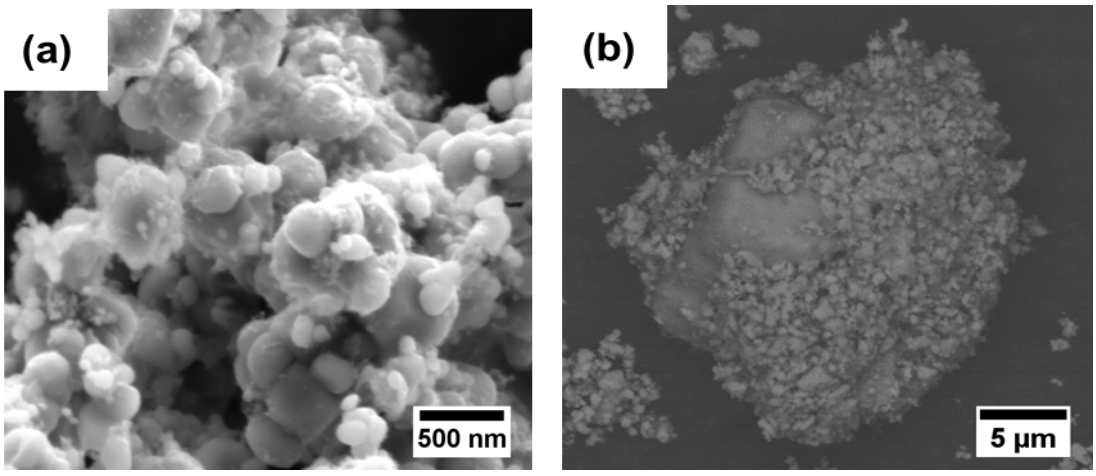

Figure 2.6 *a) SEM image of commercial carbon coated LFP powder, b) LFP-NaCl-C composite prepared after grinding of 30 minutes showing the salt particle is surrounded by LFP powder and sp-Carbon.*

450 mg of LFP-NaCl-C composite are packed in the center of the graphite die and closed by the graphite pistons on both top and bottom sides of the graphite die. Graphite paper was cut with a diameter of 10 mm and placed on either sides of the composite to maintain the electrical contact between the pistons and the powder during SPS treatment. The graphite papers also help to remove the pellet easily from the pistons after the SPS reaction. Then, the graphite die containing the composite powder is pressed at 4 tons using a cold pressing machine in ambient atmosphere before SPS densification. This helps to ensure a physical contact between the components of the composite. Finally, the cold pressed die was then moved to an argon filled glove box which is attached to the SPS machine.

2.2.2 Densification of $LiFePO_4$-NaCl-C by SPS technique

The as prepared LFP-NaCl-C composite was densified using the SPS device with the optimized temperature, pressure and reaction time. The SPS program was set at 650 °C, pressure of 10 kN with holding time of 5 minutes. Higher pressure above 10 kN leads to the breakage of graphite die during SPS process. The graphite die was placed inside the SPS chamber which is attached with the glove box with an initial applied pressure of 2 kN. Then, the thermocouple was attached to the exterior of the center of the die for which the set temperature of the die can be controlled and continuously followed.

The SPS reaction consists of 6 steps which were pre-saved in the SPS computer and the total duration of the SPS reaction is 22 minutes:

(1) The initial step is the evacuation of SPS chamber containing graphite die hosting the powder for 2 minutes.

(2) The second step includes the uniaxial pressing of the graphite die at 4 kN for 2 minutes without applying temperature. A minor variation of displacement in the second step can be observed as shown in figure 2.7.

(3) The third step was further increase of temperature from 25 °C to 600 °C in 5 minutes while keeping a pressure of 4 kN.

(4) The fourth step includes the simultaneous application of pressure from 4 to 10 kN in 5 minutes and small increase in temperature from 600 °C to 650 °C. During this step, the densification process of LFP-NaCl-C can occur and be observed thanks to the displacement of pistons as shown in Fig. 2.7.

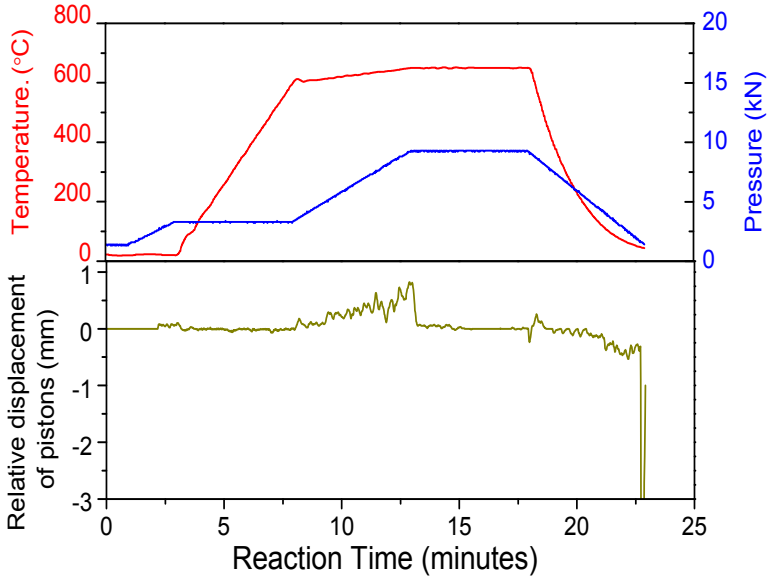

Figure 2.7 *SPS protocol of preparing LFP-NaCl-C pellet at 650 ° C and 10 kN for 5 minutes holding time, placed in 10 mm diameter graphite matrix.*

(5) The maximum temperature was reached at 650 °C and holding time was maintained for 5 minutes at 650 °C and 10 kN. The temperature was well controlled at 650 °C and effective sintering of particles was done in this step and also elimination of gaps was performed, leading to high compactness.
(6) The final step, the rapid cooling step from 650 °C to 30°C and simultaneous release of the pressure from 10 kN to 2 kN in 5 minutes was done by using a cold water circulation unit attached to the SPS machine. The corresponding displacement of pistons (green) is shown in the figure 2.7 explaining the complete release of graphite pistons at a speed of 9 mm/min.

After the completion of the SPS program, since the LFP and LTO pellets are not sensitive to air and moisture, the graphite die was taken out of the glove box (this is not applicable for air sensitive materials like sulphides) and processed in the ambient conditions. The graphite pistons are removed using cold press by slowly pushing downwards and the cylindrical LFP-NaCl-C pellet was recovered. The pellet surface was covered by the graphite papers on the top and bottom surfaces and this was subjected to polishing using sand paper and to achieve the desired thickness and a diameter of 10 mm. The digital photo of the 1-mm thick LFP pellet electrode is shown in figure 2.9 illustrating the diameter of the LFP pellet corresponds to the inner diameter of the graphite dye used for the SPS densification.

Pellet compactness is determined based on the weight of pellet and powder and defined as the ratio of the pellet density to the powder density. The initial mass of the pellet after SPS was noted as well as its geometrical dimensions, as shown in equation 2.2 where W is mass (g), d_x is density of materials where x is LFP/ LTO, NaCl and sp-Carbon (g/cc). After the sintering by SPS, the geometrical dimensions such as pellet thickness t (cm) and the surface area of the pellet SA (cm^2) were measured using Vernier caliper and IpWin software, respectively. The surface area measurement is based on the measurement of pixels of the pellet surface and the pre-determined area and the detailed procedure of the determination of pellet surface area is shown in annexe. The compactness value is determined as being 95% for both LFP/LTO-NaCl-C pellets according to the relation below. The apparent density of LFP-C pellet after NaCl dissolution is 1.8 g/cc and plotted in the figure 2.8.

$$Pellet\ Compacity\ \% = \frac{\left(\frac{W_{before\ NaCl\ dissolution}}{SA_{pellet} * t_{pellet}}\right)}{(d_{LFP} * vol.\%) + (d_{NaCl} * vol.\%) + (d_C * vol.\%))} * 100 \quad (2.2)$$

Density measurements were done using Helium gas Pycnometer for the powders such as LFP, NaCl, carbon and LFP-NaCl-C (50:40:10 vol.%) composite and 1-mm thick LFP-pellet with 44% porosity are shown in figure 2.8. The density of the LFP and LTO is 3.5 g/cc, NaCl is 2.15 g/cc and sp-Carbon is 1.7 g/cc are measured using Helium gas Pycnometer and the results are shown in figure 2.8. This measurement involves the measurement of density by flushing helium gas over the powder and pellet placed in a specified volume container (3.5 cc). The slight difference in density of sp-carbon compared to the theoretical density was observed due to its amorphous nature. The Pycnometer density of 1-mm thick LFP-C electrode is 3.1 g/cc which is almost two times higher than the apparent density value (1.8 g/cc) as shown in figure 2.8. From the apparent (ρ_a) and Pycnometer density values (ρ_p), the porosity of the 1-mm thick LFP electrode is calculated using the relation $\left(\varepsilon = 1 - \left(\frac{\rho_a}{\rho_p}\right)\right)$ as 42%. The porosity values determined from the various methods such as weight loss, pycnometry and micro computed tomography (µCT) data are compared in the table 2.1. Alternative methods like Mercury intrusion porosimetry are available in the literature to measure the average pore size of porous materials, composite electrode and separator containing macro-pores (higher than 50 nm) of lithium ion batteries [46], [47].

Table 2.1 *Porosity values of 1-mm thick LFP determined by various methods.*

Method	Weight loss method	Pycnometer	Micro-Tomography
1-mm thick LFP electrode porosity (%)	44.0	42.0	43.7

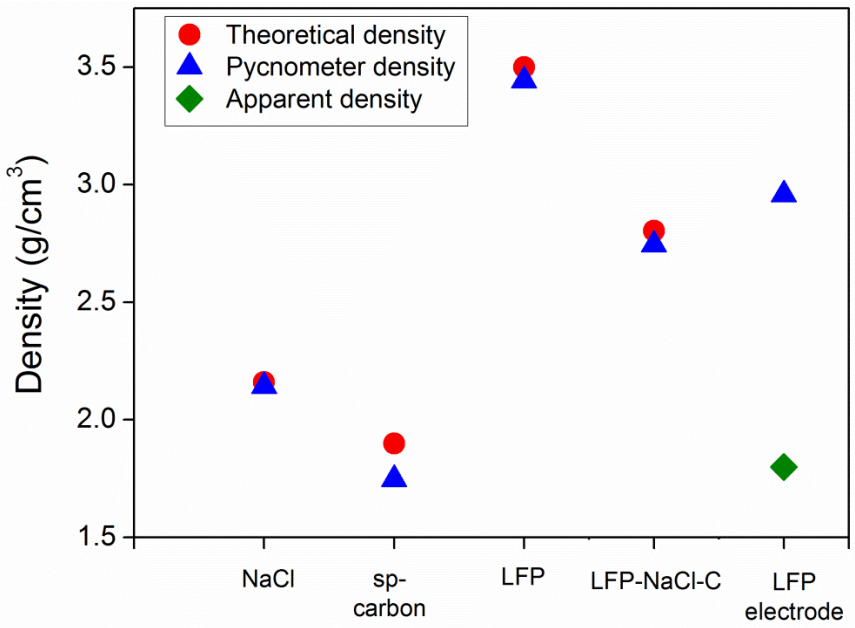

Figure 2.8 *Density measurement of initial powders of NaCl, sp-C, LFP-NaCl-C and 1-mm thick LFP electrode using Helium gas Pycnometer.*

X-ray diffraction (XRD) analysis of the sintered LFP-NaCl-C pellet was performed using laboratory D8 Advance Bruker diffractometer (Cu Kα radiation, λ= 1.5418 Å) and the 2θ values are recorded from 15 to 45°. Figure 2.9c exhibits the XRD profiles of LFP/NaCl/C after the SPS treatment showing the narrow crystalline peaks of NaCl (JCPDS no.88-2300) and well indexed to the ordered orthorhombic olivine structure of LFP (Pmna). The XRD profiles clearly show that no reaction occurs during the SPS treatment at 650 °C, due to both the strong covalent bonding of P-O atoms in olivine LFP and the inertness of NaCl particles. Thanks to the Argon atmosphere, no oxidation of carbon is observed either.

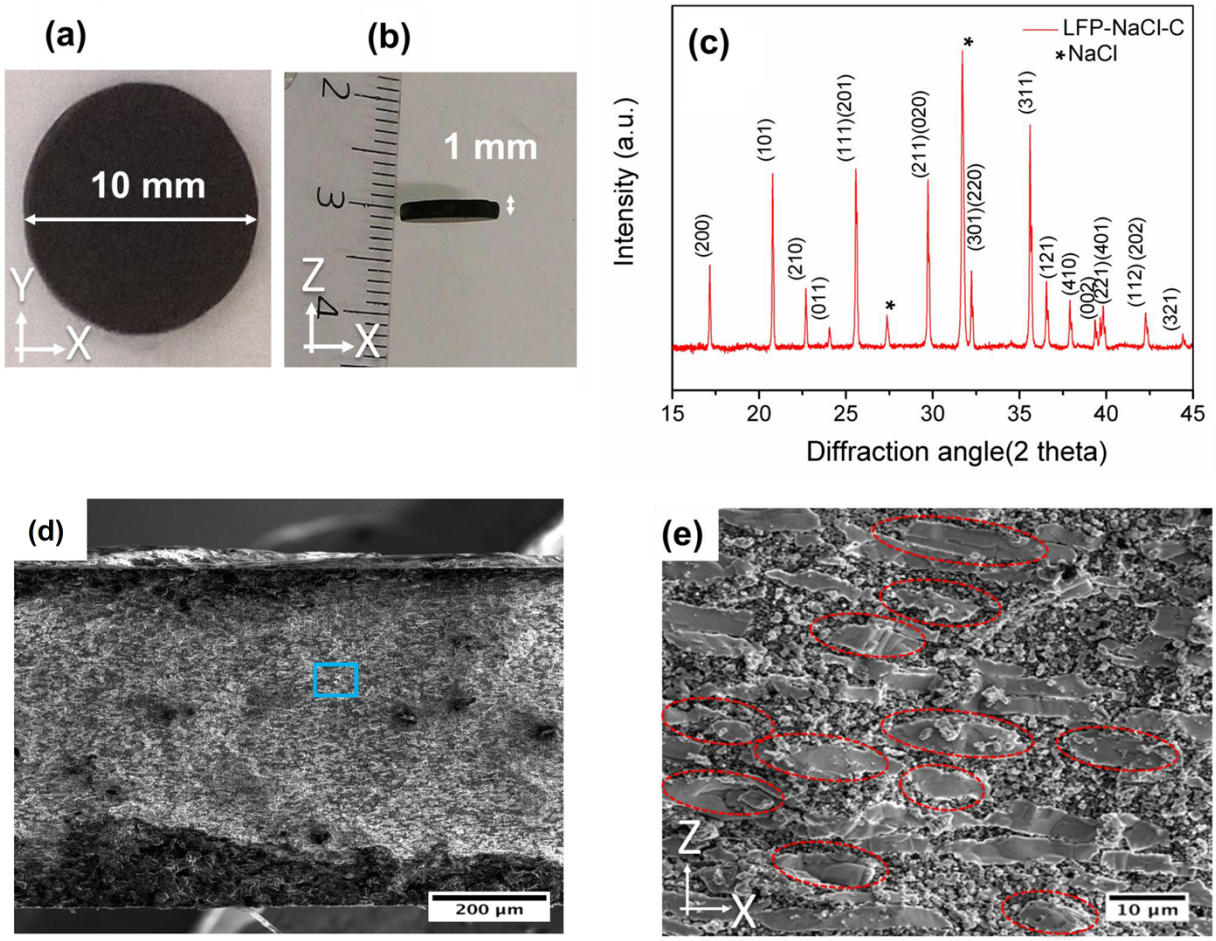

Figure 2.9 a-b) *Digital photo of the LFP-C pellet obtained after SPS treatment, c) XRD pattern of sintered LFP-NaCl-C pellet, d,e) SEM image of cross section of LFP-NaCl-C pellet showing the embedded NaCl particles along with LFP and Carbon.*

SEM images (figure 2.9d-e) show the cross section of the LFP-NaCl-C pellet after the SPS reaction in which larger grains (marked in red) are the salt particles, which get elongated and aligned perpendicular to z-direction due to the application of pressure during sintering. Also, LFP grains (spherical particles) are well sintered showing good grain-grain bonding and a clear interface between the LFP and salt particles illustrates the inertness of sodium chloride.

2.2.3 Chemical characterization of 1-mm thick LFP electrode

The 1-mm thick LFP-NaCl-C pellet was subjected to the dissolution of salt particles in water to create pores inside the thick electrode. The washing step was carried out by injecting the water using a syringe into a evacuated vial containing the thick pellet electrode. In this case, water is forced to the pellet so that salt particles are dissolved rapidly and completely. The porous electrodes are washed 3 times with

running distilled water to make sure no salt particle is still present inside the pellet. After thorough washing with water and ethanol, the LFP (or LTO)-C electrodes are dried in the vacuum oven at 120 °C overnight. Ethanol is used to wash, which helps promote fast drying of electrodes in the vacuum oven.

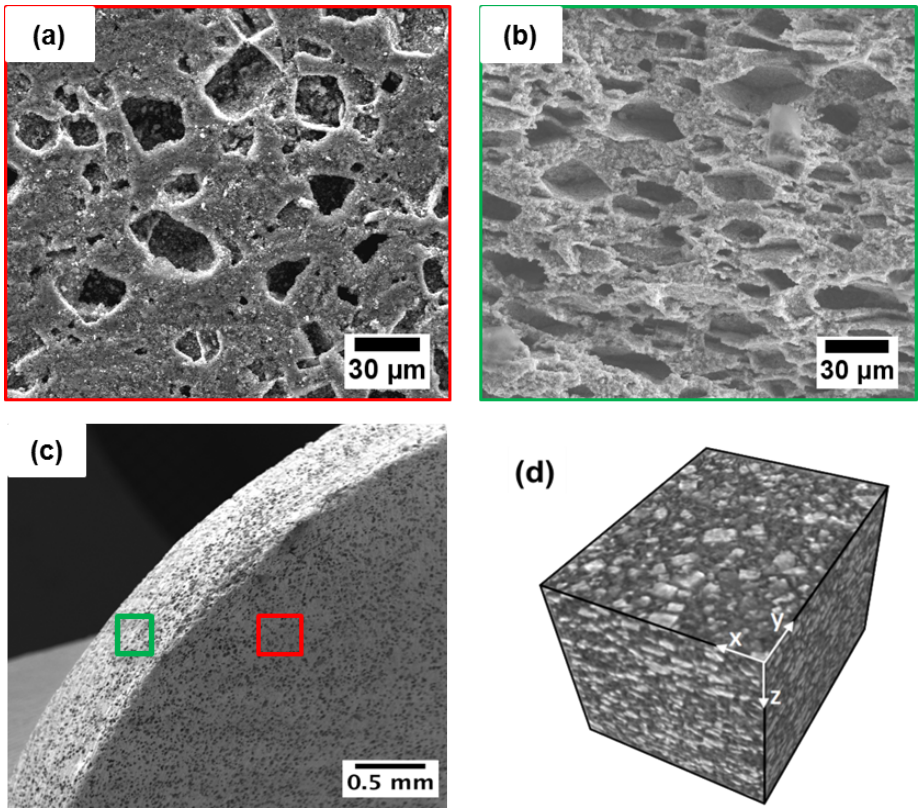

Figure 2.10 *SEM images of 1-mm thick LFP-C porous electrodes a) Top surface view, b) Cross section of the fractured surface of LFP electrode showing the uniformly arranged pores perpendicular to the z direction, c) Low magnification SEM image showing the uniformity of pores in the edge of pellet, d) Stacked SEM images in 3D view showing orthogonal directions.*

As shown in figure 2.10a-b, SEM image of the top view (red square) clearly shows that the squared pore shape with clear edges due to the salt crystals, whereas the cross section SEM image of the porous electrode represents the elongated pores perpendicular to z-direction. This anisotropy of pores is due to uniaxial pressing during SPS reaction. The measurement of porosity was done by weight loss method and compared with Pycnometer.

$$Porosity_{Wt.loss.}\,(\%) = 1 - \left[\left(\frac{m_{\,before}}{\frac{d_{theo}}{A*t}}\right) + \left(\frac{m_{before} - m_{after}}{\frac{d_{NaCl}}{A*t}}\right)\right] * 100 \qquad (2.3)$$

$$Porosity_{Pyc}\,(\%) = \frac{Volume\ of\ pellet - Pycnometer\ volume}{Volume\ of\ pellet} * 100 \qquad (2.4)$$

The difference in mass of the pellet before and after NaCl dissolution was estimated using equation 2.3 where m is mass of electrode (before and after NaCl dissolution) (g), d is density (g/cc), A is electrode area (cm^2), t is thickness of electrode (cm). The electrode porosity is found to be 44% based on the weight loss method. The total LFP electrode porosity is due to the dissolution of NaCl as well as the residual closed pores formed after SPS process because of the compactness of the LFP-NaCl-C pellet after the SPS reaction is 95%. The final LFP-C electrode composition after NaCl dissolution is 90-10 weight %. Apparent density (in g/cc) is the ratio of the electrode mass to the product of surface area and the thickness, and found to be 1.8 g/cc. The porosity of the LFP electrode can be compared with the weight loss method and Pycnometer measurements using the equations 2.3 and 2.4 and the values are tabulated in table 2.1.

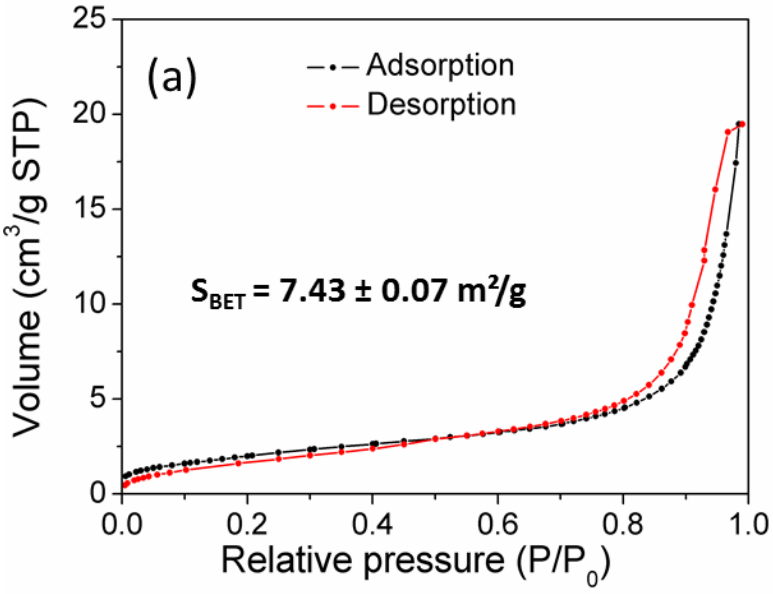

Figure 2.11 *Nitrogen adsorption/desorption isotherms of the 1-mm thick porous LFP electrode at 77 K.A small hysteresis is showing at P/P_0=0.9 due to the porous nature of the LFP electrode.*

The BET surface area of the 1-mm thick LFP electrodes was measured by ASAP ® 2420 porosimetry analyzer. This system works on the principle of the adsorption-desorption mechanism of nitrogen gas passing inside the pores of the electrode as shown in figure 2.11. According to the N_2 adsorption/desorption isotherms for LFP-C electrode, an obvious hysteresis loop was obtained between 0.8 and 1 of relative pressure *(P/Po)* and the surface area is found to be 7 m^2/g. These nano-sized pores

present in the LFP particles surface can greatly promote the migration of Li^+ ion during the cell operation. BET surface area of LFP and sp-carbon powder was also measured for comparison and measured as 17 m^2/g and 60 m^2/g respectively. The surface areas of LFP and sp-carbon powders are relatively higher compared to the LFP thick electrode and this difference can be due to the sintering of the particles in the bulk electrodes during SPS operation.

Nevertheless, the electrode porosity value cannot be obtained from N_2 adsorption/desorption analysis because this technique is accurate for analyzing materials having pore size less than 100 nm and is not suitable for measuring the volume of macroscopic pores in the thick electrode [48].

The 1-mm thick LFP pellet electrodes are characterized by Energy Dispersive X-ray (EDX) analysis using SEM to confirm the absence of sodium chloride after dissolution. EDX is a chemical characterization technique that helps to quantify the elements present in the specimen and the mapping of individual elements of the electrodes can be done in the selected area of acquisition. FEI Quanta SEM FEG equipped with an EDX Oxford detector (X-Max, SDD) was used. Cross section of LFP-C electrode was placed in the SEM chamber (high vacuum) and the acceleration voltage was set at 20 kV (working distance at 10 mm). Mapping of the individual elements in the acquisition area are presented in figure 2.12 showing that the carbon atoms are uniformly coated on the surface of the LFP particles. The quantification analyses of the porous LFP electrode gave the Fe/Cl/Na atomic ratios of 96:0:4. This clearly shows that no chlorine atom and a negligible amount of sodium (may be due to formation of sodium hydroxide) were present in electrode, proving that there are no salt particles still remaining in the electrode after the dissolution.

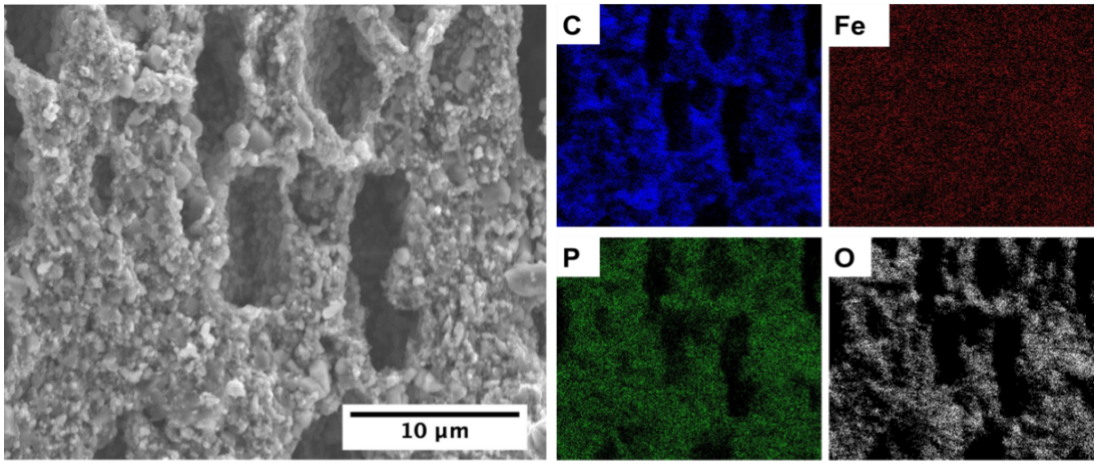

Element	Weight (%)	Atomic (%)
Na	1.59	3.79
Cl	0	0
Fe	98.4	96.21
Total	100.0	

Figure 2.12 *EDX mapping analysis of LFP-C electrode showing the atoms are present uniformly over the surface of the particles with spectrum showing Fe, P and O atoms in LFP with no chlorine atoms after NaCl dissolution present in LFP electrode.*

2.2.4 Electrochemical properties characterizations

The electrochemical reaction of $LiFePO_4$ is described as a two phase redox reaction occurring with a plateau at 3.45 vs Li. The maximum exchange of 1 mol of Li per formula unit corresponds to the theoretical capacity of 170 mAh/g. The corresponding electrochemical reaction during charge is shown in equation 2.5 and cell reaction is reversed during discharge.

$$LiFePO_4 \leftrightarrow Li_{1-x}FePO_4 + xLi^+ + xe^- \quad (2.5)$$

Before the cell assembly, the thick binder free sintered electrodes are subjected to the filling of pores by the liquid electrolyte using the vacuum impregnation method. This was done by evacuating the pellet in a rubber cork closed vial using a vacuum pump. Then, the liquid electrolyte is injected into the porous electrode using a syringe inside the glove box and this allows the liquid electrolyte to fill the pores completely at a faster rate. Then, the pellet electrode is assembled against lithium separated by 2 layers of glass fiber separators. Conventional liquid electrolyte composed of 1M $LiPF_6$ dissolved in 1:1 wt.%

of ethylene carbonate and di-ethylene carbonate (LP30) was used (200 µL). After the Swagelok cell assembly, the cells were tested at a constant temperature of 25°C. It is worth noticing that coin cell designs are not applicable to cycle our thick electrodes because the overall thickness of the standard coin cell (2025) is not enough to host our 1-mm thick pellet and would also lead to the breakage of pellet electrodes.

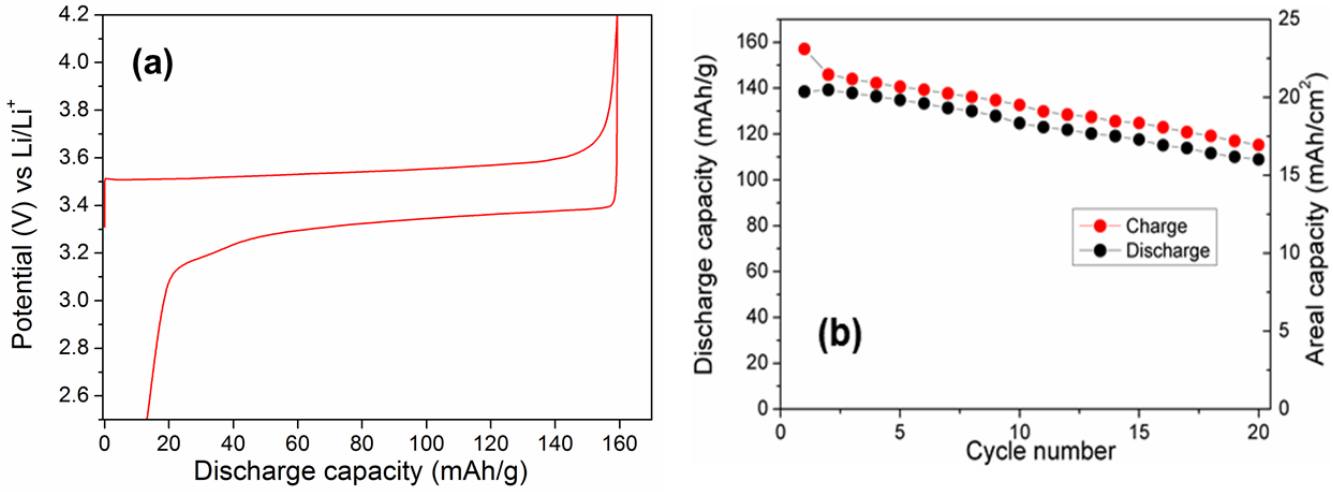

Figure 2.13 *Electrochemical characterization of LFP electrodes vs Li. a) Charge-discharge profile at C/20 rate, b) Capacity retention curve of LFP vs Li at C/20 rate.*

The 1-mm thick LFP electrode was electrochemically tested in the galvanostatic potential limiting (GCPL) mode with a constant current applied equivalent to C/20 rate between 2.5 V and 4.2 V against metallic lithium. 1C rate is defined as insertion or reinsertion of 1 Li^+ in one hour. The charge-discharge profile of LFP/Li is showed in figure 2.13a which highlights a clear plateau at 3.5 V which is close to thermodynamical potential (3.45 V) of LFP and 0.2 V polarization between charge and discharge was observed at C/20 rate. This polarization is relatively low regarding the thickness of the electrode due to the good electronic contact between the carbon coated LFP particles and sp-carbon ensuring good transport of electrons through all directions. The initial discharge capacity is 140 mAh/g with 75% capacity retention for 20 cycles and a coulombic efficiency of 98%. The poor capacity retention can be ascribed to the volumetric expansion of LFP particles upon cycling and loss of mechanical properties. Full theoretical capacity of LFP (170 mAh/g) was not achieved and the initial LFP powder vs lithium delivers the practical capacity of 140 mAh/g. This is due to the presence of some impurities and the large macro LFP particles (200-400 nm) and can be improved by minimizing the initial particle size of LFP.

Nevertheless, our thick electrodes exhibit remarkable high values of areal capacity, which are equal to 20 mAh/cm^2, which has been never obtained before at the best of our knowledge. These areal capacity values of 1-mm thick LFP electrodes are 4-5 times higher than those of the conventional Li-ion batteries. In order to determine the lithium ion diffusion limitations in the liquid phase of thick LFP electrode, Charge-discharge tests at different C-rates were performed and shown in figure 2.14a.

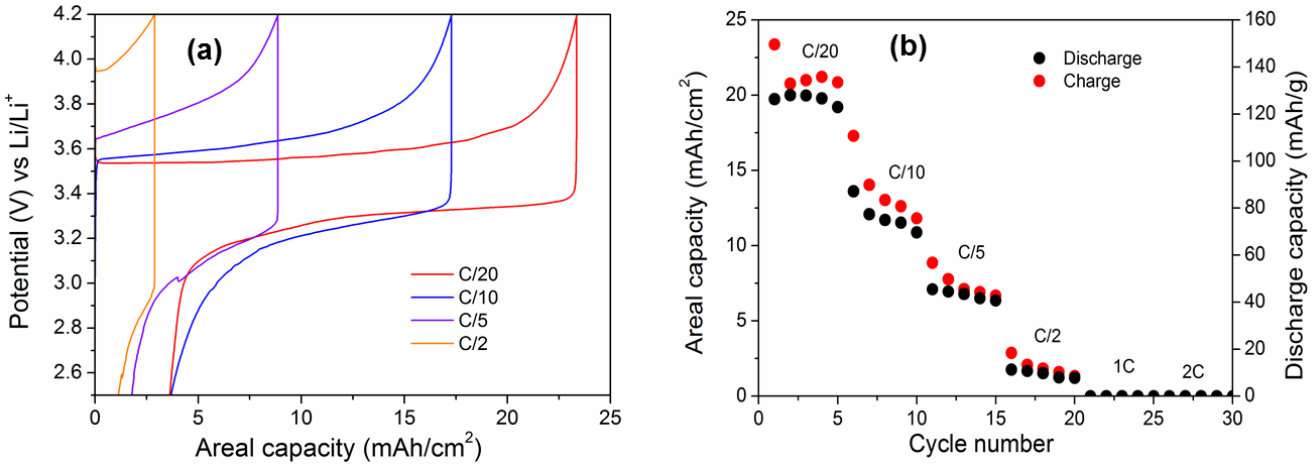

Figure 2.14 *a) Charge-discharge profile of LFP-C electrode at different C-rates such as C/20, C/10, C/5, C/2, 1C and 2C rate, b) Rate capability of 1-mm thick LFP-C/Li.*

One can observe an increase in polarization (over potential) and decrease in specific capacity at higher C-rates from C/20 to 2C. The decrease in capacity at high rates is associated with Li ion diffusion resistance within the bulk electrode which is more pronounced especially for the thick electrodes.

2.2.5 Effect of additional carbon

In our work, the commercial LFP powder (c-LFP) is already carbon coated by synthetic methods. To confirm the importance of the additional carbon content used with the sintered electrodes, an electrode formulation without adding additional carbon was prepared with a composition of LFP-NaCl-Csp 60-40-0 vol.%. 450 mg of the mentioned composite is sintered with the same conditions: 650 °C with 10 kN and 5 minutes holding time. After the SPS reaction, the compacity of the pellet is 98%, which is comparable to the one densified with additional carbon. After water immersion all the NaCl particles are dissolved. The thick electrodes are then dried in a vacuum oven at 120 °C. The physical properties of the LFP electrodes with and without carbon are compared in Table 2.2.

Table 2.2 Physical of the thick binder free LFP electrodes obtained using SPS and templating approach having two electrode LFP-C compositions (100-0 wt.% and 90-10 wt.%).

Properties	**LFP-C (wt.%)**	
	100-0	**90-10**
Compacity (%)	98	95
Porosity (%)	41	45
Thickness (mm)	1.01	1.0

The two 1-mm thick LFP-C electrodes are tested in a galvanostatic mode using Swagelok cells. The conventional liquid electrolyte made of 1M $LiPF_6$ in 1:1 EC: DMC (wt.%) was used, and kept being used for all the electrochemical measurements unless it is described specifically. From the galvanostatic curve of 1-mm thick LFP-C/Li system (100-0 wt.%) at C/20 rate (Figure 2.15a), a sloppy discharge curve with large cell polarization (~0.4 V) and lesser capacity (100 mAh/g) was obtained. This is due to the charge kinetics limitations or low electronic percolation due to the insufficient carbon content present in the electrode with LFP-C (100-0 wt.%) composition.

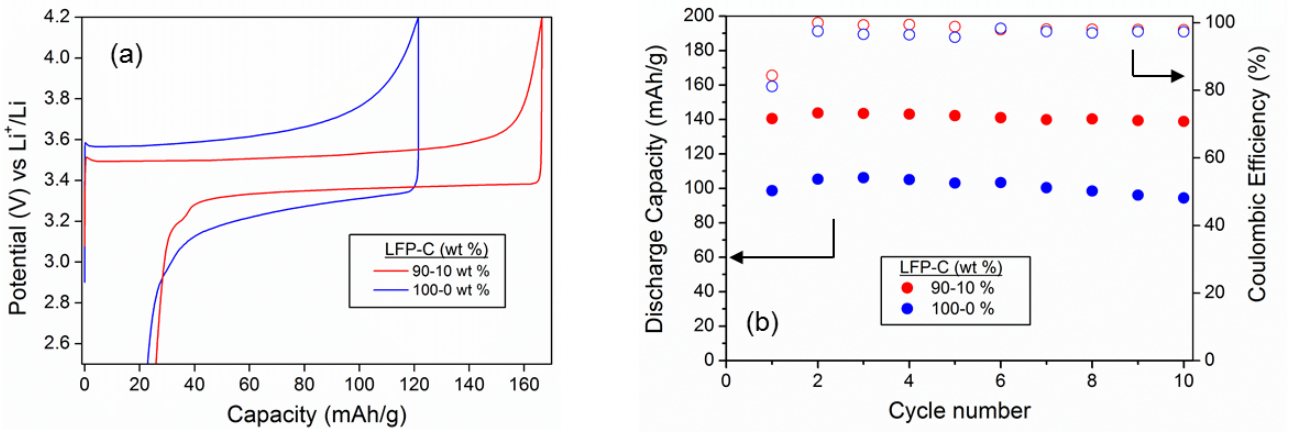

Figure 2.15 *Comparison of electrochemical performance of LFP-C pellet having two different compositions of 90-10 and 100-0 wt.% (a) Charge-discharge profile at C/20 rate and (b) capacity retention curve at C/20 rate of 1-mm thick LFP electrodes with and without extra carbon added.*

At the same time, higher discharge capacity (140 mAh/g) with less cell polarization was obtained for 1-mm thick LFP-C (90-10 wt.%) electrode as shown in figure 2.15b. Coulombic Efficiency (CE) was measured for the electrodes with two different compositions and CE is the ratio of discharge to charge

capacity [58] and the CE value is above 97% for both LFP-C electrodes. After observing the better cycling performance, 10 wt.% of carbon are added for all the LFP electrodes reported hereafter.

2.2.6 Effect of inhomogeneity of pores: Full pellet vs broken piece

Based on SEM investigations, a great level of inhomogeneity of pores can be observed after dissolution of the salt between the edges and the center of the electrode. This pore inhomogeneity was created due to the blocking of pores by polishing of pellet in the edges after the SPS operation and due to the "migration" of the NaCl crystals during the sintering process. Figure 2.16-b shows clearly the numerous and homogenous repartition of the pores in the cross section of center of a full pellet in comparison to the SEM picture of the edge of a full pellet where no porosity can be detected (Figure 2.16a).

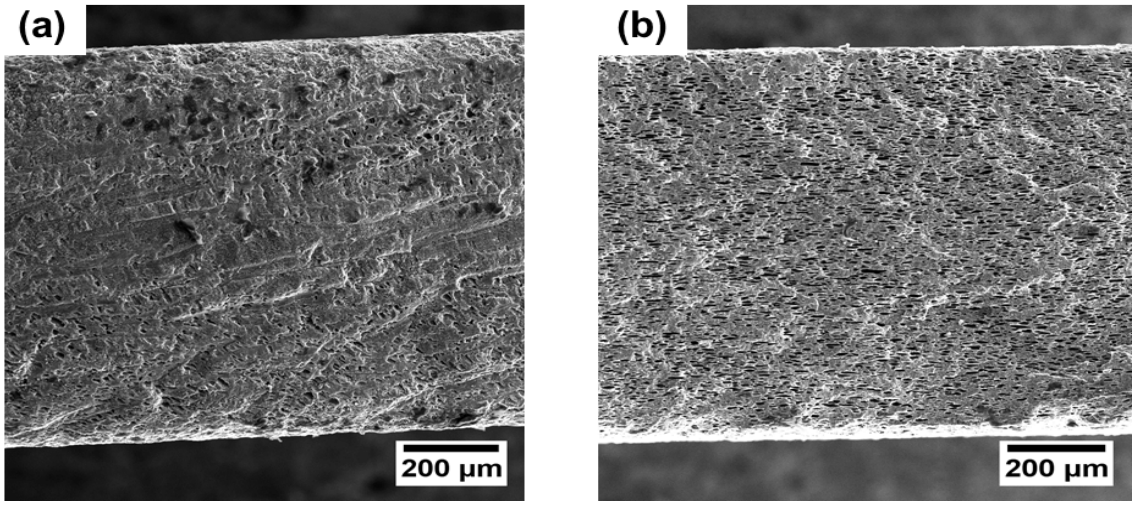

Figure 2.16 *Comparison of SEM images of cross section in the full pellet and fractured surface in the middle of the 1-mm thick binder free LFP electrodes. Pore non-uniformities are present in the edges of the full pellet than the middle of the pellet.*

As a consequence, the electrochemical performances of the porous electrode will be different depending if a full pellet is considered, or only a piece from the middle or from the edge of the pristine pellet. The porosity of the LFP-C (90-10 wt.%) electrode, irrespective of the pellet surface, is 44%. Figure 2.17a compares the galvanostatic curve of a full porous electrode (full pellet 10 mm diameter and 1-mm thickness to a piece of electrode cut in the middle). First of all, the cell polarization is much more important (~2 times) for the full pellet with respect to the piece of electrode. Secondly, the initial discharge capacity for the full LFP pellet electrode is 100 mAh/g at C/20 rate whereas for the broken

piece of LFP/Li cell, the discharge capacity is 130 mAh/g. Similar results are obtained at different C-rates (Fig 2.17b) and the increase of the cycling rate raises the difference between these two samples.

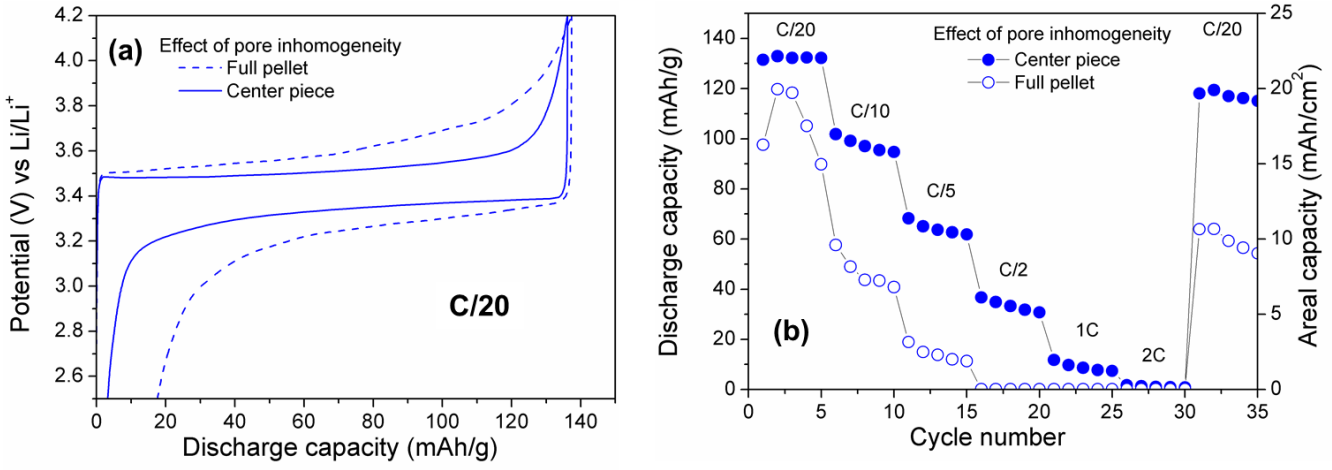

Figure 2.17 *Effect of pore inhomogeneity observed in the LFP-C electrode: (a) Charge-Discharge curve of 2nd cycle of full LFP-C pellet and broken piece of LFP-C pellet showing big difference in polarization, (b) Comparison of rate capability curve of LFP-C electrodes with full pellet and a broken piece taken from the center.*

The reason for the improved rate performances can be explained based on the pore morphology observed in cross sectional SEM image (Figure 2.18b) for the center of the electrode. In this case, pores are distributed homogeneously over the entire cross section with a good inter-connectivity. This allows good diffusion of the liquid electrolyte inside the thick electrode so that better accessibility of all the active materials was achieved. However, on the pellet edge where less pores are present as shown in figure 2.18a, a huge part of the active material cannot have access to the liquid electrolyte and, therefore, can be considered as dead material. This means that considering a piece of electrode cut in the middle, it will be possible to obtain "optimized" performances compared to a full pellet whose electrochemical performances will finally be an average result between the porous center and the non-porous edges.

In the cross section of the full LFP pellet, the incomplete dissolution of NaCl particles is observed after overnight as shown in figure 2.18a. This can be explained by the difficulty of water to penetrate through the NaCl particles from top to bottom sides of the full pellet electrode. However, this incomplete dissolution effect is not observed for the broken piece of the electrode because the exposed salt particles in broken LFP pellet are directly in contact with water and hence easy dissolution in all directions was achieved. Due to this problem, and in the aim to be the more reproducible, all the electrochemical tests

presented in the manuscript where performed on 1-mm thick slices cut in the middle of the sintered electrode.

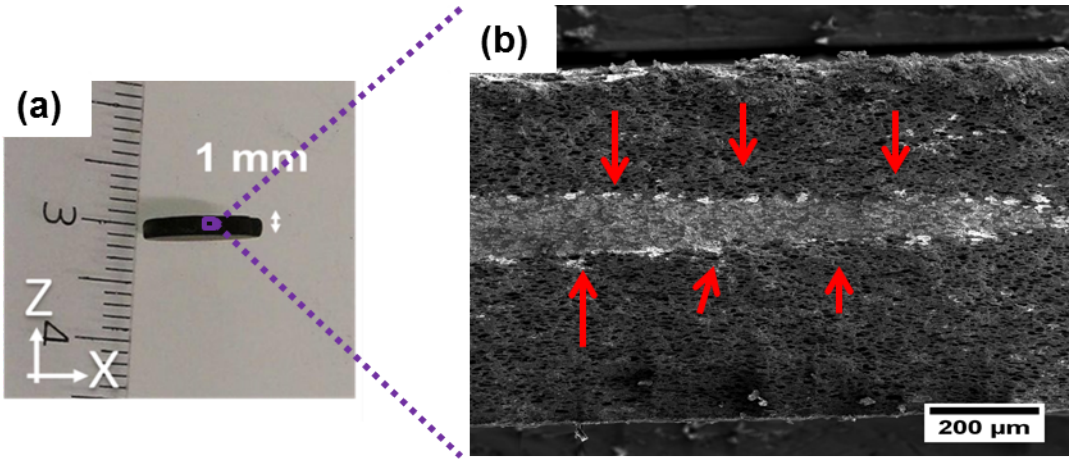

Figure 2.18 *(a) Digital photo showing 1-mm thickness of LFP electrode, (b) SEM image of 1-mm thick LFP pellet after dissolution of salt particles. Incomplete dissolution of salt particles was observed in the middle (white) of the cross section of the full LFP-C pellet. The water penetrates to dissolve salt particles from the either sides of the pellet and shows the salt crystals (in bright) due to incomplete NaCl dissolution.*

2.3 Fabrication of 1-mm thick $Li_4Ti_5O_{12}$ electrodes using SPS technique and templating approach

2.3.1 Densification of $Li_4Ti_5O_{12}$-NaCl-C by SPS

$Li_4Ti_5O_{12}$ is serving as a prominent anode material for lithium ion batteries due to its high safety and referred to as a zero strain material due to the negligible volume change (~0.2%) occurred during the charge-discharge process [50]. Unlike carbon coated LFP powder, pristine $Li_4Ti_5O_{12}$ powder is used for the densification of LTO electrode using SPS. As shown in figure 2.19a, SEM images of the LTO powder are composed of spherical shape particles with an average particle size of 100 nm. The composite powder of LTO-NaCl-C (50:40:10 vol. % or 62.4- 30.8- 5.8 wt.%) was grounded for 20 minutes using a mortar. After the composite preparation, 450 mg of composite were packed in the graphite die and subjected to cold pressing of the composite at 4 tons. Various SPS tests were conducted with the holding time from 0 to 5 minutes and applying pressure from 10 to 20 kN (using WC die). Then, the same temperature was set at 650 °C with 5 minutes holding time and pressure at 10kN. X-ray diffraction of sintered LTO electrodes was performed from 10° to 70° showing narrow crystalline peaks of NaCl together well indexed to spinel (LTO) structure (Figure 2.19b). No side reaction during SPS reaction was observed

such as the decomposition of LTO material and no oxidation of carbon forming carbon dioxide gas was observed due to the SPS densification taking place in Argon atmosphere.

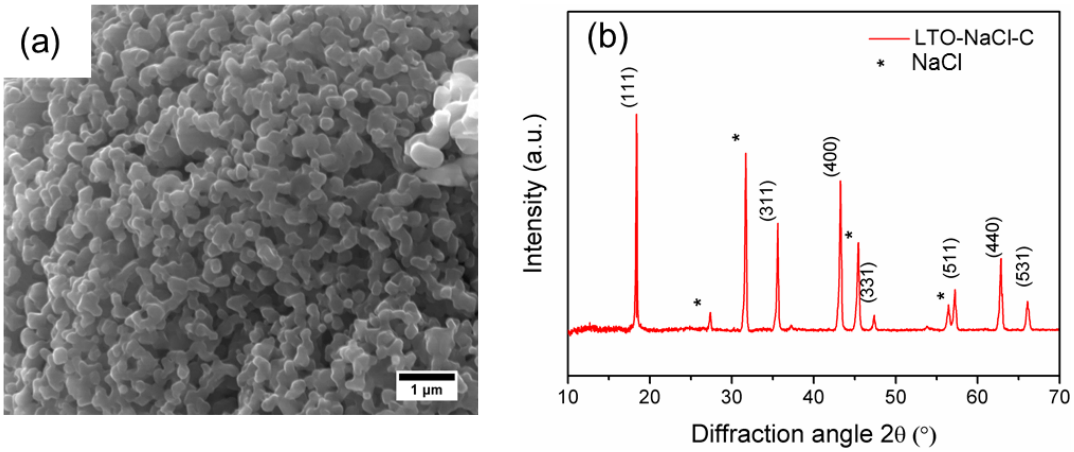

Figure 2.19 *(a) SEM image of pristine LTO particles, (b) XRD pattern of LTO-NaCl-C pellet after SPS reaction.*

After complete NaCl dissolution, the porosity of 1-mm thick LTO electrode is 42% determined by the weight loss method. The uniform pore size distribution of the LTO electrode can be clearly observed from the SEM images (Figure 2.20). The cross section of the thick electrode shows the overall thickness of 1-mm (figure 2.20a). Higher magnification of the LTO electrode identifies the average pore size of about 10 µm and the inner wall of the pores. Top surface view (Figure 2.20c) of the LTO-C electrodes is seen with pores having clear edges corresponding to the dissolution of the cubic shape of crystal, and pores are arranged homogeneously as shown in figure 2.20b.

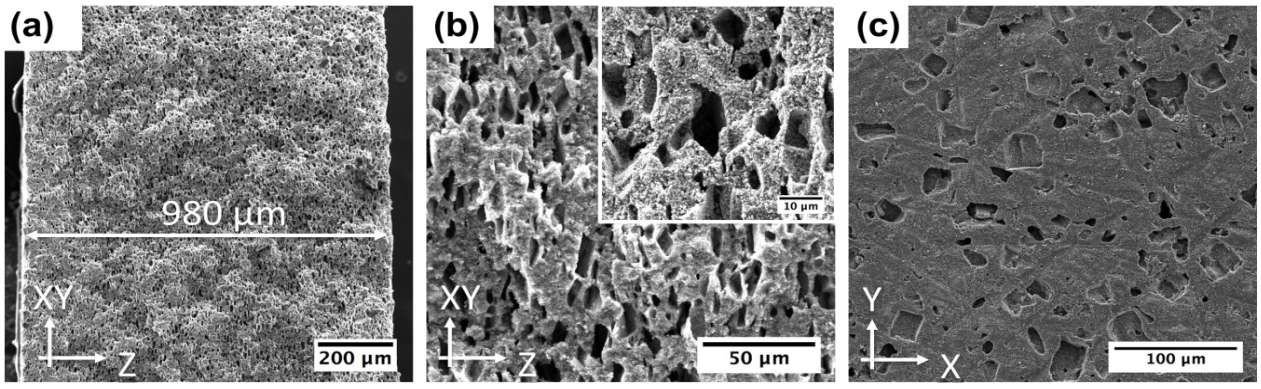

Figure 2.20 *a) SEM images of LTO electrode: (a) Cross section of LTO electrode showing 1-mm thickness, (b) Uniform distribution of pores is seen in cross section and (c) top surface view of LTO electrodes.*

2.3.2 Electrochemical Characterization of 1-mm thick LTO electrode

The charge-discharge curve for the LTO electrode is characterized by a flat and extended voltage plateau around 1.55 V which represents the phase transition between a lithium rich phase to lithium poor phase. During lithium insertion, three Ti $^{4+}$ ions are reduced to three Ti^{3+} ions during the two phase transition from spinel LTO ($Li_4Ti_5O_{12}$) to rock salt LTO ($Li_7Ti_5O_{12}$) and the electrochemical reaction is shown in equation 2.6 for the discharge and will be reversed during charge.

$$Li_4Ti_5O_{12} + 3Li^+ + 3e^- \overset{Discharge}{\rightarrow} Li_7Ti_5O_{12} \quad (2.6)$$

The electrochemical performance of the 1-mm thick LTO-C (90-10 wt.%) electrodes was assessed using conventional Swagelok cells. The 1-mm thick, porous carbon coated LTO is cycled against lithium between 1 and 2.5 V at very slow C-rate (C/60) (Fig. 2.21). A flat plateau was obtained at 1.5 V during discharge corresponding to the thermodynamic potential of LTO (1.55 V) and delivers 95 % of the theoretical capacity of 167 mAh/g of LTO equivalent to the exchange of 2.86 lithium ion to the $Li_4Ti_5O_{12}$ structure (Q_{theo}=175 mAh/g). Good capacity retention (94%) was observed over 10 cycles with 99 % Coulombic efficiency. Hence, the unstable capacity retention seen after 15 cycles could be due to a poor ability to sinter compared with LFP/ less mechanical stability and not due to the intercalation process. During the SPS operation, the sintering capacity of non-carbon coated LTO seems to be poorer compared with LFP particles because the pulsed DC current was unable to pass equally to all the insulating particles during the SPS operation. This can lead to a poor grain-grain bonding between particles. Thus, one can expect that the electrochemical performances can be increased by using carbon coated LTO powders.

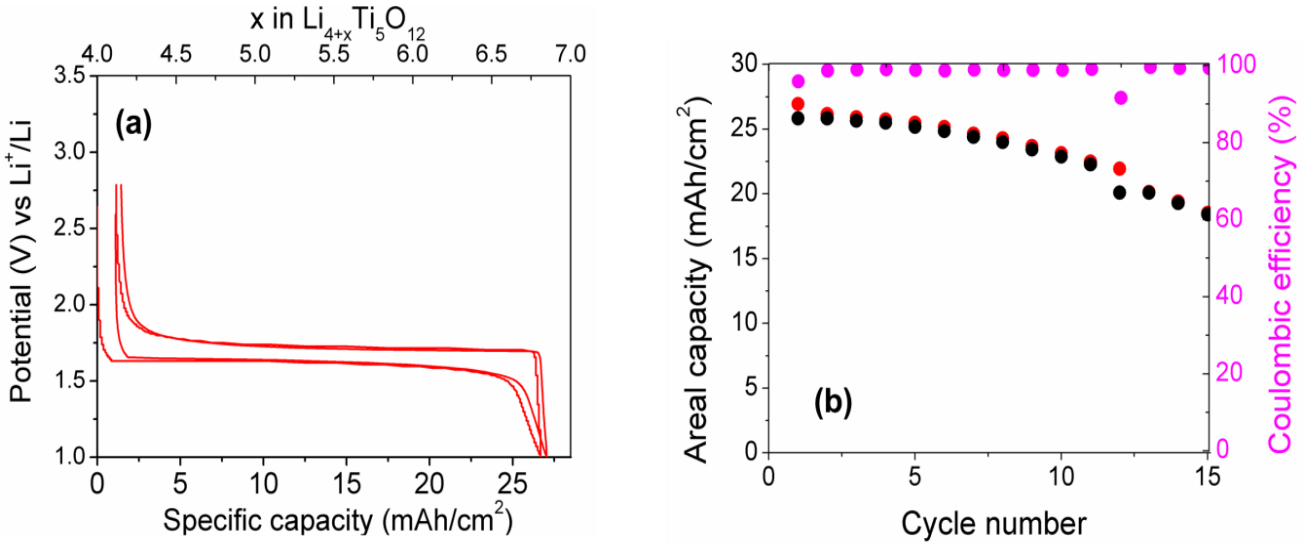

Figure 2.21 *(a) Charge-Discharge profile of LTO-C electrodes, (b) Capacity retention curve of 1-mm thick LTO electrode delivering at C/60 rate,*

Rate capability tests were carried out for 1-mm thick LTO electrodes at different C-rates to determine the lithium ion diffusion limitations inside the sintered LTO electrode. The charge-discharge performance at different C-rates is shown in figure 2.22a-b which illustrates the C-rate capability of LTO electrode and lower capacity was obtained at higher C-rate, which is mainly due to the increase in Ohmic drop and mass transport loss, which leads to longer diffusion and migration paths for lithium ions within 1-mm thick electrodes. The low C-rate performance of LTO electrode can be due to the electrode conductive resistance of carbon mixed LTO particles. This also leads to increase of the charge transfer resistance of lithium ion intercalation in the electrode-electrolyte interface.

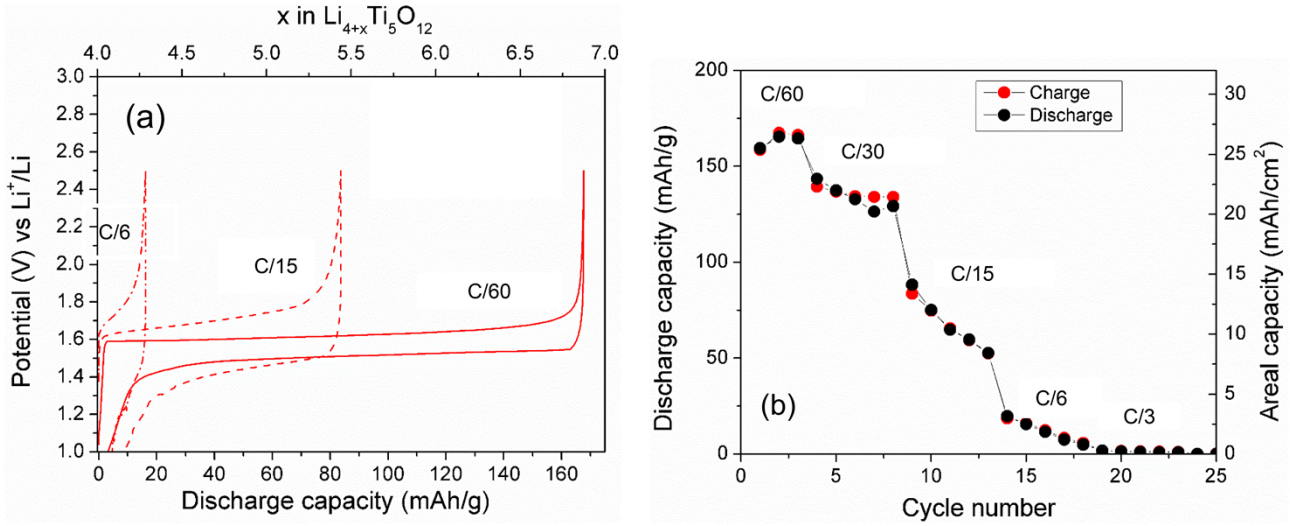

Figure 2.22 *(a) Charge-Discharge profile of 1-mm thick LTO/Li at C/60, C/15 and C/6 rates, (b) Rate capability of LTO vs Li showing the decrease in specific capacity due to mass transport limitations in the liquid phase.*

2.3.3 Full cell assembly of 1-mm thick LFP vs LTO electrodes

The excellent electrochemical performance of LFP and LTO electrodes against lithium encouraged us to assemble a full cell (LFP vs LTO) in the voltage range between 1.0 and 2.5 V. Equal mass of LFP and LTO electrodes are taken for cycling since the practical capacity of both electrodes (LFP-140 mAh/g and LTO-150 mAh/g) vs Li are almost equal at C/20 rate. As expected, a clear plateau was obtained around 1.9 V (E_{cell}=3.5-1.6=1.9 V) with a stable capacity of 20 mAh/cm^2 equivalent to 124 mAh/g and good capacity retention up to 20 cycles was achieved as shown in figure 2.23b. The capacity limitation of LFP/LTO full cell was not observed at C/20 rate unlike LTO half-cell. The lithium metal in the LTO half-cell is mainly limited and thus the effect of lithium metal is avoided in the full cell. The areal or gravimetric capacity is obtained by dividing the capacity by the geometric surface area or weight of the LFP electrode respectively.

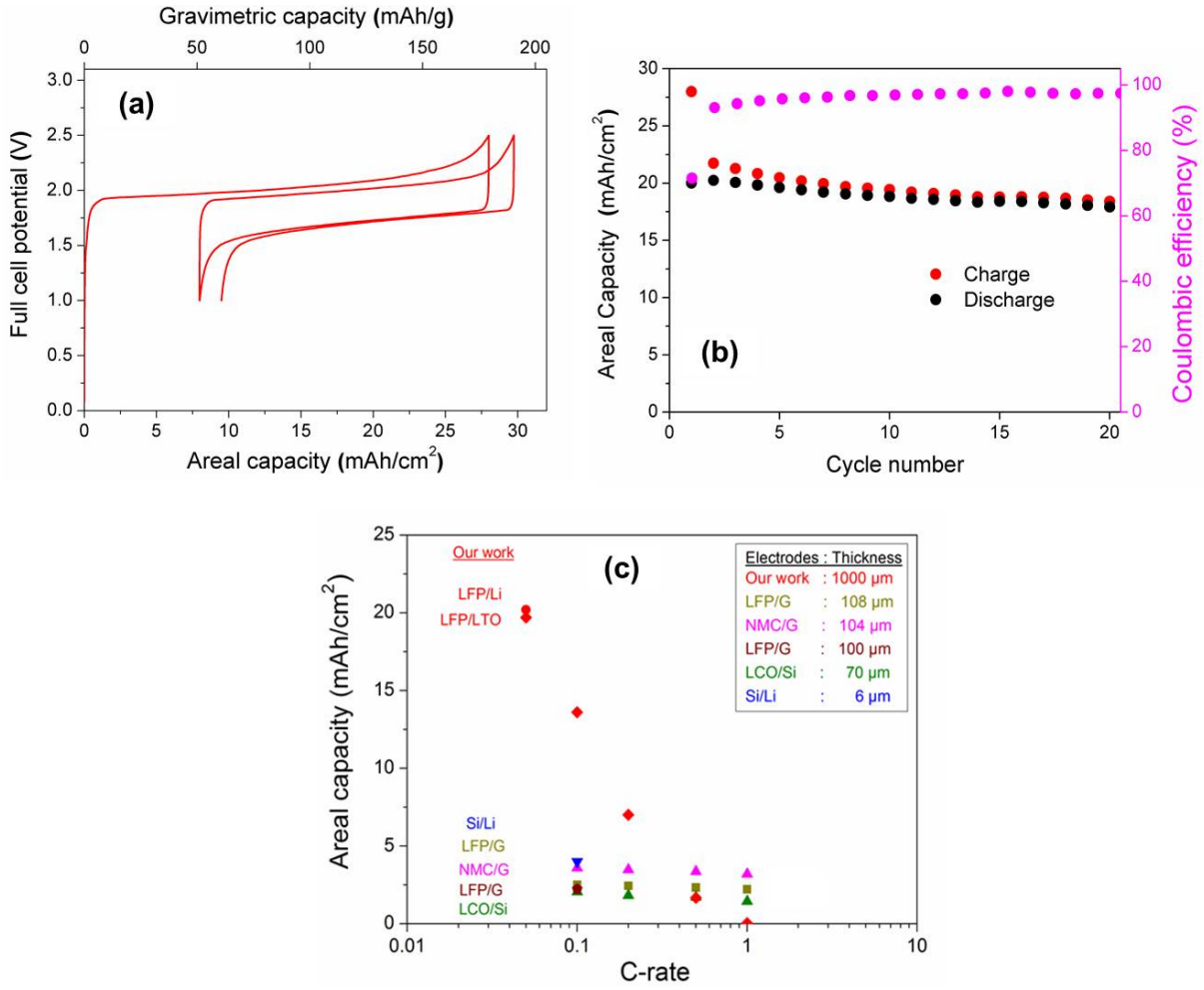

Figure 2.23 *(a) Charge-Discharge profile of 1mm thick LFP/LTO full cell at C/20 rate, (b) Capacity retention curve of the LFP/LTO at C/20 rate. LP30 was used as an electrolyte for the electrochemical cycling. (c) Ragone plot of LFP/Li and LFP/LTO battery systems compared with conventional battery systems.*

The areal capacity of LFP/Li and LFP/LTO electrodes at higher C-rates is displayed in figure 2.23c and the values are found to be 4-5 times higher than the conventional electrodes at lower C-rate. The cathode thicknesses of our system and conventional battery systems are shown in the legend of figure 2.23c for comparison. Thanks to the good interconnection of pores obtained by the templating approach and also Thanks to SPS it was possible to achieve very high loading of active materials of the electrodes (165 mg/cm^2) thereby achieving higher areal capacity. The 1-mm electrode thickness obtained by SPS is 6-8 times higher than conventional electrodes (100 microns). The uniaxial pressing and thermal activation of particles during the SPS process enables the well bonded grains to achieve high electrical conductivity and the pores created by the templating method help to achieve good ionic flow throughout the entire volume. The areal capacity values of LFP and LTO electrodes along with the literature are written in table 2.3 in annexe.

2.4 Conclusion

The templating approach is a powerful method for preparing porous electrodes with interconnected, well-controlled pore sizes and pore morphologies. The first experiments of the 1-mm thick LFP electrodes were done by SPS without any templating agent showing the poor electrochemical performance at higher C-rates. This explains the need of porosity in the thick electrode so that the liquid electrolyte can diffuse into the pores and thus the incorporation of the templating strategy in our work was reasoned. The advantages of SPS, templating and the need for the combined SPS/templating methodological approach are explained. The fabrication procedure of 1-mm thick, binder free porous LFP and LTO electrodes using SPS and templating approach was shown with the first results. The SPS reaction conditions for LFP and LTO electrodes were determined. The chemical reactivity of the individual particles (LFP/LTO, NaCl, C) after SPS reaction was studied using X-ray Diffraction. It is very clear that the remarkable chemical stability was observed between the three components such as LFP(/LTO), sodium chloride crystals and sp-Carbon up to 650 °C and no decomposition of initial components was reporeted. The washing step of salt particles using de-ionized water helps to dissolve the salt particles completely due to higher solubility of NaCl crystals in water thereby increasing the contact surface area of the electrode so that the electrolyte can reach the surface of the active material.

After the NaCl dissolution, the dried electrodes present a large porosity (44%). No traces of water or NaCl are detected in the EDX analysis. The electrochemical performance of the LFP (20 mAh/cm^2) at C/20 and LTO (25 mAh/cm^2) at C/60 against lithium was achieved for the first time, which is 4-5 times higher than that of the conventional lithium ion batteries. The full battery (LFP vs LTO) delivered an areal capacity of 20 mAh/cm^2 at C/20 rate with stable capacity retention up to 20 cycles. The combined SPS and templating approach was employed to create high active material loading (165 mg/cm^2), low tortuosity electrodes which are helpful to achieve very high C-rate electrochemical performance. These results show a proof of concept of increasing the areal capacity by successfully increasing the electrode thickness with the simultaneous reduction of inactive material like the binder. These results also demonstrate that the coupling between the salt templating method and the SPS technique is a promising way to reach the ultimate goal of achieving high energy density. Next, chapter 3 will focus on the experimental study towards the optimization of the pore size, porosity and thickness of LFP electrodes and their influence on the electrochemical properties will be discussed.

2.5 Annexes

Measurement of geometric surface area of electrode

The geometric surface area of an irregular shape of the pellet electrode was measured using Ipwin Pro Plus® software. The electrode was placed on a known area (6.76 cm^2) of white space and the digital photo was taken using a camera as shown in figure 2.24. The number of pixels of the pellet is counted as S_1. The pixels of the outside of the reference box are not counted. Then, a photo of the blank square reference area (without pellet) was taken and the corresponding pixels are measured using the software and noted as as S_2. Knowing the area of the reference, A_{ref} is 2.6 x 2.6 = 6.76 cm^2, the surface area of the pellet can be measured as $A_{pellet} = A_{ref}$ x S_1/S_2= 6.76 x 13903/291229 = 0.322 cm^2.

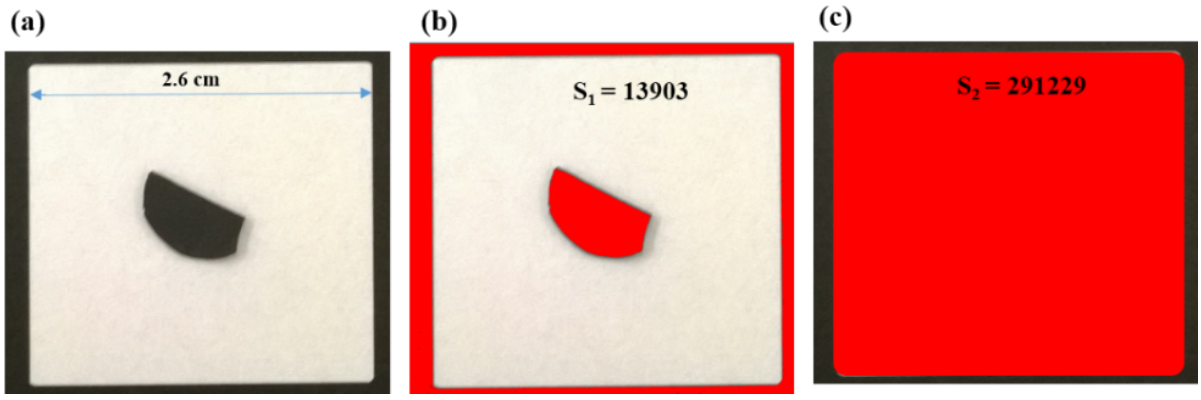

Figure 2.24 *(a) Digital photo of the pellet placed in the reference area, (b) counting of pixels in the sample, c) counting of pixels in the reference area.*

The electrochemical performances of our thick sintered LFP and LTO electrodes are compared with the literature as shown in table 2.3.

Table 2.3 Areal capacity values obtained for LFP/Li and LFP/LTO full cell compared with literature.

	Battery systems	**Thickness (mm)**	**C-rate**	**Areal Capacity (mAh/cm^2)**
References	LFP/G [51]	0.108	0.1	2.5
			0.2	2.4
			0.5	2.3
			1	2.2
			2	2.0
	NMC/G [51]	0.104	0.1	3.6
			0.2	3.4
			0.5	3.3
			1	3.2
			2	2.6
	LCO/Si [52]	0.070	0.1	1.9
	Si/Li [52]	0.006	0.1	4.0
	LFP/G [53]	0.124	0.1	2.1
Our work	LFP/Li	1.0	0.05	20.3
			0.1	12.08
			0.2	6.94
			0.5	1.67
			1	0.0003
	LTO/Li	1.0	0.016	25.45
			0.033	21.2
			0.06	12.7
			0.16	2.82
			0.33	0.8
	LFP/LTO	1.0	0.05	20

2.6 References

[1] M. Omori, "Sintering, consolidation, reaction and crystal growth by the spark plasma system (SPS)," *Mater. Sci. Eng. A*, vol. 287, no. 2, pp. 183–188, 2000.

[2] S. Z. Jin, H. L. Zhang, J. F. Li, and S. S. Jia, "TiB2/AlN/Cu Functionally Graded Materials (FGMs) Fabricated by Spark Plasma Sintering (SPS) Method," *Key Eng. Mater.*, vol. 280–283, pp. 1881–1884, 2005.

[3] M. Nygren and Z. Shen, "On the preparation of bio-, nano- and structural ceramics and composites by spark plasma sintering," *Solid State Sci.*, vol. 5, no. 1, pp. 125–131, Jan. 2003.

[4] A. Mukhopadhyay and B. Basu, "Consolidation–microstructure–property relationships in bulk nanoceramics and ceramic nanocomposites: a review," *Int. Mater. Rev.*, vol. 52, no. 5, pp. 257–288, Sep. 2007.

[5] R. Orrù, R. Licheri, A. M. Locci, A. Cincotti, and G. Cao, "Consolidation/synthesis of materials by electric current activated/assisted sintering," *Mater. Sci. Eng. R Rep.*, vol. 63, no. 4–6, pp. 127–287, Feb. 2009.

[6] D. Jain, K. M. Reddy, A. Mukhopadhyay, and B. Basu, "Achieving uniform microstructure and superior mechanical properties in ultrafine grained TiB2–TiSi2 composites using innovative multi stage spark plasma sintering," *Mater. Sci. Eng. A*, vol. 528, no. 1, pp. 200–207, Nov. 2010.

[7] J. Galy, M. Dolle, T. Hungria, P. Rozier, and J.-P. Monchoux, "A new way to make solid state chemistry: Spark plasma synthesis of copper or silver vanadium oxide bronzes," *Solid State Sci.*, vol. 10, no. 8, pp. 976–981, Aug. 2008.

[8] J. R. Groza, J. D. Curtis, and M. Krämer, "Field-Assisted Sintering of Nanocrystalline Titanium Nitride," *J. Am. Ceram. Soc.*, vol. 83, no. 5, pp. 1281–1283, May 2000.

[9] R. Van Noorden, "A better battery," *Nature*, vol. 507, no. 7490, p. 26, 2014.

[10] T. Takeuchi *et al.*, "Preparation of dense LiFePO4/C composite positive electrodes using spark-plasma-sintering process," *J. Power Sources*, vol. 146, no. 1–2, pp. 575–579, Aug. 2005.

[11] X. Zhang, Y. Liu, J. Ye, and R. Zhu, "Fabrication of Ti4O7 electrodes by spark plasma sintering," *Mater. Lett.*, vol. 114, pp. 34–36, Jan. 2014.

[12] G. Delaizir *et al.*, "The Stone Age Revisited: Building a Monolithic Inorganic Lithium-Ion Battery," *Adv. Funct. Mater.*, vol. 22, no. 10, pp. 2140–2147, May 2012.

[13] A. Aboulaich *et al.*, "A New Approach to Develop Safe All-Inorganic Monolithic Li-Ion Batteries," *Adv. Energy Mater.*, vol. 1, no. 2, pp. 179–183, Mar. 2011.

[14] F. Lalère *et al.*, "An all-solid state NASICON sodium battery operating at 200 °C," *J. Power Sources*, vol. 247, pp. 975–980, Feb. 2014.

[15] X. Dong, F. Lü, L. Yang, Y. Zhang, and X. Wang, "Influence of spark plasma sintering temperature on electrochemical performance of La0.80Mg0.20Ni3.75 alloy," *Mater. Chem. Phys.*, vol. 112, no. 2, pp. 596–602, Dec. 2008.

[16] K. Amezawa, Y. Nishikawa, Y. Tomii, and N. Yamamoto, "Electrical and Mechanical Properties of Sr-Doped LaPO4 Prepared by Spark Plasma Sintering," *J. Electrochem. Soc.*, vol. 152, no. 6, pp. A1060–A1067, Jan. 2005.

[17] T. Takeuchi, M. Tabuchi, A. Nakashima, H. Kageyama, and K. Tatsumi, "Preparation of Dense Li1.05Mn1.95O4 / C Composite Positive Electrodes Using Spark-Plasma-Sintering-Process," *Electrochem. Solid-State Lett.*, vol. 8, no. 4, pp. A195–A198, Jan. 2005.

[18] B. Daffos, G. Chevallier, C. Estournès, and P. Simon, "Spark plasma sintered carbon electrodes for electrical double layer capacitor applications," *J. Power Sources*, vol. 196, no. 3, pp. 1620–1625, Feb. 2011.

[19] P. P. Prosini, M. Carewska, S. Scaccia, P. Wisniewski, S. Passerini, and M. Pasquali, "A New Synthetic Route for Preparing LiFePO[sub 4] with Enhanced Electrochemical Performance," *J. Electrochem. Soc.*, vol. 149, no. 7, p. A886, 2002.
[20] J. Galy, M. Dolle, T. Hungria, P. Rozier, and J.-P. Monchoux, "A new way to make solid state chemistry: Spark plasma synthesis of copper or silver vanadium oxide bronzes," *Solid State Sci.*, vol. 10, no. 8, pp. 976–981, Aug. 2008.
[21] S. Okada, M. Ueno, Y. Uebou, and J. Yamaki, "Fluoride phosphate Li2CoPO4F as a high-voltage cathode in Li-ion batteries," *J. Power Sources*, vol. 146, no. 1–2, pp. 565–569, Aug. 2005.
[22] Y. Arachi, Y. Higuchi, R. Nakamura, Y. Takagi, and M. Tabuchi, "Synthesis and electrical property of Li2−xFeSi1−xPxO4 as positive electrodes by spark-plasma-sintering process," *J. Power Sources*, vol. 244, pp. 631–635, Dec. 2013.
[23] E. Dumont-Botto, C. Bourbon, S. Patoux, P. Rozier, and M. Dolle, "Synthesis by Spark Plasma Sintering: A new way to obtain electrode materials for lithium ion batteries," *J. Power Sources*, vol. 196, no. 4, pp. 2274–2278, Feb. 2011.
[24] Z. Li, W. Wang, Z. Li, Z. Qin, J. Wang, and Z. Liu, "Bridging porous Si–C composites with conducting agents for improving battery cycle life," *J. Power Sources*, vol. 286, no. Supplement C, pp. 534–539, Jul. 2015.
[25] W. Lai *et al.*, "Ultrahigh-Energy-Density Microbatteries Enabled by New Electrode Architecture and Micropackaging Design," *Adv. Mater.*, vol. 22, no. 20, pp. E139–E144, May 2010.
[26] T. Annen and M. Epple, "A facile synthesis of dispersable NaCl nanocrystals," *Dalton Trans.*, no. 44, p. 9731, 2009.
[27] K. Park, J.-S. Kim, and A. L. Miller, "A study on effects of size and structure on hygroscopicity of nanoparticles using a tandem differential mobility analyzer and TEM," *J. Nanoparticle Res.*, vol. 11, no. 1, pp. 175–183, Jan. 2009.
[28] S. Range and M. Epple, "Nanoscopic NaCl crystals as water-soluble porogens for polymer membranes," *RSC Adv.*, vol. 2, no. 16, p. 6650, 2012.
[29] C. Gaillard, J. F. Despois, and A. Mortensen, "Processing of NaCl powders of controlled size and shape for the microstructural tailoring of aluminium foams," *Mater. Sci. Eng. A*, vol. 374, no. 1–2, pp. 250–262, Jun. 2004.
[30] C. Gaillard, J. F. Despois, and A. Mortensen, "Processing of NaCl powders of controlled size and shape for the microstructural tailoring of aluminium foams," *Mater. Sci. Eng. A*, vol. 374, no. 1–2, pp. 250–262, Jun. 2004.
[31] T. Annen and M. Epple, "A facile synthesis of dispersable NaCl nanocrystals," *Dalton Trans.*, no. 44, p. 9731, 2009.
[32] S. Range and M. Epple, "Nanoscopic NaCl crystals as water-soluble porogens for polymer membranes," *RSC Adv.*, vol. 2, no. 16, p. 6650, 2012.
[33] G. Biskos, A. Malinowski, L. M. Russell, P. R. Buseck, and S. T. Martin, "Nanosize Effect on the Deliquescence and the Efflorescence of Sodium Chloride Particles," *Aerosol Sci. Technol.*, vol. 40, no. 2, pp. 97–106, Feb. 2006.
[34] A. Lähde, J. Raula, and E. I. Kauppinen, "Combined synthesis and in situ coating of nanoparticles in the gas phase," *J. Nanoparticle Res.*, vol. 10, no. S1, pp. 121–130, Dec. 2008.
[35] S.-L. Chung, C.-W. Chang, and F. J. C. S. Aires, "Reaction mechanism in combustion synthesis of α-Si3N4 powder using NaN3," *J. Mater. Res.*, vol. 23, no. 10, pp. 2720–2726, Oct. 2008.
[36] H. Bi *et al.*, "Study of LiFePO4 cathode modified by graphene sheets for high-performance lithium ion batteries," *Electrochimica Acta*, vol. 88, pp. 414–420, Jan. 2013.
[37] M. Chen *et al.*, "Porous α-Fe2O3 nanorods supported on carbon nanotubes-graphene foam as superior anode for lithium ion batteries," *Nano Energy*, vol. 9, pp. 364–372, Oct. 2014.

[38] K.-S. Park, S. B. Schougaard, and J. B. Goodenough, "Conducting-Polymer/Iron-Redox- Couple Composite Cathodes for Lithium Secondary Batteries," *Adv. Mater.*, vol. 19, no. 6, pp. 848–851, Mar. 2007.
[39] Y. Hu, X. Li, J. Wang, R. Li, and X. Sun, "Free-standing graphene–carbon nanotube hybrid papers used as current collector and binder free anodes for lithium ion batteries," *J. Power Sources*, vol. 237, pp. 41–46, Sep. 2013.
[40] L. Wang, X. He, W. Sun, J. Wang, Y. Li, and S. Fan, "Crystal Orientation Tuning of LiFePO4 Nanoplates for High Rate Lithium Battery Cathode Materials," *Nano Lett.*, vol. 12, no. 11, pp. 5632–5636, Nov. 2012.
[41] N. Li, G. Zhou, F. Li, L. Wen, and H.-M. Cheng, "A Self-Standing and Flexible Electrode of Li4Ti5O12 Nanosheets with a N-Doped Carbon Coating for High Rate Lithium Ion Batteries," *Adv. Funct. Mater.*, vol. 23, no. 43, pp. 5429–5435, Nov. 2013.
[42] X. Meng, B. Han, Y. Wang, and J. Nan, "Effects of samarium doping on the electrochemical performance of LiFePO4/C cathode material for lithium-ion batteries," *Ceram. Int.*, vol. 42, no. 2, pp. 2599–2604, Feb. 2016.
[43] M. Gaberscek, R. Dominko, M. Bele, M. Remskar, D. Hanzel, and J. Jamnik, "Porous, carbon-decorated LiFePO4 prepared by sol–gel method based on citric acid," *Solid State Ion.*, vol. 176, no. 19, pp. 1801–1805, Jun. 2005.
[44] R. Dominko *et al.*, "Porous olivine composites synthesized by sol–gel technique," *J. Power Sources*, vol. 153, no. 2, pp. 274–280, Feb. 2006.
[45] F. Wang, J. Chen, M. Wu, and B. Yi, "Propylene oxide-assisted fast sol–gel synthesis of mesoporous and nano-structured LiFePO<Subscript>4</Subscript>/C cathode materials," *Ionics*, vol. 19, no. 3, pp. 451–460, Mar. 2013.
[46] A. Jena, H. Sanders, J. Miller, and R. Wimberly, "Comparison of mercury porosimetry and flow porometry for the testing of battery separator materials," in *Sixteenth Annual Battery Conference on Applications and Advances. Proceedings of the Conference (Cat. No.01TH8533)*, 2001, pp. 71–75.
[47] "Electrode Analysis | Micromeritics." [Online]. Available: http://www.micromeritics.com/Product-Showcase/Battery-Technology/Electrode-Analysis.aspx. [Accessed: 08-Feb-2018].
[48] X. Qin, X. Wang, J. Xie, and L. Wen, "Hierarchically porous and conductive LiFePO4 bulk electrode: binder-free and ultrahigh volumetric capacity Li-ion cathode," *J. Mater. Chem.*, vol. 21, no. 33, p. 12444, 2011.
[49] R. Elango, A. Demortière, V. De Andrade, M. Morcrette, and V. Seznec, "Thick Binder-Free Electrodes for Li-Ion Battery Fabricated Using Templating Approach and Spark Plasma Sintering Reveals High Areal Capacity," *Adv. Energy Mater.*, p. 1703031, Jan. 2018.
[50] X. Sun, P. V. Radovanovic, and B. Cui, "Advances in spinel Li $_4$ Ti $_5$ O $_{12}$ anode materials for lithium-ion batteries," *New J Chem*, vol. 39, no. 1, pp. 38–63, 2015.
[51] H. Zheng, J. Li, X. Song, G. Liu, and V. S. Battaglia, "A comprehensive understanding of electrode thickness effects on the electrochemical performances of Li-ion battery cathodes," *Electrochimica Acta*, vol. 71, pp. 258–265, Jun. 2012.
[52] J. Yin, M. Wada, K. Yamamoto, Y. Kitano, S. Tanase, and T. Sakai, "Micrometer-Scale Amorphous Si Thin-Film Electrodes Fabricated by Electron-Beam Deposition for Li-Ion Batteries," *J. Electrochem. Soc.*, vol. 153, no. 3, p. A472, 2006.
[53] S. Yu, Y. Chung, M. S. Song, J. H. Nam, and W. I. Cho, "Investigation of design parameter effects on high current performance of lithium-ion cells with LiFePO4/graphite electrodes," *J. Appl. Electrochem.*, vol. 42, no. 6, pp. 443–453, Jun. 2012.

Chapter 3

Optimization of thick $LiFePO_4$ electrode parameters prepared using SPS and templating approach

The overall Li-ion battery performance is dependent on many factors such as active materials, cell design, pack design, temperature and type of charging methodologies [1]–[6]. Out of which, the optimization of the electrode microstructural parameters is one of the essential requirements to achieve superior battery performance. The cell engineering is equally important, as is finding new materials with high potential or high specific capacity to increase the energy density. In Li-ion batteries, the electrodes are made up of porous microstructures in which the mass transport is mainly controlled by the microstructural characteristics such as electrode porosity, pore size and tortuosity. Electrolyte intrinsic properties such as ionic conductivity, salt diffusion coefficient, transference number are measured with the assumption of simplified cell design [3], [7], [8] which is helpful to increase the accuracy of the models. Various modeling works have been done to predict the power limitations of an actual electrode design such as Newman's model that relies on the porous electrode theory [9]. The porous electrode is considered as a superposition of liquid and solid phases that are defined by their respective volume fraction and interfacial surface area. Over the past 20 years, Newman and his co-workers simulated the battery performance by updating the effects of several parameters such as temperature, electrolyte properties and studying the macroscopic electrochemical behavior of porous electrodes [10], [11].

In this chapter, the influence of critical LFP electrode parameters such as average pore size, pore size distribution, porosity, electrode thickness on the electrochemical performance were studied and the overall summary is shown in figure 3.1 for a better clarity. First, in our approach, the effects of pore size in 1-mm thick LFP electrodes are studied by using different sizes of salt particles as templating agent. The pore volume fraction is kept constant at 44% for the three LFP electrodes. The rate capability of the electrodes was tested for the three LFP electrodes and the impact of ionic resistance due to varied pore size distribution is measured using electrical impedance spectroscopy with a symmetrical cell approach. μCT-TXM analysis was also performed for three pore sized LFP electrodes to determine 3D morphological parameters, especially the tortuosity values, which are compared with EIS-SC approach. Tomography analysis also includes the determination of porosity and tortuosity distribution inside the specified volume of thick electrodes. Tomography analysis using Tau factor software helps to identify the heterogeneities present in the thick electrodes due to difference in pore size distribution created by templating method. In general, the electrode porosity for commercial Li-ion batteries is around 30-40 %. However, this porosity range may be varied according to the electrical and ionic properties of the active materials. Higher porosity values above this range will lead to a massive decrease in volumetric energy density due to the decrease of the volume of active materials and increase in electrical resistivity of active

materials due to low active material content. At the same time, lower porosity values will lead to higher ionic resistance causing poor liquid electrolyte diffusion to the bulk electrodes. For the conventional film based Li-ion batteries, the electrode porosity are adjusted by varying the calendaring pressure applied on the film coated electrodes. This will control the thickness and density of the electrodes. As discussed in the chapter 1, the overall energy density of the batteries can be improved to a greater extent by increasing the thickness of the electrode. But, effectiveness of thick electrodes is feasible only when there is good pore interconnectivity and appropriate amount of pores for lithium to diffuse. It is well known that charge and ionic transport are limited by the current rate especially for thick electrodes. So, the mass transport limitations are studied by preparing three 1-mm thick LFP electrodes with same pore size but three different porosity values obtained by the templating method. Finally, a systematic study of the effect of electrode thickness or active material loading was done for LFP electrodes to understand the effect of active material loading and corresponding mass transport limitations of the thick LFP sintered electrodes.

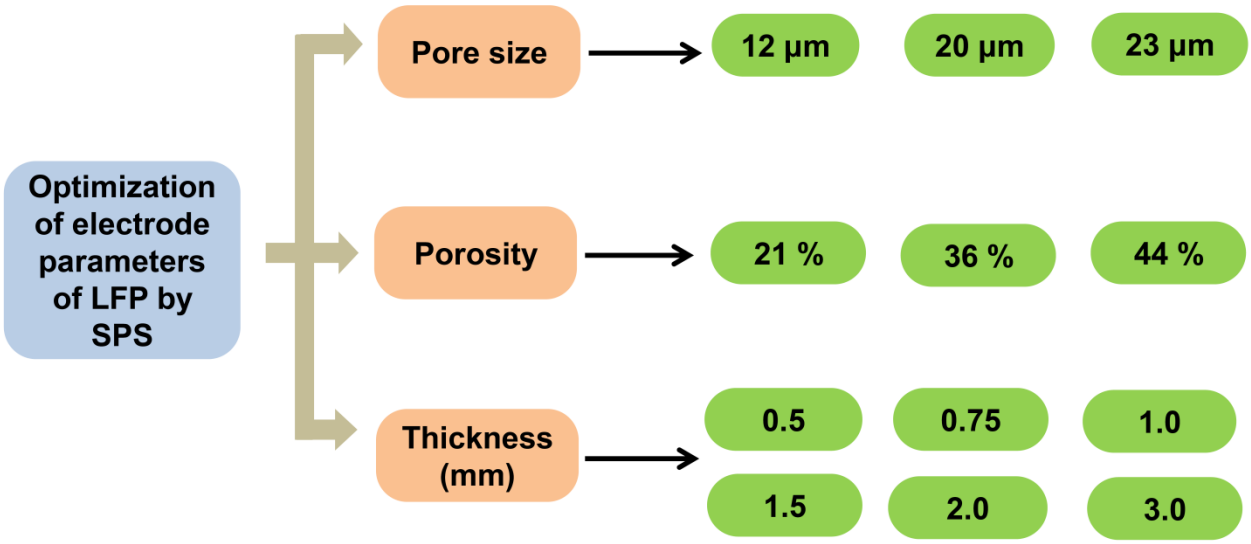

Figure 3.1 *Schematic of optimization of electrode parameters for the thick binder free LFP electrodes obtained using SPS and templating approach.*

3.1 Effect of electrode pore size for 40% porous LFP electrodes

The influence of mean pore size and pore size distribution was studied for many electrochemical systems such as super capacitors, Li-ion and lithium air batteries to optimize the electrochemical performance [12]–[14]. In Li-ion batteries, the electrode topology control such as ordered macro-porous structures with defined pore size and hierarchical pore size distributions is more important to achieve high rate capability [15]. The uniform particle size distribution of pore forming agents is crucial to maintain homogeneity in the pore size distribution of the porous electrodes for Li-ion batteries. In this chapter, three different particle sizes of NaCl cubic crystals are used as templating agents. To understand the effect of pore size distribution, the composition of LFP particles, NaCl and sp-Carbon (50-40-10 vol.%) in the composite are kept constant. The electrode thickness is maintained at 1-mm with an electrode porosity of 44%. The slight increase in porosity compared to the initial volume fraction of templating agent is due to the closed pores obtained after the SPS densification.

3.1.1 Synthesis of NaCl crystals

Three different average particle sized salt crystals are prepared with three different preparation methods. First of all, the chemical synthesis of NaCl crystals was done using acetyl chloride and sodium acetate as reactants, as prepared in the literature [16]. Initially, the 2 g of sodium acetate are taken with 10 ml of ethanol in a round bottomed flask. Later, 20 ml of acetyl chloride are added drop-wise with the simultaneous stirring of the solution. Acetyl chloride acts as a strong donor of chlorine which reacts with sodium acetate forming sodium chloride crystals with the evolution of HCl gas. After a few minutes, NaCl particles are well formed with a slight increase in temperature of the solution and absolute ethanol (99.9% pure) is added to cool down the mixture. Finally, the solution is centrifuged at 6000 rpm for three times with subsequent washing with ethanol and the final product was dried in oven at 70 °C for overnight. SEM images of as prepared sodium chloride crystals (Figure 3.2a) show well defined cubic shape and the average particle size of 2 ± 0.6 μm was determined using FIJI software.

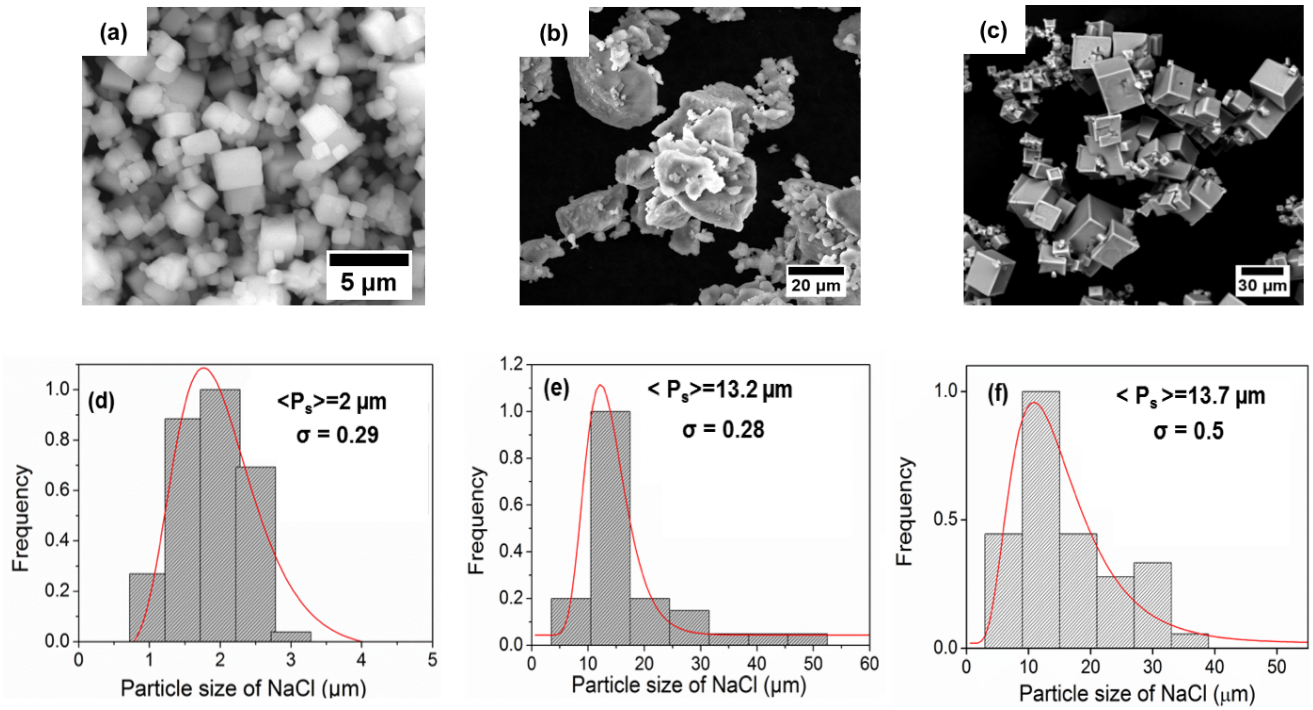

Figure 3.2 *(a-c) SEM images of NaCl particles prepared by three methods. (d-f) Corresponding particle size distribution obtained for the three NaCl crystals using FIJI software and fitted with log- normal distribution.*

Second**,** the as received commercial salt particles are crushed for 20 minutes using a mortar and the crushed salt particles are shown in figure 3.2b. The average particle size was 13.2 ± 3.7 µm measured using FIJI software. Third, evaporative crystallization was adopted to prepare NaCl crystals (Fig.3.2c) with an average particle size of 13.7± 6.85 µm and the experimental procedure was already described in chapter 2. The particle size distribution of three NaCl crystals prepared is shown in figure 3.2d and the average and standard deviation are obtained by fitting with log-normal distribution function.

The LFP-NaCl-C composite preparation, densification by SPS and dissolution of templating agents were done as explained in chapter 2. The same SPS parameters of the LFP-NaCl-C powder composite were applied for the three LFP electrodes *i.e.* a temperature of 650 °C, 10 kN pressure and 5 minutes holding time. The compactness of the LFP-NaCl-C pellet is found as 94% irrespective of the different particle sizes of NaCl crystals used in the composite. Later, the NaCl particles are dissolved completely by water thereby creating pores in the LFP electrode using the vacuum dissolution method. The physical properties of the three LFP electrodes prepared with different average pore sizes are written in table 3.1. The pore size distribution of the three LFP electrodes is obtained from the tomography analysis (discussed later) and the average pore size is found to be 12 ± 2 µm, 20 ± 8 µm and 23 ± 9 µm respectively and the results

are shown in figure 3.4. These average pore size values are denoted in the rest of this chapter for comparison. A slight difference in initial particle size of NaCl crystals and electrode pore size is obtained which may arise due to the agglomeration of salt particles present in the composite and porous electrode after NaCl dissolution.

Table 3.1 Physical properties of three different pore sized LFP electrodes fabricated using SPS.

Average NaCl particle size used (μm)	2.0 ± 0.6	13.2 ± 3.7	13.7 ± 6.8
Average electrode pore size (μm)	12 ± 2.0	20 ± 8.0	23 ± 9.0
Compacity (%)	93.0	93.8	94.0
Porosity (%)	45.2	43.7	44.0
Thickness (mm)	1.01	1.01	0.99
Active material loading (mg/cm^2)	165	165	165

From the SEM images of thick LFP electrodes as shown in figure 3.3, the cubic pore shape and pore size due to the dissolution of pore forming agents are clearly observed in the surface and cross section view. The average pore spacing is reduced for 12 μm than 20 μm and 23 μm pore sized LFP electrodes as clearly observed in figure 3.3a-c. The cross section of the thick electrodes (Fig.3.3 e-g) shows an elongation of cylindrical pores in z-direction which is due to the uniaxial pressing of the electrodes. This anisotropy was clearly displayed in 20 μm and 23 μm pore sized LFP electrodes due to the bigger salt particles used as pore forming agent. As shown in figure 3.3a-c, the average pore spacing or the midpoint of the two individual pores are greatly minimized for 12 μm sized pores leading to better connectivity of pores compared to 20 μm and 23 μm average pore sized LFP electrodes. Thus, we can expect the closer arrangement of uniform pores in 12 μm pore sized LFP electrodes will lead to the faster Li-ion diffusivity in the liquid phase thereby better rate capability.

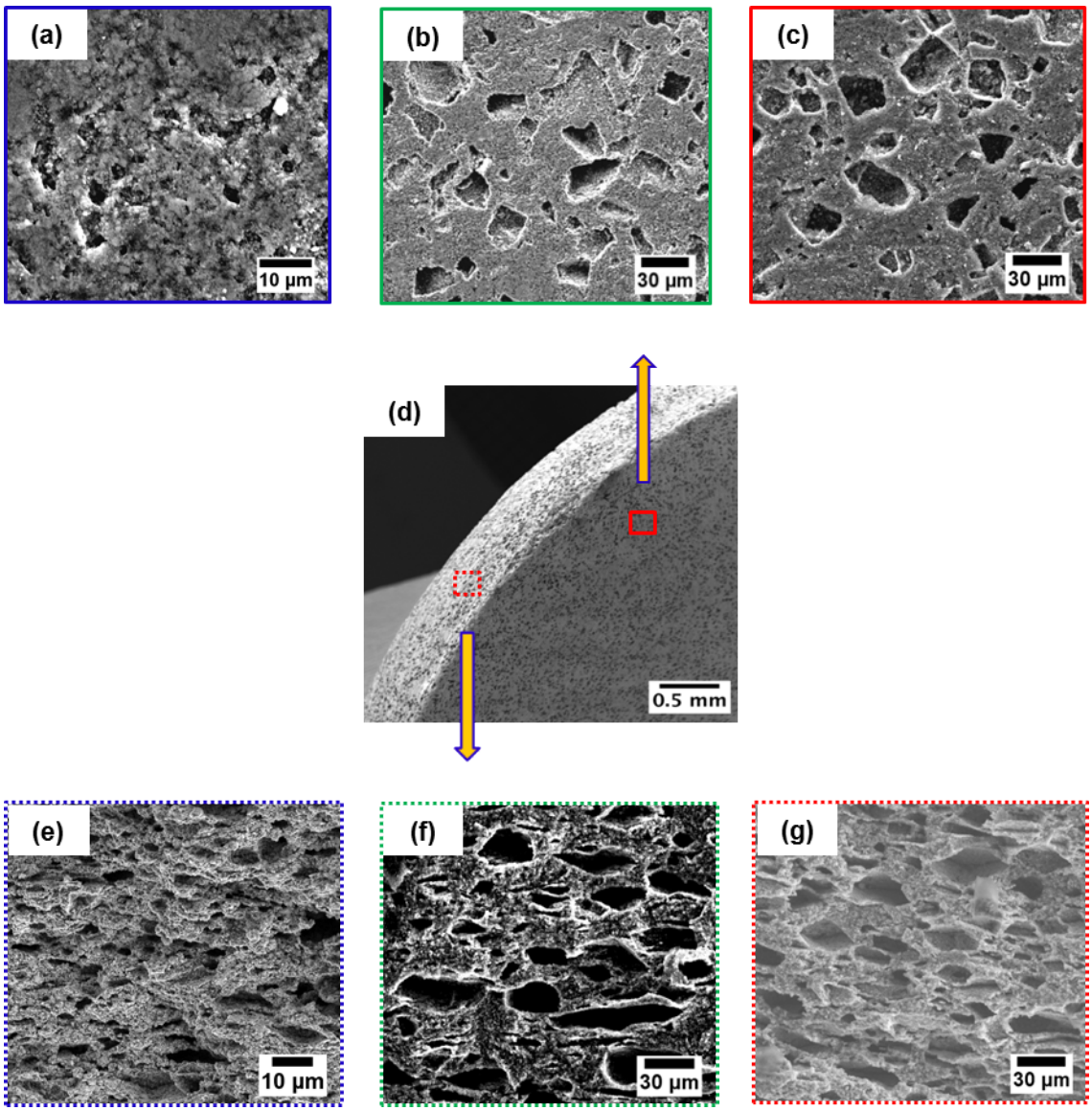

Figure 3.3 *SEM images of porous LFP electrodes containing the pores created by the NaCl dissolution. (a, b, c) top surface view of the electrodes showing the cubic shape of the crystals with corresponding sizes of the crystals used, (e,f,g) Cross section of thick LFP electrodes showing the pore shape aligned perpendicular to the z-direction due to the uniaxial pressing of SPS operation.*

3.1.2 Tomography analysis of the 1-mm thick LFP electrodes using µCT-FFTXM

Micro-computed tomography (µCT) analysis is an advanced characterization method for studying the morphology and transport phenomena of 3D structures such as battery and fuel cells [17], [18]. Tomography imaging analysis can provide qualitative as well as quantitative information of three-dimensional structures like electrodes of Li-ion battery electrodes in which SEM images could not provide 3D view. In our work, µCT tomography measurements of thick binder free LFP electrodes are carried out at the synchrotron source at Advanced Photon Source (APS) in Argonne National Laboratory (ANL, USA) in the beamline 32ID with the Full Field Transmission X-ray Microscopy setup. The experimental setup of the X-ray computed tomography mainly consists of TXM optical X-ray line with condenser, pinhole, zone plate, rotary stage, scintillator and CCD camera. Transmission images are collected by rotating the electrode sample at discrete angular steps from 0° to 180° at a beam time of 5 minutes. The 1-mm thick electrode is characterized with nearly 1200 images generated at an angular step of 0.15°. In the µCT mode, the field of view is 1-mm with a spatial resolution of 1.3 µm. The detailed description and experimental setup is reported in annexe and in this literature [19]. The tomography data set acquired as a function of the rotation angle is reconstructed into a XYZ dataset using a back projection method based on Radon transformation. The reconstruction of the tomogram was done using APS python library in Tomopy. The segmentation was done using FIJI® software. The TXM and binary images after thresholding step of the three LFP electrodes in z direction are seen in figure 3.4d-f. In our work, the 3D reconstructed images of the LFP electrodes are illustrated by AMIRA software [20] as shown in figure 3.7a-c. This clearly distinguishes the solid matter and the pores (yellow in fig.3.7a-c) and found that the pores are well distributed throughout the entire volume of the electrodes.

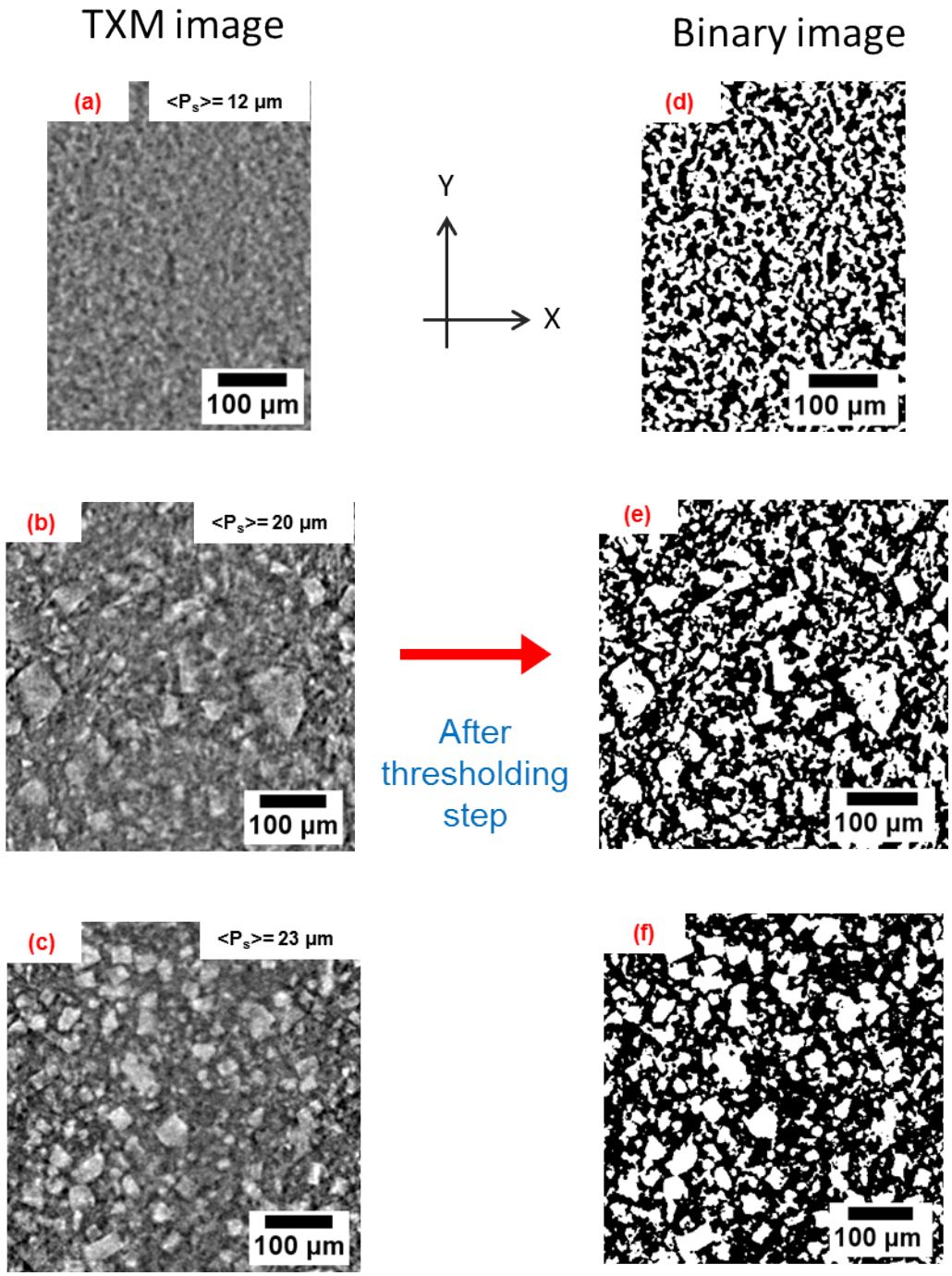

Figure 3.4.*a-c) 2D-TXM images of 12 µm, 20 µm and 23 µm average pore sized LFP electrode, d-f) corresponding thresholded image of the electrodes showing pores in white and solid as black.*

The pore tortuosity in the porous electrodes is one of the important properties leading to high macroscopic ohmic resistance thereby affecting the energy and power density of Li-ion batteries. Tortuosity is a measure of elongation of the transport path due to the convoluted porous structure with respect to the

straight distance $\left(\boldsymbol{\mathcal{T}} = \frac{L_p}{L_{cv}}\right)$ as shown in figure 3.5. Geometrically, tortuosity can be defined as the ratio of the average ion diffusion length to the electrode thickness $\left(\boldsymbol{\mathcal{T}} = \frac{l}{L}\right)$ where l is average ion diffusion length across the electrode and L is the electrode thickness (L). The schematic representation of tortuosity in a composite electrode is shown in figure 3.5. This significant parameter is highly dependent on the microstructural properties such as pore size, porosity and particle size distribution of the active materials present in the composite electrode.

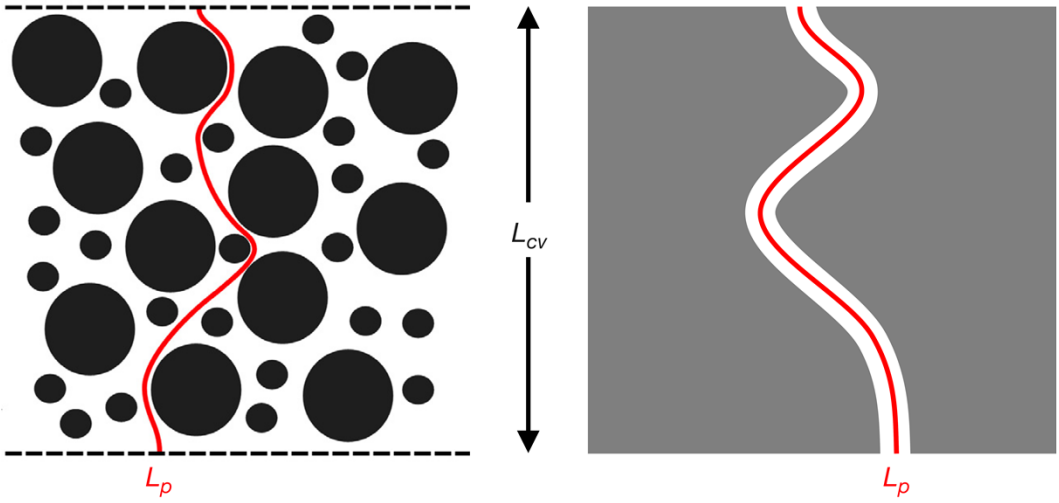

Figure 3.5 *a-b Geometrical tortuosity representation in the composite electrode showing the effective path length L_p and edge length of the control volume, L_{cv} ($\boldsymbol{\mathcal{T}} = L_p / L_{cv}$) [21].*

The determination of accurate values of tortuosity is so helpful to model the porous medium in a macroscopic way to assess the electrode performance. In the early 70s, the tortuosity of the porous electrodes was expressed with the classical Bruggeman relation ($\boldsymbol{\mathcal{T}} = \epsilon^{1-\beta}$) where $\boldsymbol{\mathcal{T}}$ is the tortuosity, ϵ is the electrode porosity and β is the Bruggeman coefficient [22]. For the spherical particles, the relation turned to ($\boldsymbol{\mathcal{T}} = \epsilon^{-0.5}$) as $\beta = 0.5$. However, the accuracy of this relation was missing, confirmed by various experimental methods for anisotropic particles based electrodes such as graphite [23].

First, Thorat et *al*. combined the polarization interrupt methods along with a numerical model to measure directly the tortuosity of LFP based active material films [24] by preparing different compositions and porosities. An empirical relation ($\boldsymbol{\mathcal{T}} = 1.8\epsilon^{-0.53}$) was obtained by fitting the tortuosity-porosity plot. Another method to measure tortuosity of electrode is by performing steady state diffusion simulations in

the reconstructed image stack obtained from tomography such as FIB/SEM and synchrotron transmission X-ray microscopy (TXM) [17], [25].

The pore network from the tomography data is extracted by fitting with spheres and cylinders by Blunt *et al*. [26], [27] as shown in figure 3.6b. First, the pore is assigned to every void voxel of the tomography data and expanded until the solid voxel is reached. Then, an iterative process is carried out to identify the cluster of overlapping pores called as pore families as shown in figure 3.6a. After the identification of two different pore families (i and j) connected by the bottleneck pores, effective pore are determined for each pore family. The total volume of each pore family is equal to the volume of the effective pore. The detailed description of the pore network model is reported in this literature [28]. The effective pore radii, cylinder radius and length of the overall electrode sample are extracted for the three LFP electrodes and the distribution of the pore dimensions are shown in figure 3.7d-f.

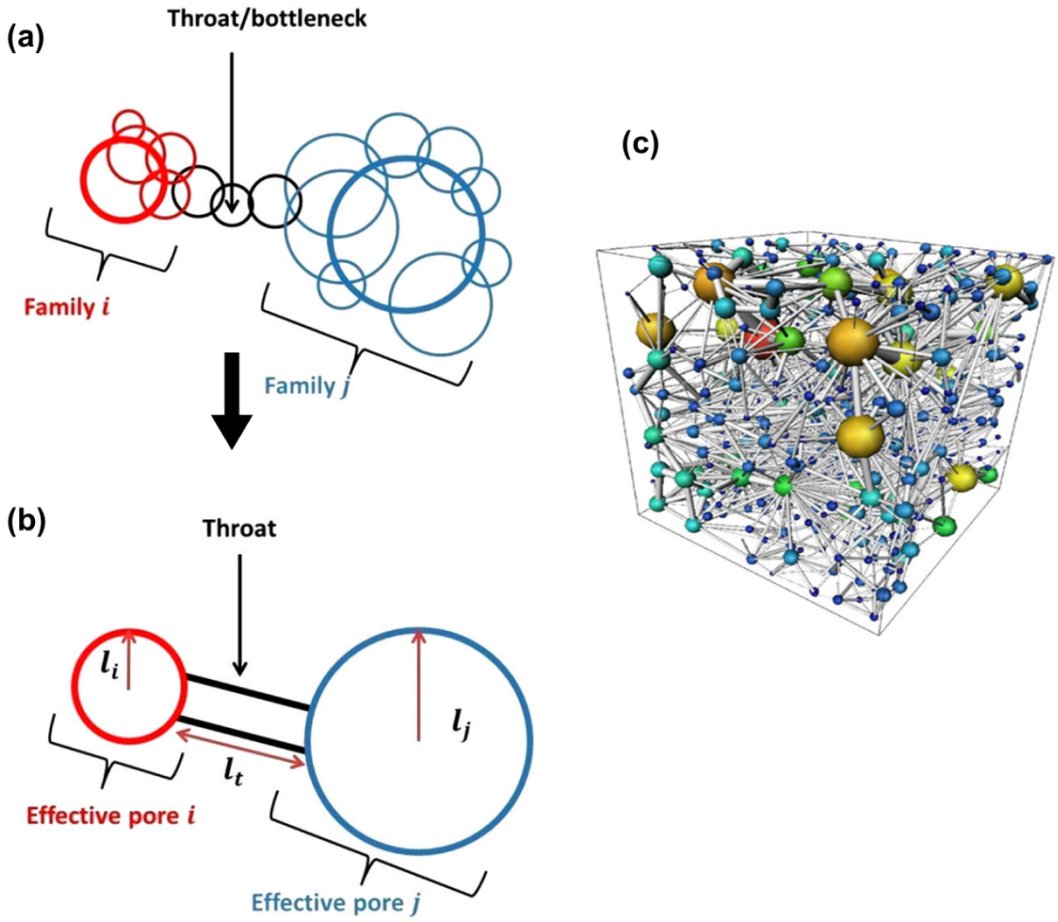

Figure 3.6.*a) Two pore families connected by the pore throat (b) Effective pores and throat obtained after assigning effective pore radii and throat lengths. b) Schematic showing the spheres and cylinders forming the interconnected pore network [26].*

Comparing the spherical pore radius (Figure 3.7d) between three different LFP electrodes, the narrow pore radius distribution is observed for 12 µm pore sized electrodes than other two electrodes with average pore sizes of 20 µm and 23 µm. In terms of cylinder length and radius also (Figure 3.7e-f), relatively narrow distribution is shown in figure 3.7e-f and well in-line with spherical pore radius distribution.

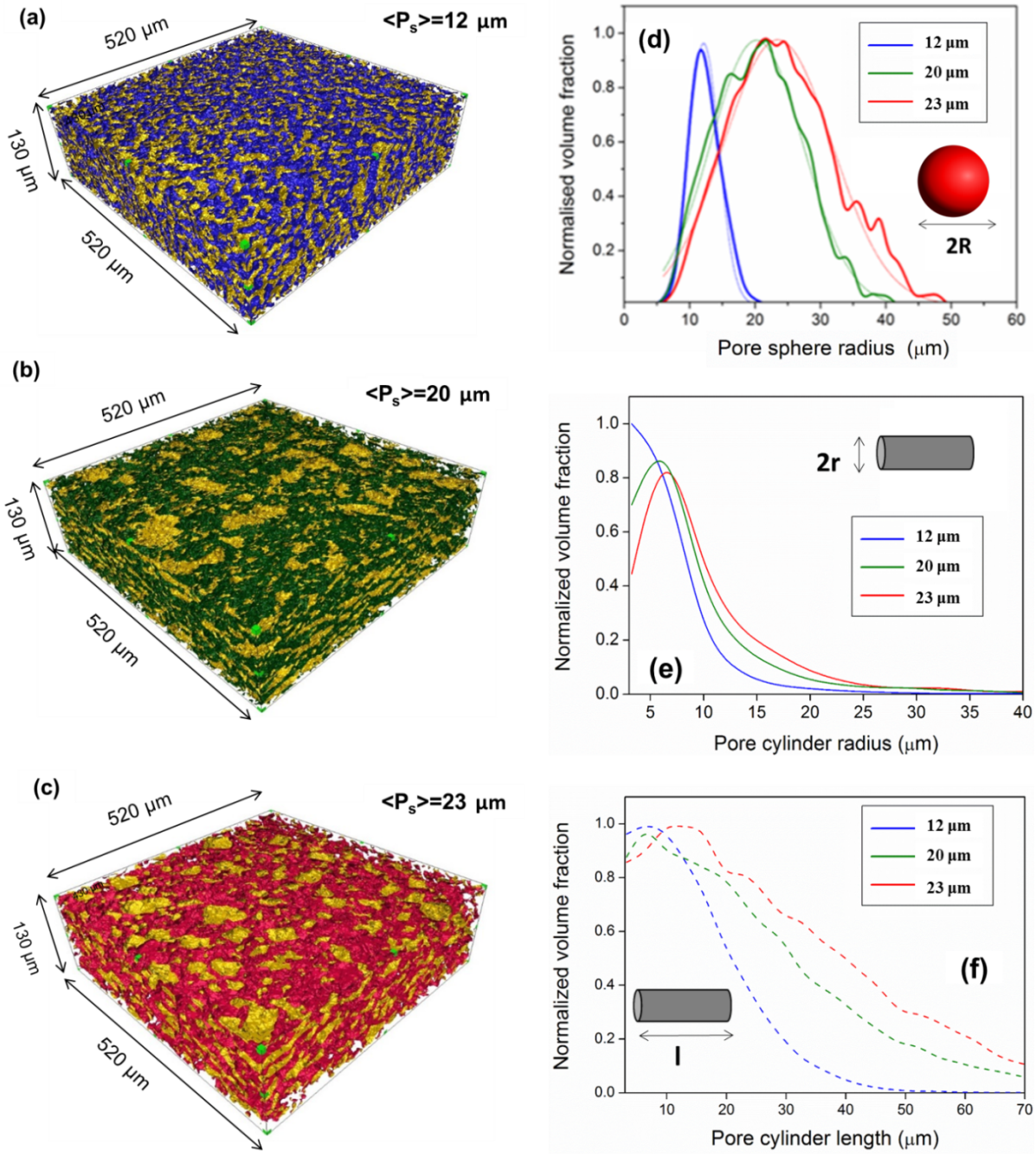

Figure 3.7 *3D reconstructed images of three 1-mm thick LFP electrodes using AMIRA software. d-e) The individual pore size distribution obtained by fitting as spheres and cylinders using Blunt algorithm.*

The ratio of volume of spheres to cylinders for 12, 20 and 23 µm pore sized LFP electrodes are 1: 2.7, 1: 2.9 and 1: 2.4 respectively. The microstructural properties such as open and closed porosity, pore size distribution, specific surface area of the three different LFP electrodes are determined using the pore network model as reported in the literature [28] and the values are written in table 3.2. The three LFP electrodes irrespective of pore size are showing less than 0.1% of closed pores (pore area surrounded only by solid region) out of total porosity proving that the templating approach is the most simple and effective method to achieve interconnected pore network in the sintered electrodes. No significant difference in specific surface area from 23 µm to 12 µm is determined from the tomography analysis as shown in the table 3.2. To compare these results, the theoretical calculations of the specific surface area (in m^2/g) for the 1-mm thick LFP electrode with 48% porosity and 12 µm pore size are shown in annexe and the specific surface area is found as 0.126 m^2/g which is one order higher than that deducted by tomography analysis (0.035 m^2/g). This underestimation of the specific surface area by the tomography method is due to the low spatial resolution of 1.3 µm in µ-CT mode. The pores less than 1.3 µm are taken into account for the specific surface area calculations.

Table 3.2: *Porosity, pore size and specific surface area values of 1-mm thick LFP electrodes are determined using pore network extraction model by Blunt et al. [26].*

Electrode average pore size $<P_s>$	**12 µm**	**20 µm**	**23 µm**
Total porosity (%)	47.91	45.02	43.70
Open porosity (%)	47.9	44.92	43.6
Closed Porosity (%)	0.01	0.10	0.107
Geo. density (g/cc)	1.83	1.80	1.80
Sp. surface Area (m^{-1})	64 156	58 288	47 868
Sp. surface area (m^2/g)-Tomo	0.035	0.032	0.027
Sp. surface area (m^2/g)-Theo.	0.126	0.068	0.042

Estimation of pore uniformity in an electrode volume:

The pore uniformity and interconnectivity in the entire volume of the thick electrode is very important in order to achieve high rate capability. The tomography analysis is widely used to quantify the porosity and solid matter throughout the thick electrode with high precision. The geometrical method is used to determine the porous and solid region of the electrode from the thresholded image of the tomography data. In our work, the total volume of the image stack of each electrode is composed of 400 x 400 x 400 pixels. The pixel size (smallest unit of resolution) is 1.3 µm and the entire volume of the studied electrode is equivalent to 520 x 520 x 520 μm^3. Geometrically, the images at regular intervals (every 50 images) are selected for measuring the porosity from the image stack. For example, the threshold images from the image stack of 20 µm pore sized electrode is illustrated in figure 3.8a and the same study was done for the other two pore sized LFP electrodes. From figure 3.8 (b,c), a very small deviation of localized porosity values from the mean value was observed for 12 µm and 20 µm pore sized LFP electrodes as shown in figure 3.8 (b,c), whereas there is a higher deviation of porosity for the 24 µm pore sized LFP electrodes as a function of voxels (thickness), which shows poor interconnectivity of pores that can be correlated to the poor diffusion of lithium ions during cell operation.

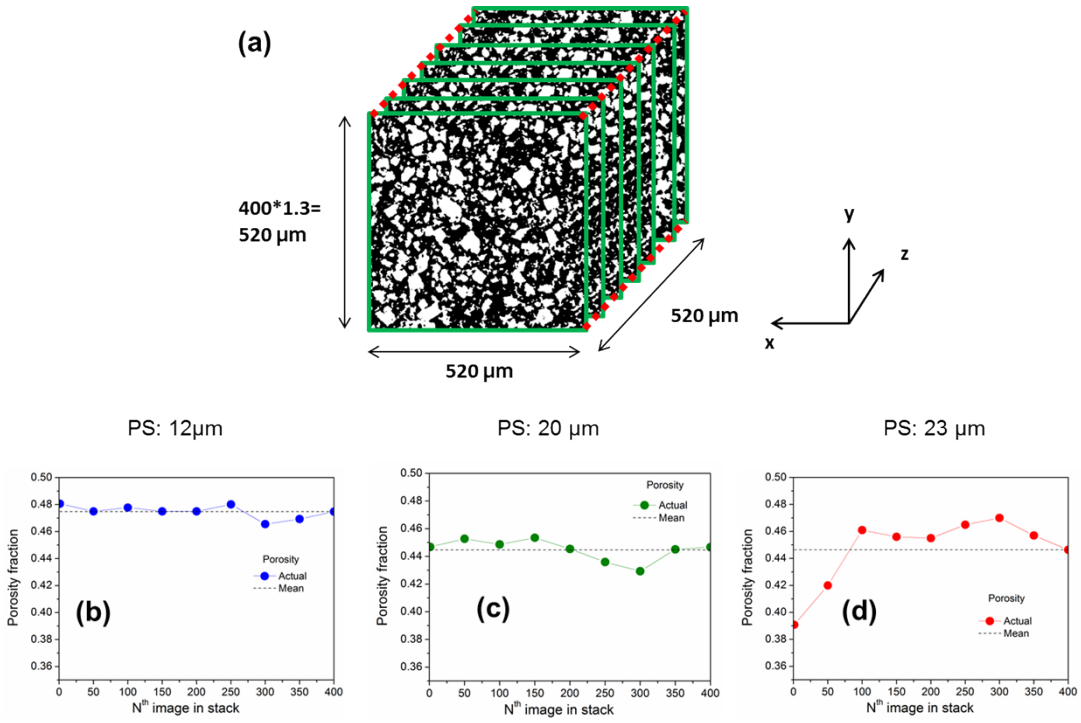

Figure 3.8 *Quantification of porosity values in the entire volume of the LFP electrode for three different LFP electrodes using geometrical method.*

Estimation of pore tortuosity in an electrode volume:

An important parameter called pore tortuosity of thick electrodes is determined in three orthogonal directions using Tau factor, a MATLAB application® developed by Cooper *et al.*, Imperial College of London,UK. This works was based on the Fick's law of diffusion [29] which states that the flux (*J*) is directly proportional to the concentration gradient (*dC/dx*). It involves the calculation of the reduction in diffusive transport due to convoluted electrode geometry of heterogeneous media based on microstructural image data. The solid state diffusion of lithium ion is eliminated. In other words, the tortuosity is determined by the ratio of steady state diffusive flow through a porous volume network to the fully dense control volume of electrode as shown in equation 3.3, where F_p and F_{cv} are flux through pore network and control volume, A_{cv} is cross sectional area, L_{cv} is length, D is diffusivity.

$$F_p = -A_{cv}D_{eff}\left(\frac{\Delta C}{L_{cv}}\right) \tag{3.1}$$

$$F_{cv} = -A_{cv}D\left(\frac{\Delta C}{L_{cv}}\right) \tag{3.2}$$

$$D_{eff} = D\left(\frac{\varepsilon}{\mathcal{T}^2}\right) \tag{3.3}$$

where D_{eff} is the effective diffusivity through a porous volume where one phase is conducting and the other phase is insulating, D is the intrinsic diffusivity of the conductive phase, ε is the volume fraction of conductive phase. The tortuosity in z-direction for 23 μm pore sized electrode was obtained using tau factor simulations software. The thresholded image stack is given as input for the tau factor application software. The report figure generated by the Tau factor is shown in Fig. 3.9. The three slices (Fig. 3.9a, b, c) represent the binary image of the sample (LFP electrode with 20 μm in z-direction) and the corresponding initial and steady state diffusion simulations performed in a local volume of the electrode. The distribution of concentration and flux in a slice of the volume is illustrated. Fig. 3.9d shows a graph of the effective diffusivity calculated at the top and bottom faces against iteration number. Convergence of the system was established by analyzing both the rate of change of top and base effective diffusivity values. The tortuosity of the as studied electrode in z-direction is 2.56 with phase volume fraction (ε) of 44.4% and effective diffusivity (D_{eff}) is 0.0678 m^2/s.

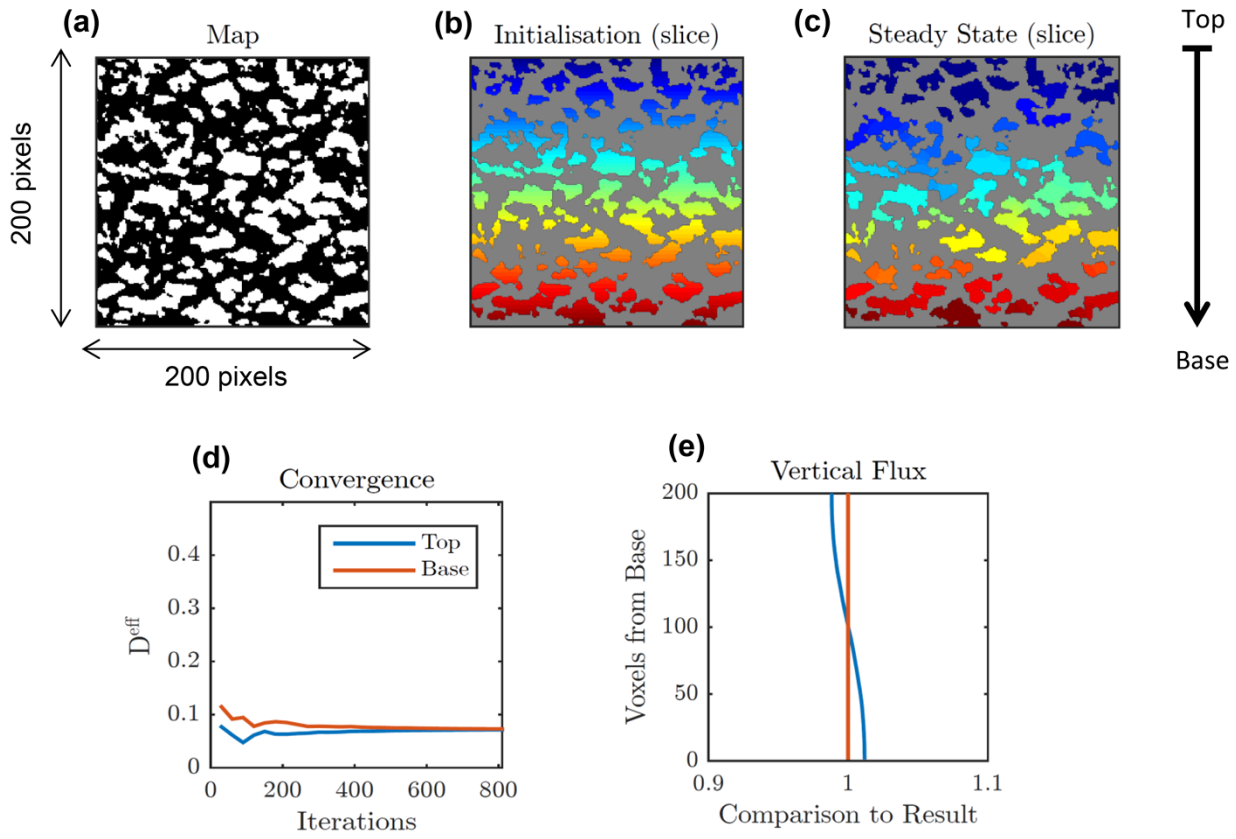

Figure 3.9 *Report figure of Tau factor software in MATLAB for 20 µm pore sized 1-mm thick LFP electrode: a) Thresholded image of LFP electrode (<P_s>=20 µm) showing pores (white) are elongated perpendicular to z-direction, b, c) Slice of initial and steady state diffusion simulations applied on the tomography data, d) Convergence of effective diffusion coefficient obtained in top and base of tomography image. e) The vertical flux is showing the deviation from the straight line from top to base.*

Clearly, Tau factor analysis allows carrying out fast and simple calculation of the tortuosity directly from the microstructural data. In addition, tau factor also provides microstructural parameters such as volume fraction, specific surface area and directional percolation fraction. The tau factor results reproduce the same results generated by the GEODICT software which works on the same principle of steady state diffusion simulations. These tortuosity analysis are helpful to compare the values obtained from different methods such as EIS, pore centroid and random walk method.

Next, tortuosity analysis of our thick electrodes was carried out by incrementing the sub-volume at regular intervals up to a total studied volume as shown in figure 3.10a. The representation of stacked .tiff files pore size of 23 µm is used for the diffusion simulations. The pore tortuosity in z-direction is stabilized after reaching a sufficient volume (150 voxels^3) for the three LFP electrodes as shown in figure 3.10 b, c, d. This study helps to report the distribution of local tortuosities instead of reporting a single

value for the whole electrode. From figure 3.10 c, d, the non-uniform pore size distribution of 20 and 23 µm pore sized electrodes will directly affect the tortuosities in z-direction showing higher value than the other two directions. Also, the z-axis tortuosity is almost the same as x-axis for the 12 µm pore sized LFP electrode and this anisotropy effect is more pronounced for the 20 µm pore sized LFP electrode which can be due to the bigger commercial salt particles used as templates in the electrode preparation. Characteristic tortuosity ($\mathcal{T}_c$) is an overall contribution of the tortuosity of electrodes by taking account of tortuosity in all three directions ($\mathcal{T}_x, \mathcal{T}_y$ *and* $\mathcal{T}_Z$) as written in equation 3.4.

$$\mathcal{T}_C = 3[(\mathcal{T}_X{}^{-1}) + (\mathcal{T}_Y{}^{-1}) + (\mathcal{T}_Z{}^{-1})]^{-1} \tag{3.4}$$

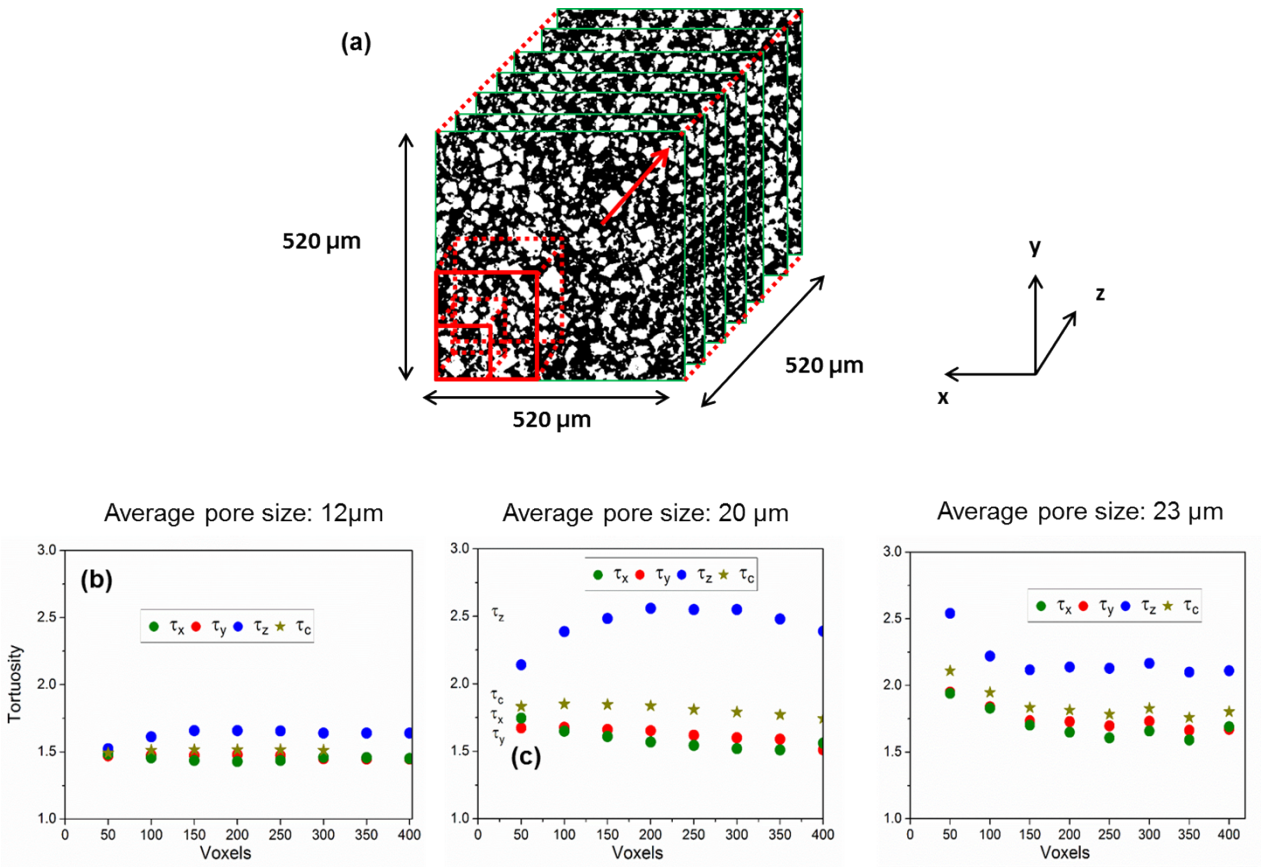

Figure 3.10 *Scale effect of the three 1-mm thick LFP electrode showing the tortuosity values determined from each sub section. Tortuosity stabilization was obtained after 150 voxels for 23 µm pore sized LFP electrode in 3.8d.*

To analyze further, the definite volume of LFP electrode (520x520x520 μm^3) is divided into 8 smaller sub-sections with equal cubic volumes (130x130x130 μm^3) as shown in figure 3.11a,b. The three orthogonal tortuosities of each sub volume were determined for the three LFP electrodes and plotted in figure 3.11 c-e. Each representation volume is subjected to the mass transport diffusive simulations using tau factor application and the set of localized tortuosity values in three directions is extracted instead of representing a single tortuosity value for the whole electrode. For the 12 µm pore sized LFP electrode, the tortuosity values on each subsection are more repetitive to each other as shown in figure 3.11c. However, the dispersion of tortuosity values is observed for the 20 µm and 23 µm pore sized LFP electrode, which is explained by the non-uniform pore size distribution. The highest anisotropy of pores was observed in the 20 µm pore sized LFP electrodes which was prepared based on the raw commercial salt particles grounded for the 20 minutes as pore forming agent. These local tortuosity values are well consistent with the tortuosity obtained in the previous macroscopic analysis of tortuosity shown in figure 3.10.

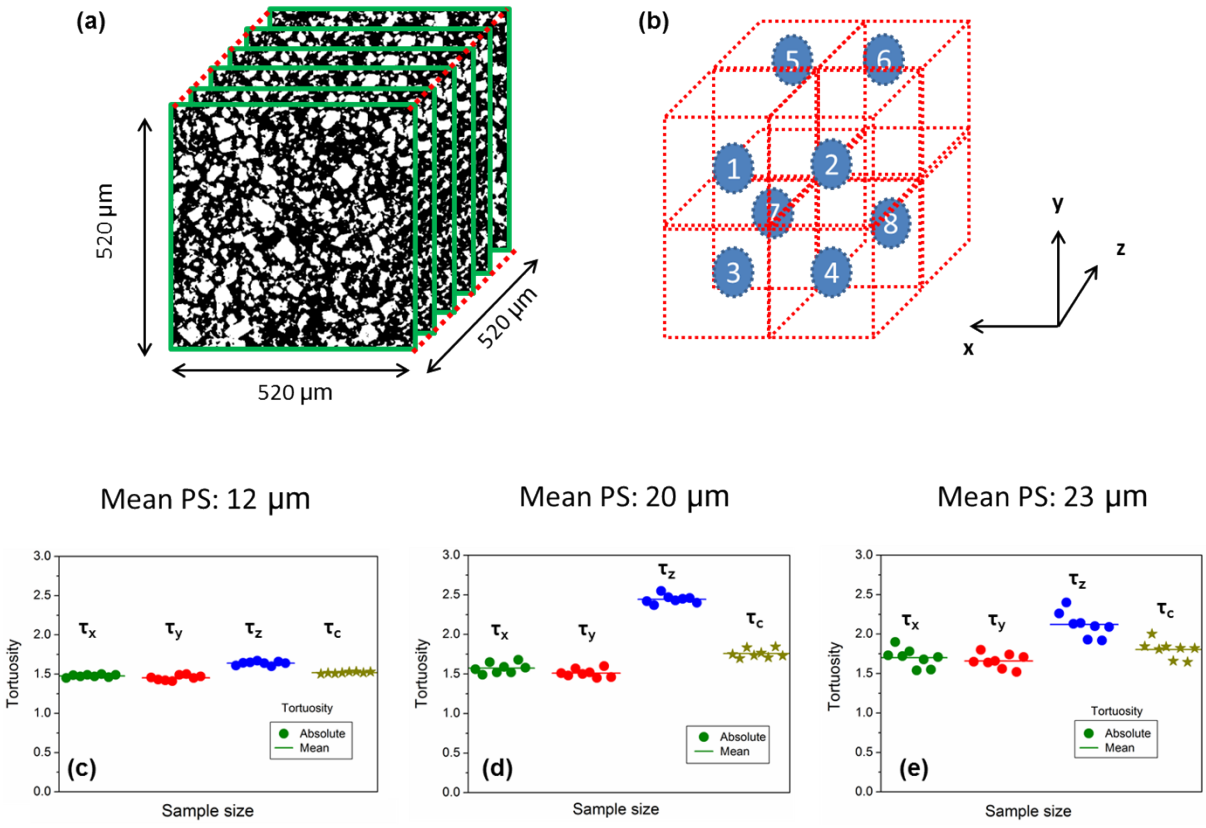

Figure 3.11 *Tortuosity distribution of the orthogonal directions of the three different pore sized LFP electrode with three different pore size distributions.*

The average $\mathcal{T}_c$ values of the three LFP electrodes (1.52, 1.76 and 1.8) are found in line with the classical Bruggeman and less than the Thorat relation as shown in figure 3.12. The anisotropy factor (α) was obtained according to the equation 3.5 which is a degree of cylindrical pores aligned in z-direction and perpendicular to the primary lithium diffusion direction in the electrode. Anisotropy factor was lower (0.12) for 12 µm pore sized electrodes rather than for the other two pore sized electrodes for 20 µm and 23 µm pores sized LFP electrodes (0.54 and 0.24) respectively.

$$\alpha = \frac{(\mathcal{T}_{max} - \mathcal{T}_{min})}{\mathcal{T}_C} \tag{3.5}$$

The z-axis tortuosity has been greatly minimized for the lesser pore size (12 µm) LFP electrode compared to x and y directions which are due to its uniform pore size distribution. The lowest value of tortuosity explains that this electrode is made up of relatively straight channels for lithium ion diffusion in the liquid phase compared to the other two electrodes. The tortuosity values of three LFP electrodes are tabulated in 3.3. The $\mathcal{T}_z$ value is higher than the other two tortuosity values ($\mathcal{T}_x$ and $\mathcal{T}_y$) irrespective of the pore size. But, this pore anisotropy effect is much reduced for the 12 µm pore sized LFP electrode which can be explained by the reduction of pore size and by the narrow pore size distribution present throughout the volume of the electrode.

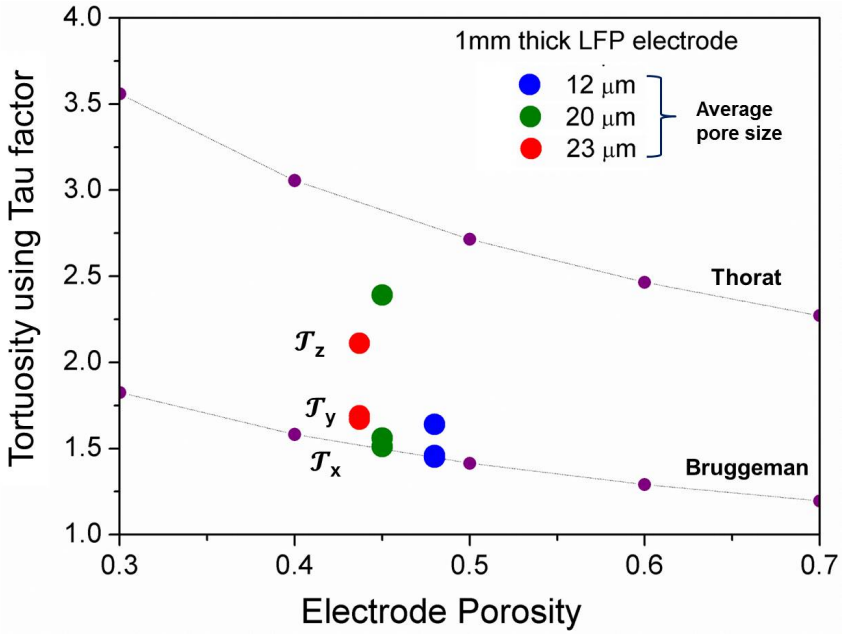

Figure 3.12 *Comparison of LFP electrode tortuosity values obtained by micro computed tomography analysis*

This important property is correlated to the electrochemical results which will be discussed later. In the literature, the correlation of particle anisotropy, tortuosity and rate capability is well studied by Wood *et al.* [30] for the different commercial electrodes of lithium ion battery. For example, the ellipsoidal graphite particles show increased particle anisotropy which leads to a high tortuosity in z-axis determined by the tomography analysis. The graphite particles are aligned parallel to the current collector and this arrangement reduces the lithium ion diffusion efficiency at higher rates. This phenomenon is less pronounced for the spherical shaped particles such as LCO in composite electrode. Overall, the tomography analysis was carried out for the 1-mm thick LFP sintered electrodes to understand the electrode architecture, inhomogeneity analysis and determine useful parameters like tortuosity which has a direct influence on the rate capability.

Table 3.3 *Comparison of LFP electrode tortuosity values obtained by μCT-TXM by-Tau factor analysis.*

Method	**Tortuosity**	**Pore size of LFP electrode**		
		12 µm	**20 µm**	**23 µm**
TXM-μCT	$\mathcal{T}_X$	1.48	1.59	1.69
	$\mathcal{T}_Y$	1.45	1.51	1.66
	$\mathcal{T}_Z$	1.64	2.44	2.12
	$\mathcal{T}_c$	1.52	1.76	1.8
	Ȯ	0.12	0.54	0.24
	ε_{total}	48.0	44.7	43.7
Literature	($\mathcal{T}_{Bruggeman}= \varepsilon^{-0.5}$)	1.44	1.49	1.51
	($\mathcal{T}_{Thorat}= 1.8\varepsilon^{-0.53}$)	2.65	2.75	2.79

3.1.3 Solvent impregnation test of LFP electrodes

Impregnation tests are done for the three different pores sized LFP electrodes (12, 20 and 23 µm) with same porosity (44%). A mixture of dimethyl carbonate: propylene carbonate (1:1 vol.%) was taken in a beaker and the LFP electrodes are submerged in the solvent mixture. At a regular interval of time, the absolute mass increase due to the uptake of solvent was noted after the excess solvent present on the surface of the electrode was removed. The solvents are conveniently chosen on purpose because the experiments can be done in ambient atmosphere. With the electrode porosity (44%) and density of the solvent (1.123 g/cc) used, the relative mass increase (%) was calculated, which is the ratio of the increased electrode mass to the theoretical mass increase after solvent uptake and the values are plotted in figure 3.13. At the first hour impregnation, the relative mass increases of 12 µm, 20 µm and 23 µm pore sized LFP electrodes are 84%, 62% and 59% respectively. This clearly shows that 12 µm pore sized LFP electrode has good interconnectivity of pores due to narrow pore size distribution so that fast filling of solvent was obtained.

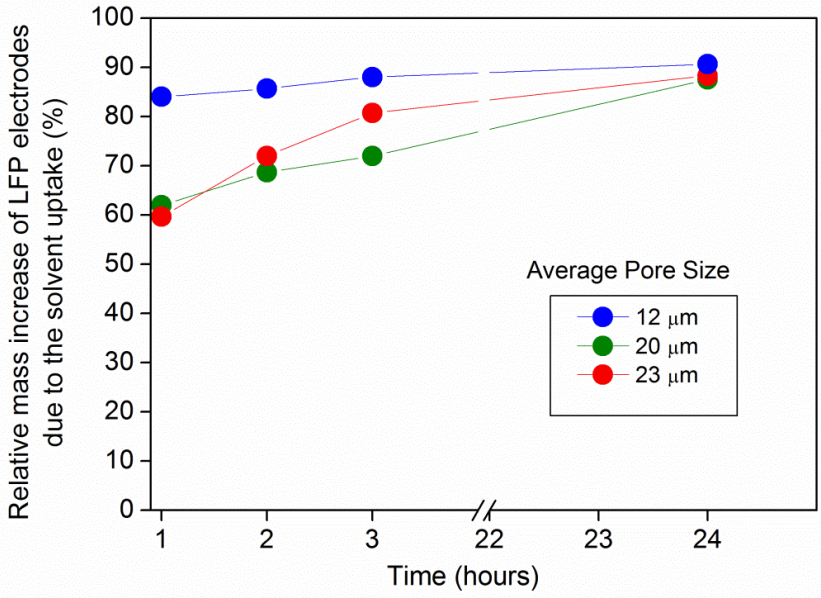

Figure 3.13 *Impregnation test result showing the behavior of rate of filling of solvent as a function of time. The rapid increase in electrode mass was obtained for the 12 µm pore sized electrodes.*

At the 24th hour of solvent impregnation, the relative mass increase of the thick electrodes is considered as a saturation point where no more penetration of solvents was achieved. The relative mass increase values are 91%, 88% and 87% for 12 µm, 20 µm and 23 µm pore sized LFP electrodes respectively. The electrode pores are not 100% filled by the solvent irrespective of the pore size which can be due to the

isolated closed pores formed during the SPS reaction. So, these results shows that the solvent filling is much more improved for the uniform pore sized LFP electrode and can be correlated with the electrode tortuosity.

3.1.4 Electrical Impedance Spectroscopy using symmetrical cells

The rate capability of Li-ion batteries is largely determined by the ionic resistivity of a porous electrode filled with the liquid electrolyte. In the EIS-Symmetrical cell approach, the ionic resistance of the porous electrode can be measured without the interference of the counter electrode and lithium insertion reaction mechanisms. The electrode tortuosity can be extracted from EIS-SC technique by fitting with Transmission Line Model [23], [31] and Newman equation (Eqn. 3.3) as reported in the literature [32]. In general, the tortuosity of any porous media for the electrochemical systems is measured to quantify the resistance of a microstructure towards a flux.

From the state of art, electrical impedance and diffusion cells are used to measure the diffusion resistance of the lithium of the porous electrodes in the liquid phase. For instance, Ogihara *et al.*[31], [33] measured the ionic resistance of the porous electrodes at 0% and 100 % SOC using EIS-symmetrical cells technique and the experimental results are validated using the transmission line model. In their work, the blocking condition is achieved by assembling $LiNi_{0.75}Co_{0.15}Al_{0.05}Mg_{0.05}O_2$ electrodes taken at 0% state of charge. Liquid electrolyte (1M $LiPF_6$ in EC: DMC: EMC mixture) and polypropylene separator was used in their symmetrical cell experiments. At 0% or 100% SOC, intercalation/deintercalation reaction is suppressed and hence the ionic resistance of lithium present in the liquid phase was measured. However, this blocking condition is not valid anymore when they use the electrodes assembled at 50% SOC as it was characterized with a semicircle due to the charge-transfer resistance arising due to the lithium intercalation. Later, the contribution of lithium intercalation can be avoided by replacing the LP30 electrolyte by a non-intercalating electrolyte (Gasteiger *et al.*[32]). The same approach of symmetric cells was used by Liu *et al.* [34] to measure the effective ionic conductivity of mud-crack formed electrodes and correlated with the rate capability which is helpful for electric vehicle applications.

In our work, we used the electrical impedance spectroscopy-symmetrical cell approach for the measurement of diffusion resistance inside the pores of 1-mm thick LFP electrodes. A pair of 1-mm thick LFP electrodes with similar microstructural features (porosity, pore size and thickness) was used for the

impedance measurements. In this experiment, n-tetra butyl ammonium perchlorate (n-$TBAClO_4$) was used as salt dissolved in ethylene carbonate and di-methylene carbonate in a weight ratio of 1:1 (EC: DMC) meaning that there is no charge transfer across the solid/liquid interface or the surface is ideally polarizable. The intrinsic ionic conductivity of the as prepared electrolyte was measured from the intercept of real impedance axis measured by a conductivity cell. The EIS spectrum obtained for two different concentrations (10 mM and 1M $TBAClO_4$ in EC: DMC (1:1)) weight % using conductivity cell was shown in figure 3.14. The intrinsic ionic conductivity of the electrolyte (10 mM $TBAClO_4$ in EC: DMC (1:1)) is found to be 0.062 mS/cm at 20 °C which is close to the one reported in literature [32].

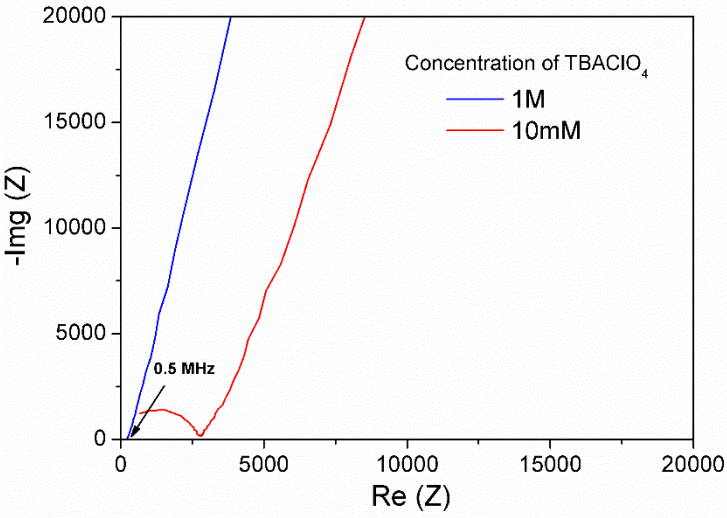

Figure 3.14 *Electrical impedance spectrum obtained from the conductivity measurements using tetra-n-butyl ammonium perchlorate dissolved in EC: DMC solvent mixture. The intercept in the real axis represent the electrolyte resistance thereby electrolyte bulk ionic conductivity can be measured.*

A low concentration of 10 mM of n-$TBAClO_4$ was used for the impedance measurements in order to minimize the error in the resistance values especially on the low frequency intercept obtained in the Nyquist plot. The electronic resistance in the solid phase becomes negligibly small compared to the ionic resistance in the electrolyte phase. A frequency range of 200 kHz to 0.5 mHz was applied with an amplitude signal of 10mV. The symmetrical LFP electrodes were assembled in the glove box and tested at a constant temperature of 25 °C. The measured ionic impedance (R_{ion}) of the cell was obtained by the sum of impedances of the individual electrodes and hence the factor two is written in the equation 3.6 where A is geometric surface area (cm^2), κ is bulk conductivity of the used electrolyte (S/cm), $\boldsymbol{\varepsilon}$ is electrode porosity (%), d is the thickness of the electrode (cm). The care was taken that the two LFP electrodes having same thickness and geometric surface area used for impedance measurements.

EIS-SC impedance spectra mainly consist of three domains: 1) High frequency intercept corresponds to the electrolyte resistance in the separator and other ohmic contacts due to the induction cables and connection wires; 2) Middle frequency region consists of a Warburg line close to 45° which is more crucial for the determination of ionic resistance through the pores of the electrode. The elongation of this line is due to higher ionic resistance arise due to the increase in pore length and radius, decrease in electrode porosity and increase in thickness. This region represents the mobility of ions inside the porous electrode and large deviation from 45 ° corresponds to the pore shape and non-uniform pore size distribution present inside the porous electrode. The ionic resistance of the electrodes (R_{ion}) can be extracted via the extrapolation of the low frequency branch to the real impedance axis which is equal to the sum of high frequency resistance and one third of ionic resistance inside the pores as shown in equation 3.7. 3). The low frequency region consists of a straight line theoretically to 90° corresponding to the capacitive behavior of the electrical double layer formed in the electrode-electrolyte interface. The non-uniformities in the pore network and side reactions cause the non-uniform current distribution leading to the non-vertical line.

$$\tau = \frac{R_{ion}.A.\kappa.\varepsilon}{2d} \tag{3.6}$$

$$Z_{El\,(\omega_{low\to\infty})} = R_{HFR} + \frac{R_{ion}}{3} \tag{3.7}$$

The tortuosity values are extracted from the impedance spectra based on the equation (3.6 and 3.7) where A is geometric surface area of thick LFP electrode, κ is the bulk ionic conductivity of the electrolyte used, ε is the electrode porosity, d is thickness of one electrode. The impedance spectra of the thick electrode were fitted by the equivalent circuit model referred to as Transmission line model (TLM) and the modeling results were obtained with the collaboration of Dr. Charles Delacourt, CR-CNRS researcher at LRCS, Amiens. The TLM model is based on the equations used in Newman's model adopted by the porous electrode theory [35]. The tortuosity values are also extracted from the fitted TLM model similar to the recent work of thick graphite electrodes as reported in the literature [23]. As shown in figure 3.15a, the first region is the high frequency intercept which is same for all the three LFP electrodes because of the same electrolyte used in the measurements. The second region is the Warburg impedance close to 45° line obtained for the 12 μm pore sized electrodes and this region is elongated with the increase in pore size of the LFP electrodes. In the third capacitive behavior region, relatively

less deviation from the straight line was seen for 12 µm pores sized LFP electrodes (blue) which is due to the uniform distribution of pores present in the electrodes as confirmed by micro tomography-Tau factor analysis. However, the EIS spectrum of the symmetrical sintered LFP electrodes is not very well fitted with the TLM model especially the low frequency part (not shown here). From TLM model fitting, the tortuosity values obtained for the three different pore sized LFP electrodes (12, 20 and 23 µm) are 3.8± 0.7, 4.6± 0.9 and 5.6± 0.9 which are comparable to the tortuosity values obtained from the equation 3.6. Lower tortuosity value of 12 µm pore sized LFP electrode is well in agreement with the better rate capability performance as shown in figure 3.15b.

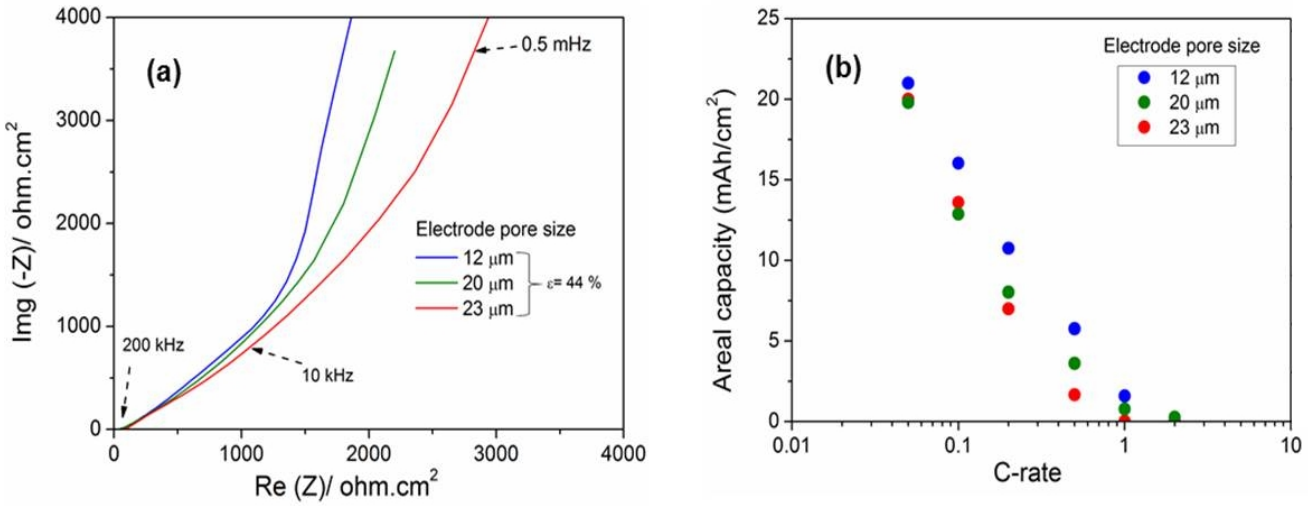

Figure 3.15 *a) Impedance spectrum of LFP-C electrodes obtained from the EIS-symmetric cell experiments. The ionic pore resistances are measured as an effect of pore size by fitting the experimental curve with the transmission line model. b) Rate capability performance in-line with the EIS experiments.*

It is important to mention that the tortuosity values obtained by diffusion simulations using Tau factor are self-consistent compared with our EIS-SC measurements. A similar comparative study was done by Wood *et al.* [36] by analyzing the PE16A separator pore network and the corresponding tortuosity values were compared by three methods such as diffusion simulations, fractal analysis-Random walk and EIS methods. In their work, tortuosity obtained by the EIS (5.47) is in close agreement with the fractal analysis-random walk method (5.77) and found two times higher than the diffusion simulations (2.76) which show a similar trend as our work. Skeleton analysis of pore network was also carried out in their work and found that 7.5% of the total pore network length is composed of dead end pore and this will not contribute to the ionic diffusion of the main pore network leading to the under-estimation of tortuosity value in the pore network by the steady state diffusion simulations.

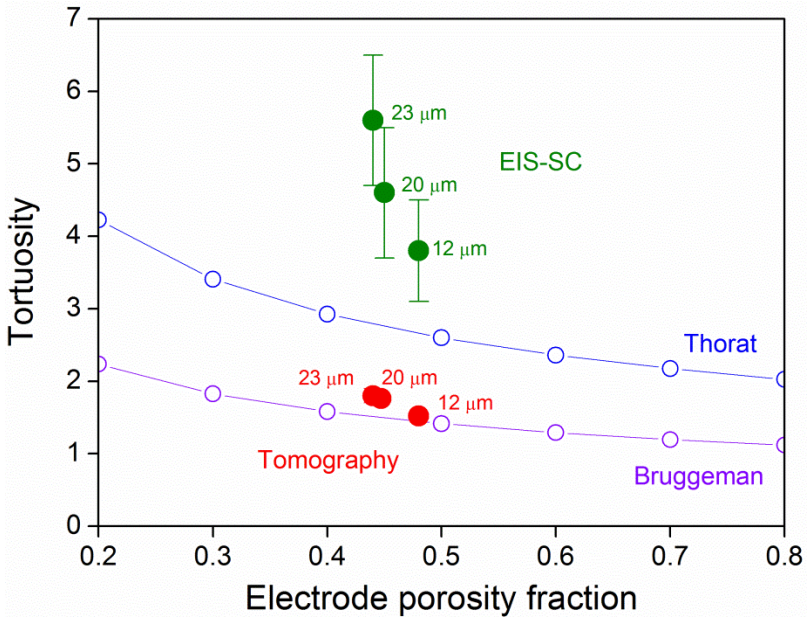

Figure 3.16 *Tortuosity compared between the EIS and micro tomography methods for the three different pore sized LFP electrodes (12,20 and 23µm). Average pore size values are written for comparison.*

EIS-SC experimental results fitted with the TLM model (Figure 3.16) show two times higher tortuosity values than Tau factor diffusion simulations of micro-tomography data. One reason for this underestimation of tortuosity using the tomography analysis is the non-accountability of the dead end pores (pores not connected to the main pore network) and this contributes significantly to the transport of lithium ions through the structure. So, clearly quantification of dead end pores should be done using skeleton analysis of the tomography data using AVIZO software and this will be done in the future. The tau factor simulations can be updated in the future with the inclusion of dead end pores. Another limitation of the tomography method is the low spatial resolution used, i.e. the pixel size is 1.3 µm. This explains that in the µCT mode pores less than 1.3 µm are not captured and the tortuosity contribution from those smaller pores is neglected here. So, the results should be compared by using nano-CT mode in the future to understand the effect of spatial resolution during tomography measurements. However, the EIS-SC technique is a macroscopic measurement of the overall lithium motion and tortuosity of the full pore network of the thick electrode which includes the effect of dead end and closed pore. EIS-SC is an average measurement technique in which local inhomogeneities cannot be probed. In the TLM model fitting of EIS-SC approach, electrical conductivity of the LFP electrodes is assumed as infinity but this assumption is not completely true because the electrical conductivity of the LFP particles is very low leading to the large statistical error bars obtained from the repetitive experiments.

3.1.5 Electrochemical characterization of 1-mm thick LFP electrodes

Rate capability tests were done for the three different pore sized LFP electrodes (12, 20 and 23 µm) with the same loading (165 mg/cm^2) against metallic lithium. Charge-discharge cycling curve of the three different pore sized LFP electrodes/Li at C/20 and C/5 rate are shown in figure 3.17a. Higher capacity values at any C-rate were obtained for 12 µm pore sized electrodes as shown in figure 3.17b. This can be correlated with the lowest tortuosity value determined by the tomography and EIS methods. The smaller average pore sized electrodes (12 µm) are possessed with uniform pore size distribution with less pore spacing. This phenomenon leads to higher interconnectivity of pores and higher rate capability compared to the larger pore sized electrodes (20 and 23 µm).

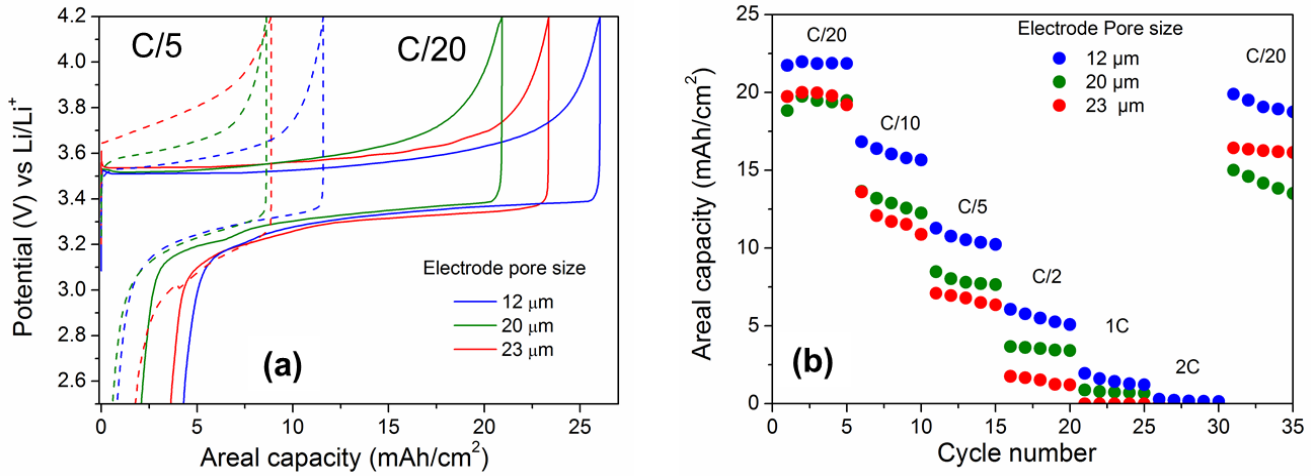

Figure 3.17 *(a) Charge-discharge profile of 1-mm thick LFP-C electrodes against lithium at C/5 rate with three different pore sizes. (b) Rate capability curve showing highest capacity for smallest pore sized LFP electrode.*

The reduction of lateral diffusion length of lithium ions was observed due to close packing of pores in 12 µm pore sized LFP electrode and this enhances the overall ion transport compared with the 20 µm and 23 µm pore sized LFP electrode. A similar trend of results was obtained in literature by minimizing the pore channel spacing in the co-extruded and sintered LCO electrodes leading to better rate capability [37].

3.2 Effect of electrode pore size for 20% porous LFP electrodes

The effect of electrode pore size in the electrochemical properties was also studied for 20% porous 1-mm thick LFP electrodes. The composite preparation, thick electrode fabrication steps remained the same as mentioned before. The volume composition of initial LFP-NaCl-C composite is 70:20:10. Two different salt particles (2.0 ± 0.6 µm and 13.7 ± 6.8 µm) were used as templating agents. After the SPS densification, the initial compacity of the LFP-NaCl-C pellets were calculated as 98-100%. It can be noticed that reduction of volume % of salt particles in the LFP-NaCl-C composite allows increasing the compacity of the LFP electrodes after the SPS treatment. After the removal of salt particles, the final electrode porosity obtained for the electrodes irrespective of the pore size was 21%. The surface and cross sectional views of SEM images of three LFP electrodes with average pore sizes (12 µm and 23 µm) are displayed in figure 3.18. Similar to the 40% porous electrodes, pores are oriented perpendicular to the z-direction as observed in the cross sectional images of the thick electrode (Figure 3.18c-d).

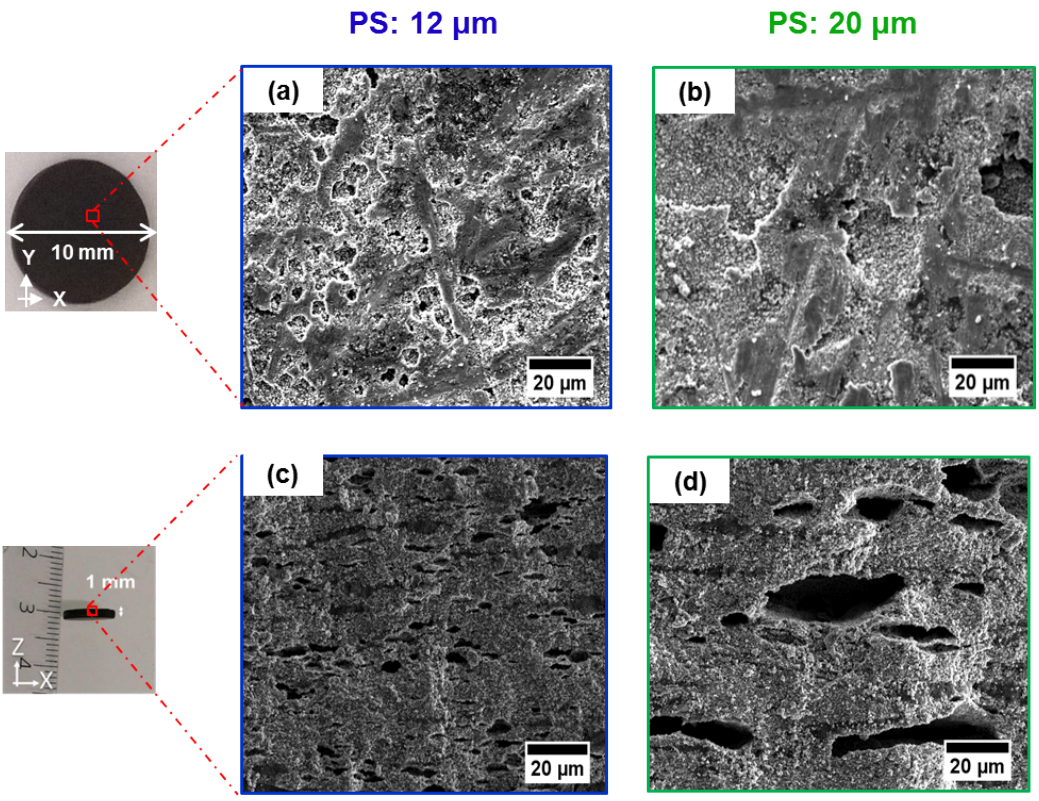

Figure 3.18 *SEM images of 1-mm thick LFP electrodes prepared with 21% porosity: a, b) Top surface view showing the pore shape and size corresponding to the initial crystal size of 12 and 20 µm ; c, d) Cross sectional images of the porous electrodes showing the distribution of cylindrical pores.*

Galvanostatic cycling curves at C/20 are shown in figure 3.19a for 12 µm and 20 µm pore sized LFP electrodes against lithium metal. Increased cell polarization was obtained for 20 µm pore sized LFP electrode and elongated charge and discharge capacity curves are obtained for 12 µm pore sized electrode. This clearly shows that good accessibility of liquid electrolyte was obtained for 12 µm pores sized electrode due to the relatively uniform pore size distribution compared with the 20 µm pores sized electrodes. Rate capability tests were done for the 21% porous LFP electrodes with 1-mm thickness against lithium metal. Higher discharge capacities at faster C-rates for 12 µm pore sized LFP electrode were obtained as shown in figure 3.19b which can be due to the low tortuosity due to good uniformity of pore size distribution and better pore connectivity. The areal capacity obtained is 3-4 times higher than the conventional Li-ion batteries. The higher active material loading (235 mg/cm^2) was achieved by reducing the electrode porosity and the areal capacity increased due to the 1-mm thickness. The gravimetric discharge capacity of 21% porous LFP electrodes for 12 µm and 20 µm pore size are 61.2 and 42 mAh/g. Comparing with the full practical capacity of 145 mAh/g, these capacity values correspond to 42% and 29% of the total practical capacity. This clearly shows the incomplete active material utilization for the 21% porous LFP half cells which is due to the poor accessibility of liquid electrolyte to the surface of active materials in the dense electrodes. The comparison of specific capacities of 21 % and 44 % porous electrode with same average pore size (12 µm) is shown in table 3.4.

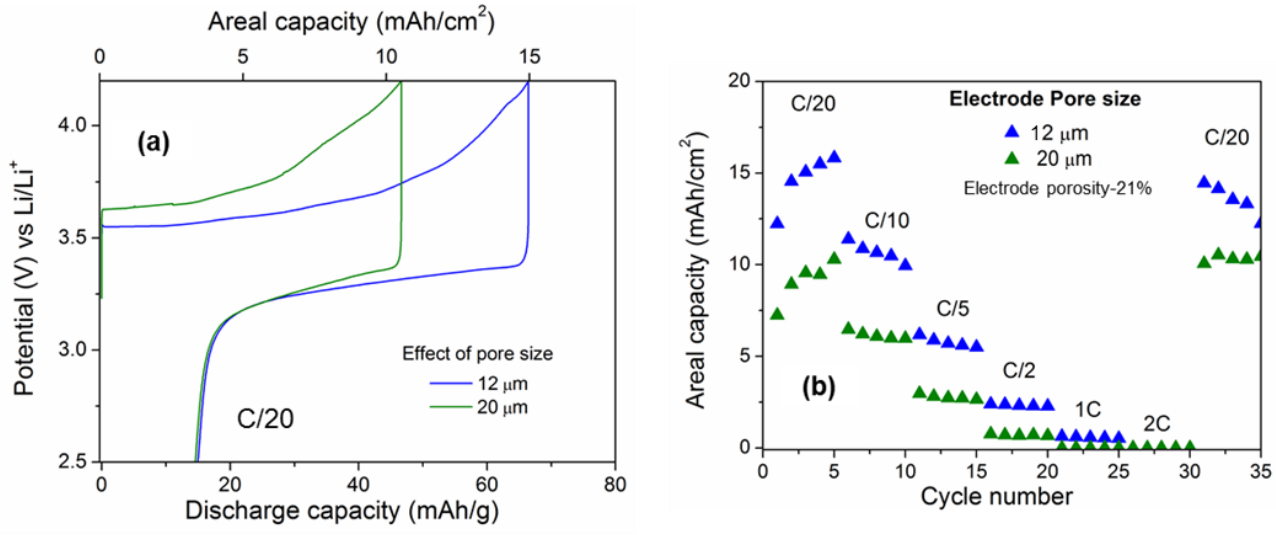

Figure 3.19 *Effect of pore size for 21% porosity electrodes. a) Charge-discharge profile of first cycle at C/20 rate of 1-mm thick LFP-C electrodes showing high polarization. b) Rate capability curve showing significant capacity increase for smaller pore sized electrodes at different C-rates.*

Table 3.4 *Comparison of specific capacities of 1mm thick LFP electrodes with two different porosities.*

LFP thick electrode porosity	Electrode pore size (12 µm)	
	Areal capacity @ C/20 rate-3rd cycle (mAh/cm²)	**Gravimetric capacity @ C/20 rate-3rd cycle (mAh/g)**
21%	15.1	61.2
44%	21.8	132

3.3 Effect of porosity of 1-mm thick LFP electrodes

The optimization of electrode porosity is important to design the electrode for superior electrochemical performance. Various experimental and modeling works are done in the literature to optimize the porosity according to the integrated material chemistry to yield high rate capability for Li-ion batteries [38]–[41]. The larger electrode porosity leads to electrical conductivity limitations due to the relatively lesser amount of active materials and also leading to lower volumetric energy density and loss in mechanical properties. The importance of porosity effect and its influence on the electrochemical performance was well quantified by many experimental works in the literature. For example, M. Singh *et al.* reported the effect of porosity for NMC-Graphite full cells in terms of galvanostatic cycling by measuring discharge capacity and volumetric density of the full cells [41]. In their work, discharge current pulse for 20 seconds was applied at 3.9 V for the NMC-G full cells and the corresponding voltage profiles are recorded. The low porous electrodes (cathode side-38%) show a smaller voltage drop (56 mV) than the higher porous cells (C44%) of showing high voltage drop of 205 mV. This lesser voltage drop for the lower porous electrodes is providing evidence to achieve the complete utilization of the active materials.

Various modeling studies were focused on the optimization of electrochemical performance using the porous electrode theory [9], [11], [35]. For example, Taleghani *et al.* reported the discharge capacity and energy density of $LiMn_2O_4$/Graphite cell based on the effect of cathode porosity using the pseudo 2D model [38]. The model is based on the porous electrode theory and the cell voltage as a function of capacity was obtained during the discharge process for different porosities. The discharge capacity of LMO/G with cathode porosities from 20 to 65 % are simulated and the highest discharge capacity (in terms of mAh/g of active material) was attained for 50% cathode porosity, which is due to the presence of a sufficient amount of pore volume for the electrolyte to flow inside the electrodes, reaching the full

battery utilization. However, the highest porosity of 65% electrode is delivering less capacity, which is due to the kinetics limitation of charges due to the low active material content. The low porous electrode (20 %) is delivering lesser gravimetric capacity due to not enough lithium ions being present in solution phase to reach the reaction zone. The decrease in porosity of the electrodes is leading to the change in electrode-electrolyte interface area thereby in the increase in transport resistances. One direct impact can be seen in the capacity loss when the electrodes are discharged at high C-rates. In our work, the effect of porosity was studied by preparing the LFP-NaCl-C composite with three different compositions such as 70:20:10, 60:30:10 and 50:40:10 vol.%. The electrode fabrication and NaCl leaching steps are same as reported in chapter 2. The three (LFP-C) electrodes with different porosities (21%, 36%, 44%) are obtained by the templating approach. Cross sectional SEM images with three different porosities are shown in figure 3.20 and a clear difference in pore volume fraction was seen between different porous electrodes. The physical properties of the porous LFP electrodes are written in table 3.5.

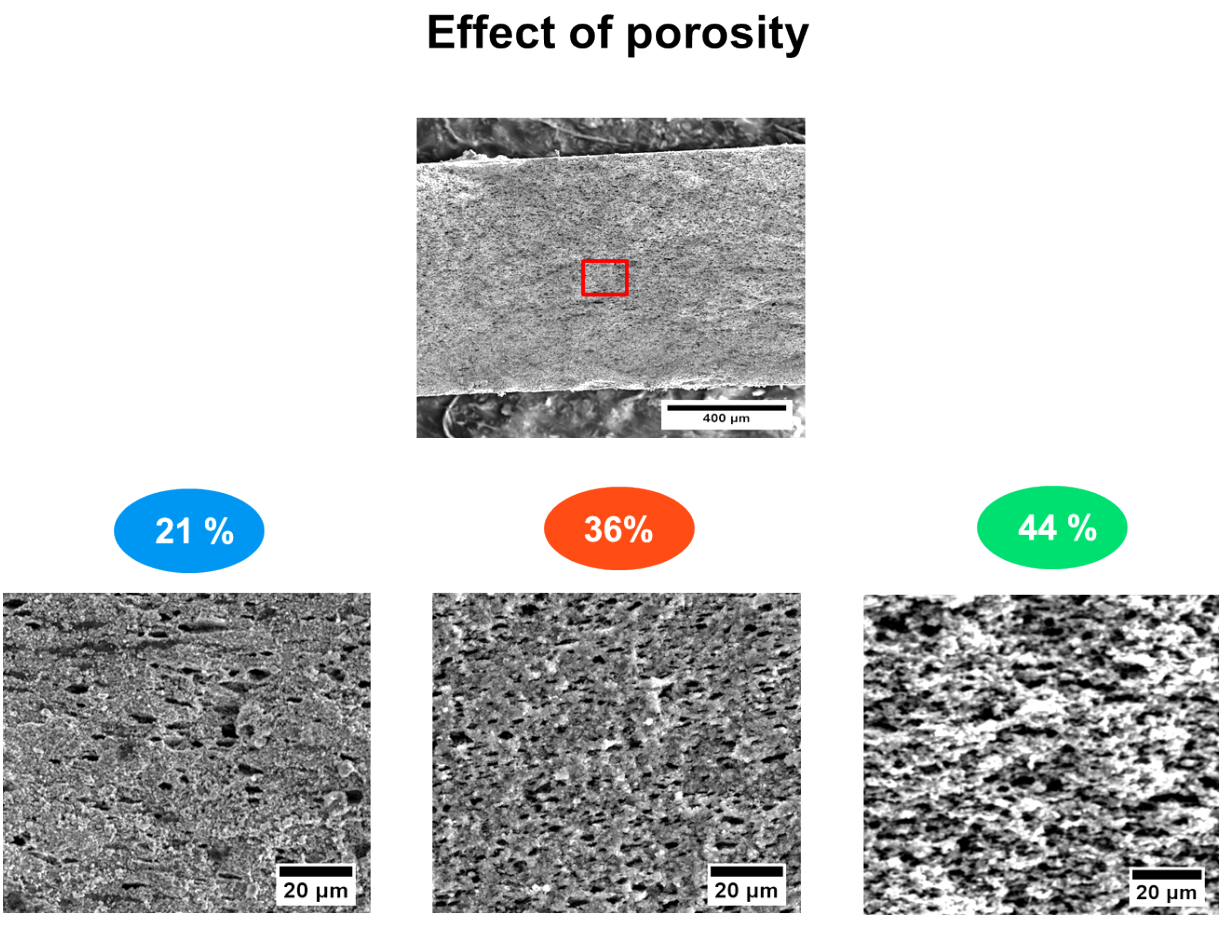

Figure 3.20 *Cross section SEM images of 1-mm thick LFP electrodes with three different porosities (21, 36 and 44%).*

Table 3.5 *Physical properties of the thick binder free LFP electrodes obtained using SPS and templating approach having three different porosities (21%, 36% and 44%).*

LFP-NaCl-C (vol.%)	70:20:10	60:30:10	50:40:10
Compacity (%)	99	94	93
Porosity (%)	21	36	44
AM loading (mg/cm^2)	235	195	165
Apparent density (g/cm^3)	1.83	2.07	2.55

The average particles size of the NaCl crystals used is the same at 2 μm for making three different electrode porosity. For example, at 44% porous electrodes (b,d), the pores are closely arranged with lesser amount of active material but in 20% porous LFP electrodes, the pores are scarcely distributed. The active material loading is determined as 235, 195 and 165 mg/cm^2 respectively, determined based on the mass and geometrical dimensions. The apparent density values are 2.55, 2.07 and 1.83 g/cm^3 for the 21 %, 36% and 44% porous 1-mm thick LFP electrodes and the values are plotted as a function of porosity in figure 3.21. The extrapolation of the porosity- density line reachesclose to the density of the 1-mm thick LFP electrode (3.2 g/cc) corresponding to the 92% compacity. No trace of remaining NaCl was observed when 20 vol.% of NaCl are used and confirmed by the electrochemistry curves.

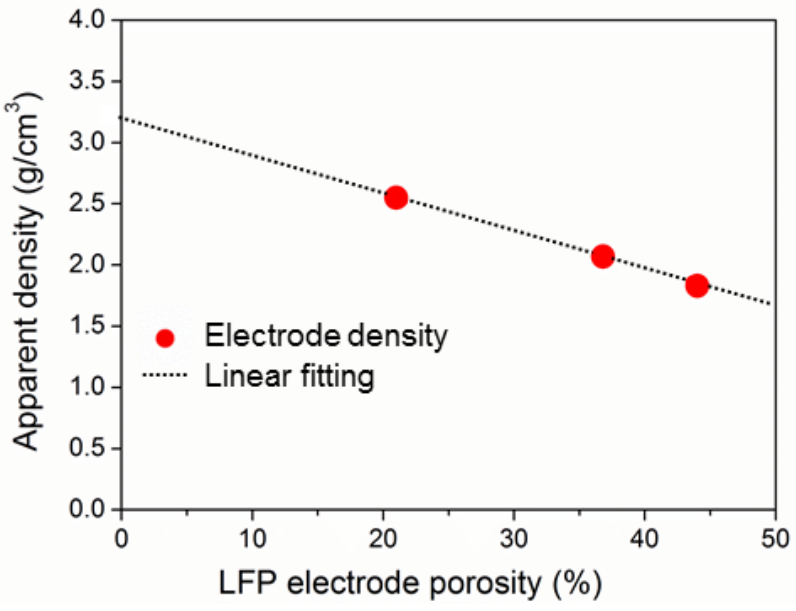

Figure 3.21 *Apparent density vs electrode porosity showing the linear increase of density when porosity is decreased and the intercept of the line corresponds to the 1-mm thick LFP electrode (99% compacity).*

The three different as prepared porous 1-mm thick LFP electrodes are cycled against Li in a galvanostatic operating mode at different C-rates from C/20 to 2C (Figure 3.22a). The charge and discharge capacities for 21% porous LFP electrode show lesser values than 44% porous electrodes. The cell polarization was greatly reduced as the electrode porosity increased from 20 to 44%. At C/20 rate, both charge and discharge capacities of 1-mm thick LFP electrodes increased linearly at C/20 rate (15, 17 and 21.7 mAh/cm^2) for 21%, 34% and 44% respectively.

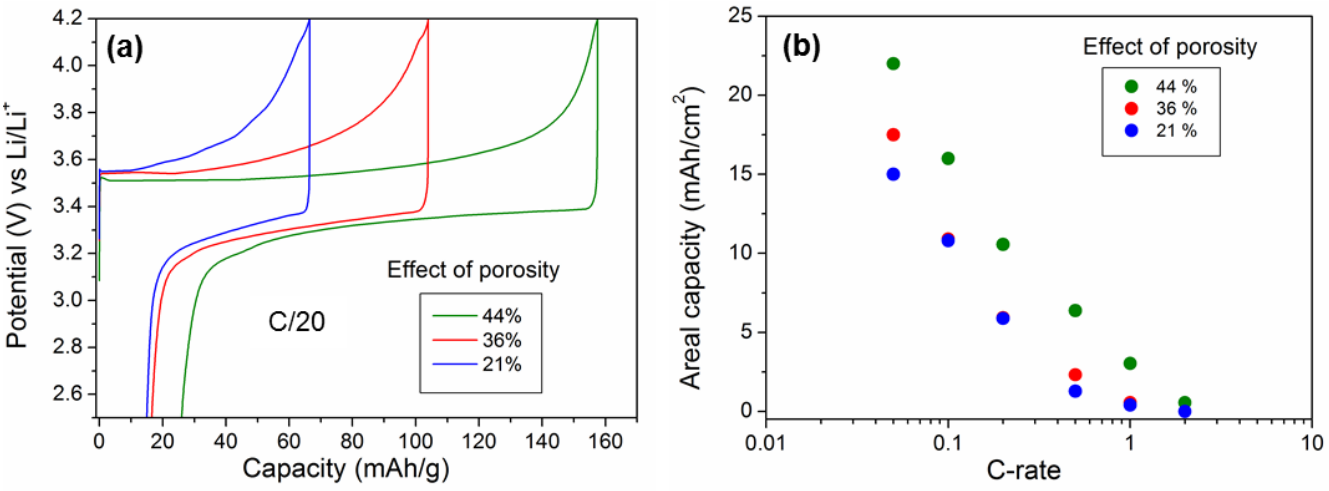

Figure 3.22 *a) Charge-discharge cycling curve of the 1-mm thick LFP electrodes with three different porosities at C/20 rate, b) Ragonne plot showing the improved C-rate performance for 44 % porous LFP electrodes.*

As shown in figure 3.22a, the 21% porous LFP electrodes are show high cell polarization and deliver the lowest discharge capacity of 61 mAh/g and areal capacity of 15.1 mAh/cm^2 which is still higher compared to the conventional lithium ion batteries [42]. Though relatively more active materials are present in the solid phase of 21% porous than 44% porous LFP electrode, the lower specific capacity is due to the mass transfer limitation or poor accessibility of electrolyte inside the pores of the electrode and higher tortuosity compared to 44% porous LFP electrodes.

3.4 Effect of electrode thickness

Electrode thickness is the one of important design parameters affecting the energy and power capability of the cell. The effect of active material loading was reported in the literature to improve the energy density [30]–[32]. For example, Zheng *et al.* reported that the increase in positive electrode thickness of commercial lithium ion batteries from 10-102 μm electrodes can improve the energy density but at the same time, the power density trend goes inverse as you increase the thickness of the electrodes [42] due to the mass transport limitations. There is always a tradeoff made between energy and power densities when the battery manufacturer designs the thickness of the electrodes. The strategies to improve both energy and power density are critical. In our work, as a motivation to increase the areal capacity of the LFP electrodes, a systematic study was carried out by fabricating LFP electrodes using SPS of different thicknesses of 0.5 mm, 0.75 mm, 1.0 mm, 1.5 mm, 2.0 mm and 3.0 mm. The electrode thickness is controlled by varying the amount of composite powder taken in the graphite dye and further modified by the polishing step after the SPS densification. Complete NaCl dissolution was achieved from 0.5 mm upto 3.0 mm thick electrodes which are mainly due to the good pore interconnectivity and uniform pore size distribution. The electrode porosity (44%) and average pore size (12 μm) are taken same for all thick LFP electrodes. The digital photo of three different thick LFP electrodes is shown in figure 3.23.

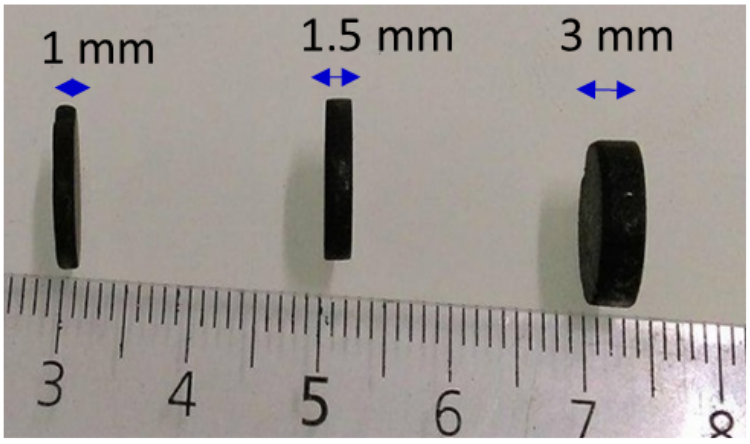

Figure 3.23 *Digital photo of various thick LFP electrodes at different thickness.*

As displayed in the figure 3.24, an increase in active material loading per geometric surface area of the electrode was observed when increasing the electrode thickness. The slope of the line (LFP loading/thickness) is 1.6 g/cc corresponding to the geometric density of ~1.8 g/cc. This clearly shows that the same densification was achieved for the whole set of thick LFP electrodes fabricated by SPS.

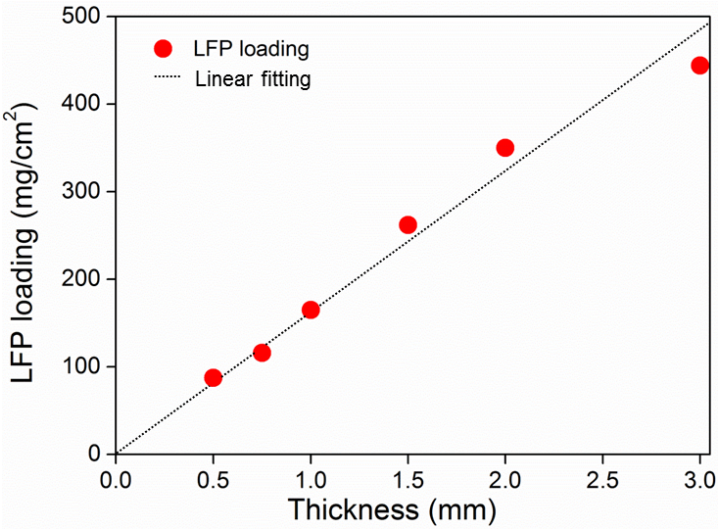

Figure 3.24 *LFP loading vs electrode thickness showing linear increase in LFP loading from 0.5 mm to 3mm.*

The different LFP electrodes from 0.5 mm to 3 mm thickness were cycled against lithium at C/20 rate and the corresponding charge-discharge curves of the second cycle are shown in figure 3.25a. The increase of polarization was observed from 0.5 mm to 3-mm thick LFP electrode due to the sluggish lithium ion kinetics and delivering discharge capacity ranging from 145 to 84 mAh/g respectively. Full practical capacity of LFP electrode (145 mAh/g or 11.8 mAh/cm^2) was achieved for the 0.5 mm thick LFP half-cell at C/20. The obtained practical capacities were compared with the theoretical capacity for 0.5-mm to 3-mm in figure 3.25b. The areal capacity values were stabilized after 1.5 mm to 3-mm thick LFP half cells. The gap between the practical and theoretical capacity is significantly increasing after 1.5 mm which can be explained by the low active material utilization (Figure 3.25b). For example, the 3-mm thick LFP half-cell delivers only 84 mAh/g at C/20 rate, which shows that the lithium intercalation reaction is occurring partially in the electrode thickness. This clearly shows that the specific capacity of 3-mm thick LFP half-cell is limited at this C-rate (C/20) and the remaining incoming ions need to migrate longer distances in the deeper lying regions in the electrodes. So slower cycling rates such as C/100 or C/200 are need to be tested to achieve full practical capacity (145 mAh/g). Nevertheless, these results clearly show that our ultra-high thick sintered LFP electrodes seemed to be promising candidates for the slow C-rate/ high energy applications.

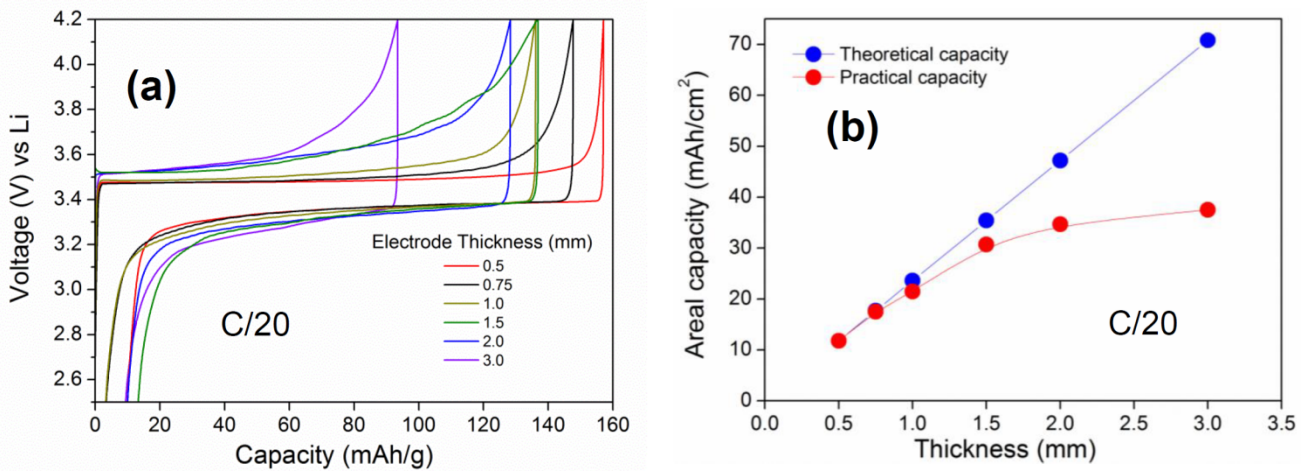

Figure 3.25 *Electrochemical performance as a function of electrode thickness at C/20 rate: a) Charge-Discharge profile of second cycle for six different thicknesses of LFP electrodes, b) Practical vs theoretical capacity showing less active material utilization for 3mm thick LFP electrode.*

Later, the various thick LFP half cells were cycled at different C-rates from C/20 to 2C rate and the results are shown in figure 3.26. The significant deterioration of gravimetric discharge capacities at higher C-rates is due to the lithium ion diffusion limitations as shown in figure 3.26b. One main aspect for this capacity fade at higher C-rates is due to the longer diffusion and migration paths for lithium ions to enter or leave an electrode. This contributes to ohmic and mass transport losses, and to the increase in overpotential in the electrode as seen in figure 3.25a. On the contrary, the corresponding areal capacities are increasing from 11.8 to 37.5 mAh/cm^2 as shown in figure 3.26a due to the high loading of LFP material in the thick electrodes. The rate performance of the electrodes can be explained by considering the two continuous phases: The porous solid matrix and liquid electrolyte within the pores. The resistance of lithium ions inside the pores is linearly increasing with thickness due to the increase in the diffusion length of lithium in the liquid phase.

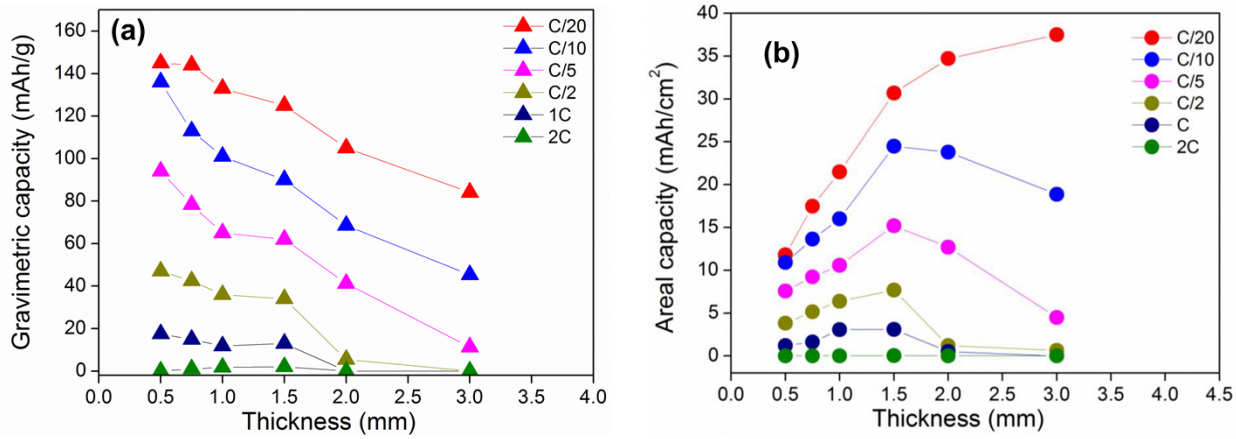

Figure 3.26 *Comparison of a) gravimetric capacity and b) areal capacity as function of electrode thickness at different C-rates. Increase in areal capacity was observed due to high active material loading and corresponding decrease of gravimetric capacity is seen due to the mass transport limitations.*

As shown in figure 3.27, the Ragone plot is showing the decrease of capacity values at higher C-rates for six different LFP half cells. The poor rate capability of the thick electrodes can be explained by the increase in internal resistances of the porous electrodes, mainly the charge transfer resistance at the electrode/ electrolyte interface (R_{ct}) and ionic resistance of lithium in the electrode pores (R_{ion}). Ogihara *et al.* determined these two resistances (R_{ion} and R_{ct}) using Electrical impedance spectroscopy-symmetrical cell (EIS-SC) approach by assembling a pair of same electrodes at a state of charge of 0% and 50% respectively at different temperatures and electrode thicknesses [31], [33]. It is determined that the ionic resistance of pores increases linearly with the thickness and is found more dominant than the R_{ct} for the thick electrodes. EIS-SC studies will be done in the future to determine the ionic resistance of pores in a thick electrode, which is the dominant contribution for the rate capability of the thick LFP electrodes.

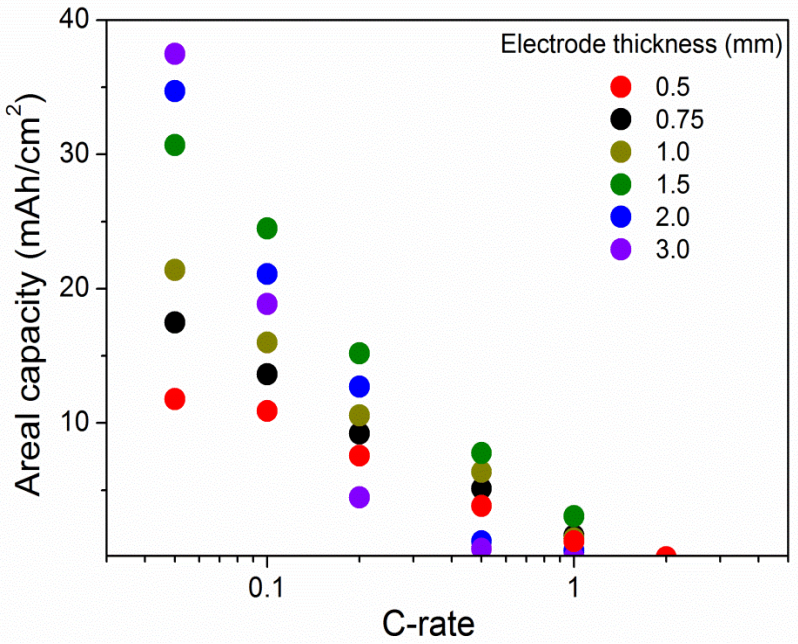

Figure 3.27 *Ragonne plot showing the areal capacity as a function of electrode thickness at different C-rates.*

The 2mm thick LFP electrodes are cycled against lithium at slower C-rates such as C/100 and C/50 because the capacities values are already limited at C/20 rate and the charge-discharge profile is shown in figure 3.28a. Lower cell polarization (~ 0.2V) was observed at C/100 and C/50 compared to the C/5 rate (~ 0.6V) which is due to the lower Ohmic resistance at slower C-rates. The discharge capacities at C/100 and C/50 are 124 and 115 mAh/g and corresponding areal capacity are 40.25 and 39.25 mAh/cm^2, and the capacity values are tabulated in table 3.7 in annexe. As shown in figure 3.28b, the discharge capacities versus C-rate are plotted and show an elbow at C/5 rate that divides the capacities into two regions. In the first region up to C/100 and C/50 rate, a slow decrease in the specific capacity was observed due to the electro-kinetic limitations rather than mass transfer limitations.

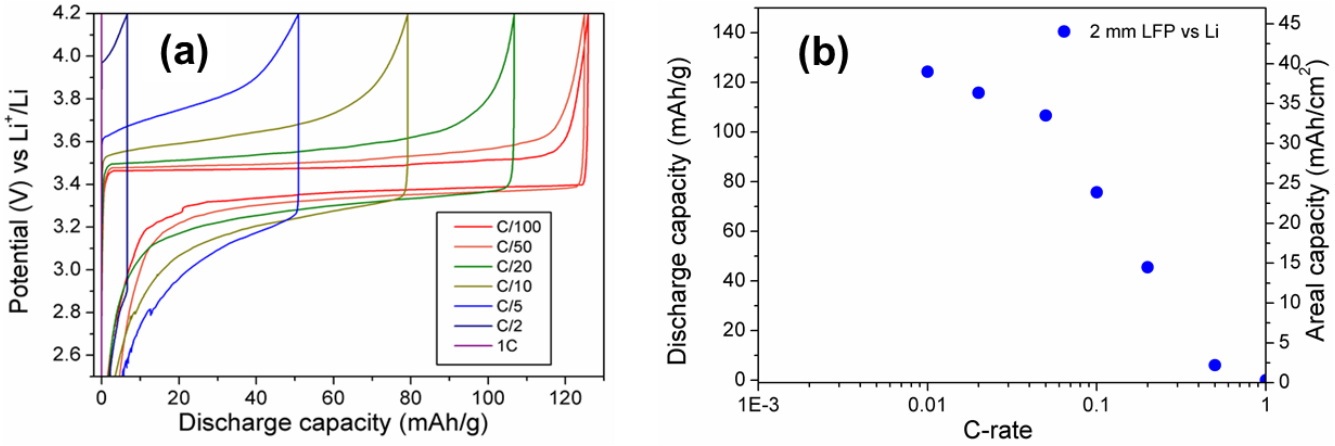

Figure 3.28 *a) Charge-discharge profile for of 2mm thick LFP/Li at different C-rates such as C/100, C/50, C/20, C/10, C/5, C/2, 1C rate. Very low polarization at C/100 rate and increase in polarization as C-rate was increased. b) Ragone plot showing the discharge capacities plotted at different C-rates. A sudden decrease of capacity was seen after C/20 rate due to the mass transport limitations.*

Then sudden decrease in capacity in the second region was seen due to the mass transport limitations or increase of ionic resistance of pores in the electrode. As shown in figure 3.29, the areal capacities of our thick electrodes performance are compared with literature [45]–[50]. In figure 3.19, the applied current density was plotted in X-axis calculated by dividing the applied current value by the geometrical surface area of the LFP thick electrode.

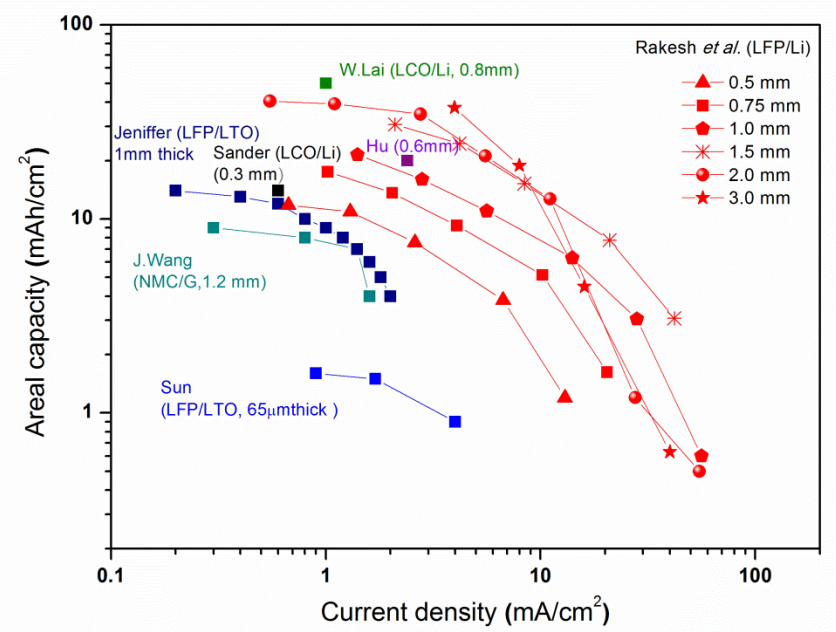

Figure 3.29 *Ragone plot comparing areal capacity versus current density of the thick electrodes prepared with SPS/templating and reported literature values. [Note: Thickness and battery systems are given in brackets] [45]–[50].*

The areal capacity values of the biphasic LFP thick electrode half cells are exceeding the presently reported literature work of thick electrodes [45]–[50]. As a proof of concept, the areal capacity is linearly increasing as a function of electrode thickness and we believe that this significant improvement will play a vital role in fabricating thick electrodes for low C-rate applications such as portable electronics in the future.

3.5 Conclusion

In this chapter, thick binder free LFP electrodes were fabricated with a varied range of parameters such as pore size, porosity and thickness, and their influence in the electrochemical performances are reported. Initially, the as-prepared cubic salt particles and their particle size distributions were determined from their microscopic images using FIJI software. Complete NaCl dissolution is confirmed by the weight loss measurements due to its good pore interconnectivity. SEM images of the 1-mm thick LFP electrodes with different pore sizes clearly show the pore sizes corresponding to the initial particle size of the NaCl crystals and cross section images illustrate the pore anisotropy in the z-direction due to the application of pressure during SPS treatment.

The 1-mm thick LFP electrode with three different pore sizes (12 µm, 20 µm and 23 µm) is characterized by the µCT TXM tomography. This highly advanced method is not so common and helps to visualize the interior of the thick electrodes in 3D structure and helps to identify the pore inhomogeneity leading to poor electrochemical performance. The 3D reconstructed images are used to distinguish the pore and solid matter and also to determine the microstructural properties such as closed and open porosity, pore size distribution, anisotropy factor, specific surface area using tomography analysis. The influence of the pore anisotropy in the rate capability was confirmed with the electrochemical performance was reported using galvanostatic cycling and rate capability tests. The diffusion resistances of three different pore sized LFP electrodes and corresponding tortuosities were determined using electrical impedance spectroscopy and their rate capability performance was correlated. The rate of filling of the electrolyte was studied by the impregnation tests to understand the electrode architecture and correlated with the microstructural properties of the electrodes such as tortuosity and pore size distribution. Three different porous 1-mm thick LFP electrodes are reported by varying the initial amount of templating agents with same pore size and confirmed by the SEM images. The electrochemical charge-discharge curve of 44% porosity electrode is showing less cell polarization and high discharge capacity. The poor electrolyte accessibility to the active material limitations are realized for 21% porous 1-mm thick LFP electrode compared to the 44% porous LFP electrodes leading to the incomplete utilization of active materials.

LFP sintered electrodes with 0.5 mm to 3 mm thickness are reported for the first time with excellent mechanical properties. The compacity of LFP electrodes shows very high relative density values of above 95 % for all the thick electrodes which is very difficult to obtain by using the conventional sintering or solid state preparation process. To the best of our knowledge, very high active material loading of 3-mm thick LFP electrodes (444 mg/cm^2) was not reported so far in the literature. The benefits of the SPS

process for the electrode fabrication were greatly enjoyed by achieving high mechanical strength thereby increasing electrical conductivity and also avoiding the formation of any cracks or delamination for the sintered electrodes unlike conventional electrodes. The galvanostatic cycling of LFP half cells from 0.5mm to 3 mm cathode thickness at C/20 rate shows that the increase in areal capacity, and the effect of increase in diffusion length was studied. The mass transfer limitations were studied for different thick LFP electrodes against lithium at different C-rates. The good pore interconnectivity was observed in these thick electrodes up to 3-mm thickness proving that this templating method is easily adaptable and is working, with excellent microstructural properties. The highest areal capacity values of thick LFP electrodes up to 37.5 mAh/cm^2 are obtained for the first time which will greatly improve in the application point of view such as portable applications.

3.6 Annexes

TXM experimental setup:

The TXM images have been acquired on the beamline 32-ID of the APS synchrotron at Argonne National Laboratory and the experimental setup is shown in figure 3.30. Measurements were performed in phase contrast at 25 keV, without any optic in between the sample and the U18 undulator. The first harmonic of this undulator providing X-ray with a bandwidth equivalent to a pink beam ($dE/E=10^{-2}$), eliminating the need to use a monochromator, was used. It makes a clean and intense beam. Propagation distance=distance sample to charge coupled device (CCD)= 30 cm. The sample was at 70 m from the source. Detector: Point Gray, GS3-U3-23S6M-C, 1920 x 1200 pixels, Objective lens=long working distance. Mitutoyo High Resolution with a NA of 0.21, providing an optical resolution of 1.30 µm. Objective lens=long working distance Mitutoyo with a NA of 0.14, providing an optical resolution of 1.96 µm. Reconstruction was done by TomoPy [51], [52] using the algorithm from the ASTRA toolbox [53].

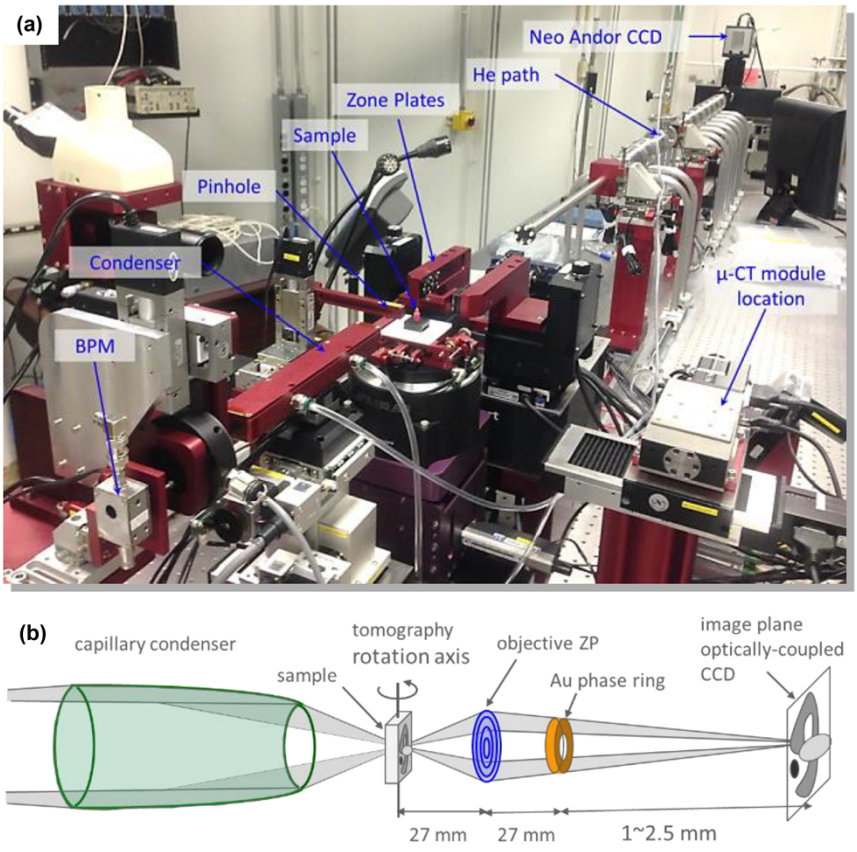

Figure 3.30 *a) Experimental setup of TXM. X-ray with a beamline 32-ID of the APS -ANL is focused on to the sample with a condenser where the field of view is increased. Pinhole removes the unfocused beam and the sample is rotated from 0 to 180 in 5 minutes. The detector system with scintillator screen converts X-rays to visible light and recorded by CCD camera on*

the other end. b)Schematic representation of TXM instrumentation showing condensed X-ray beam focused on the desired sample rotating in the rotor stage and captured by the optically coupled CCD camera on the other end.

Specific surface area calculation:

The theoretical calculation of specific surface area of the 1-mm thick LFP electrode is shown below. The pore shape is considered as a sphere, porosity is 48% and pore radius as 12 μm.

Volume of electrode (V_t)	=	1 m^3
Total porosity (V_p)	=	0.48
Radius of pore (r)	=	0.000012 m
Volume of 1 pore (V_{1pore})	=	$(4/3)*3.14*r^3$
	=	7.2E-15 m^3
Number of pores (N)	=	V_t/V_{1pore}
	=	6.63E13
Density of electrode (ρ)	=	1.83 g/cc
Surface area of 1 pore (SA_{1pore})	=	$4*3.14*r^2$
		1.8E-9 m^2
Total Sp.surface area $_{(Theo)}$	=	$N \times SA_{1pore} / ((1-V_p) \times V_t \times \rho)$
	=	0.126 m^2/g

Effect of thickness in electrochemical properties:

The gravimetric and areal capacities of different thick LFP half cells at C/20 rate are tabulated in 3.6.

Table 3.6 Gravimetric and areal capacity values of LFP electrodes with different thickness at C/20 rate.

Thickness (mm)	**LFP loading (mg/cm^2)**	**Discharge capacity @ C/20 rate Electrode pore size (12 µm)**	
		Gr. Cap. (mAh/g)	**Ar. cap. (mAh/cm^2)**
0.5	82	145	11.8
0.75	131	142	17.5
1.0	165	132	21.47
1.5	257	125	30.7
2.0	350	106	34.7
3.0	444	84	37.5

The specific capacities in terms of active material and surface area for the 2mm thick LFP electrodes against Li are shown in table 3.7.

Table 3.7 Gravimetric and areal capacities of 2mm thick LFP electrodes at different C-rates.

C-rate	**Gravimetric capacity (mAh/g)**	**Areal capacity (mAh/cm^2)**
0.01	124	40.5
0.02	115	39.2
0.05	106	34. 7
0.1	75.7	21.1
0.2	45.5	12.7
0.5	06	1.2

3.7 References

[1] S. Goutam, J.-M. Timmermans, N. Omar, P. V. den Bossche, and J. Van Mierlo, "Comparative Study of Surface Temperature Behavior of Commercial Li-Ion Pouch Cells of Different Chemistries and Capacities by Infrared Thermography," *Energies*, vol. 8, no. 8, pp. 8175–8192, Aug. 2015.

[2] M. Abdel Monem *et al.*, "Lithium-ion batteries: Evaluation study of different charging methodologies based on aging process," *Appl. Energy*, vol. 152, pp. 143–155, Aug. 2015.

[3] H. Lundgren, M. arten Behm, and G. Lindbergh, "Electrochemical characterization and temperature dependency of mass-transport properties of LiPF6 in EC: DEC," *J. Electrochem. Soc.*, vol. 162, no. 3, pp. A413–A420, 2015.

[4] T. Aoshima, K. Okahara, C. Kiyohara, and K. Shizuka, "Mechanisms of manganese spinels dissolution and capacity fade at high temperature," *J. Power Sources*, vol. 97–98, pp. 377–380, Jul. 2001.

[5] F. Mestre-Aizpurua, S. Hamelet, C. Masquelier, and M. R. Palacín, "High temperature electrochemical performance of nanosized LiFePO4," *J. Power Sources*, vol. 195, no. 19, pp. 6897–6901, Oct. 2010.

[6] B. Kang and G. Ceder, "Battery materials for ultrafast charging and discharging," *Nature*, vol. 458, no. 7235, pp. 190–193, Mar. 2009.

[7] S. G. Stewart and J. Newman, "The Use of UV/vis Absorption to Measure Diffusion Coefficients in LiPF[sub 6] Electrolytic Solutions," *J. Electrochem. Soc.*, vol. 155, no. 1, p. F13, 2008.

[8] A. Nyman, T. G. Zavalis, R. Elger, M. Behm, and G. Lindbergh, "Analysis of the Polarization in a Li-Ion Battery Cell by Numerical Simulations," *J. Electrochem. Soc.*, vol. 157, no. 11, p. A1236, 2010.

[9] J. S. Newman and K. E. Thomas-Alyea, *Electrochemical systems*, 3. ed. Hoboken, NJ: Wiley-Interscience, 2004.

[10] A. Mehrotra, P. N. Ross, and V. Srinivasan, "Quantifying polarization losses in an organic liquid electrolyte/single ion conductor interface," *J. Electrochem. Soc.*, vol. 161, no. 10, pp. A1681–A1690, 2014.

[11] V. Srinivasan and J. Newman, "Discharge Model for the Lithium Iron-Phosphate Electrode," *J. Electrochem. Soc.*, vol. 151, no. 10, p. A1517, 2004.

[12] N. Ding, S. Wei Chien, T. S. Andy Hor, R. Lum, Y. Zong, and Z. Liu, "Influence of carbon pore size on the discharge capacity of Li–O 2 batteries," *J. Mater. Chem. A*, vol. 2, no. 31, pp. 12433–12441, 2014.

[13] J. Chmiola, G. Yushin, R. Dash, and Y. Gogotsi, "Effect of pore size and surface area of carbide derived carbons on specific capacitance," *J. Power Sources*, vol. 158, no. 1, pp. 765–772, Jul. 2006.

[14] S. Kondrat, C. R. Pérez, V. Presser, Y. Gogotsi, and A. A. Kornyshev, "Effect of pore size and its dispersity on the energy storage in nanoporous supercapacitors," *Energy Environ. Sci.*, vol. 5, no. 4, p. 6474, 2012.

[15] A. Vu, Y. Qian, and A. Stein, "Porous Electrode Materials for Lithium-Ion Batteries - How to Prepare Them and What Makes Them Special," *Adv. Energy Mater.*, vol. 2, no. 9, pp. 1056–1085, Sep. 2012.

[16] S. Range and M. Epple, "Nanoscopic NaCl crystals as water-soluble porogens for polymer membranes," *RSC Adv.*, vol. 2, no. 16, p. 6650, 2012.

[17] M. Ender, J. Joos, T. Carraro, and E. Ivers-Tiffée, "Three-dimensional reconstruction of a composite cathode for lithium-ion cells," *Electrochem. Commun.*, vol. 13, no. 2, pp. 166–168, Feb. 2011.

[18] N. Epstein, "On tortuosity and the tortuosity factor in flow and diffusion through porous media," *Chem. Eng. Sci.*, vol. 44, no. 3, pp. 777–779, 1989.
[19] P. R. Shearing *et al.*, "Exploring electrochemical devices using X-ray microscopy: 3D micro-structure of batteries and fuel cells," p. 4, 2013.
[20] C. Lore, "HOME - Amira-Avizo Software," 11-Oct-2017. [Online]. Available: https://www.fei.com/software/amira-avizo/. [Accessed: 19-Feb-2018].
[21] B. Tjaden, S. J. Cooper, D. J. Brett, D. Kramer, and P. R. Shearing, "On the origin and application of the Bruggeman correlation for analysing transport phenomena in electrochemical systems," *Curr. Opin. Chem. Eng.*, vol. 12, pp. 44–51, May 2016.
[22] V. D. Bruggeman, "Berechnung verschiedener physikalischer Konstanten von heterogenen Substanzen. I. Dielektrizitätskonstanten und Leitfähigkeiten der Mischkörper aus isotropen Substanzen," *Ann. Phys.*, vol. 416, no. 7, pp. 636–664, 1935.
[23] S. Malifarge, B. Delobel, and C. Delacourt, "Determination of Tortuosity Using Impedance Spectra Analysis of Symmetric Cell," *J. Electrochem. Soc.*, vol. 164, no. 11, pp. E3329–E3334, Jan. 2017.
[24] I. V. Thorat, D. E. Stephenson, N. A. Zacharias, K. Zaghib, J. N. Harb, and D. R. Wheeler, "Quantifying tortuosity in porous Li-ion battery materials," *J. Power Sources*, vol. 188, no. 2, pp. 592–600, Mar. 2009.
[25] T. Hutzenlaub, A. Asthana, J. Becker, D. R. Wheeler, R. Zengerle, and S. Thiele, "FIB/SEM-based calculation of tortuosity in a porous LiCoO2 cathode for a Li-ion battery," *Electrochem. Commun.*, vol. 27, pp. 77–80, Feb. 2013.
[26] M. J. Blunt *et al.*, "Pore-scale imaging and modelling," *Adv. Water Resour.*, vol. 51, pp. 197–216, Jan. 2013.
[27] H. Dong and M. J. Blunt, "Pore-network extraction from micro-computerized-tomography images," *Phys. Rev. E*, vol. 80, no. 3, Sep. 2009.
[28] A. Torayev *et al.*, "Stochasticity of Pores Interconnectivity in Li–O_2 Batteries and its Impact on the Variations in Electrochemical Performance," *J. Phys. Chem. Lett.*, vol. 9, no. 4, pp. 791–797, Feb. 2018.
[29] S. J. Cooper, A. Bertei, P. R. Shearing, J. A. Kilner, and N. P. Brandon, "TauFactor: An open-source application for calculating tortuosity factors from tomographic data," *SoftwareX*, vol. 5, pp. 203–210, Jan. 2016.
[30] M. Ebner, D.-W. Chung, R. E. García, and V. Wood, "Tortuosity Anisotropy in Lithium-Ion Battery Electrodes," *Adv. Energy Mater.*, vol. 4, no. 5, p. 1301278, Apr. 2014.
[31] N. Ogihara, Y. Itou, T. Sasaki, and Y. Takeuchi, "Impedance Spectroscopy Characterization of Porous Electrodes under Different Electrode Thickness Using a Symmetric Cell for High-Performance Lithium-Ion Batteries," *J. Phys. Chem. C*, vol. 119, no. 9, pp. 4612–4619, Mar. 2015.
[32] J. Landesfeind, J. Hattendorff, A. Ehrl, W. A. Wall, and H. A. Gasteiger, "Tortuosity Determination of Battery Electrodes and Separators by Impedance Spectroscopy," *J. Electrochem. Soc.*, vol. 163, no. 7, pp. A1373–A1387, Jan. 2016.
[33] N. Ogihara, S. Kawauchi, C. Okuda, Y. Itou, Y. Takeuchi, and Y. Ukyo, "Theoretical and experimental analysis of porous electrodes for lithium-ion batteries by electrochemical impedance spectroscopy using a symmetric cell," *J. Electrochem. Soc.*, vol. 159, no. 7, pp. A1034–A1039, 2012.
[34] B.-S. Lee *et al.*, "Analysis of Rate-Limiting Factors in Thick Electrodes for Electric Vehicle Applications," *J. Electrochem. Soc.*, vol. 165, no. 3, pp. A525–A533, 2018.
[35] M. Doyle, T. F. Fuller, and J. Newman, "Modeling of Galvanostatic Charge and Discharge of the Lithium/Polymer/Insertion Cell," *J. Electrochem. Soc.*, vol. 140, no. 6, pp. 1526–1533, Jan. 1993.

[36] R. Zahn, M. F. Lagadec, and V. Wood, "Transport in Lithium Ion Batteries: Reconciling Impedance and Structural Analysis," *ACS Energy Lett.*, vol. 2, no. 10, pp. 2452–2453, Oct. 2017.
[37] C.-J. Bae, C. K. Erdonmez, J. W. Halloran, and Y.-M. Chiang, "Design of Battery Electrodes with Dual-Scale Porosity to Minimize Tortuosity and Maximize Performance," *Adv. Mater.*, vol. 25, no. 9, pp. 1254–1258, Mar. 2013.
[38] S. T. Taleghani, B. Marcos, K. Zaghib, and G. Lantagne, "A Study on the Effect of Porosity and Particles Size Distribution on Li-Ion Battery Performance," *J. Electrochem. Soc.*, vol. 164, no. 11, pp. E3179–E3189, Jan. 2017.
[39] C.-W. Ahn, B.-D. Hahn, D.-S. Park, and Y.-E. Sung, "Effect of Porosity on Cycle Performance in Three-Dimensional Disk Electrode for Li Ion Battery," *Jpn. J. Appl. Phys.*, vol. 50, no. 10R, p. 100201, Oct. 2011.
[40] Dimitrios Antartis, Shen Dillon, and Ioannis Chasiotis, "Effect of porosity on electrochemical and mechanical properties of composite Li-ion anodes," *J. Compos. Mater.*, vol. 49, no. 15, pp. 1849–1862, Jun. 2015.
[41] M. Singh, J. Kaiser, and H. Hahn, "Effect of Porosity on the Thick Electrodes for High Energy Density Lithium Ion Batteries for Stationary Applications," *Batteries*, vol. 2, no. 4, p. 35, Nov. 2016.
[42] H. Zheng, J. Li, X. Song, G. Liu, and V. S. Battaglia, "A comprehensive understanding of electrode thickness effects on the electrochemical performances of Li-ion battery cathodes," *Electrochimica Acta*, vol. 71, pp. 258–265, Jun. 2012.
[43] H. Kim, B. Han, J. Choo, and J. Cho, "Three-Dimensional Porous Silicon Particles for Use in High-Performance Lithium Secondary Batteries," *Angew. Chem.*, vol. 120, no. 52, pp. 10305–10308, Dec. 2008.
[44] M. Singh, J. Kaiser, and H. Hahn, "A systematic study of thick electrodes for high energy lithium ion batteries," *J. Electroanal. Chem.*, vol. 782, pp. 245–249, Dec. 2016.
[45] T.-S. Wei, B. Y. Ahn, J. Grotto, and J. A. Lewis, "3D Printing of Customized Li-Ion Batteries with Thick Electrodes," *Adv. Mater.*, p. 1703027, Mar. 2018.
[46] W. Lai *et al.*, "Ultrahigh-Energy-Density Microbatteries Enabled by New Electrode Architecture and Micropackaging Design," *Adv. Mater.*, vol. 22, no. 20, pp. E139–E144, May 2010.
[47] J. S. Sander, R. M. Erb, L. Li, A. Gurijala, and Y.-M. Chiang, "High-performance battery electrodes via magnetic templating," *Nat. Energy*, vol. 1, no. 8, p. 16099, Jul. 2016.
[48] L. Hu *et al.*, "Lithium-Ion Textile Batteries with Large Areal Mass Loading," *Adv. Energy Mater.*, vol. 1, no. 6, pp. 1012–1017, Nov. 2011.
[49] J. S. Wang, P. Liu, E. Sherman, M. Verbrugge, and H. Tataria, "Formulation and characterization of ultra-thick electrodes for high energy lithium-ion batteries employing tailored metal foams," *J. Power Sources*, vol. 196, no. 20, pp. 8714–8718, Oct. 2011.
[50] Sun Ke, Wei Teng-Sing, Ahn Bok Yeop, Seo Jung Yoon, Dillon Shen J., and Lewis Jennifer A., "3D Printing of Interdigitated Li-Ion Microbattery Architectures," *Adv. Mater.*, vol. 25, no. 33, pp. 4539–4543, Sep. 2013.
[51] D. Gürsoy, F. De Carlo, X. Xiao, and C. Jacobsen, "TomoPy: a framework for the analysis of synchrotron tomographic data," *J. Synchrotron Radiat.*, vol. 21, no. 5, pp. 1188–1193, Sep. 2014.
[52] F. De Carlo *et al.*, "Scientific data exchange: a schema for HDF5-based storage of raw and analyzed data," *J. Synchrotron Radiat.*, vol. 21, no. 6, pp. 1224–1230, Nov. 2014.
[53] D. M. Pelt and K. J. Batenburg, "A method for locally approximating regularized iterative tomographic reconstruction methods," *ArXiv160402292 Cs Math*, Apr. 2016.

Chapter 4

Towards the improvement in surface mechanism and fabrication of thick electrodes using other active materials

This chapter discusses the improvements in surface mechanism and the first results of the fabrication of thick binder free electrodes using other active materials for Li-ion batteries. The chapter was mainly divided into three sub sections as following: (1) Towards the improvement in surface mechanism of 1-mm thick LFP electrode using Atomic Layer Deposition (ALD), (2) Thick electrode fabrication of other active materials and (3) New electrode designs using SPS/Templating approach.

The first sub-section is about the experimental results of nano-coating of alumina (Al_2O_3) layer on the surface of thick LFP electrodes. The discharge capacity at high C-rates was compared between the non-coated and alumina coated 1-mm thick LFP electrodes. Secondly, sodium vanadium phosphate as cathode material for the sodium ion batteries and tin-antimony alloy as anode material were sintered for the fabrication of thick electrodes using the SPS/templating approach. The morphological and textural properties of the porous electrode were investigated and the first results of the electrochemical performance are reported against metallic sodium or lithium counterpart. The third sub-section includes the new possible cell designs of thick sintered electrodes using the SPS/Templating approach. Here we reporta three multi-layered single step battery consisting of $LiFePO_4$-$Li_{1.2}Zn_{1.9}Ca_{0.1}(PO_4)_3$-$Li_4Ti_5O_{12}$ layers and the first cycling performance of the full battery using a liquid electrolyte was investigated. The SPS/templating combined approach was also adopted for preparing new porous configurations with two layers of different pore sizes in the same electrode to promote better lithium ion diffusion inside the electrode.

4.1 Atomic Layer Deposition Al_2O_3 coating of 1-mm thick LFP electrodes

Surface coating of the active material/composite electrode was studied from the literature to provide the protective passivation film on the surface of the electrodes and to improve the interfacial reaction of the active material with the electrolyte [1]. The advantages of surface coatings are multi-fold and explained based on the type of coating materials, cycling conditions and type of coating methods.

First, surface coating of insulating materials (Ex. metal oxides) such as alumina is helpful in the inhibition of volume expansion of active materials when the electrodes undergo repeated charge/discharge cycling. For example, Xiao *et al.* [2] reported that Al_2O_3 coated Si thin films by ALD technique show better coulombic efficiency and capacity retention than the bare Si thin film, which is due to the suppression of volume change confirmed by the reduction of the formation of cracks. This improved colulombic efficiency was attributed to the fewer cracks generated on the Si film during cycling because the fractured surface would create a new unstable SEI layer. They also claimed that the formation of Al_2O_3/ AlF_3 and $LiAlO_2$ on the Si surface during cycling was confirmed by X-ray photoelectron spectroscopy (XPS) studies and this layer is going through a formation process and became ionically conductive and thereby providing a better Li^+-ion conductivity and enhance the charge transfer kinetics. Second, the conductive materials such as carbon nanotubes and conductive polymer binder are coated on the active material surface such as silica anodes [3]. This helps to improve the electron transfer through the interface of cathode material particles and provide extra electron conducting pathways among the cathode materials and current collector.

Another problem faced by the $LiPF_6$ based electrolyte systems in conventional lithium ion batteries is the decomposition of liquid electrolyte when the electrodes are cycled at extremely low or high potentials and at high current rates. The formation of HF occurs when it reacts with moisture, leading to the dissolution of transition metals and surface corrosion of cathode materials. In the literature to solve the problem, coating of nanosized ZnO particles is done to reduce the local acidity of electrolyte near the material surface [4]. The surface coating can also act as a physical protection barrier to suppress the chemical reaction on the surface of the active materials and liquid electrolyte such as oxidation of solvents and evolution of oxygen at high potential [5]. To avoid such problems, transition metal oxides

are coated such as ZrO_2[6], SiO_2[7], ZnO [8], Al_2O_3[9], $Al(OH)_3$[10], CeO_2[11], $AlPO_4$[12] and AlF_3[13]. All these inorganic oxides have a common nature that all the metal atoms have one stable valence state. One disadvantage of these materials is their low lithium ion conductivity and inactivity to lithium ion. So, excessive coating above the limiting range thickness leads to the loss of rate capability when coated after the limiting thickness of these insulating layers [14].

The coating method plays a vital role in achieving the uniform morphology of coating layer, which is important to achieve the better electrochemical properties. Though several methods such as rough coating [15] or core shell coating [16] strategy are available in the literature, Atomic layer deposition (ALD) is a prominent technique used to coat the conducting/insulating layer with uniform and controllable nanometer thickness on the surface of the complex substrates [7], [14], [17], [18]. The deposition of thin, pin-hole free conformal layers on the substrate helps to increase the mechanical and electrical properties of the electrodes. Alumina is an insulting material used to improve the mechanical stability of the particles by suppressing the volume expansion of lithiated transition metal oxides. Recently Jung *et al.* reported 2-6 atomic layers of alumina coated on the surface of $LiCoO_2$ that significantly increased the capacity retention of the electrode materials due to the suppression of LCO dissolution [19]. But, thick coating increases the interfacial impedance and electrochemical performance of LCO is deteriorated. Also, ALD process coupled with nanoindentation and nanoscratch techniques of the nano MoO_3 electrode enhances the mechanical properties thereby improving the cycling stability especially at high C-rates [20].

In our work, alumina (Al_2O_3) was coated on the entire cross volume of 1-mm thick LFP sintered electrodes using Atomic layer deposition (ALD) technique. This work was done in collaboration with Dr. Christophe Lethien, Institut d'électronique, de microélectronique et de nanotechnologie (IEMN), University of Lille, France. The main motivation of this work is to improve the mechanical properties of the thick pellet electrodes. Using ALD technique, the enhancement of the AM/electrolyte interface is achieved by the alumina coating of individual LFP particles in the entire volume of the full thick electrode. The entire electrode is uniformly coated with a pinhole free layer of alumina with different thickness done by the increase of ALD cycles. For a clear comparison, the three different thicknesses (1, 3 and 5 nm) of alumina layers were mentioned in the rest of this chapter. The chosen alumina coated LFP electrodes possess a porosity of 44% with 12 μm average pore size. The cross section SEM image

(Figure 4.1a) is shows the electrode thickness of 1-mm and the uniform pore size distribution was observed in the electrode morphology (Figure 4.1b). The thickness of alumina layer cannot be measured by SEM due to its lower thickness in nanometer range.

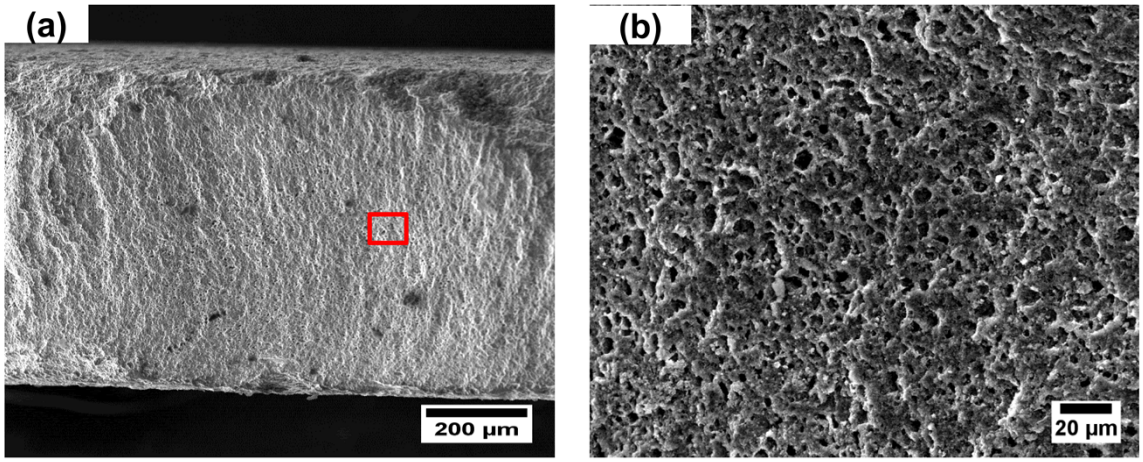

Figure 4.1 *(a) Cross sectional SEM image of the alumina coated 1-mm thick LFP electrode by ALD technique showing the 1-mm electrode thickness (b) higher magnification shows the uniform arrangement of pores present in the LFP electrode.*

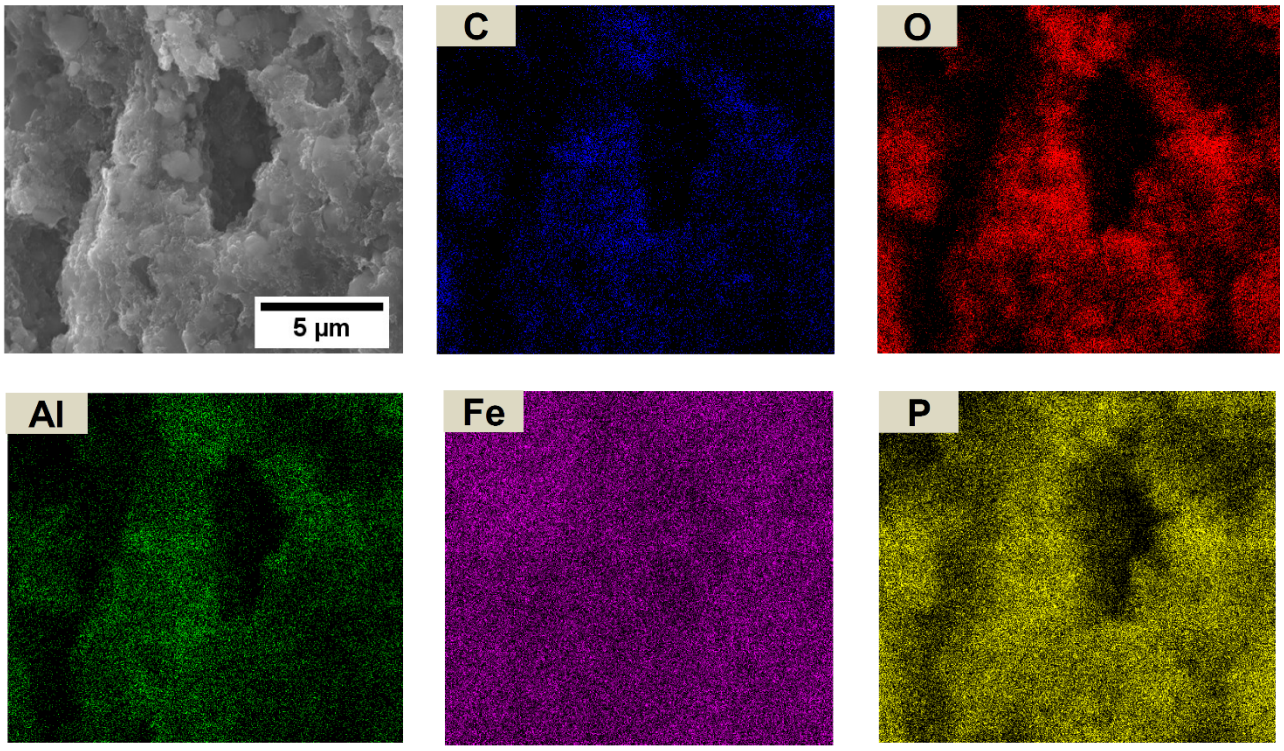

Figure 4.2 *EDX mapping of LFP electrode coated with 3nm thick Al_2O_3 using ALD technique. Crosss section of LFP electrode is shown in top left. The presence of Aluminium atoms confirm the alumina layer coating done on the surface of the LFP particles.*

Energy Dispersive X-ray mapping was done at the cross section of alumina coated LFP electrodes as acquisition area. A relatively uniform dispersion of aluminium along with other atoms was identified (Fig. 4.2) and proving that the coating was done uniformly over the surface of the cross section of LFP electrode. The atomic ratio of Al is increasing linearly as shown in the quantification table 4.1 confirming that there is an increase of alumina thickness.

Table 4.1 *EDX quantification results of the alumina coated LFP electrode showing the increase in aluminium content with the increase in layer thickness.*

Element	**Al_2O_3 thickness in LFP electrodes (atomic %)**			
	0 nm	**1 nm**	**3 nm**	**5 nm**
C	44.15	40.16	33.47	35.39
O	40.59	46.08	51.94	41.72
P	6.6	7.08	6.99	9.29
Fe	8.58	6.19	5.63	11.28
Al	0	0.24	1.37	2.32

The capacity retention tests were done for the alumina coated and non-coated 1-mm thick LFP electrodes against lithium at C/20 rate. As shown in figure 4.3a, the cell polarization is increased with the increase of insulating alumina layer in the LFP electrodes. At the end of 20th cycle, the discharge capacities of 0 nm, 1 nm, 3 nm and 5 nm are 45, 102 and 118 and 18 mAh/g and the corresponding capacity retention values are 32%, 77%, 89.7% and 13%. The increased capacity retention due to the alumina coating can be explained by the inhibition of volume expansion of LFP particles after repeated cycling. The limiting thickness (5nm) of alumina was identified due to its low capacity retention and poor rate capability as shown in figure 4.4b and 4.5. The poor performance of 5nm thick alumina coated LFP electrode can be linked to the increased charge transfer resistance of thick insulating layer which blocks the diffusion of lithium ions between the active material and electrolyte interface. The columbic efficiency (ratio of discharge to charge capacity) of all the four LFP electrodes with alumina thickness (0 nm, 1 nm, 3 nm and 5 nm) are 88%, 94%, 97% and 69% respectively.

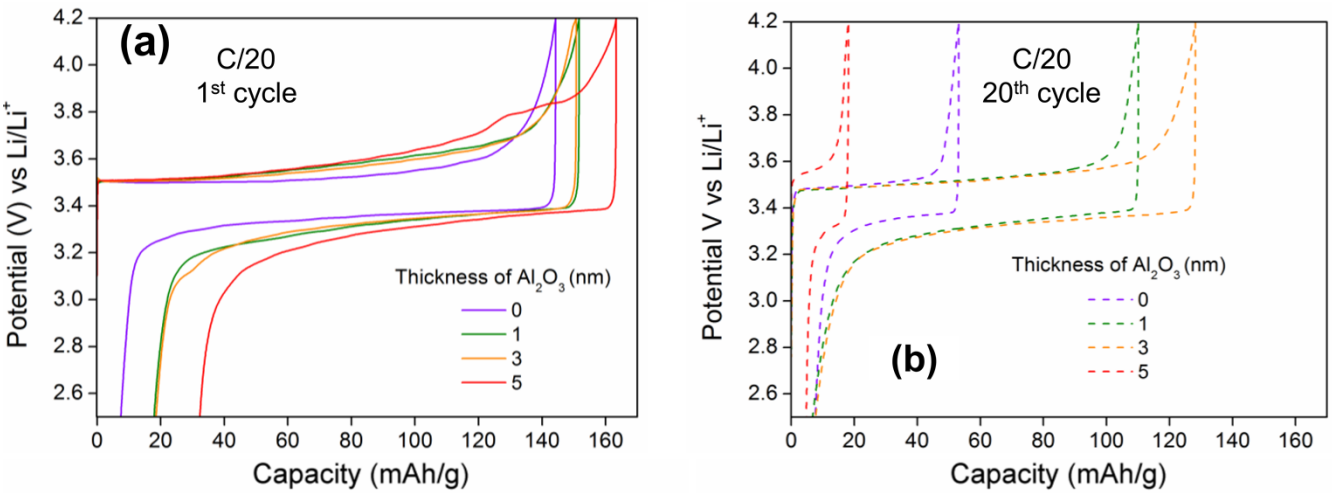

Figure 4.3 *a-b) Charge-discharge curve of 1-mm thick LFP electrodes with and without alumina coated by ALD vs lithium at C/20 rate:1st & 20th cycle.*

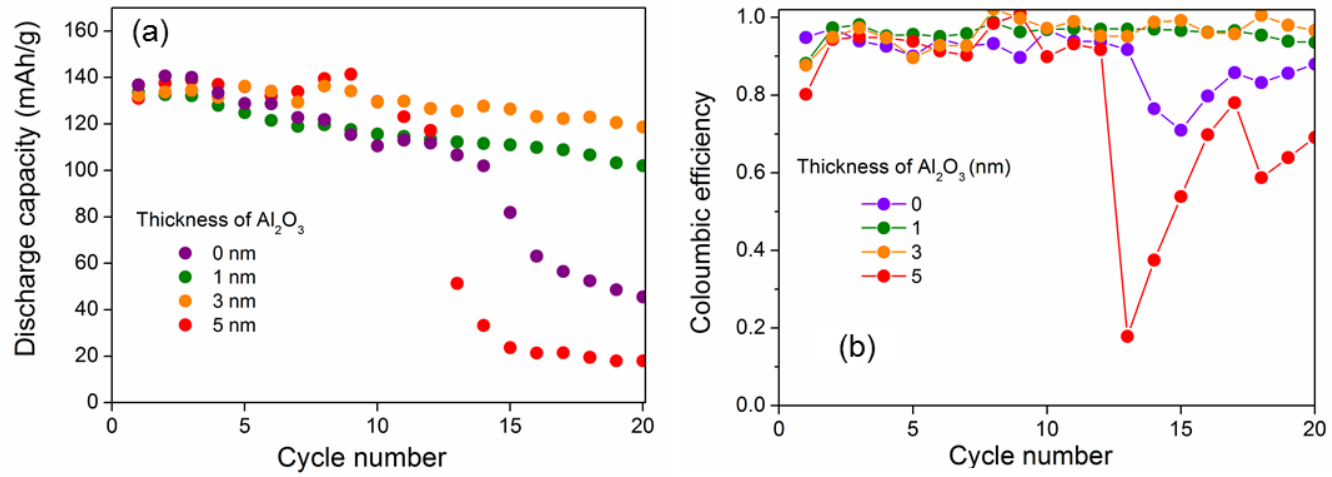

Figure 4.4 *a-b Capacity retention and Coulombic efficiency of alumina coated LFP electrodes using Atomic Layer Deposition (ALD).*

Rate capability tests were done for Al_2O_3 coated LFP electrodes against metallic lithium from C/20 to 1C rate and LP30 is used as liquid electrolyte. No significant difference in rate capability was observed between uncoated and Al_2O_3 coated LFP electrodes which shows no significant improvement of lithium ion diffusion limitations was achieved. At the same time, a lower C-rate performance of 5nm thick alumina coated LFP electrode was observed due to the increased interfacial resistance between the alumina and LFP particles. The poor performance of 5-nm thick alumina coated LFP was correlated with

the poor capacity retention as shown in figure 4.5 due to the blocking of the thick alumina layer preventing the diffusion of lithium ions at high C-rate.

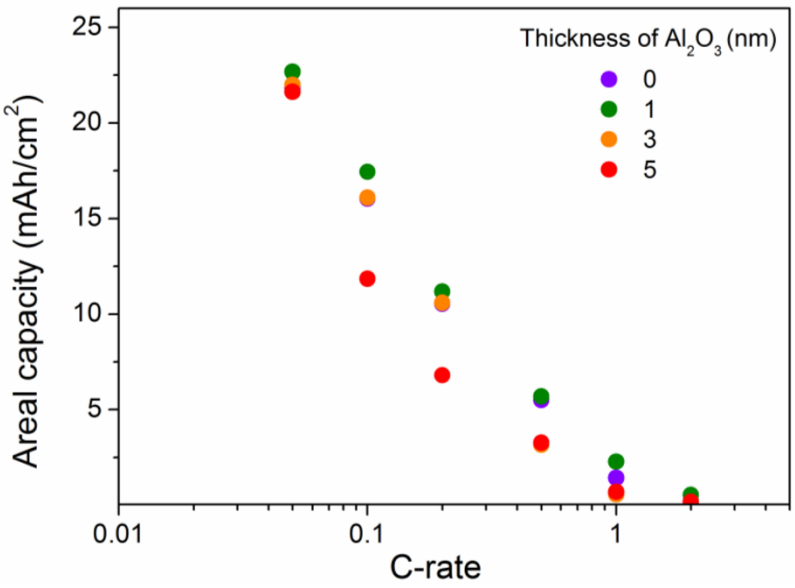

Figure 4.5 *Ragone plot showing the areal capacity of the alumina coated LFP electrodes at different C-rates.*

To sum up, the possibility of fine coating of foreign (either conducting or insulating) materials on the thick LFP electrodes can be performed using ALD technique. The alumina coating can also be done for the alloy based anodes such as large strain materials like silica or SnSb so that the volume expansion of active materials during lithium insertion and extraction can be greatly suppressed. Also, the mechanical strength of the relatively weak LTO sintered electrodes can be increased by the alumina coating to enhance the cycling retention. In the future, the ALD coating technique will be applied to extreme low/ high potential materials such as SnSb and NVPF thick electrodes to avoid electrolyte decomposition thereby stable SEI formation can be achieved to increase the coloumbic efficiency. The mechanical properties must be checked in the future for the alumina coated LFP electrodes thanks to indentation studies in order to know if the ALD technique is really a necessity at least from a mechanical point of view.

4.2 Thick electrode fabrication of other active materials

4.2.1 $Na_3V_2(PO_4)_2F_3$ thick electrodes for Sodium ion batteries

Sodium ion batteries (SIB) are considered as a potential alternative for Li-ion batteries due of their lower cost and the abundant nature of elemental sodium [22]. Sodium is the second lightest metal after lithium and the smallest alkali metal. The redox couple of Na^+/Na has a standard electrochemical potential of -2.71 V vs Standard Hydrogen Electrode (SHE), slightly higher than -3.04 V. Recently, it was estimated that the global market of sodium ion batteries will triple in value by 2022 [23]. The steady development of Na-ion batteries in terms of discovery of high voltage materials and high capacities are leading to the increase the energy density of SIB [24]. Steven *et al*. first reported the hard carbon as anode for sodium ion battery delivering high reversible capacity of 300 mAh/g which is comparable to the graphite anodes for lithium ion batteries [25]. Another major discovery is reported by Okada and coworkers that $NaFeO_2$ is electrochemically active in Na cells based on the $Fe^{3+/}Fe^{4+}$ redox couple [26] and this is the first positive electrode material commercialized for sodium ion battery. Recently, research interest for sodium ions was greatly improved and focused on the exploration of positive electrode materials for Na-ion batteries. The exploration of new sodium based materials with high capacity and high potential are aimed to fulfill the worldwide energy demand for electric vehicles and manufacture large scale batteries.

The polyanionic material $NaV_2(PO_4)_2F_3$ is serving as a promising cathode material for sodium ion batteries [27], [28]. NVPF is first proposed by Barker *et al.* as a positive electrode for Li ion batteries by assembling NVPF/Li^+ electrolyte/Graphite [29]. In this work, NVPF are reported as single-phase material with a tetragonal structure with space group of $P4_2/mnm$. The unit cell parameters (a= 9.0304(5) Å, c = 10.6891(9) Å) are determined from the least squares refinement procedure. In the first charge of an electrochemical reaction against metal sodium, the sodium ions are extracted from the flourophosphate material and at the same time, lithium ion intercalation takes place at the graphite counter electrode. After subsequent cycling, the mixed Li/Na insertion mechanism occurs and at the same time, the highly lithiated graphite is found to be electrochemically stable in the presence of Na^+ in the electrolyte phase. It can reversibly intercalate two moles of sodium ions in the crystal structure. The operating potential of NVPF vs Na is 3.95 V and the theoretical capacity of NVPF/Na is 128 mAh/g. The extraction of 2 Na^+ ions was observed by following the two main voltages -composition plateaus at about

3.7 V and 4.2 V vs sodium and delivering a theoretical energy density of 507 Wh/kg (128 Ah/kg at an average potential of 3.95 V) [29], [30]. This value is comparable to the commercial positive electrodes $LiFePO_4$ (580 Wh/kg) and $LiMn_2O_4$ (480 Wh/kg). NVPF material is well known for the excellent rate capability against metallic sodium reported in the literature [31]. Being a potential cathode material for sodium ion batteries, NVPF is chosen and 1-mm thick NVPF electrodes for sodium ion batteries were fabricated using SPS and templating approach.

Carbon coated NVPF material was obtained from the LRCS platform and was synthesized by the sol-gel method [32], [33]. First, commercial NaCl crystals with average particle size of 20 μm were used as a pore forming agent and mixed with the active material and sp-carbon with the composition of 50:40:10 vol. % (NVPF-NaCl-C). The experimental procedures such as composite preparation, SPS processing and NaCl dissolution process were followed in the same manner as for LFP electrode. After the SPS densification, the compacity of the NVPF-NaCl-C pellet is measured as 81%, which is very low compared to the LFP electrode. Cross sectional SEM images of NVPF electrodes (Fig.4.6a) show the thickness of 1.3 mm and pores are distributed through the entire volume of the NVPF electrodes with an average pore size of 10-20 μm as shown in figure 4.6b.

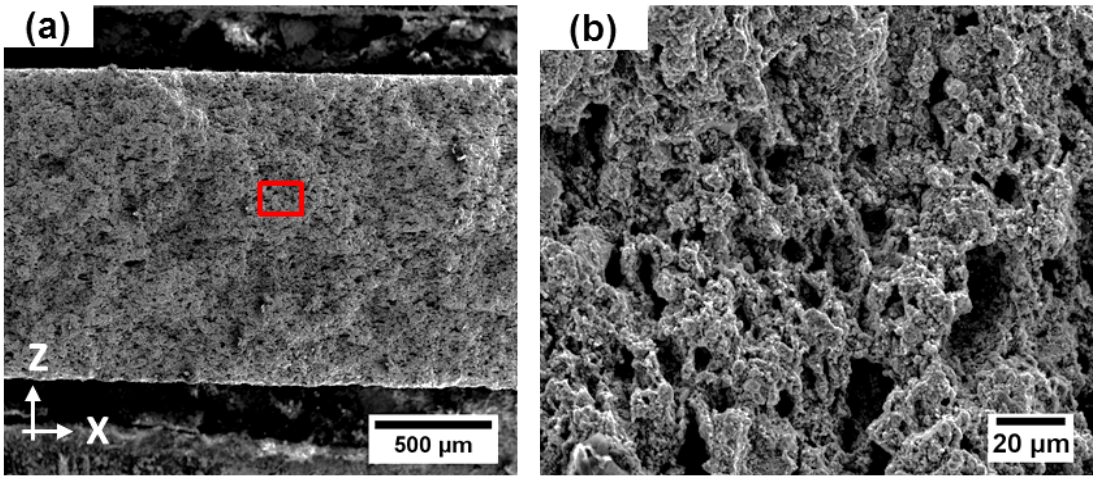

Figure 4.6 *Cross section SEM images of NVPF electrodes showing 1-mm thickness and closer magnification shows the pore size of 10-20 μm corresponds to the particle size of the NaCl crystal.*

Using the same experimental procedure, the NVPF electrode is fabricated with lesser pore size (5-10 μm) and porosity of 43% by reducing the initial particle size of NaCl crystals. SEM images of thick NVPF

electrode are shown in figure 4.8, which illustrates the electrode morphology with uniform pores and thickness of 0.75 mm. The electrochemical performance of the thick NVPF electrode with a mean pore size (5-10 µm) is cycled against sodium metal. The electrolyte used was 1M $NaPF_6$ in 1:1 EC: DMC with 3% Fluoroethylene carbonate (FEC) dissolved in the electrolyte and 2 layers of glass fiber separators were used. Recently, Dugas *et al.* reported that the addition of Flouro-ethylene carbonate (FEC) can minimize the irreversible capacity of NVPF/Na cells and increase the conductivity of the electrolyte [34].

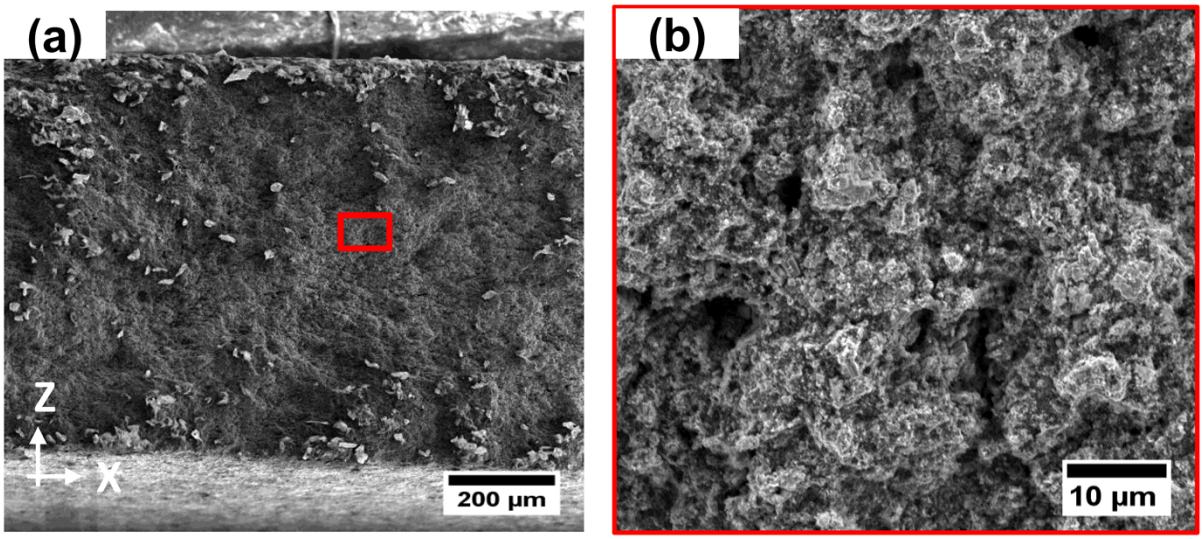

Figure 4.7 *a) Cross sectional SEM images of the 1-mm thick NVPF electrodes, b) Higher magnification.*

The charge-discharge cycling of the NVPF/Na cell at C/20 rate with a voltage range between 2.5 and 4.3 V is shown in figure 4.8. The two characteristic plateaus are observed for 1-mm thick NVPF/ Na at 3.7 V and 4.1 V, which corresponds to the oxidation of V^{2+} to V^{4+} and is found well in agreement with the literature [34], [35]. The sodiation/desodiation reactions are written in equations (4.1 and 4.2).

De-sodiation: $$Na_3V_2(PO_4)_2F_3 \leftrightarrow NaV_2(PO_4)_2F_3 + 2Na^+ + 2e^- \quad (4.1)$$

Sodiation: $$NaV_2(PO_4)_2F_3 + 2Na^+ + 2e^- \leftrightarrow Na_3V_2(PO_4)_2F_3 \quad (4.2)$$

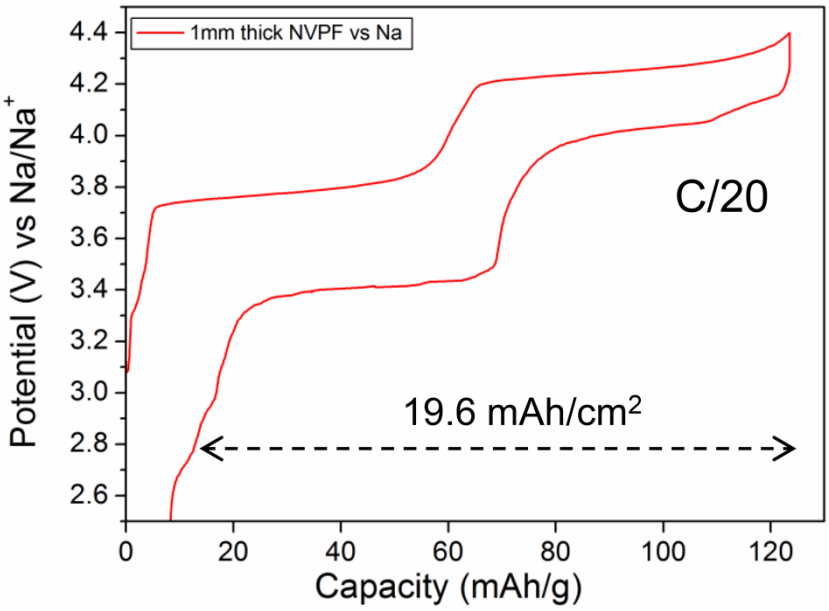

Figure 4.8 *Charge-discharge profile of 1-mm thick NVPF/Na at C/20 rate. Two composition plateaus are observed at 3.7V and 4.2 V due to de-intercalation of two sodium ions during charging.*

The first discharge capacity of first cycle of NVPF/Na cell is 113 mAh/g and equivalent to the areal capacity of 19.6 mAh/cm^2. The columbic efficiency of the first cycle is 92%. However, after the 2nd cycle, the cell was stopped due to the short-circuiting and the same problem occurred for the two repetitive cells tested with the same conditions. The dendrite formation in the sodium metal anode is a reason for the short circuiting which is observed after the post mortem analysis of the cell. The first results of the NVPF thick electrode are promising and the study will be continued in the future for further optimization.

4.2.2 Sn-Sb alloy anodes using SPS

Alloy based materials such as Si, Sn or Sb are possess higher theoretical capacities of 4200, 993, 660 mAh/g respectively than commonly used graphite material (372 mAh/g) as anode and lower working voltage compared to LTO electrode (1.5 V) [36]–[38]. The main problem of alloy based anode materials is the large volume expansion which occurs during the alloying/de-alloying reaction [39], [40]. For example, Li_xSn alloy undergoes ~257% of volume expansion after the charge-discharge which is leading to the unstable SEI formation, in turn leading to poor capacity and columbic efficiency [41]. Therefore, several approaches such as carbon coating matrix element with active/inactive materials and improved synthesis strategies like electrostatic spray deposition, ink-jet printing, radio-frequency sputtering to reduce the capacity fading in Sn based anodes [42]–[44].

In our work, the thick porous Sn-Sb anode was prepared by the combined approach of SPS and salt templating. SnSb material was chosen due to its relatively higher thermal stability (Melting point of SnSb: 420 °C) compared to the pristine Sn metal (Melting point: 246 °C). This facilitates to adopt the SPS process for making thick SnSb electrode where the NaCl crystals are also stable at this temperature during SPS densification. Before electrode fabrication, Sn-Sb alloy material was first synthesized by ball milling of nanosized tin and antimony powders (1:1 molar ratio) as per the literature [45]. The two batches of 1 g and 8 g (total amount) were ball milled for 1 hour using high-speed planetary ball milling. The powder:ball ratio taken was 1:30 and milled in Argon atmosphere. The obtained two batches of Sn-Sb alloy materials were characterized by X-ray diffraction to analyze the crystalline nature and confirmed the alloy formation of the Sn-Sb material. The lattice parameters of the pure SnSb material (green) (a=b=4.3255 A, c=5.3465 A) were obtained with a rhombohedral crystal structure (R-3m) which is in-line with literature [45] and showed no other impurities .

As shown in the XRD diffraction pattern (Figure 4.9), the crystalline peaks of Sn-Sb alloy (8g batch) were obtained with the presence of unreacted Sn impurity peak at 28°. The impurities were observed due to the incomplete reaction occurred due to large amount of precursors taken in the ball milling jar. The as-prepared Sn-Sb materials were mortared with NaCl and sp-carbon in 50:40:10 vol%. The carbon particles mixed to the surface of Sn-Sb alloy ensure a percolated electronic network to increase the electrical conductivity of the thick electrode.

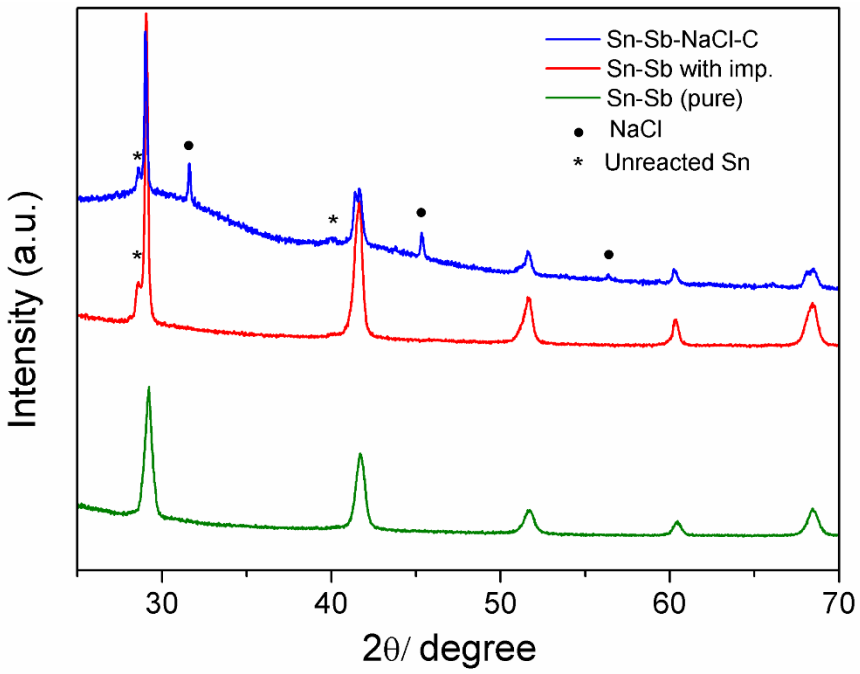

Figure 4.9 *XRD pattern of as prepared SnSb alloy powders and SnSb-NaCl-C powder composite fabricated by SPS.*

The as prepared Sn-Sb-NaCl-C powder composite is subjected to DSC analysis to determine the thermal stability of the Sn-Sb materials and thus the SPS conditions for sintering the SnSb-NaCl-C composite are optimized. The temperature was limited to 700 °C in order to prevent the melting of NaCl crystals at its melting point (800 °C). As shown in figure 4.10, the peak at 420.9 °C showed the melting of Sn-Sb alloy and thus the SPS temperature was limited to 350 °C to avoid the melting of SnSb material during SPS reaction. The small peak at 246.6 °C corresponds to the melting of unreacted tin components still present during the synthesis of Sn-Sb and also confirmed by the X-ray diffraction.

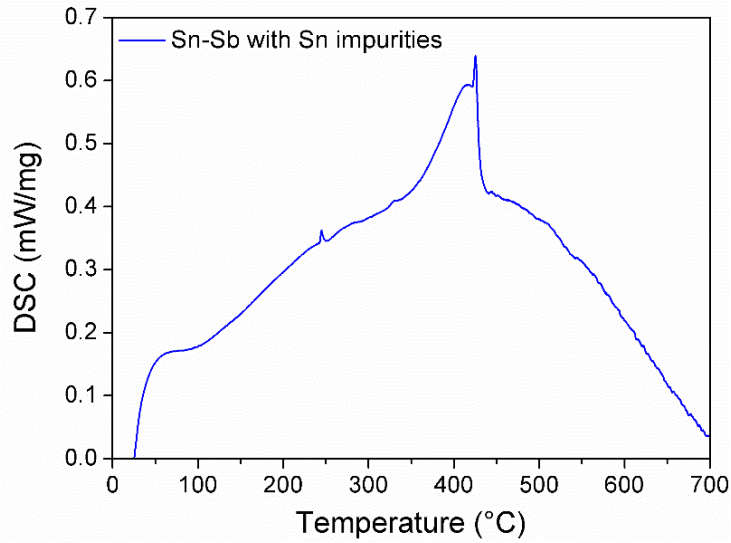

Figure 4.10 *DSC curve of Sn-Sb-NaCl-C composite confirming the melting point of Sn-Sb alloy at 423.9 C and Sn impurities at 225 C present during the alloy preparation.*

Later, the total amount of Sn and Sb particles taken for ball milling was reduced to 1 g for 1 hour. This helps to prevent incomplete ball milling of initial components. In this case, no unreacted tin impurities were observed in the X-ray diffraction (Figure 4.9). DSC analysis of the as prepared pure Sn-Sb material were done, and showing one melting peak was observed at 425 °C due to SnSb alloy. This confirms that no impurity is present in the anode material (Fig. 4.11). The small peak at 80°C is due to the removal of moisture present in the Sn-Sb material.

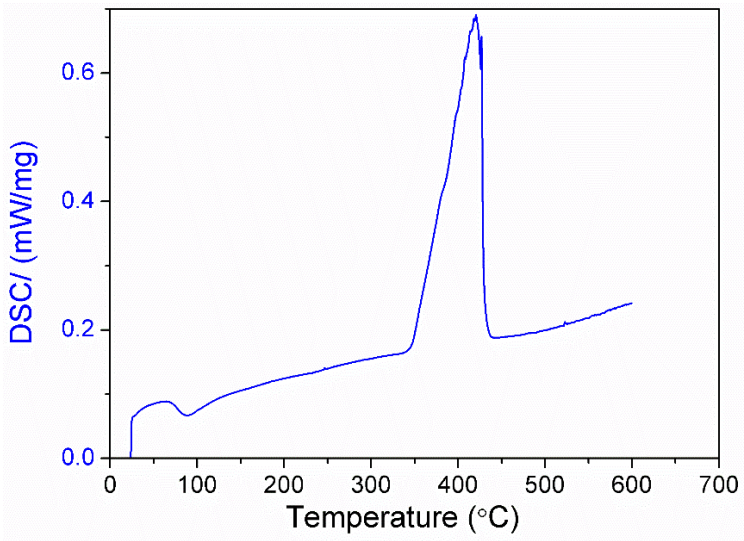

Figure 4.11 *DSC curve of Sn-Sb-NaCl-C composite confirming the melting point of Sn-Sb alloy and Sn impurites present during te alloy prepapration.*

The as prepared Sn-Sb-NaCl-C composite (350 mg) were placed in the graphite dye and cold pressed at 4kN before SPS operation. Then, the SnSb-NaCl-C powder composite was sintered at a temperature of 350 °C with an applied pressure of 10 kN and holding time of 5 minutes in Argon atmosphere. After the SPS operation, the thick Sn-Sb pellet was carefully recovered from the graphite dye. The compactness of the Sn-Sb-NaCl-C pellet after the SPS operation was determined as 80%, which is lower than the LFP (95%). The as prepared SnSb-NaCl-C pellet was subjected to water for dissolving the templating agents present inside the pellet and creating a porosity of 51% determined from the weight loss of NaCl. A cross-section SEM image of SnSb-C electrode shows the thickness of 0.65 mm with uniform pore arrangement in the entire volume of thick electrode (Figure 4.12a). The pores are clearly visible in the morphology of the SnSb electrode with average pore size of around 10-20 µm as shown in SEM images (Figure 4.12b).

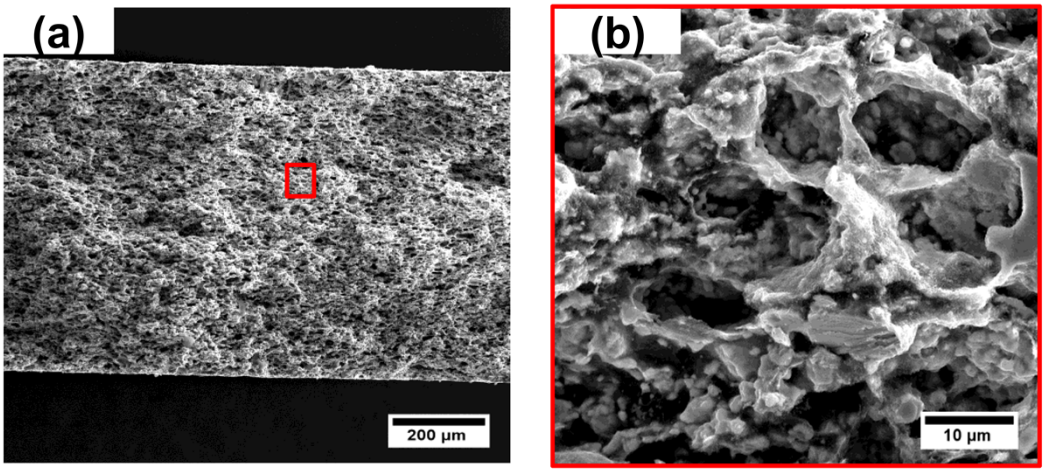

Figure 4.12 *SEM images of SnSb electrode showing the 0.65 mm thickness and electrode morphology with uniform distribution of pores created by the NaCl dissolution.*

The vacuum dried Sn-Sb-C pellet was subjected to SEM-EDX mapping as shown in figure (4.13a) to detect the presence of individual elements and found that Sn, Sb and C are uniformly dispersed in the cross section. The quantification analysis in figure 4.13b shows that the oxygen atoms are present along with the C, Sn and Sb atoms, which is due to the formation of SnO_2 because of the water washing of NaCl in the SnSb electrode.

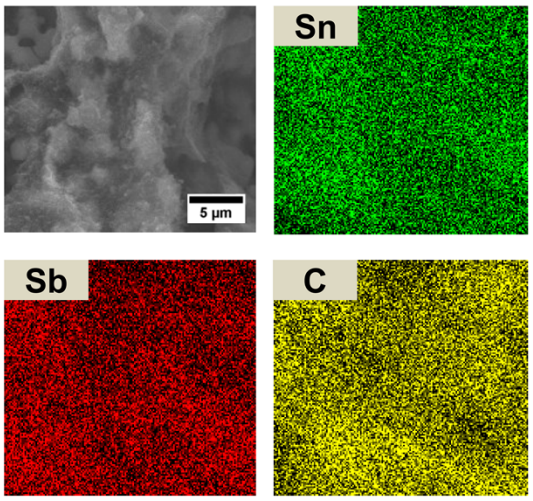

(b)

Element	Weight %	Atomic %
C	12.06	75.89
O	2.23	10.51
Sn	11.27	7.17
Sb	9.99	6.20
Total	35.55	

Figure 4.13 *a) EDX mapping of 1-mm thick SnSb electrode fabricated using SPS and templating strategy showing the tin and antimony are homogeneously distributed in the Sn-Sb surface, b) Quantification of individual components present in the SnSb alloy electrode.*

The electrochemical testing of Sn-Sb/Li was done by using 0.65 mm thick Sn-Sb as working electrode and metallic lithium as a counter electrode. The selected voltage range of half-cell was 0.01 to 1V. Conventional liquid electrolyte (LP30) was used with 2 layers of glass fiber separator. The first charge-discharge profile of SnSb/Li is shown in figure 4.14 which displays the discharge plateaus at 0.8 V, 0.7 V, 0.55 V and 0.35 V which is well in agreement with the literature [46].

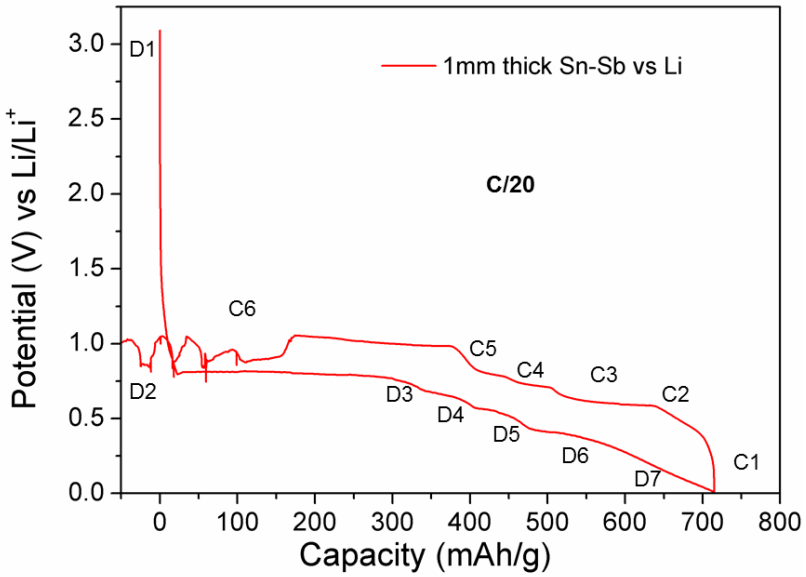

Figure 4.14 *Charge-discharge profile of 0.65 mm thick SnSb/ Li showing the plateaus representing the alloying/ de-alloying reaction of Sn and Sb with lithium.*

The discharge of the SnSb/Li cell is associated with the lithium-SnSb alloying process as per the equation 4.3 and shown in figure 4.14. A large flat plateau (D2-D3) was obtained at 0.8 V, corresponding to the lithium antimony alloy formation, Li_3Sb and metallic tin. It involves a ternary phase formation of Li_xSnSb where $0 < x < 0.1$. The corresponding discharge capacity from D1-D3 region is determined as 330 mAh/g which is already two times higher than the theoretical capacity of LTO electrode (175 mAh/g).

$$3Li^+ + SnSb + 3e^- \leftrightarrow Li_3Sb + Sn \tag{4.3}$$

The second region from D3 to D7 corresponds to lithium alloying with tin as shown in the equation 4.4. This lithium-tin alloying is taking place with 3 plateaus at D4, D5 and D6 between the voltage range of 0.7-0.01 V vs lithium. The theoretical capacity of the Sn-Sb alloy is calculated according to equation 4.5.

$$xLi^+ + Sn + xe^- \leftrightarrow Li_xSn\ (0 < x < 4.4) \tag{4.4}$$

$$Theoretical\ capacity\ of\ SnSb = 26.8 * \left[\frac{(0.5 * 3) + (0.5 * 4.4)}{(0.5 * MW_{Sn}) + (0.5 * MW_{Sb})}\right] = 825\ \text{mAh/g} \tag{4.5}$$

The discharge capacity of the first cycle at C/20 was calculated as 714 mAh/g which is two times higher than the theoretical capacity of the graphite anode (372 mAh/g). The corresponding areal capacity of SnSb/Li is 46.2 mAh/cm^2, which is due to the high loading of Sn-Sb electrode (228 mg/cm^2). The irreversible nature of the SnSb electrode was observed in the second cycle and this same problem was observed repetitively for two cells. The performance of the SnSb electrode is strongly affected by the formation of an unstable SEI layer which takes place due to the discharge at low potential close to zero. Large volume expansion during the de-alloying of SnSb was taking place and the electrode cracking was observed from the SEM images as reported in the literature [46]. The SnSb electrode will start degrading at 0.68 V leading to the unstable SEI formation. To avoid these problems, SnSb/Li cell can be limited up to 0.7 V because the cell is already delivering a discharge capacity of 300 mAh/g up to this region which is two times higher than LTO electrode (175 mAh/g). The assembly of full cell (LFP/SnSb) system can be done in the future to prevent the bad effects of lithium metal. The LFP/SnSb full cell will operate at a cell potential of 3 V which is higher than that of LFP/LTO cell (1.9 V) and hence the energy density of the lithium ion batteries can be increased.

4.3 New electrode designs using SPS/Templating

4.3.1 $LiFePO_4$ -$Li_{1.2}Zn_{1.9}Ca_{0.1}$ $(PO_4)_3$ -$Li_4Ti_5O_{12}$ full battery

Spark Plasma Sintering (SPS) has been recently used for fabricating all solid state batteries (ASSB) [47], [48]. One main reason for the ASSB fabrication using SPS is the enhanced interfacial properties achieved in a short time when sintering the electrode and solid electrolyte layers. The SPS technique helps to achieve the structural stability of the electrode-electrolyte interfaces with reduced grain boundary resistances in the ASSB probed by impedance spectroscopy [49]. Also, good charge transfer and mechanical integrity upon cycling were obtained leading to the development of all solid state batteries using SPS [50]–[52]. Since this approach is easily applicable, it is decided to make a multilayered single step battery made up of $LiFePO_4$ -$Li_{1.2}Zn_{1.9}Ca_{0.1}(PO_4)_3$ -$Li_4Ti_5O_{12}$ (LFP-LCZP-LTO). For the positive and negative layers, the powder composites were prepared by mortaring three different components (LFP/ LTO, NaCl and sp-Carbon) for each layer in a composition of 50:40:10 vol.%. The corresponding weight composition of each layer (LFP-LCZP-LTO) is 1:1.25:1. The weighed composite was taken in the graphite dye for the SPS operation and each layer was cold pressed at 4kN. The SPS conditions were 650 °C at 8 kN pressure. The solid electrolyte, $Li_{1.2}Zn_{1.9}Ca_{0.1}(PO_4)_3$ (LCZP) was synthesized by the sol gel method according to the literature [53]. The middle ceramic layer is acting as an electronic insulating medium between positive and negative electrode layer and the conventional liquid electrolyte was used as an ionic conducting medium. The solid electrolyte layer possesses a relatively lower compacity than the electrode layer sintered at 650 °C and this porosity enables the liquid electrolyte to flow through the porous ceramic layer during cell operation. The thickness of the as prepared three layered battery (LFP-LCZP-LTO) is 2.3 mm and with a diameter of 10 mm. The SEM image of the full battery is shown in inset of fig. 4.15a. Later, the thick pellet was subjected to NaCl dissolution to create pores in the electrode layers.

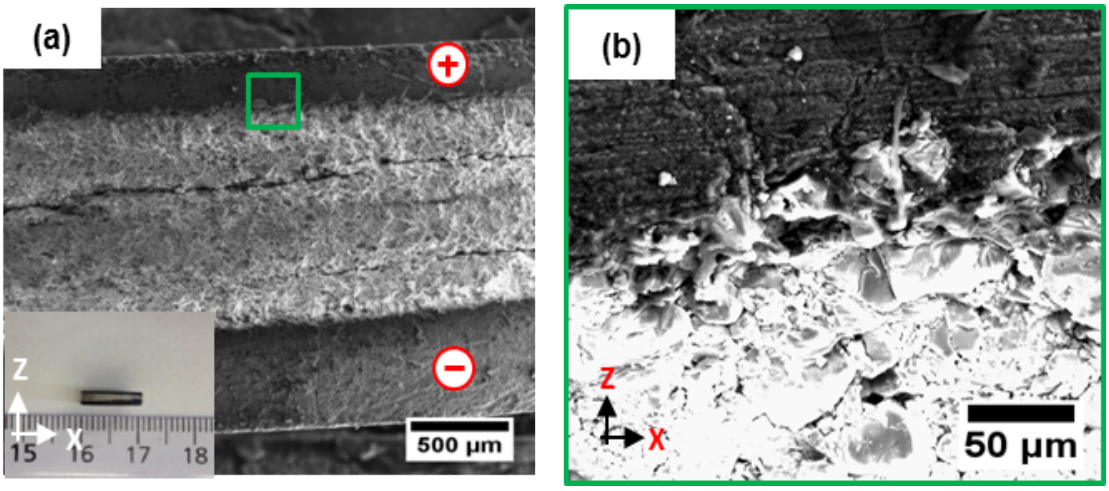

Figure 4.15 *a) SEM image of Cross section of LFP:LCZP:LTO battery system showing 2.3 mm overall thickness, b)LFP-LCZP interface showing strong interface obtained with grain-grain bonding.*

The obtained mass loss is found to be 37% of the total salt particles present in the three layered pellet. Cross sectional SEM image (Figure 4.15) shows the clear interface obtained between each layer and cracks are obtained in the ceramic layer due to less compacity. In the closer view of the full battery as shown in figure 4.15b, the electrode-electrolyte interface is obtained with a good grain-grain contact within the LFP particles as well as between the active materials and the solid electrolyte. SEM images (Figure 4.16) of the surface of the LFP and LTO individual layer show the pores created after the NaCl dissolution with cubic shape.

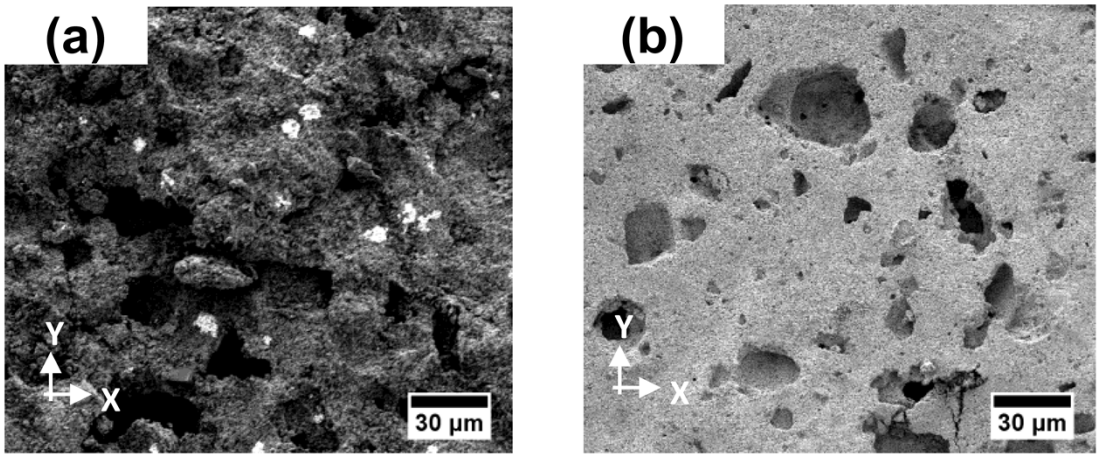

Figure 4.16 *The surface view of LFP and LTO layer present in the LFP-LCZP-LTO battery system showing the pores created in the thick electrode due to the NaCl dissolution*

The galvanostatic charge-discharge of multi-layered single step battery (LFP-LZCP-LTO) was done initially at C/20 rate but the cell was stopped after the first discharge. Later, the full battery was cycled at C/200 rate using LP30-classical liquid electrolyte as ionic medium. The lithium ion was cycled between LFP and LTO electrode layer by showing a flat plateau at 1.9 V (Ecell=3.5-1.6 V) in the first charge as shown in figure 4.17. The input current was applied as per the mass of LFP material present in the positive electrode layer.

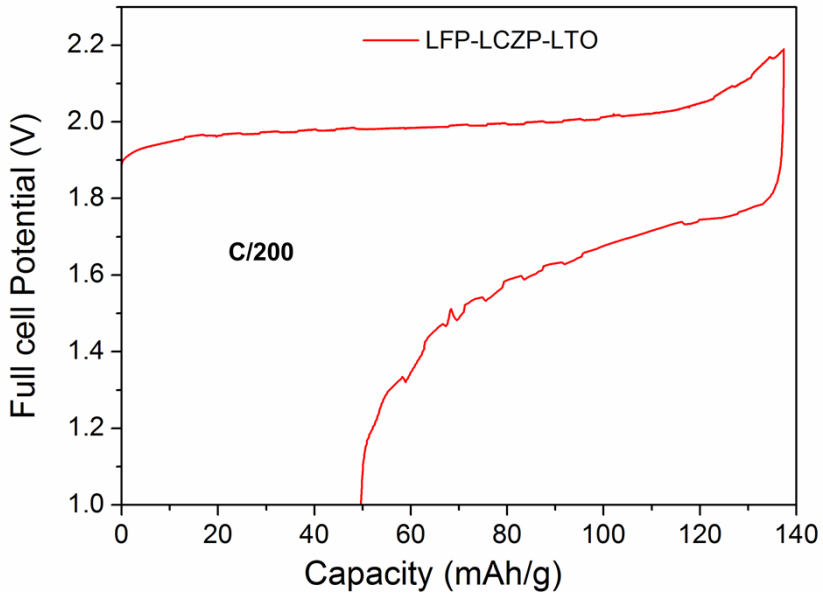

Figure 4.17 *Charge-discharge profile of LFP/LCZP/LTO full battery at C/200 rate showing the charge plateau close to 1.9 V due to the LFP/LTO full cell.*

The first charge and discharge capacity of the complete battery is 130 and 88 mAh/g obtained at C/200 rate. A huge cell polarization was observed as shown in figure 4.17 due to the solid electrolyte thickness and the cell was showing a decrease in cell potential after the first cell discharge, which may be due to the volume expansion of LFP particles after the first cycle. Nevertheless, this study is a first attempt and the optimization of SPS conditions, amount of composite in each electrode layer and thickness of the solid layer region has to be done in future. This multilayer fabrication concept of sintering electrode and solid electrolyte layer using SPS opens up a new way to assemble a full lithium ion battery in a single step so that the processing cost can be reduced compared to the conventional Li-ion battery technology.

4.3.2 Porous configurations of LFP electrode

Templating is a simple and efficient method to create controllable porosity and pore size in the battery electrodes. This helps to optimize the lithium ion diffusion during cell operation. In our SPS/ templating approach, there is an extra benefit of preparing thick electrodes with graded porosity or pore size in it. Two layers of different sized pores in the same electrode are created to enhance the diffusion process of liquid electrolyte. The two LFP-NaCl-C composites are stacked, having two template particle sizes (14 and 2 μm) present in the composite and the composition remained same (50:40:10 vol.%). The graphite dye containing the LFP-NaCl-C composite is cold pressed at 4 tons before the sintering operation. Using SPS, the composite is densified and the compacity of the LFP-NaCl-C pellet is determined as 95%. SEM image of the as prepared LFP electrode is showing the overall thickness of 1.2 mm (Figure 4.18a). After SPS sintering, the LFP electrode is subjected to NaCl dissolution by water and the two layers of porous regions (20 and 2 μm) are observed. The obtained LFP electrodes are obtained with 44% of total porosity measured by the weight loss method.

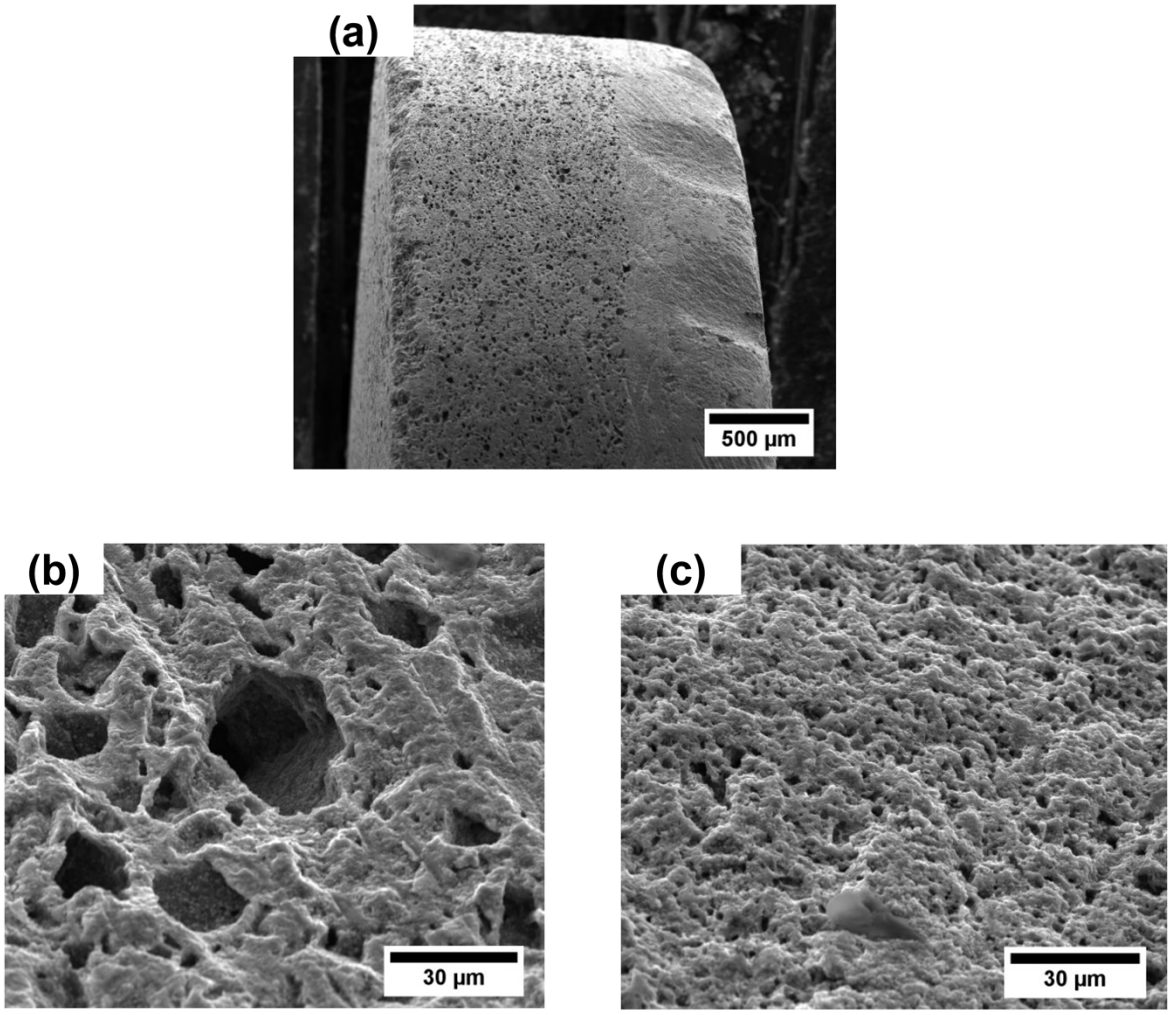

Figure 4.18 *(a) The thick LFP electrode with two layers of different pore sizes obtained by using two different particeles sized templates. (b-c) Higher magnification of LFP electrodes in each layer showing the larger and smaller pores.*

From figure 4.18b,c the left side layer of LFP electrode is made up of relatively bigger pores (20 µm) obtained by dissolving the mortared bigger salt particles and the right side layer is obtained by dissolving smaller particle sized NaCl crystals (2 µm). The concept of making thick LFP electrode with graded pore size is helpful for promoting the electrolyte transport depending on the separator-electrode interface and current collector side-electrode interface. The electrochemical testing was not done for this graded pore sized LFP electrode. This concept shows the possibility of preparing such electrodes for the complex battery systems such as Li-air or Li-sulphur battery systems because the pores in the electrode are blocked by the super-oxides or sulphides that prevent lithium ion diffusion leading to poor electrochemical performance.

4.4 Conclusion

In this chapter, the thin, pinhole free and uniform layer of alumina (1, 3 and 5 nm thick) are 3D coated on the surface of 1-mm thick binder free electrodes using ALD technique. The presence and well dispersion of aluminium atoms over the surface of LFP particles are confirmed by EDX-mapping analysis on the cross section of thick LFP electrode. An increase of Al atomic ratios was observed, which confirms the increase of alumina layer thickness. The pores of the thick LFP electrodes were coated by alumina so that the surface of the active materials is protected by the physical layer helpful in suppressing the volume expansion of LFP particles due to the repeated cycling. Compared to the bare LFP electrode, an Al_2O_3 coated LFP electrode shows better capacity retention which is due to the suppression of volume expansion of LFP particles. No significant difference was observed in rate capability. This ALD coating approach is applicable for less mechanically stable negative electrodes to enhance the indentation properties, prevent HF formation at low and high potentials and avoid dendrite formation at high C-rates for the metal based lithium ion batteries.

The thick electrode fabrication was done for the NVPF and SnSb material using SPS/templating. First, the 1-mm thick NVPF electrode with around 40% porosity was fabricated. The well-connected 3D diffusion pathways for the liquid electrolyte inside the NVPF electrode was achieved using templating strategy and helpful for ionic conduction. The pore morphology was studied by the SEM confirming the uniform arrangement of pores distributed throughout the entire electrode volume. No trace of salt particles is present in the thick NVPF electrode after NaCl dissolution based on the weight loss as well as clear galvanostatic curve. The galvanostatic cycling of 1-mm thick NVPF/Na has revealed higher areal capacity (~20 mAh/cm^2) due to the high loading of the active materials.

Secondly, SnSb alloy material was synthesized using the ball milling technique and the well crystalline nature of the SnSb alloy was detected by XRD diffraction pattern. TGA and DSC analysis of SnSb-NaCl-C were done to determine the thermal stability of these materials and optimize the SPS reaction parameters. The fabrication of 0.65 mm thick SnSb electrode was done using SPS and templating approach. SEM images of SnSb thick electrodes show the pore distribution was distributed ver the entire electrode and helpful for the lithium ion diffusion. The first electrochemical testing of thick SnSb/Li at C/20 revealed the lithium alloying/ de-alloying reactions with the characteristic plateaus at their

respective potentials. This clearly shows that thick electrode fabrication using SPS/templating approach can be successfully applied to other active materials to obtain higher areal capacity.

The third subsection of the chapter reported the preparation of new electrode designs such as the fabrication of a single step (LFP-LCZP-LTO) full battery using SPS and templating approach. For the first time, the electrode and electrolyte layer are sandwiched along the templating agents and sintered using SPS. No decomposition of active materials or solid electrolyte was observed after the SPS reaction. SEM images of the full battery show good interfacial properties between different layers and within the solid grains in the electrodes. The first electrochemical cycling curve at C/200 at room temperature shows a flat plateau at 1.9 V and delivering an initial discharge capacity of 88 mAh/g. This clearly shows that the full battery (LFP-LCZP-LTO) was able to cycle lithium ion between positive and negative electrode by using liquid electrolyte. The optimization of the SPS reaction conditions, formulation of electrode layers, ceramic layer thickness and cycling temperature are need to be improved in the future and this work will be continued by a new PhD student who will start in this academic year. Overall, several possibilities to fabricate thick electrodes and a full battery using SPS and templating approach are discussed and this clearly shows that our approach is not only easily adaptable to understand the fundamental concepts behind the thick electrodes but also considered worthwhile to manufacture high energy batteries to power the small scale devices.

4.5 References

[1] Z. Chen, Y. Qin, K. Amine, and Y.-K. Sun, "Role of surface coating on cathode materials for lithium -ion batteries," *J. Mater. Chem.*, vol. 20, no. 36, pp. 7606–7612, 2010.

[2] X. Xiao, P. Lu, and D. Ahn, "Ultrathin Multifunctional Oxide Coatings for Lithium Ion Batteries," *Adv. Mater.*, vol. 23, no. 34, pp. 3911–3915, Sep. 2011.

[3] J. Liu *et al.*, "Rational Design of Atomic-Layer-Deposited $LiFePO_4$ as a High-Performance Cathode for Lithium-Ion Batteries," *Adv. Mater.*, vol. 26, no. 37, pp. 6472–6477, Oct. 2014.

[4] Y.-K. Sun, Y.-S. Lee, M. Yoshio, and K. Amine, "Synthesis and Electrochemical Properties of ZnO-Coated LiNi[sub 0.5]Mn[sub 1.5]O[sub 4] Spinel as 5 V Cathode Material for Lithium Secondary Batteries," *Electrochem. Solid-State Lett.*, vol. 5, no. 5, p. A99, 2002.

[5] A. R. Armstrong *et al.*, "Demonstrating Oxygen Loss and Associated Structural Reorganization in the Lithium Battery Cathode Li[Ni0.2Li0.2Mn0.6]O2," p. 5.

[6] A. Nakajima, T. Kidera, H. Ishii, and S. Yokoyama, "Atomic-layer deposition of ZrO2 with a Si nitride barrier layer," *Appl. Phys. Lett.*, vol. 81, no. 15, pp. 2824–2826, Sep. 2002.

[7] J. D. Ferguson, E. R. Smith, A. W. Weimer, and S. M. George, "ALD of SiO2 at Room Temperature Using TEOS and H 2 O with NH 3 as the Catalyst," *J. Electrochem. Soc.*, vol. 151, no. 8, pp. G528–G535, Jan. 2004.

[8] M. Schuisky, J. W. Elam, and S. M. George, "In situ resistivity measurements during the atomic layer deposition of ZnO and W thin films," *Appl. Phys. Lett.*, vol. 81, no. 1, pp. 180–182, Jun. 2002.

[9] M. D. Groner, J. W. Elam, F. H. Fabreguette, and S. M. George, "Electrical characterization of thin Al2O3 films grown by atomic layer deposition on silicon and various metal substrates," *Thin Solid Films*, vol. 413, no. 1, pp. 186–197, Jun. 2002.

[10] S. B. Jang, S.-H. Kang, K. Amine, Y. C. Bae, and Y.-K. Sun, "Synthesis and improved electrochemical performance of Al (OH)3-coated Li[Ni1/3Mn1/3Co1/3]O2 cathode materials at elevated temperature," *Electrochimica Acta*, vol. 50, no. 20, pp. 4168–4173, Jul. 2005.

[11] F. Wu, M. Wang, Y. Su, L. Bao, and S. Chen, "Surface of LiCo1/3Ni1/3Mn1/3O2 modified by CeO2-coating," *Electrochimica Acta*, vol. 54, no. 27, pp. 6803–6807, Nov. 2009.

[12] B. Xiao *et al.*, "Highly stable Li1.2Mn0.54Co0.13Ni0.13O2 enabled by novel atomic layer deposited AlPO4 coating," *Nano Energy*, vol. 34, pp. 120–130, Apr. 2017.

[13] J. M. Zheng, Z. R. Zhang, X. B. Wu, Z. X. Dong, Z. Zhu, and Y. Yang, "The Effects of AlF3 Coating on the Performance of Li [Li0.2Mn0.54Ni0.13Co0.13] O2 Positive Electrode Material for Lithium-Ion Battery," *J. Electrochem. Soc.*, vol. 155, no. 10, pp. A775–A782, Jan. 2008.

[14] H. Sopha *et al.*, "ALD Al2O3-Coated TiO2 Nanotube Layers as Anodes for Lithium-Ion Batteries," *ACS Omega*, vol. 2, no. 6, pp. 2749–2756, Jun. 2017.

[15] Z. Chen and J. R. Dahn, "Studies of LiCoO[sub 2] Coated with Metal Oxides," *Electrochem. Solid-State Lett.*, vol. 6, no. 11, p. A221, 2003.

[16] Y.-K. Sun, S.-T. Myung, M.-H. Kim, J. Prakash, and K. Amine, "Synthesis and Characterization of $Li[(Ni_{0.8}Co_{0.1}Mn_{0.1})_{0.8}(Ni_{0.5}Mn_{0.5})_{0.2}]O_2$ with the Microscale Core−Shell Structure as the Positive Electrode Material for Lithium Batteries," *J. Am. Chem. Soc.*, vol. 127, no. 38, pp. 13411–13418, Sep. 2005.

[17] M. Létiche *et al.*, "Atomic Layer Deposition of Functional Layers for on Chip 3D Li-Ion All Solid State Microbattery," *Adv. Energy Mater.*, vol. 7, no. 2, p. 1601402, Jan. 2017.

[18] V. Aravindan, K. B. Jinesh, R. R. Prabhakar, V. S. Kale, and S. Madhavi, "Atomic layer deposited (ALD) SnO2 anodes with exceptional cycleability for Li-ion batteries," *Nano Energy*, vol. 2, no. 5, pp. 720–725, Sep. 2013.

[19] Y. S. Jung, A. S. Cavanagh, A. C. Dillon, M. D. Groner, S. M. George, and S.-H. Lee, "Enhanced Stability of LiCoO2 Cathodes in Lithium-Ion Batteries Using Surface Modification by Atomic Layer Deposition," *J. Electrochem. Soc.*, vol. 157, no. 1, pp. A75–A81, Jan. 2010.
[20] "Conformal Surface Coatings to Enable High Volume Expansion Li-Ion Anode Materials - Riley - 2010 - ChemPhysChem - Wiley Online Library." [Online]. Available: https://onlinelibrary.wiley.com/doi/full/10.1002/cphc.201000158. [Accessed: 27-May-2018].
[21] Y. S. Jung, A. S. Cavanagh, Y. Yan, S. M. George, and A. Manthiram, "Effects of Atomic Layer Deposition of Al2O3 on the Li[Li0.20Mn0.54Ni0.13Co0.13]O2 Cathode for Lithium-Ion Batteries," *J. Electrochem. Soc.*, vol. 158, no. 12, pp. A1298–A1302, Jan. 2011.
[22] V. Palomares, P. Serras, I. Villaluenga, K. B. Hueso, J. Carretero-González, and T. Rojo, "Na-ion batteries, recent advances and present challenges to become low cost energy storage systems," *Energy Environ. Sci.*, vol. 5, no. 3, pp. 5884–5901, Mar. 2012.
[23] B. C. C. Research, "Global Market for Sodium-ion Batteries to Nearly Triple in Value by 2022," *GlobeNewswire News Room*, 18-Jan-2018. [Online]. Available: http://globenewswire.com/news-release/2018/01/18/1296529/0/en/Global-Market-for-Sodium-ion-Batteries-to-Nearly-Triple-in-Value-by-2022.html. [Accessed: 16-Feb-2018].
[24] N. Yabuuchi, K. Kubota, M. Dahbi, and S. Komaba, "Research Development on Sodium-Ion Batteries," *Chem. Rev.*, vol. 114, no. 23, pp. 11636–11682, Dec. 2014.
[25] D. A. Stevens and J. R. Dahn, "High Capacity Anode Materials for Rechargeable Sodium-Ion Batteries," *J. Electrochem. Soc.*, vol. 147, no. 4, pp. 1271–1273, Jan. 2000.
[26] S. Okada, Y. Takahashi, T. Kiyabu, T. Doi, J.-I. Yamaki, and T. Nishida, "Layered Transition Metal Oxides as Cathodes for Sodium Secondary Battery," *Meet. Abstr.*, vol. MA2006-02, no. 4, pp. 201–201, Jun. 2006.
[27] H. Kim, J. Hong, Y.-U. Park, J. Kim, I. Hwang, and K. Kang, "Sodium Storage Behavior in Natural Graphite using Ether-based Electrolyte Systems," *Adv. Funct. Mater.*, vol. 25, no. 4, pp. 534–541, Jan. 2015.
[28] H. Jin *et al.*, "Three dimensional architecture of carbon wrapped multilayer Na 3 V 2 O 2 (PO 4) 2 F nanocubes embedded in graphene for improved sodium ion batteries," *J. Mater. Chem. A*, vol. 3, no. 34, pp. 17563–17568, 2015.
[29] J. Barker, R. K. B. Gover, P. Burns, and A. J. Bryan, "Hybrid-Ion A Lithium-Ion Cell Based on a Sodium Insertion Material," *Electrochem. Solid-State Lett.*, vol. 9, no. 4, pp. A190–A192, Jan. 2006.
[30] R. Gover, A. Bryan, P. Burns, and J. Barker, "The electrochemical insertion properties of sodium vanadium fluorophosphate, Na3V2(PO4)2F3," *Solid State Ion.*, vol. 177, no. 17–18, pp. 1495–1500, Jul. 2006.
[31] T. Broux *et al.*, "VIV Disproportionation Upon Sodium Extraction From Na3V2(PO4)2F3 Observed by Operando X-ray Absorption Spectroscopy and Solid-State NMR," *J. Phys. Chem. C*, vol. 121, no. 8, pp. 4103–4111, Mar. 2017.
[32] T. Broux *et al.*, "Strong Impact of the Oxygen Content in Na3V2(PO4)2F3–yOy ($0 \leq y \leq 0.5$) on Its Structural and Electrochemical Properties," *Chem. Mater.*, vol. 28, no. 21, pp. 7683–7692, Nov. 2016.
[33] T. Broux *et al.*, "Temperature Dependence of Structural and Transport Properties for Na3V2(PO4)2F3 and Na3V2(PO4)2F2.5O0.5," *Chem. Mater.*, vol. 30, no. 2, pp. 358–365, Jan. 2018.

[34] R. Dugas, A. Ponrouch, G. Gachot, R. David, M. R. Palacin, and J. M. Tarascon, "Na Reactivity toward Carbonate-Based Electrolytes: The Effect of FEC as Additive," *J. Electrochem. Soc.*, vol. 163, no. 10, pp. A2333–A2339, Jan. 2016.
[35] T. Broux *et al.*, "Strong Impact of the Oxygen Content in Na3V2(PO4)2F3–yOy ($0 \leq y \leq 0.5$) on Its Structural and Electrochemical Properties," 19-Oct-2016. [Online]. Available: http://pubs.acs.org/doi/abs/10.1021/acs.chemmater.6b02659. [Accessed: 11-Jan-2018].
[36] W.-J. Zhang, "A review of the electrochemical performance of alloy anodes for lithium-ion batteries," *J. Power Sources*, vol. 196, no. 1, pp. 13–24, Jan. 2011.
[37] Y. Idota, T. Kubota, A. Matsufuji, Y. Maekawa, and T. Miyasaka, "Tin-Based Amorphous Oxide: A High-Capacity Lithium-Ion-Storage Material," *Science*, vol. 276, no. 5317, pp. 1395–1397, May 1997.
[38] P. Nithyadharseni *et al.*, "Spark plasma-sintered Sn-based intermetallic alloys and their Li-storage studies," *J. Solid State Electrochem.*, vol. 20, no. 6, pp. 1743–1751, Jun. 2016.
[39] J. O. Besenhard, J. Yang, and M. Winter, "Will advanced lithium-alloy anodes have a chance in lithium-ion batteries?," *J. Power Sources*, vol. 68, no. 1, pp. 87–90, Sep. 1997.
[40] J. Yang, M. Winter, and J. O. Besenhard, "Small particle size multiphase Li-alloy anodes for lithium-ionbatteries," *Solid State Ion.*, vol. 90, no. 1, pp. 281–287, Sep. 1996.
[41] C.-M. Park, J.-H. Kim, H. Kim, and H.-J. Sohn, "Li-alloy based anode materials for Li secondary batteries," *Chem. Soc. Rev.*, vol. 39, no. 8, pp. 3115–3141, 2010.
[42] X. J. Zhu *et al.*, "Highly porous reticular tin–cobalt oxide composite thin film anodes for lithium ion batteries," *J. Mater. Chem.*, vol. 19, no. 44, p. 8360, 2009.
[43] Y. Zhao, Q. Zhou, L. Liu, J. Xu, M. Yan, and Z. Jiang, "A novel and facile route of ink-jet printing to thin film SnO2 anode for rechargeable lithium ion batteries," *Electrochimica Acta*, vol. 51, no. 13, pp. 2639–2645, Mar. 2006.
[44] Z. Cui, Y. Huang, and X. Guo, "Electrochemical properties of SnO2 thin-film anodes improved by introduction of Cu intermediate and LiF coating layers," *Electrochimica Acta*, vol. 60, pp. 7–12, Jan. 2012.
[45] A. Darwiche, M. T. Sougrati, B. Fraisse, L. Stievano, and L. Monconduit, "Facile synthesis and long cycle life of SnSb as negative electrode material for Na-ion batteries," *Electrochem. Commun.*, vol. 32, pp. 18–21, Jul. 2013.
[46] A. T. Tesfaye *et al.*, "The Electrochemical Behavior of SnSb as an Anode for Li-ion Batteries Studied by Electrochemical Impedance Spectroscopy and Electron Microscopy," *Electrochimica Acta*, vol. 256, pp. 155–161, Dec. 2017.
[47] A. Aboulaich *et al.*, "All-Solid-State Thick Li-Ion Batteries: New Concept and Performances at High Temperature," in *Meeting Abstracts*, 2010, pp. 728–728.
[48] Y. Kobayashi *et al.*, "All-solid-state lithium secondary battery with ceramic/polymer composite electrolyte," *Solid State Ion.*, vol. 152, pp. 137–142, 2002.
[49] A. Aboulaich *et al.*, "A New Approach to Develop Safe All-Inorganic Monolithic Li-Ion Batteries," *Adv. Energy Mater.*, vol. 1, no. 2, pp. 179–183, Mar. 2011.
[50] T. Takeuchi *et al.*, "All-Solid-State Lithium Secondary Battery with Li[sub 2]S–C Composite Positive Electrode Prepared by Spark-Plasma-Sintering Process," *J. Electrochem. Soc.*, vol. 157, no. 11, p. A1196, 2010.
[51] G. Delaizir, N. Manafi, G. Jouan, P. Rozier, and M. Dollé, "All-solid-state silver batteries assembled by Spark Plasma Sintering," *Solid State Ion.*, vol. 207, pp. 57–63, Jan. 2012.

[52] D. Jain, K. M. Reddy, A. Mukhopadhyay, and B. Basu, "Achieving uniform microstructure and superior mechanical properties in ultrafine grained TiB2–TiSi2 composites using innovative multi stage spark plasma sintering," *Mater. Sci. Eng. A*, vol. 528, no. 1, pp. 200–207, Nov. 2010.
[53] A. Cassel, B. Fleutot, M. Courty, V. Viallet, and M. Morcrette, "Sol-gel synthesis and electrochemical properties extracted by phase inflection detection method of NASICON-type solid electrolytes LiZr2(PO4)3 and Li1.2Zr1.9Ca0.1(PO4)3," *Solid State Ion.*, vol. 309, no. Supplement C, pp. 63–70, Oct. 2017.

General Conclusion

The ultimate goal of this research work was to fabricate and study thick binder-free electrodes to improve the areal capacity and energy density of Li-ion batteries. To achieve this objective, the advanced sintering process called Spark Plasma Sintering (SPS) was used to make thick electrodes for Li-ion batteries in a short span of time with excellent mechanical integrity. The templating strategy was adopted to prepare porous sintered electrodes which are suitable for liquid electrolyte to flow through the pores to reach the full active material utilization. The main results and discussion of the manuscript were presented below.

- **Design of new functional thick electrodes using SPS and templating for Li-ion batteries**

  In the work presented herein, 1-mm thick LFP and LTO electrodes were fabricated using SPS and templating. Our experimental studies revealed that these thick binder free electrodes possess very high relative density (95%). After SPS treatment, using X-ray diffraction pattern, we determined that there is no chemical reactivity between the initial components and no structural decomposition of initial materials occurred. Importantly, complete dissolution of templating agents is determined by the weight loss method and further confirmed by Energy Dispersive X-ray diffraction and electrochemical curves. Using SEM images, the cross section and surface view show the pores are well distributed in the overall volume of the thick electrodes. The porosity of the thick LFP electrodes is quantified by pycnometry, tomography techniques and weight loss calculations and are found comparable to each other. The specific surface area of 44% porous 1-mm thick LFP electrodes is calculated theoretically (~0.12 m^2/g) and the values are compared with the experimental ASAP porosimetry (7 m^2/g) and tomography measurements (0.03 m^2/g). The underestimation of specific surface area by the tomography measurements is due to the low spatial resolution and over estimation of ASAP porosimetry technique is due to the non-accountability of macropores used in the specific surface area calculation. The thick binder free LFP electrodes show good mechanical integrity and no cracking was observed after cycling, confirmed by visual analysis.

- **High areal capacity obtained for 1-mm thick LFP and LTO half cells and full battery:**

The 1-mm thick LFP half-cell delivered around 20 mAh/cm^2 at C/20 with capacity retention (75%) and Coulombic efficiency of 98% for 20 cycles. Similarly, the LTO half cells also delivered very high areal capacity of 25 mAh/cm^2 at C/60 rate. The full battery was assembled by using 1-mm thick LFP and LTO electrodes are working at cell potential of 1.9 V which is close to the thermodynamic potential of the LFP/LTO couple and higher areal capacity (20 mAh/cm^2) with good Coulombic efficiency is obtained. Thanks to SPS it was possible to achieve higher active material loading (165 mg/cm^2) for 1-mm thick LFP electrodes and with the templating approach, good pore interconnectivity in the thick electrodes. As a proof of concept, the electrochemical results presented here are some clear evidence for the ability of 1-mm thick LFP and LTO thick sintered electrodes to achieve four to five times higher areal capacity compared to conventional Li-ion batteries.

- **High geometric density LFP electrodes**

The three different geometric densities of the thick LFP electrodes are prepared by varying the amount of templating agents in the composition of LFP-NaCl-C composite or studying the effect of porosity. Same electrode pore size (12 μm) but three different porosities (21 %, 36% and 44%) were tested using the salt templating approach. This study shows that the micro structural parameters such as porosity, pore size are adaptably controlled in thick electrode using the templating approach. The difference in spreading of pores in the three porous LFP electrodes was clearly illustrated by the cross sectional SEM images. The corresponding apparent densities of the 1-mm thick LFP electrodes is 2.55 g/cc, 2.05 g/cc and 1.83 g/cc. The increased geometric density of 21% LFP electrode reached up to 2.55 g/cc which helps to increase the volumetric and gravimetric energy density of Li-ion batteries. The 21 % porosity LFP electrodes show the relatively lower capacity of 61 mAh/g or 15 mAh/cm^2 when cycled against lithium at C/20 rate. Though the practical capacity is fully reached, the obtained value is still higher than the areal capacity obtained by the conventional Li-ion batteries. These experimental results proved that the ion transport in the electrolyte phase is clearly limiting in the dense electrode. This is confirmed by the voltage drop at the end of discharge, which was suddenly reaching the cut off voltage before achieving the full active material utilization. The effect of pore accessibility by the electrolyte to the active materials and mass transfer limitations

in the liquid phase are studied in the three different porous LFP electrodes by cycling against lithium at different C-rates.

- **3D morphological study of thick LFP electrodes using TXM µCT**

The effect of pore size in the 1-mm thick LFP electrodes is studied by varying the particle size of salt particles (2 µm, 13 µm and ~14 µm). The cross sectional SEM images reveal that the distribution of pores is observed in the entire area of the thick electrodes. 3D morphological studies by TXM-µCT were carried out for the three different pore sized LFP electrodes. Following the pore network extraction model using modified Blunt algorithm, the average pore size, porosity and specific surface area were compared. The uniform sphere pore size distribution was observed for the 12 µm compared to 20 µm and 23 µm average pore size. The slight increase is observed in the final pore size after the SPS treatment compared to the initial particle size of salt particles. The tortuosity measurements for the three LFP electrodes were determined in three orthogonal directions and found that pore anisotropy is observed in z-direction which is due to the uni-directional pressing of the electrodes during SPS densification process. The characteristic tortuosities (1.52, 1.76 and 1.8) are determined using tomography analysis which is close to Bruggeman relation.

- **Impedance with symmetric cell and comparison of crucial tortuosity with tomography**

The lithium ion mobility in the liquid phase of the three different pore sized thick LFP electrodes (12 µm, 20 µm and 23 µm) are studied using the EIS-SC approach. The lithium intercalation/de-intercalation effect is neglected by using a blocking condition of using LFP symmetrical cells with a non-intercalation electrolyte. The tortuosities were extracted from the impedance spectrum (3.8±0.7, 4.6±0.9 and 5.6±0.9) for the three different pore size LFP electrodes (12 µm, 20 µm and 23 µm) respectively. The higher ionic conductivity of pores (R_{ion}) was obtained for the lower mean pore sized electrode (12 µm) using impedance spectrum and the decreasing trend of ionic conductivity in pores was found with the increase of electrode pore size. The crucial parameter called tortuosity was a main reason for the rate capability of the Li-ion batteries. The tortuosity values are extracted by TLM model and compared with tomography analysis and it is found that the tortuosity values by the EIS-SC approach are two times higher than the tomography studies. The difference is due to the low spatial resolution of micro-tomography used (1.3 µm) and non-

accountability of dead end pores present in the actual LFP thick electrodes. The quantification of dead end pore network will be done in the future using skeleton analysis of the tomography data.

- **Rate capability of three LFP electrodes with different pore size**

The ionic resistance in the liquid phase is one of the main reasons for the rate capability performance. The same amount of electrode porosity (44%) with different pore sizes are prepared for the LFP sintered electrodes. The LFP electrode with lesser average pore size (12 μm) with narrow pore size distribution shows a higher rate capability than the other two electrodes (20 and 23 μm). One reason for the enhanced lithium ion transport is due to the good pore interconnectivity confirmed by the impregnation test and relatively lesser tortuosity determined by EIS and tomography measurements. This leads to the reduction of lithium ion migration distances for the 12 μm pore sized LFP electrodes compared to other pore sized LFP electrodes. The same enhanced performance was seen for 12 μm pore sized LFP electrodes with 21% porosity with relatively higher areal capacity of 15 mAh/cm^2 at C/20 rate compared to the 20 μm pore sized LFP electrode.

- **Influence of LFP electrode thickness up to 3 mm on electrochemical properties**

A systematic study of LFP electrodes was done with varied thickness from 0.5 mm to 3mm using the SPS/ salt templating approach. High relative density of around 95% was obtained for the whole set of electrodes. The salt particles are completely dissolved confirmed by the weight loss of salt particles after the dissolution process. The good interconnectivity of the pores was achieved for the thick electrodes by cycling at different C-rates using liquid electrolyte. The uniform pore size distribution with an average mean pore size of 12 μm and 44% porosity was obtained for all the thick electrodes.

In terms of slow cycling C-rate (C/20), a linear increase in areal capacity from 11.8 to 37.5 mAh/cm^2 was observed from 0.5 to 3mm thick LFP electrodes. As a proof of concept, this result clearly is explained by the higher active material loading. At the same time, the simultaneous increase in diffusion length or electrode thickness greatly reduces the gravimetric capacity at high C-rates due to the mass transport limitations. For the lowest thick LFP electrode tested (0.5 mm), the practical capacity of 145 mAh/g and surface capacity of 11.8 mAh/cm^2 was obtained at C/20 rate due to the full active material utilization. However, the 3mm thick LFP/Li cell delivered 84 mAh/g at C/20 rate. At

slower cycling of C/100 and C/50 rates, the 2mm thick LFP half cells delivered an areal capacity of 40.5 and 39.2 mAh/cm^2 respectively which is almost 8 times higher than the conventional thin film electrodes.

- **Al_2O_3 ALD coating of 1-mm thick LFP electrodes**

A pinhole-free insulating layer of alumina with three different nanometer thicknesses was coated on the surface of the LFP electrode using the well sophisticated ALD technique. A strong chemical bond was created between the coating layer and the LFP electrode by Atomic Layer Deposition (ALD) technique. The presence and linear increase of alumina content were characterized by EDX technique. The main motivation of this work is to enhance the mechanical properties of the thick binder free electrodes after cycling for a long term. Thus the alumina can form a uniform passivation layer on thick LFP electrodes and further indentation studies will be carried out in the future. A stable capacity retention was observed for the 1-nm and 3-nm thick alumina coated LFP electrodes (77% and 90%) compared to the uncoated 1-mm thick LFP electrode (32%) after 20 cycles. The 5-nm thick alumina coating on LFP electrode shows poor capacity retention (13%) which is due to the dramatic increase in interfacial impedance between alumina and carbon coated LFP particles surface in the thick electrode. No significant difference in terms of rate capability was observed between the alumina coated and non-coated 1-mm thick LFP electrodes.

From the first results of improved chemical stability and the increased mechanical properties achieved by ALD technique, alumina is expected to be a promising candidate to improve the capacity retention and mechanical properties. A future avenue to improve the mechanical properties will be done for 1-mm thick LTO electrode using SPS, which are found less stable compared to LFP thick electrodes.

- **One step full battery using SPS/templating approach**

New cell designs are proposed by sintering multilayered battery materials such as $LiFePO_4$ (LFP), $Li_{1.2}Zn_{1.9}Ca_{0.1}(PO_4)_3$ (LCZP) and $Li_4Ti_5O_{12}$ (LTO) in a single step using SPS. A full battery (LFP-LCZP-LTO) was sintered along with the templating agents with appropriate proportions in each layer. After the dissolution of the templating agents, the first electrochemical test of the full battery using liquid electrolyte at C/200 in room temperature shows the cycling of lithium ions between the positive and negative layer. The expected plateau for the full cell was observed at 1.9 V and delivered a discharge capacity of 80

mAh/g in the first cycle. Further improvements in optimizing the thickness of each electrode layer and cycling conditions need to be done to improve the cycling retention issue.

- **Bi-layered LFP electrode with two different pore sizes**

A two layered LFP electrode for Li ion batteries was fabricated using SPS and templating approach. Two different sized macroporus morphologies were placed in discrete layers within the electrode to achieve good rate capability. The carefully controlled mass fraction of active materials was reported. This approach helps to assemble large pore sized layer farthest from the separator where lithium concentrations are more limited and smaller pore sized electrode can be located near to the separator where lithium ion concentrations are relatively high. The same concept can be done by preparing two dense layers by optimizing the pore volume fraction in each discrete layer. This methodology is used to improve the volumetric capacity and rate capability which was unachievable by an electrode layer of its own. The local lithium ion concentrations through the positive electrode can be measured directly by X-ray photoelectron spectroscopy (XPS) depth profiling and the improvements of lithium ion diffusion in the layered electrode structure can be assessed.

- **Thick electrode using NVPF and SnSb materials**

The combined approach of SPS and salt templating was successfully applied for other active materials such as NVPF and SnSb materials which are used for sodium and lithium ion batteries. First, the NVPF electrodes with 0.85 mm thickness are made with the uniform pore size distribution confirmed by the SEM images. A higher areal capacity of nearly 20 mAh/cm^2 was achieved for the NVPF/Na cell at first cycle of C/20. From the first results, to our knowledge, this higher areal capacity has not ever reported in the literature and further optimization will be done in the future. We believe that this improved performance of sodium based electrodes at lower C-rates are helpful for powering safe, small scale devices such as stopwatches and ipad.

Another anode material, pure Sn-Sb alloy material was prepared using ball milling approach. Then, as prepared pure SnSb material was mixed with NaCl and conductive carbon composite and later densified using SPS. No side reaction of NaCl crystal with the active materials and complete dissolution of NaCl crystals was confirmed by XRD studies. The first electrochemical curve of 0.65 mm thick Sn-Sb/Li at C/20 rate shows the characteristic plateaus at the respective oxidation and reduction potentials in agreement with the literature. High gravimetric capacity of

714 mAh/g was reached in the first cycle. However, due to the volume expansion of the alloy based materials, the cell stops after the first cycle but this can be improved by minimizing the discharge potentials to 1V and avoiding the side reactions such as electrolyte decomposition at lower potentials closer to zero. From the first presented results, we believe that this SPS and templating strategy will be adopted to fabricate thick electrodes using other battery materials and make possibly the next generation of high-energy-density lithium-ion batteries.

Collaborations developed during the thesis

This thesis would not have been possible without the support from different collaborations at different institutions and they are listed below.

- Collaboration with Vincent De Andrade in Argonne Photon Source, Argonne National Laboratory, USA was done for characterization of the thick LFP electrodes using TXM-µCT technique.
- The microstructural analysis and pore network extraction of the thick LFP electrodes using modified Blunt algorithm was done in collaboration with Amangeldi Torayaev, PhD student in LRCS, Amiens- University of Cambridge, UK.
- The collaboration work with Christophe Lethien in L'Institut d'électronique, de microélectronique et de nanotechnologie (IEMN), Lille, France has been done for the promising results of alumina coating using Atomic Layer Deposition technique.

Perspectives

The thick porous electrodes manufactured by SPS and templating approach can be improved in terms of SPS conditions, size of templating agents and rate capability. It is necessary to direct the search to various directions mentioned below:

In-terms of templating agents:

- Synthesize and optimize the nano-sized NaCl or KCl or CaCl templating agents at sub-zero temperatures (Ex: -200 °C) and electrochemical performance of the thick electrodes can be studied. These nano-sized crystals can also improve the compactness of the thick electrodes even at relatively lower temperature of around 400 °C than the present investigating temperature (650 °C).
- Use thermally stable silica as templating agents for graphite sintered electrodes to improve the energy density of lithium ion batteries by working at high full cell potential.

- Prepare conducting polymers and added along with active materials and burnt out during SPS operation. These materials can also act simultaneously as a conductive agent to improve the electrochemical performance. Though the SPS temperature and pressure are limiting for polymer based electrode materials, the durability, flexibility of the thick electrodes can be enhanced to mitigate the volume expansion of LFP particles after repeated cycling. These approaches can be tested to a wider choice of electrode materials such as $LiCoO_2$ with good electronic conductivity and low expansion coefficient after cycling.

In terms of full battery fabrication:

- Metallic current collector can be directly coupled with active material when packed with the graphite dye before the SPS operation. The interfacial resistance between the electrode and current collector can be greatly minimized to improve the electrochemical properties.
- Another perspective can be electrolyte impregnation inside the thick positive and negative electrodes by incorporating soft ionogel into the pores of the thick electrodes. This can improve the safety aspects by neglecting the combustible liquid electrolytes.

In terms of electrode architecture:

- Though the insulating alumina layer was coated on the surface of LFP electrodes to improve the mechanical properties, ion conductive materials can be coated to improve the lithium ion diffusion through the thin layer when subjected to high C-rates. Hence, lithium ion conducting Li_3PO_4 layers are coated using ALD technique with five different thicknesses on the 1-mm thick LFP electrodes. The electrochemical performance of the coated and uncoated LFP electrodes will be tested in the future. The major advantages of this approach are 1) improvement of rate capability by enhancing lithium ion conductivity at higher C-rates; 2) improving the electrode/ electrolyte interface to achieve better physical contact, higher stability and reduced polarization. This approach will be done for the lesser mechanically stable LTO electrodes to further enhance the electrochemical properties.

In terms of crystallography studies:

- Collaboration with Tatiana Renzi, Laurence Croguennec and Christian Masquelier in ILL-ICMCB –LRCS are done for the quality neutron diffraction measurements on the thick LFP electrode prepared using SPS and templating approach. The indexing of diffraction peaks will be done during cycling and this assures that neutron diffraction is a good way to observe the evolution in the structural materials present in a massive battery and investigate the influence of crystal parameters in the electrochemical performance.

This thesis highlights the influence of microstructural and geometric properties of the thick electrodes on the electrochemical performance of the lithium ion batteries. The powerful multi techniques such as X-ray diffraction, Scanning Electron Microscopy, Transmission X-ray microscopy, EIS, Galvansotatic cycling has been applied to obtain information concerning the textural and electrochemical properties of the thick electrodes fabricated using SPS and templating approach.

Overall, a broad knowledge was gained during the studies of thick electrodes fabricated by SPS and templating approach. These insights are of great importance in developing new innovative strategies for optimizing the electrochemical performance to fulfill the energy demand. This thesis is a first step in introducing the thick electrode fabrication and assessing the performance fabricated by the SPS and templating approach and further improvements will be done. The project will be taken forward by a new PhD student starting in October 2019 with collaboration between LRCS, Amiens and University of Toulouse. The same approach can be applicable with different electrode couples in the future possessing higher overall cell potential thereby high energy density of lithium ion batteries. From an industrial point of view, we believe that the combined approach of SPS/templating is of great interest to a broad audience for the micro batteries manufactures and engineers. We hope that our work will encourage them to further delve the exploration of new portable electronics devices such as mobile phones and laptops.

Résumé développé de la thèse en français

Introduction:

L'augmentation continue de la demande énergétique due à l'augmentation de la population et au développement économique rapide est principalement due à la combustion de combustibles fossiles au cours des quatre dernières décennies, comme le montre la figure 1.1. Cela conduit par conséquent à une augmentation continue des niveaux globaux de CO_2 et ce problème vital peut être résolu en utilisant un stockage d'énergie alternatif et le développement de systèmes de stockage d'énergie est considéré comme un impératif mondial. Bien que de nombreux dispositifs de stockage d'énergie tels que des batteries à débit redox, des piles à combustible, des accumulateurs d'hydrogène pompés soient disponibles sur le marché, les batteries Li-ion se distinguent énergie et densité de puissance. Récemment, LIB est de plus en plus populaire dans le développement de véhicules électriques sans pollution en remplaçant les véhicules à moteur à combustion interne en raison de sa capacité élevée de charge / décharge électrochimique avec une bonne durée de vie.

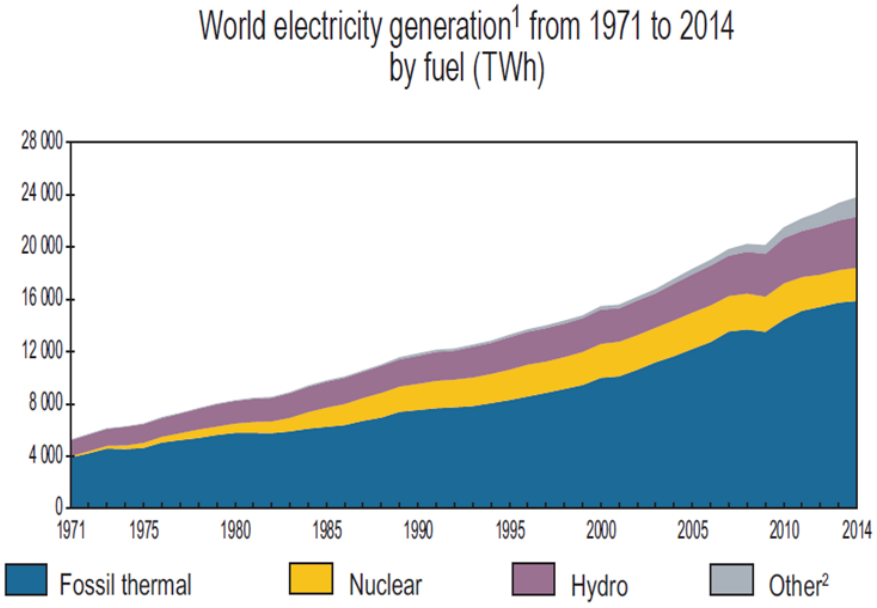

Figure 1.1 Différents types de sources d'énergie ont contribué à la production mondiale d'électricité de 1971 à 2014 [1].

Classiquement, la batterie Li-ion contient une anode (par exemple, du graphite), une cathode (par exemple $LiCoO_2$, $LiNi_{1/3}Mn_{1/3}Co_{1/3}O_2$ ou $LiFePO_4$). Les deux électrodes sont capables d'insérer et

de désinsérer de manière réversible des ions Li de leurs structures respectives. Les électrodes sont séparées par un électrolyte non aqueux qui transporte les ions Li entre les électrodes. L'électrolyte est un mélange de sel de lithium (par exemple, $LiPF_6$) dissous dans un solvant mixte organique (par exemple, carbonate d'éthylène-diméthylcarbonate, EC-DMC). Les batteries Li-ion actuellement sur le marché ont ce type de configuration. Le mécanisme de la batterie Li-ion est illustré à la figure 1.2.

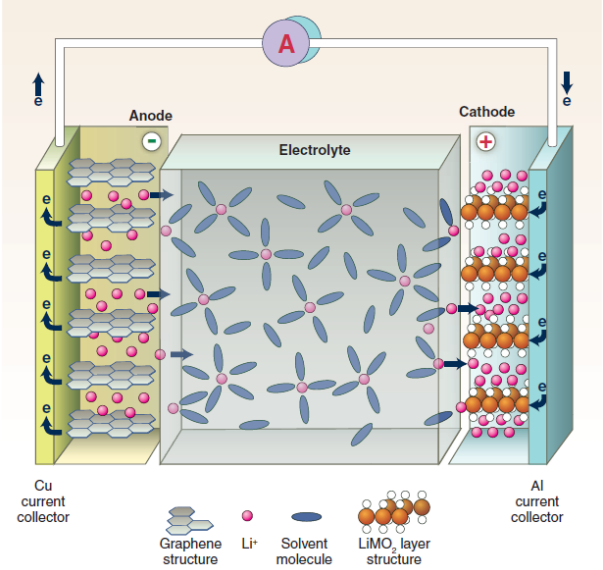

Figure 1.2 Schéma du mécanisme de la batterie lithium-ion. Reproduit de [2].

La densité d'énergie de cette batterie Li-ion actuelle est comprise entre 100 et 200 Wh / kg, ce qui en fait la technologie de batterie la plus puissante. Cependant, les batteries du commerce ont presque 50% en poids de matériaux inactifs sur le plan électrochimique, ce qui réduit considérablement le DE de la densité d'énergie théorique dans la plage de 1500 Wh / g. Il existe donc encore une grande marge d'amélioration de la densité énergétique des batteries Li-ion. L'une des principales stratégies est l'ingénierie cellulaire, qui est tout aussi importante que la recherche de nouveaux matériaux à fort potentiel ou à haute capacité spécifique pour augmenter la densité énergétique. L'augmentation de l'épaisseur de l'électrode avec réduction simultanée des matériaux électro chimiquement inactifs (collecteur de courant, séparateur, liant et matériaux d'emballage) peut potentiellement augmenter la densité d'énergie du LIB mais des électrodes de chargement plus élevées subissent un transport ionique limité. La figure 1.3 illustre clairement l'augmentation de la densité d'énergie linéaire avec l'épaisseur de la cathode et la diminution soudaine de la densité de puissance due à l'augmentation de la conductivité électrique et aux limitations du transport de masse pour les électrodes plus épaisses.

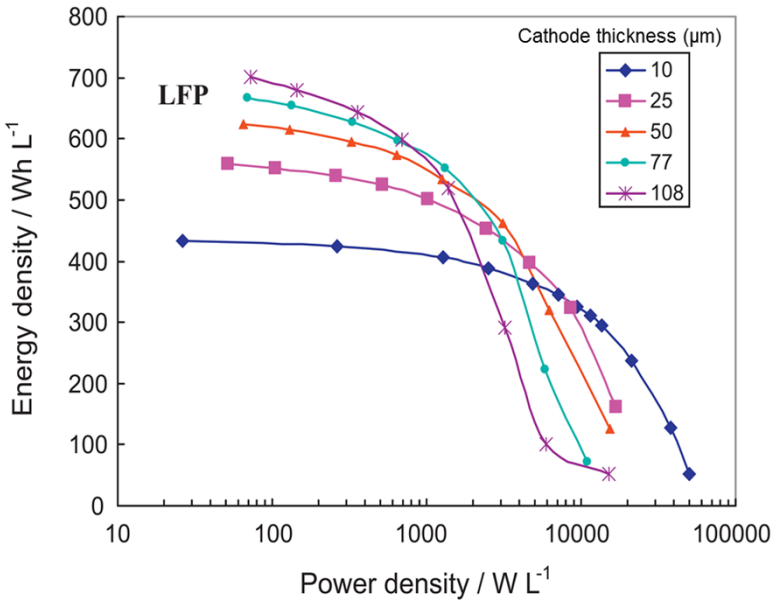

Figure 1.3 Tracé de la cellule LFP/ G avec une épaisseur de cathode différente [3].

Pour les batteries Li-ion classiques à base de film, la porosité de l'électrode est ajustée en faisant varier la pression de calandrage appliquée qui contrôle également l'épaisseur et la densité des électrodes. Malheureusement, cette étape conduit à une tortuosité élevée des électrodes ou à un chemin poreux non rectiligne pour que les ions lithium diffusent dans la zone interne des électrodes. Les pores sont alignés perpendiculairement aux voies de transport primaires, ce qui entrave le mouvement efficace des ions lithium pendant le fonctionnement des cellules. Ce problème de phénomène de transport conduit à une performance électrochimique médiocre à des taux C élevés. La tortuosité des électrodes dépend principalement de la taille des pores, de la forme et de la distribution des particules dans les électrodes et la détermination de ces propriétés est déterminée à l'aide de diverses mesures synchrotron.

Dans les batteries Li-ion, les électrodes sont constituées de microstructures poreuses dans lesquelles le transport de masse est principalement contrôlé par les caractéristiques microstructurales telles que la porosité des électrodes, la taille des pores et la tortuosité. La performance de la batterie Li-ion dépend de nombreux facteurs tels que la conductivité électronique et ionique des matériaux actifs, la température et le type de méthodes de charge. Une architecture d'électrode bien conçue est très importante pour obtenir des performances de batterie supérieures. Le fonctionnement efficace des électrodes épaisses n'est possible que lorsqu'il existe une bonne interconnectivité des pores et une quantité appropriée de pores pour la diffusion de l'ion lithium car le transport des ions dans la phase liquide limite la vitesse. Il est donc essentiel de préparer des électrodes poreuses bien alignées et peu tortueuses. La porosité de l'électrode pour les batteries Li-ion commerciales est d'environ 30 à 40%. Cependant, cette plage de porosité peut être modifiée en fonction des propriétés électriques et

ioniques des matériaux actifs. Des valeurs de porosité supérieures à cette plage entraîneront une diminution massive de la densité d'énergie volumétrique et une augmentation de la résistivité électrique globale des matériaux actifs. Dans le même temps, des valeurs de porosité plus faibles conduiront à une résistance ionique plus élevée entraînant une diffusion médiocre de l'électrolyte liquide vers les électrodes en vrac.

Objectif de la thèse:

Le but ultime de ce travail de recherche est de fabriquer et d'étudier des électrodes épaisses sans liant pour améliorer la capacité surfacique et la densité énergétique des batteries Li-ion. Pour atteindre cet objectif, le procédé de frittage avancé appelé Spark Plasma Sintering (SPS) a été utilisé pour fabriquer des électrodes épaisses pour les batteries Li-ion, où l'on peut fabriquer des électrodes rapidement et avec une excellente intégrité mécanique. De plus, la stratégie de modélisation a également été combinée pour préparer des électrodes frittées poreuses en dissolvant les agents porogènes après le procédé SPS. Dans ma thèse, les cristaux de NaCl sont utilisés comme agents porogènes puis dissous par de l'eau pour former des pores à l'intérieur desquels l'électrolyte liquide peut s'écouler pour atteindre la pleine utilisation du matériau actif. Au chapitre 2, les concepts de base et les principes de la technique SPS sont discutés avec les premiers résultats obtenus pour les électrodes LFP et LTO de 1 mm d'épaisseur. L'optimisation de la morphologie de l'électrode a été réalisée en préparant des électrodes LFP épaisses avec une large gamme de paramètres tels que la taille des pores, la porosité et l'épaisseur sont discutés dans le chapitre 3. Les performances électrochimiques sont influencées par les propriétés microstructurales l'EIS et les techniques de tomographie. Le chapitre 4 présente les développements des électrodes épaisses en utilisant la stratégie SPS et la stratégie de modélisation. Tout d'abord, un revêtement d'alumine d'électrodes LFP d'une épaisseur de 1 mm est rapporté en utilisant la technique de dépôt de couche atomique. L'impact du revêtement protecteur a été discuté en améliorant les propriétés mécaniques des électrodes épaisses. Les électrodes NVP et SnSb sont fabriquées à l'aide de SPS et l'approche par modèles est abordée au chapitre 4. Ce chapitre comprend également les premiers résultats obtenus pour la batterie à pas unique en assemblant $LiFePO_4$ (LFP) / $Li_{1.2}Zn_{1.9}Ca_{0.1}(PO_4)_3$. (LCZP) / $Li_4Ti_5O_{12}$ (LTO) et les premiers résultats de la cellule complète sont rapportés. Les principaux résultats et la discussion du manuscrit ont été présentés ci-dessous.

Conception de nouvelles électrodes épaisses fonctionnelles utilisant le SPS et la modélisation pour les batteries Li-ion

Dans le travail présenté ici, des électrodes LFP et LTO de 1 mm d'épaisseur ont été fabriquées en utilisant le SPS et la modélisation. Nos études expérimentales ont révélé que ces électrodes sans liant épais possèdent une densité relative très élevée (95%). Après le traitement au SPS, en utilisant un diagramme de diffraction des rayons X, nous avons déterminé qu'il n'y avait pas de réactivité chimique entre les composants initiaux et qu'aucune décomposition structurelle des matériaux initiaux ne s'était produite. Il est important de noter que la dissolution complète des agents de gabarit est déterminée par la méthode de perte de poids et confirmée par la diffraction des rayons X à dispersion d'énergie et les courbes électrochimiques. À l'aide d'images MEB, la coupe transversale et la vue en surface montrent que les pores sont bien répartis dans le volume global des électrodes épaisses. La porosité des électrodes LFP épaisses est quantifiée par pycnométrie, techniques de tomographie et calculs de perte de poids. La surface spécifique d'électrodes LFP poreuses de 1 mm d'épaisseur à 44% est calculée théoriquement (~ 0,12 m^2/g) et les valeurs sont comparées aux mesures expérimentales de porosimétrie ASAP (7 m^2/g) et tomographiques (0,03 m^2/g). La sous-estimation de la surface spécifique par les mesures tomographiques est due à la faible résolution spatiale et la surestimation de la technique de porosimétrie ASAP est due à la non-responsabilisation des macropores utilisés dans le calcul de la surface spécifique. Les électrodes LFP sans liant épais présentent une bonne intégrité mécanique et aucune fissuration n'a été observée après le cyclage, confirmée par analyse visuelle. La demi-cellule LFP de 1 mm d'épaisseur délivre environ 20 mAh / cm^2 à C / 20 avec une capacité de rétention (75%) et une efficacité coulombienne de 98% pendant 20 cycles, comme le montre la figure 1.4. De même, les demi-cellules LTO ont également fourni une capacité de surface très élevée de 25 mAh / cm2 à un taux de C / 60. Plus tard, la batterie complète a été assemblée en utilisant des électrodes LFP et LTO de 1 mm d'épaisseur travaillant à un potentiel de cellule de 1,9 V, proche du potentiel thermodynamique du couple LFP/ LTO et d'une capacité surfacique supérieure (20 mAh/cm^2). L'efficacité coulombienne (99%) est obtenue. Grâce au SPS, il était possible d'obtenir une charge de matière active supérieure (165 mg/cm^2) pour les électrodes LFP de 1 mm d'épaisseur et, avec l'approche par modélisation, une bonne interconnectivité des pores dans les électrodes épaisses. Comme preuve de concept, les résultats électrochimiques présentés ici sont des preuves évidentes de la capacité des électrodes frittées LFP et LTO de 1 mm d'épaisseur à atteindre une capacité surfacique quatre à cinq fois supérieure à celle des batteries Li-ion conventionnelles.

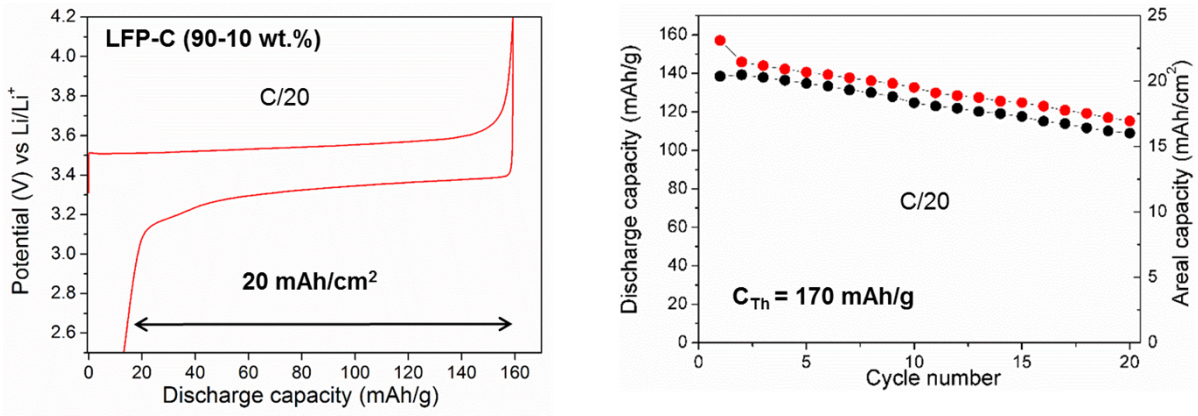

Figure 1.4 Caractérisation électrochimique d'électrodes LFP de 1 mm d'épaisseur vs Li. a) Profil de charge-décharge, b) Courbe de rétention de la capacité de la LFP par rapport au Li au taux C/20.

Vers l'optimisation de la morphologie des électrodes dans les propriétés électrochimiques

Effet de la porosité:

Les trois densités géométriques différentes des électrodes LFP épaisses sont préparées en faisant varier la quantité d'agents structurants dans la composition du composite LFP-NaCl-C ou en étudiant l'effet de la porosité. La même taille des pores de l'électrode (12 µm) mais trois porosités différentes (21%, 36% et 44%) ont été testées en utilisant l'approche par gabarit au sel. Cette étude montre que les paramètres microstructuraux tels que la porosité, la taille des pores sont contrôlés de manière adaptable en électrode épaisse en utilisant l'approche de modélisation. La différence d'étalement des pores dans les trois électrodes de LFP poreuses était clairement illustrée par les images MEB en coupe transversale. Les densités apparentes correspondantes des électrodes LFP d'une épaisseur de 1 mm sont de 2,55 g / cm^3, 2,05 g/cm^3 et 1,83 g/cm^3. L'augmentation de la densité géométrique de l'électrode LFP à 21% a atteint 2,55 g/cc, ce qui contribue à augmenter la densité d'énergie volumétrique et gravimétrique des batteries Li-ion. En copiant les perforations électrochimiques des demi-cellules LFP, les électrodes LFP poreuses à 21% présentent une capacité relativement plus faible de 61 mAh/g ou 15 mAh/cm^2 lorsqu'elles sont cyclées avec du lithium au taux C/20, comme le montre la figure 1.5. Bien que la capacité pratique soit pleinement atteinte, la valeur obtenue est toujours supérieure à la capacité surfacique obtenue par les batteries Li-ion classiques. Ces résultats expérimentaux ont montré que le transport des ions dans la phase d'électrolyte est clairement limité dans l'électrode dense. Ceci est confirmé par la chute de tension à la fin de la décharge, qui atteignait soudainement la tension de coupure avant de réaliser l'utilisation

complète du matériau actif. L'effet de l'accessibilité des pores par l'électrolyte sur les matériaux actifs et les limitations de transfert de masse dans la phase liquide sont étudiés dans les trois différentes électrodes de LFP poreuses en effectuant des cycles contre le lithium à différents taux de C.

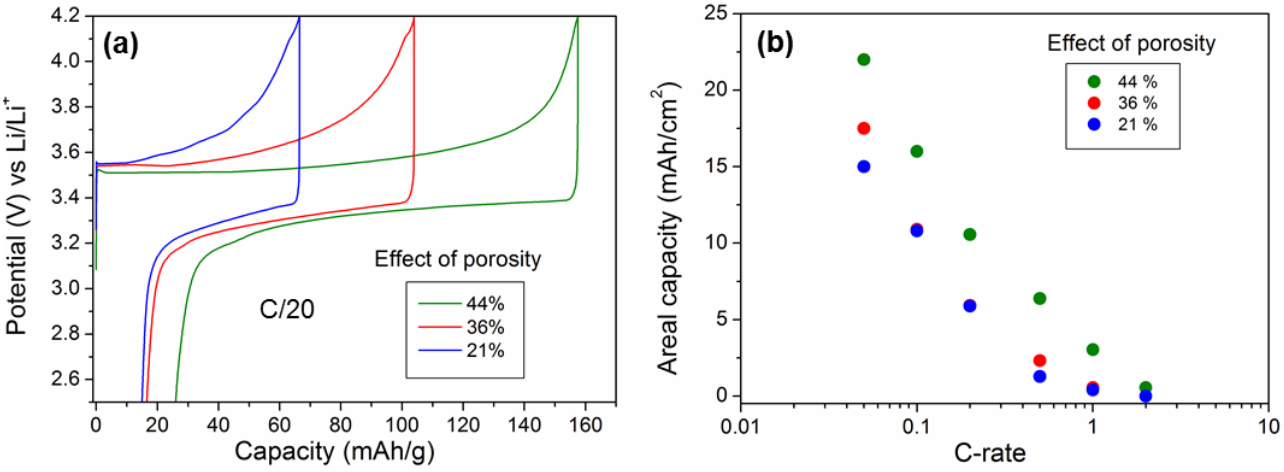

Figure 1.5 Courbe cyclique de décharge-charge des électrodes LFP de 1 mm d'épaisseur avec trois porosités différentes (44%, 36% et 21%) à un taux de C / 20 .

Effet de la taille des pores:

L'effet de la taille des pores dans les électrodes LFP d'une épaisseur de 1 mm a été étudié en faisant varier la taille des particules de sel (2 µm, 13,2 µm et 13,7 µm) dans le mélange composite LFP-NaCl-C pris dans un rapport volumique de 50: 40:10% en volume. Les images MEB de la surface des électrodes épaisses révèlent que la nette différence de taille des pores et la vue en coupe illustrent l'allongement des pores parallèle au plan de l'électrode, comme le montre la figure 1.6, due à l'application d'une pression uni-axiale.

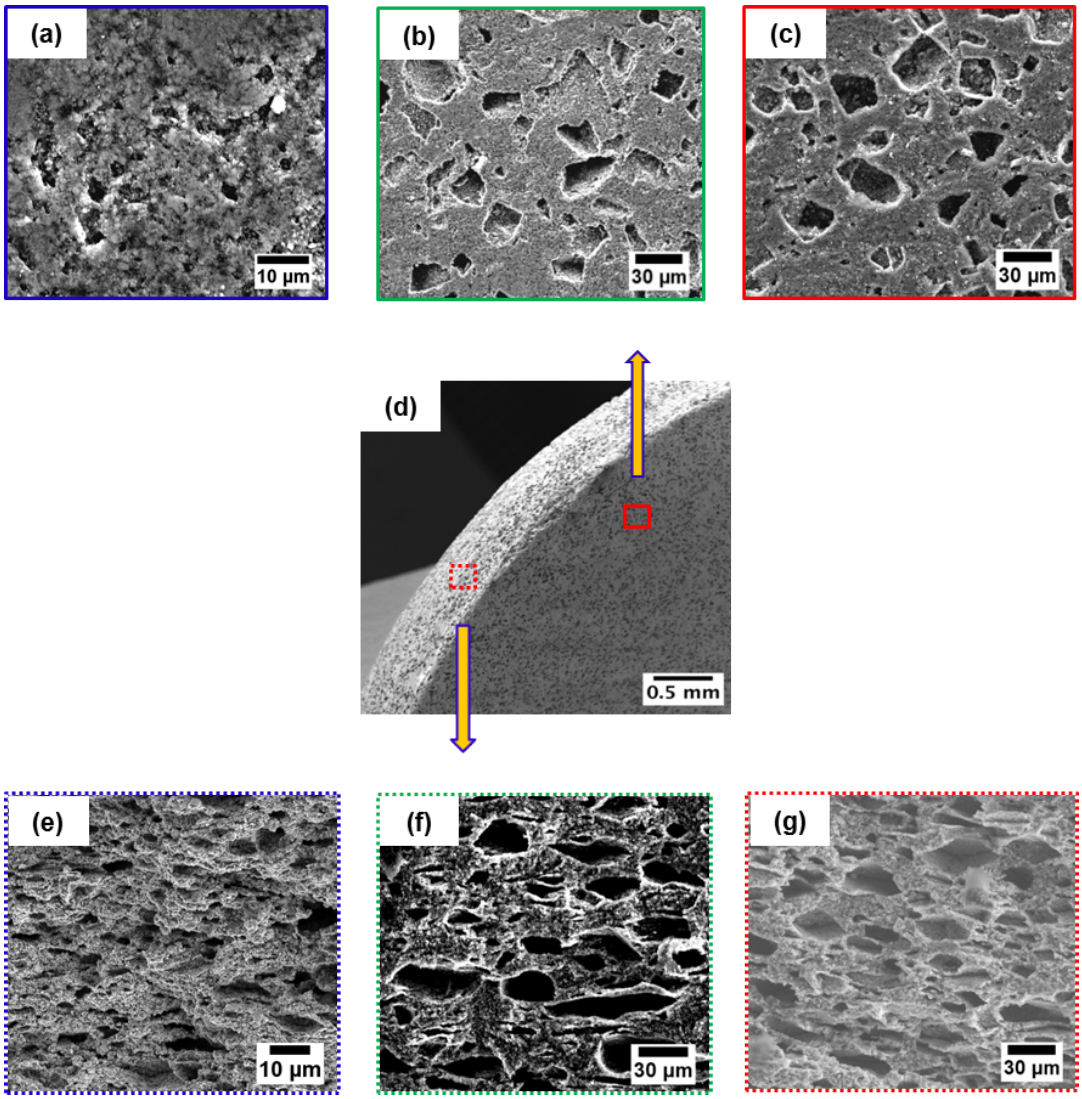

Figure 1.6 Images MEB d'électrodes poreuses LFP contenant les pores créés par la dissolution du NaCl. (a, b, c) vue de la surface supérieure des électrodes montrant la forme cubique des cristaux avec les tailles correspondantes des cristaux utilisés, (e, f, g) Coupe transversale des électrodes LFP épaisses montrant la forme des pores alignés perpendiculairement au z -direction en raison de la pression uni-axiale du fonctionnement de SPS.

Des études morphologiques 3D par TXM-µCT ont été réalisées pour les trois électrodes LFP de taille de pores différentes. Après le modèle d'extraction du réseau de pores utilisant un algorithme de Blunt modifié, la taille moyenne des pores, la porosité et la surface spécifique ont été comparées. La distribution uniforme de la taille des pores de la sphère a été observée pour une taille de pore moyenne de 12 µm contre 20 µm et 23 µm. On observe une légère augmentation de la taille finale des pores après le traitement au SPS par rapport à la taille de particule initiale des particules de sel. Les mesures de tortuosité pour les trois électrodes LFP ont été déterminées dans trois directions orthogonales et ont montré que l'anisotropie des pores est observée dans la direction z, en raison de

la pression unidirectionnelle des électrodes pendant le processus de densification SPS. Les tortuosités caractéristiques (1.52, 1.76 et 1.8) sont déterminées par analyse tomographique proche de la relation de Bruggeman. La mobilité des ions lithium dans la phase liquide des trois électrodes LFP épaisses de taille différente (12 µm, 20 µm et 23 µm) est étudiée selon l'approche EIS-SC. L'effet d'intercalation / désintercalation du lithium est négligé en utilisant une condition de blocage consistant à utiliser des cellules symétriques LFP avec un électrolyte sans intercalation. Les tortuosités ont été extraites du spectre d'impédance (3,8 ± 0,7, 4,6 ± 0,9 et 5,6 ± 0,9) pour les trois électrodes LFP de taille de pore différentes (12 µm, 20 µm et 23 µm) respectivement. La conductivité ionique plus élevée des pores (Rion) a été obtenue pour l'électrode de taille moyenne des pores inférieure (12 µm) en utilisant un spectre d'impédance et la tendance décroissante de la conductivité ionique dans les pores a été augmentée.

Le paramètre crucial appelé tortuosité était la principale raison de la capacité de débit des batteries Li-ion. Les valeurs de tortuosité sont extraites par un modèle TLM et comparées à une analyse tomographique et on constate que les valeurs de tortuosité par la méthode EIS-SC sont deux fois plus élevées que les études tomographiques. Cela s'explique par la faible résolution spatiale de la microtomographie utilisée (1,3 µm) et par la non prise en compte des pores dans le réseau de pores pour les électrodes épaisses de la LFP. La quantification du réseau de pores sans issue sera effectuée à l'avenir en utilisant l'analyse du squelette des données de tomographie utilisant le logiciel AVIZO-AMIRA. L'augmentation de la résistance ionique dans la phase liquide est la principale raison de la faible performance de la capacité. La même quantité de porosité d'électrode (44%) avec différentes tailles de pores est préparée pour les électrodes frittées LFP. L'électrode LFP avec une taille de pore moyenne inférieure (12 µm) avec une distribution étroite de la taille des pores présente une capacité de débit supérieure à celle des deux autres électrodes (20 et 23 µm). L'une des raisons de l'amélioration du transport des ions lithium est due à la bonne interconnectivité des pores confirmée par le test d'imprégnation et par la tortuosité relativement moindre déterminée par les mesures EIS et tomographiques. Cela conduit à une réduction des distances de migration des ions lithium pour les électrodes LFP de 12 µm de taille de pore par rapport aux autres électrodes LFP de taille de pore. La même performance améliorée a été observée pour des électrodes LFP de 12 µm de taille de pores avec une porosité de 21% avec une capacité surfacique relativement supérieure de 15 mAh / cm2 à un taux de C / 20 comparée à une électrode LFP de 20 µm.

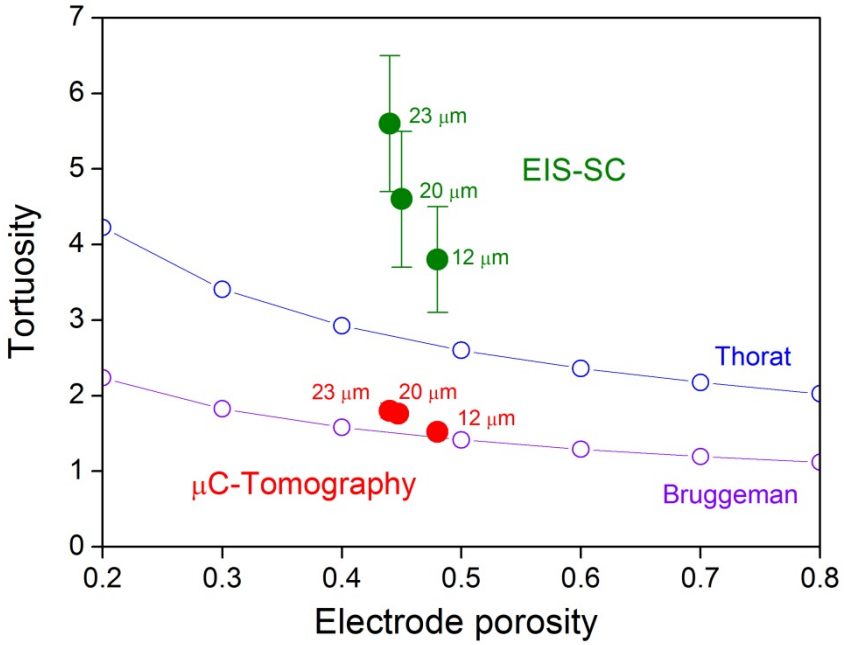

Figure 1.7 Les valeurs de tortuosité déterminées à l'aide des méthodes EIS et micro-tomographie pour les trois différentes électrodes LFP de taille moyenne des pores (12, 20 et 23 µm).

Effet d'épaisseur:

Une étude systématique des électrodes LFP a été réalisée avec des épaisseurs variées de 0,5 mm à 3 mm en utilisant l'approche SPS / sel. Une densité relative élevée d'environ 95% a été obtenue pour l'ensemble des électrodes. Les particules de sel sont complètement dissoutes, confirmées par la perte de poids des particules de sel après le processus de dissolution. La bonne interconnectivité des pores a été obtenue pour les électrodes épaisses en cyclant à différents taux de C en utilisant un électrolyte liquide. La distribution uniforme de la taille des pores avec une taille de pore moyenne moyenne de 12 µm et une porosité de 44% a été obtenue pour toutes les électrodes épaisses. À un taux de C/20, une augmentation linéaire de la capacité de surface de 11,8 à 37,5 mAh/cm^2 a été observée sur des demi-cellules LFP d'une épaisseur de 0,5 à 3 mm, comme le montre la figure 1.7.

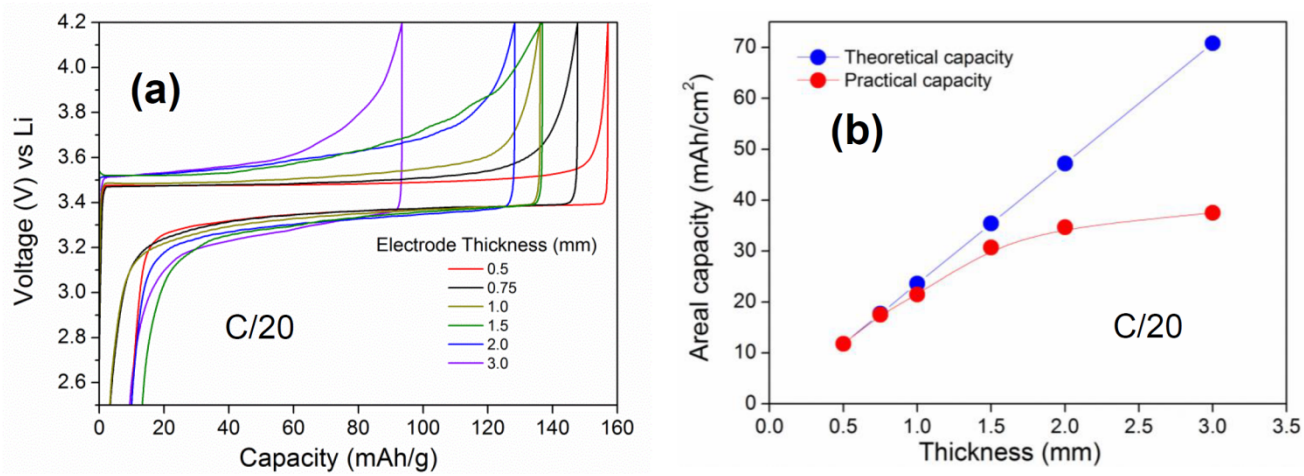

Figure 1.8 Performances électrochimiques en fonction de l'épaisseur de l'électrode au taux C/20: a) Profil de décharge-charge du second cycle pour six épaisseurs différentes d'électrodes LFP vs Li, b) Capacité théorique vs théorique montrant une utilisation de matériau moins active pour une électrode LFP de 3mm d'épaisseur.

En tant que preuve de concept, ce résultat s'explique clairement par une charge de matière active plus élevée. Dans le même temps, l'augmentation simultanée de la longueur de diffusion ou de l'épaisseur de l'électrode réduit considérablement la capacité gravimétrique à des taux C élevés en raison des limitations du transport de masse. Pour la plus faible épaisseur d'électrode LFP testée (0,5 mm), la capacité pratique de 145 mAh/g et la capacité de surface de 11,8 mAh / cm^2 ont été obtenues à un taux de C/20 grâce à l'utilisation totale du matériau actif. Cependant, la cellule LFP / Li de 3 mm d'épaisseur a fourni 84 mAh / g au taux de C / 20. À des cycles plus lents des vitesses C/100 et C/50, les demi-cellules LFP d'une épaisseur de 2 mm ont respectivement une capacité de surface de 40,5 et 39,2 mAh/cm^2, soit presque 8 fois plus que les électrodes à couche mince classiques.

Développements dans les études d'électrodes épaisses

- Une couche isolante d'alumine sans trou d'épingle avec trois épaisseurs de nanomètre différentes a été appliquée sur la surface de l'électrode LFP en utilisant la technique ALD bien sophistiquée. Une liaison chimique forte a été créée entre la couche de revêtement et l'électrode LFP par la technique de dépôt par couche atomique (ALD). La présence et l'augmentation linéaire de la teneur en alumine ont été caractérisées par la technique EDX. La principale motivation de ce travail est d'améliorer les propriétés mécaniques des électrodes sans liant après cyclage à long terme. Ainsi, l'alumine peut former une couche de passivation uniforme sur des

électrodes LFP épaisses et d'autres études d'indentation seront réalisées dans le futur. Une rétention de capacité stable a été observée pour les électrodes LFP revêtues d'alumine de 1 nm et de 3 nm d'épaisseur (77% et 90%) par rapport à l'électrode LFP d'épaisseur 1 mm non revêtue (32%) après 20 cycles. Le revêtement d'alumine de 5 nm d'épaisseur sur l'électrode LFP présente une rétention de capacité médiocre (13%) due à l'augmentation spectaculaire de l'impédance interfaciale entre les particules de LFP revêtues d'alumine et de carbone à la surface de l'électrode épaisse. Aucune différence significative en termes de capacité de débit n'a été observée entre les électrodes LFP revêtues d'alumine et non revêtues de 1 mm. D'après les premiers résultats obtenus en termes de stabilité chimique améliorée et de propriétés mécaniques accrues obtenues par la technique ALD, l'alumine devrait être un candidat prometteur pour améliorer la rétention de la capacité et les propriétés mécaniques. Une future voie pour améliorer les propriétés mécaniques sera réalisée pour une électrode LTO de 1 mm d'épaisseur utilisant le SPS, qui se révèle moins stable que les électrodes LFP.

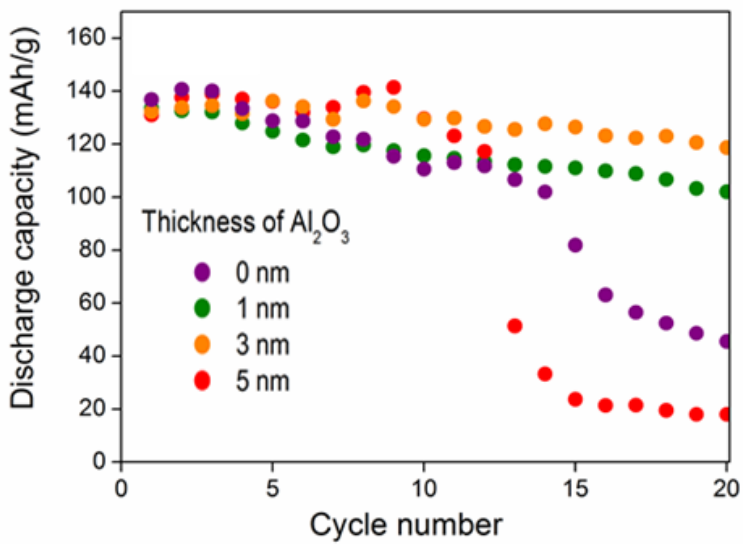

Figure 1.9 a-b Rétention de la capacité des électrodes LFP revêtues d'alumine à l'aide du dépôt par couche atomique (ALD) avec différentes épaisseurs de revêtement.

• De nouvelles conceptions de cellules sont proposées en frittant des matériaux de batterie multicouches tels que LiFePO4 (LFP), $Li_{1.2}Zn_{1.9}Ca_{0.1}(PO_4)_3$ (LCZP) et $Li_4Ti_5O_{12}$ (LTO) en une seule étape en utilisant SPS et la section transversale du la batterie est

illustrée à la figure 1.7. Une batterie pleine (LFP-LCZP-LTO) a été initialement frittée avec les agents de gabarit avec des proportions appropriées dans chaque couche. Après la dissolution complète du NaCl dans chaque couche d'électrode, le premier test électrochimique de la batterie complète utilisant l'électrolyte liquide à C/200 à température ambiante montre le cycle des ions Li entre la couche positive et la couche négative. Le plateau attendu pour la cellule complète a été observé à 1,9 V et a fourni une capacité de décharge de 88 mAh/g dans le premier cycle. D'autres améliorations dans l'optimisation de l'épaisseur de chaque couche d'électrode et de la formulation de chaque couche d'électrode doivent être effectuées pour améliorer les propriétés électrochimiques.

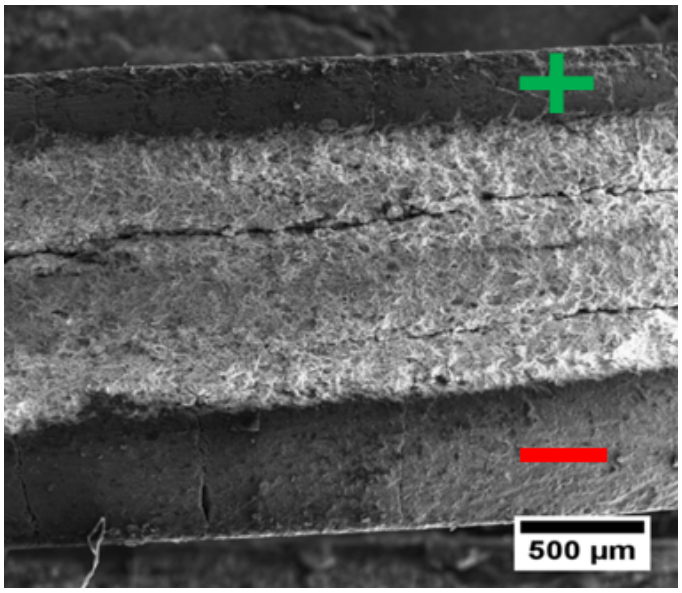

Figure 1.10 a) Image MEB de la section transversale de LFP: LFP: système de batterie LTO montrant une épaisseur de batterie de 2,3 mm avec des interfaces bien formées.

• Une taille de pore à deux couches de l'électrode LFP pour les batteries Li-ion a été fabriquée en utilisant une approche SPS et de modélisation. Deux morphologies de macropores de tailles différentes ont été placées dans des couches discrètes au sein de l'électrode pour obtenir une bonne capacité de débit. La fraction massique soigneusement contrôlée des matières actives a été rapportée. Cette approche aide à assembler la couche de grande taille de pores la plus éloignée du séparateur où les concentrations de lithium sont plus limitées et une électrode de plus petite taille de pores peut être située près du séparateur où les concentrations d'ions lithium sont relativement élevées. Le même concept peut être fait en préparant deux couches denses en optimisant la fraction volumique des pores dans chaque couche discrète. Cette méthodologie est

utilisée pour améliorer la capacité volumétrique et la capacité de débit, ce qui était impossible à réaliser avec une couche d'électrode en soi. Les concentrations locales en ions lithium à travers l'électrode positive peuvent être mesurées directement par spectroscopie de photoélectrons à rayons X (XPS) et les améliorations de la diffusion des ions lithium dans la structure d'électrodes en couches peuvent être évaluées.

• L'approche combinée du SPS et de la modélisation des sels a été appliquée avec succès pour d'autres matériaux actifs tels que les matériaux NVPF et SnSb utilisés pour les batteries au sodium et aux ions lithium. Tout d'abord, les électrodes NVPF avec une épaisseur de près de 1 mm sont fabriquées avec la distribution uniforme de la taille des pores confirmée par les images MEB. Une capacité de surface supérieure de 19,6 mAh / cm^2 a été atteinte pour la cellule NVPF / Na au premier cycle de C/20, comme le montre la figure 1.11. Depuis les premiers résultats, à notre connaissance, cette capacité de surface plus élevée n'a jamais été rapportée dans la littérature et une optimisation plus poussée sera réalisée dans le futur. Nous pensons que cette amélioration des performances des électrodes à base de sodium à des taux de C plus faibles est utile pour alimenter des appareils sécurisés et à petite échelle tels que les chronomètres et les iPad.

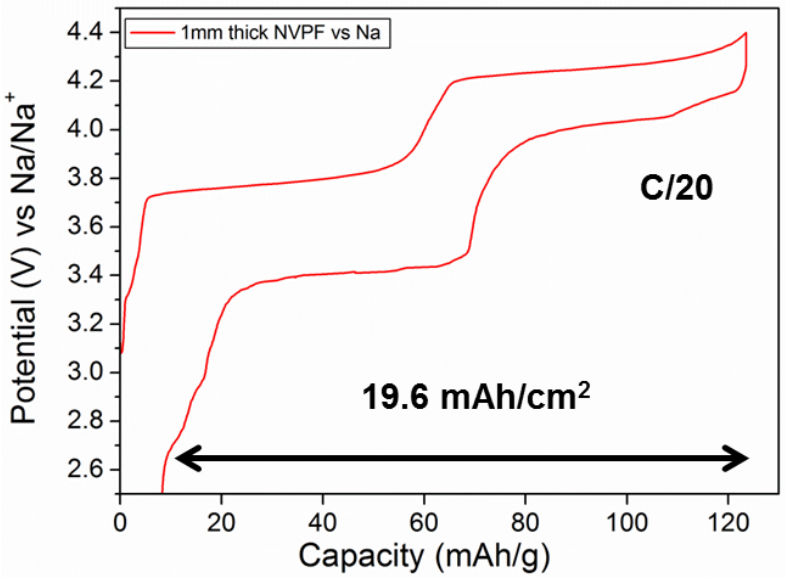

Figure 1.11 Profil de décharge de charge de 1 mm d'épaisseur de NVPF / Na au taux C / 20. Deux plateaux de composition dans la première charge sont observés à 3,7 V et 4,2 V en raison de la désintercalation de deux ions sodium pendant la charge.

- Un autre matériau d'anode, un alliage de Sn-Sb pur, a été préparé en utilisant une méthode de broyage à billes. Ensuite, comme préparé, le matériau SnSb pur a été mélangé avec du NaCl et un composite de carbone conducteur et ensuite densifié en utilisant du SPS. Aucune réaction secondaire du cristal de NaCl avec les substances actives et la dissolution complète des cristaux de NaCl n'a été confirmée par des études par DRX. La première courbe électrochimique de 0,65 mm d'épaisseur Sn-Sb / Li au taux C / 20 montre les plateaux caractéristiques aux potentiels d'oxydation et de réduction respectifs en accord avec la littérature. Une capacité gravimétrique élevée de 714 mAh /g a été atteinte au cours du premier cycle. Cependant, en raison de l'expansion volumique des matériaux à base d'alliage, la cellule s'arrête après le premier cycle mais cela peut être amélioré en minimisant les potentiels de décharge à 1V et en évitant les réactions secondaires telles que la décomposition de l'électrolyte à des potentiels plus faibles proches de zéro. À partir des premiers résultats présentés, nous pensons que cette stratégie SPS et de modélisation sera adoptée pour fabriquer des électrodes épaisses à l'aide d'autres matériaux de batterie et constituer probablement la prochaine génération de batteries lithium-ion à haute densité d'énergie.

Conclusion et perspectives

Cette thèse met en évidence l'influence des propriétés microstructurales et géométriques des électrodes épaisses sur les performances électrochimiques des batteries lithium-ion. Les puissantes techniques multiples telles que la diffraction des rayons X, la microscopie électronique à balayage, la microscopie à transmission X, l'EIS et le cycle Galvansotatic ont été utilisées pour obtenir des informations sur les propriétés texturales et électrochimiques des électrodes épaisses. Dans l'ensemble, les études sur les électrodes épaisses fabriquées par SPS et l'approche par modélisation ont permis d'acquérir de vastes connaissances. Ces informations sont d'une grande importance dans le développement de nouvelles stratégies innovantes pour optimiser les performances électrochimiques afin de répondre à la demande énergétique.

Les électrodes poreuses épaisses fabriquées par SPS et l'approche basée sur les modèles peuvent être améliorées en termes de conditions SPS, de taille d'agents de modélisation et de capacité de débit. Il est nécessaire d'orienter la recherche vers

différentes directions telles que l'agent de structuration, on peut synthétiser et optimiser les nano-agents de calibrage NaCl ou KCl ou CaCl à des températures inférieures à zéro (Ex: -200 ° C) et électrochimiques. la performance des électrodes épaisses peut être étudiée. D'autres polymères conducteurs peuvent également être ajoutés aux matériaux actifs et brûlés pendant le fonctionnement du SPS. Ces matériaux peuvent également agir simultanément comme agent conducteur pour améliorer les performances électrochimiques. Ces approches peuvent être testées pour un choix plus large de matériaux d'électrodes tels que $LiCoO_2$, $LiN_{0.33}Mn_{0.33}CoO_2$ ayant une meilleure conductivité électronique et un faible coefficient de dilatation après cyclage. Une autre stratégie consiste à coupler directement le collecteur de courant métallique au matériau actif lorsqu'il est emballé avec le colorant graphite avant l'opération SPS. La résistance interfaciale entre l'électrode et le collecteur de courant peut être grandement réduite pour améliorer les propriétés électrochimiques.

Une autre perspective peut être l'imprégnation d'électrolyte à l'intérieur des électrodes épaisses positives et négatives en incorporant de l'ionogel mou dans les pores des électrodes épaisses. Cela peut améliorer les aspects de sécurité en négligeant les électrolytes liquides combustibles. Bien que la couche d'alumine isolante ait été appliquée sur la surface des électrodes LFP pour améliorer les propriétés mécaniques, des matériaux conducteurs d'ions peuvent être revêtus pour améliorer la diffusion des ions lithium à travers la couche mince lorsqu'ils sont soumis à des taux C élevés. Par conséquent, les couches de Li_3PO_4 conductrices des ions lithium sont revêtues en utilisant la technique ALD avec cinq épaisseurs différentes sur les électrodes LFP de 1 mm d'épaisseur. Les performances électrochimiques des électrodes LFP revêtues et non revêtues seront testées dans le futur. Les principaux avantages de cette approche sont 1) l’amélioration de la capacité de débit en améliorant la conductivité des ions lithium à des débits plus élevés; 2) améliorer l'interface électrode / électrolyte pour obtenir un meilleur contact physique, une plus grande stabilité et une polarisation

réduite. Cette approche sera effectuée pour que les électrodes LTO moins stables mécaniquement améliorent encore les propriétés électrochimiques.

Dans l'ensemble, ce travail de thèse introduit le concept de la fabrication d'électrodes épaisses en utilisant l'approche SPS et de modèles ainsi que des résultats importants. Le projet sera repris par un nouveau doctorant débutant en octobre 2018 avec la collaboration du LRCS, d'Amiens et de l'Université de Toulouse. La même approche peut s'appliquer à l'avenir avec différents couples d'électrodes possédant un potentiel de cellule global plus élevé et une densité énergétique élevée des batteries au lithium-ion. D'un point de vue industriel, nous pensons que l'approche combinée du SPS / de la création de modèles présente un grand intérêt pour un large public pour les fabricants et les ingénieurs de micro-batteries. Nous espérons que notre travail les encouragera à explorer davantage de nouveaux appareils électroniques portables tels que les téléphones portables et les ordinateurs portables.

Les références :

[1] International Energy Agency, https://www.iea.org/ (accessed July 11, 2017).

[2] B. Dunn, H. Kamath, J.-M. Tarascon, Electrical Energy Storage for the Grid: A Battery of Choices, Science. 334 (2011) 928–935. doi:10.1126/science.1212741.

[3] H. Zheng, J. Li, X. Song, G. Liu, V.S. Battaglia, A comprehensive understanding of electrode thickness effects on the electrochemical performances of Li-ion battery cathodes, Electrochimica Acta. 71 (2012) 258–265. doi:10.1016/j.electacta.2012.03.161.

Summary

The achievement of energy storage and return of energy supply is crucial for several applications (EVs, cellphones, laptops). Thick electrodes with minimized inactive materials in the overall battery can improve the energy density of lithium ion batteries. Spark Plasma Sintering is an advanced densification technique has been used to prepare thick electrodes in minutes. The templating approach is adopted for preparing porous electrodes with interconnected well-controlled pore sizes and morphologies. Herein, sodium chloride micro-sized particles are used as a templating agent to create pores inside the thick electrodes. These sintered binder-free electrodes are self-supported that helps to increase the energy density of lithium ion batteries. The electrochemical performances of half and full batteries reveal a remarkable specific areal capacity (20 mA h cm^{-2}), which is 4 times higher than those of 100 μm thick electrodes present in conventional tape-casted Li–ion batteries (5 mA h cm^{-2}). The 3D morphological study is carried out by micro computed tomography to obtain tortuosity values and pore size distributions leading to a strong correlation with their electrochemical properties. These results demonstrate that the coupling between the salt templating method and the spark plasma sintering is also applied for thick electrodes fabrication using other active materials and also different cell configurations are proposed.
Key-words: Thick electrode, binder free, Spark Plasma Sintering, templating, lithium.

Résumé

La réalisation du stockage d'énergie et le retour de l'approvisionnement en énergie est crucial pour plusieurs applications (VE, téléphones portables, ordinateurs portables). Des électrodes épaisses avec des matériaux inactifs minimisés dans la batterie globale peuvent améliorer la densité d'énergie des batteries lithium-ion. Le frittage flash ou « Spark Plasma Sintering » est une technique de densification avancée qui a été utilisée pour préparer des électrodes épaisses en quelques minutes. Une approche dite de « templating » est adoptée pour préparer des électrodes poreuses avec des tailles de pores et des morphologies interconnectées bien contrôlées. Ici, des particules micrométriques de chlorure de sodium sont utilisées comme agent prorogène pour créer la porosité à l'intérieur des électrodes épaisses. Ces électrodes frittées sans liant sont autosupportées, ce qui contribue à augmenter la densité énergétique des batteries lithium-ion. Les performances électrochimiques des batteries révèlent une capacité surfacique remarquable (20 mA h cm^{-2}), ce qui est 4 fois supérieur à celle des électrodes conventionnelles de 100 μm présentes dans les batteries Li-ion classiques (5 mAh cm^{-2}). L'étude morphologique 3D des électrodes poreuses est réalisée par tomographie X afin de remonter aux valeurs de tortuosité et de distributions de tailles de pores, afin de corréler propriétés électrochimiques et structure d'électrode.

Mots-clés: Électrode épaisse, sans liant, frittage flash, templating, lithium.